



University of HUDDERSFIELD

University of Huddersfield Repository

Opoz, Tahsin Tecelli

Investigation of Material Removal Mechanism in Grinding: A Single Grit Approach

Original Citation

Opoz, Tahsin Tecelli (2012) Investigation of Material Removal Mechanism in Grinding: A Single Grit Approach. Doctoral thesis, University of Huddersfield.

This version is available at <http://eprints.hud.ac.uk/id/eprint/17818/>

The University Repository is a digital collection of the research output of the University, available on Open Access. Copyright and Moral Rights for the items on this site are retained by the individual author and/or other copyright owners. Users may access full items free of charge; copies of full text items generally can be reproduced, displayed or performed and given to third parties in any format or medium for personal research or study, educational or not-for-profit purposes without prior permission or charge, provided:

- The authors, title and full bibliographic details is credited in any copy;
- A hyperlink and/or URL is included for the original metadata page; and
- The content is not changed in any way.

For more information, including our policy and submission procedure, please contact the Repository Team at: E.mailbox@hud.ac.uk.

<http://eprints.hud.ac.uk/>

Investigation of Material Removal Mechanism in Grinding:

A Single Grit Approach

TAHSIN TECELLI OPOZ

A thesis submitted to the University of Huddersfield

in partial fulfilment of the requirements for

the degree of Doctor of Philosophy

The University of Huddersfield

August 2012

Copyright Statement

- i. The author of this thesis (including any appendices and/or schedules to this thesis) owns any copyright in it (the “Copyright”) and s/he has given The University of Huddersfield the right to use such Copyright for any administrative, promotional, educational and/or teaching purposes.
- ii. Copies of this thesis, either in full or in extracts, may be made only in accordance with the regulations of the University Library. Details of these regulations may be obtained from the Librarian. This page must form part of any such copies made.
- iii. The ownership of any patents, designs, trademarks and any and all other intellectual property rights except for the Copyright (the “Intellectual Property Rights”) and any reproductions of copyright works, for example graphs and tables (“Reproductions”), which may be described in this thesis, may not be owned by the author and may be owned by third parties. Such Intellectual Property Rights and Reproductions cannot and must not be made available for use without the prior written permission of the owner(s) of the relevant Intellectual Property Rights and/or Reproductions.

Abstract

This thesis has investigated material removal mechanisms in grinding by considering single grit-workpiece interaction. The investigation was performed both experimentally and using finite element simulation. Rubbing, ploughing and cutting mechanisms occurring during the grinding process were studied at the micro scale. Due to its nature the rubbing phase occurs in a very narrow region of grit-workpiece engagement and is difficult to examine under a microscope and so was investigated using FEM simulation. The ploughing mechanism was thoroughly investigated using both experimental tests and FEM simulations, and a similar trend was observed for the pile up ratio along the scratch path from the experimental tests and the FEM simulations. Ploughing and cutting mechanisms in grinding were found to be highly influenced by grit cutting edge shape, sharpness and bluntness. Cutting is the prominent mechanism when the grit cutting edge is sharp, but ploughing is more prominent when the grit cutting edge becomes flattened. In the case of multiple edges scratch formation, ploughing is dramatically increased compared to single edge scratches. Feasibility of ground surface simulation using FEM is demonstrated using multiple pass scratch formation in a cross direction. Although chip formation mechanism is developed at a relatively higher depth of cut (greater than 10 μm), at small scales down to 1 μm , FEM simulation was not a suitable method to use. To reduce the drawbacks of FEM simulation in micro scale cutting, a meshless simulation technique such as smooth particle hydrodynamics is recommended for future studies.

Publications

Journals:

1. T. T. Öpöz and X. Chen (2012) 'Experimental investigation of material removal mechanism in single grit grinding', *International Journal of Machine Tools and Manufacture*, Vol. 63, pp. 32-40.
2. T. T. Öpöz and X. Chen (2012) 'Influential Parameters in Determination of Chip Shape in High Speed Machining', *Key Engineering Materials*, Vol. 496, pp: 211-216
3. X. Chen, T. T. Öpöz and A. Oluwajobi, (2012), 'Grinding Surface Creation Simulation Using Finite Element Method and Molecular Dynamics', *Advanced Materials Research*, Vol. 500, pp. 314-319.
4. X. Chen and T. T. Öpöz (2010) 'Simulation of Grinding Surface Creation – A Single Grit Approach' *Advanced Materials Research*, Vol.126, pp. 23-28.

Conferences:

1. X. Chen, T.T. Öpöz and A. Oluwajobi, 'Grinding surface creation simulation using finite element method and molecular dynamics', *The 10th Asia-Pacific Conference on Materials Processing (APCMP2012)*, Jinan, China, 14-17 June 2012.
2. T. T. Öpöz and X. Chen (2011) 'Single grit grinding simulation by using finite element analysis' *American Institute of Physics Conf. Proc: Advances in Materials and Processing Technologies AMPT2010 International Conference*, Vol.1315 (1), pp. 1467-1472
3. T. T. Öpöz and X. Chen (2011) 'Process monitoring and metrology for single grit grinding performance' In: *Proceeding of the 17th Int. Conference on Automation & Computing*, University of Huddersfield, Huddersfield, UK, 10 September 2011. pp. 143-148
4. T. T. Öpöz and X. Chen (2011) 'Influential parameters in determination of chip shape in high speed machining' *6th Int. Congress on Precision Machining*, Liverpool John Moores University, Liverpool, UK. 13-15 September 2011
5. T. T. Öpöz and X. Chen (2010) 'Finite element simulation of chip formation '. In: *Future Technologies in Computing and Engineering: Proceedings of Computing and Engineering Annual Researchers' Conference 2010: CEARC'10*. Huddersfield: University of Huddersfield. pp. 166-171. ISBN 9781862180932
6. T. T. Öpöz and X. Chen (2010) 'An Investigation of the rubbing and ploughing in single grain grinding using finite element method'. In: *8th International Conference on Manufacturing Research*, 14-16 Sept 2010, Durham, UK, pp. 256-261

7. T. T. Öpöz and X. Chen (2010) 'Numerical simulation of single grit grinding'. In: Proceeding of the 16th International Conference on Automation & Computing, 11 Sept 2010, Birmingham, UK , pp. 136-140
8. X. Chen and T. T. Öpöz (2010) 'Simulation of grinding surface creation – A single grit approach'. In: The 13th International Symposium on Advances in Abrasive Technology (ISAAT 2010), 19-22 September 2010, Taipei, Taiwan
9. T. T. Öpöz and X. Chen (2009) 'Finite element simulation of grinding process and micro-scale abrasive wear'. In: Proceedings of Computing and Engineering Annual Researchers' Conference 2009: CEARC'09. Huddersfield: University of Huddersfield. pp. 165-171. ISBN 9781862180857

Table of Contents

Chapter 1 Introduction	26
1.1 Motivation	26
1.2 Aim and objectives	28
1.3 Outline of the thesis.....	30
Chapter 2 Grinding Process Technology	32
2.1 Introduction	32
2.2 Fundamentals of machining process	32
2.3 Background to the grinding process	36
2.4 Abrasives	38
2.5 Dressing.....	39
2.6 Material removal mechanism in grinding.....	41
2.6.1 Material removal at the macro level for the grinding wheel working surface	42
2.6.2 Material removal at the micrometre scale due to single grit action	44
2.6.3 Size effect in grinding	57
2.7 Summary.....	60
Chapter 3 Modelling and Simulation of the Grinding Process Using FEM	63
3.1 Introduction	63
3.2 Finite element method approach for modelling material removal	67
3.2.1 Fundamental of finite element method.....	67
3.2.2 Numerical formulation	74
3.2.3 Newton-Raphson iteration method.....	79
3.2.4 Time integration methods.....	80
3.3 Finite element simulation of chip formation in literature.....	82
3.3.1 Commonly used constitutive material models for FEM cutting simulation	82
3.3.1.1 Johnson-Cook material model.....	83
3.3.1.2 Modified Johnson-Cook material model by Calamaz	85

3.3.1.3 Modified Johnson-Cook material model by Sima and Özel	86
3.3.1.4 Flow stress model used by Childs	87
3.3.1.5 Flow stress model of Rhim and Oh	88
3.3.2 Influential factors in chip formation.....	91
3.3.3 Chip separation criteria	93
3.3.4 Friction scheme in FEM simulation	96
3.3.5 Chip generation based on FEM models in the literature	97
3.4 Finite element simulation of grinding process in literature.....	99
3.4.1 Wheel-workpiece interaction approach.....	99
3.4.2 Single grit-workpiece interaction approach.....	103
3.5 Summary.....	115
 Chapter 4 Methodology of Single Grit Grinding Investigation	 117
4.1 Introduction	117
4.2 Single grit grinding approach	118
4.3 Establishment of single grit grinding test setup	120
4.3.1 Description of machining centre used for single grit grinding tests.....	120
4.3.2 Single grit grinding test setup.....	121
4.4 Establishment of single grit grinding tests	123
4.4.1 Abrasive grit material.....	124
4.4.2 Workpiece material properties	125
4.4.3 Workpiece surface preparation.....	126
4.5 Single grit grinding methods	129
4.5.1 Longitudinal scratching.....	130
4.5.2 Traverse scratching.....	132
4.6 Process monitoring setup.....	134
4.6.1 Acoustic emission.....	136
4.6.2 Cutting force measurement	139

4.6.3 Specific energy calculation.....	144
4.7 Single grit scratch measurement method.....	146
4.7.1 White light interferometer	146
4.7.2 Scratch profile extraction by using CCI interferometer	146
4.8 Methodology of material removal mechanisms in single grit scratching.....	151
4.9 Summary.....	153
 Chapter 5 FEM Simulation Development.....	 154
5.1 Introduction	154
5.2 Framework of the FEM simulation	155
5.3 Finite element model of cutting regarding orthogonal cutting mechanism.....	157
5.3.1 Material selection	157
5.3.2 Workpiece, cutting tool model and boundary conditions.....	158
5.3.3 Element shape and meshing	160
5.3.4 Material flow behaviour	161
5.3.5 Material damage model	162
5.3.6 Application of element deletion technique.....	169
5.3.7 Contact, friction and heat generation	170
5.3.8 Summary of cutting FEM simulation procedure	172
5.4 Some cutting simulations using Deform3D	172
5.4.1 Case-1	174
5.4.2 Case-2.....	175
5.4.3 Case-3.....	177
5.4.4 Summary of the Deform3D simulations	178
5.5 Single grit grinding finite element model.....	179
5.5.1 Computational method	180
5.5.2 Grit geometry and workpiece design.....	180
5.5.3 Design of simulation to represent single and multiple grit scratching	181
5.5.4 Element shape and adaptive remeshing.....	184

5.5.5 Materials and elastic-plastic behaviour	187
5.5.6 Friction and contact description	188
5.5.7 Analysis strategy of the results.....	188
5.6 Working and non-working zone of the FEM simulations	189
5.7 Summary.....	192
Chapter 6 Experimental Investigation of Single Grit Grinding	193
6.1 Introduction	193
6.2 Material removal mechanisms in terms of pile-up ratio and chip removal strength	194
6.2.1 En24T steel.....	194
6.2.2 Inconel alloy 718	205
6.2.3 En8 steel	212
6.2.4 Material removal mechanism along a single scratch path.....	214
6.2.5 Effective grit engaging radius	223
6.3 Cutting forces during single grit grinding	230
6.4 Specific energy in single grit grinding	237
6.5 Summary.....	241
Chapter 7 Finite Element Simulation Results.....	244
7.1 Introduction	244
7.2 FEM simulation of chip formation	244
7.2.1 Influence of fracture energy on chip formation.....	247
7.2.2 Influence of depth of cut on chip shape.....	248
7.2.3 Chip type with varying rake angles	249
7.2.4 Chip breakage during serrated chip formation	251
7.2.5 Chip fracture when using high negative rake angle	252
7.2.6 Temperature during chip formation	255
7.2.7 Plastic strain and strain rate	258
7.2.8 Summary of cutting simulations.....	260
7.3 Single grit FEM simulation results.....	262

7.3.1 First group simulations: Using artificially created plastic properties.....	263
7.3.1.1 Simulation conditions.....	263
7.3.1.2 Elastic-plastic deformation.....	265
7.3.1.3 Multiple-pass simulation to represent ground surface creation.....	269
7.3.1.4 Friction effects on deformation.....	272
7.3.1.5 Force analysis.....	277
7.3.2 Second group simulations: Using CBN grit properties.....	280
7.3.2.1 Simulation conditions.....	280
7.3.2.2 Simulation results.....	282
7.3.2.3 Force analysis.....	288
7.3.3 Third group simulations: Using AISI4340 steel and CBN grit properties.....	290
7.3.3.1 Simulation conditions.....	290
7.3.3.2 Simulation results.....	292
7.3.3.3 Force analysis.....	298
7.3.3.4 A simulation using a grit radius of 250 μm	299
7.3.4 Comparison of FEM simulation results with single grit grinding experiments.....	304
7.3.5 Summary.....	306
Chapter 8 Conclusive Discussion.....	308
Chapter 9 Conclusions and Suggestions for Future Work.....	312
9.1 Conclusions.....	312
9.2 Possible future work.....	314
References.....	317

The total number of words in the thesis count as 63,959

List of Figures

Figure 2.1 Merchant's orthogonal cutting model (Merchant, 1945)	33
Figure 2.2 Three types of chips (a) continuous chips (b) serrated (or saw tooth) chips and (c) discontinuous chips obtained from different materials with different machining conditions (Childs et al., 2000)	35
Figure 2.3 Schematic of up-cut surface grinding with important process parameters	37
Figure 2.4 The variation of Knoop hardness with temperature for several hard materials: 1, diamond; 2, CBN; 3, SiC; 4, varieties of Al_2O_3 ; 5, tungsten carbide (92 w/o WC, 8 w/o Co) (after Loladze and Bockuchava 1972; Shaw, 1996)	38
Figure 2.5 Single point dressing with a stationary non-rotating dressing tool (a) single point dressing tool and (b) single point traverse dressing, where f_d is a dressing feed per revolution of grinding wheel, b_d is a width of the dressing tool, a_d is a dressing depth of cut (Rowe, 2009)	40
Figure 2.6 Rubbing, ploughing and cutting at different grain penetrations through the arc of contact	46
Figure 2.7 Machining with negative rake angle (Komanduri, 1971)	47
Figure 2.8 (a) Hardness indentation with a spherical indenter, a is the contact radius due hardness indentation, R indentation load, (b) indentation at the tip of an abrasive grit with a radius of curvature at the grit tip= ρ and resultant force R' inclined at angle α to the vertical. The deformed chip thickness is t_c and the cutting ratio is t/t_c , V_c is the cutting speed (Shaw, 1996)	48
Figure 2.9 Micrograph in (A) and schematic in (B) representing material deformation characteristic in front-ridge formed during partial scratching (Wang et al., 2001) (Cont. in next page)	53
Figure 2.10 Variation of specific energy with maximum grit depth of cut into the workpiece (a) hardness R_C32 and (b) hardness R_C60 (Ghosh et al., 2008)	60
Figure 3.1 Simulation category of abrasive process (Brinksmeier et al., 2006)	65
Figure 3.2 Finite element method illustration for a mechanical problem (Childs et al., 2000)	68
Figure 3.3 Illustration of principal stresses and principal strain increments (Childs et al., 2000)	71
Figure 3.4 Eulerian and Lagrangian view of plastic flow (Childs et al., 2000)	74
Figure 3.5 Finite element model boundary conditions for ALE formulation (Özel and Zeren, 2007)	77

Figure 3.6 Relocation of a node during a mesh sweep	78
Figure 3.7 Macro scale FEM model description (a) illustration of grinding wheel-workpiece interaction (b) illustration of FEM model (c) different heat flux distribution used as heat source in the FEM model (Klocke, 2003)	101
Figure 3.8 Illustration of (a) rubbing, (b) ploughing, and (c) chip formation phases of material removal by an individual grit (Doman et al., 2009 ^a)	104
Figure 3.9 Temperature distribution during chip formation of single grit scratching (Klocke et al., 2002)	108
Figure 3.10 Single grit grinding simulation (a) 2D and (b) 3D model (Klocke, 2003)	108
Figure 3.11 (a) Workpiece mesh and (b) simulation results (Anderson et al., 2012).	112
Figure 3.12 Schematic of the effect of the minimum chip thickness (R_e , radius of cutting tool; h , undeformed chip thickness; h_m , minimum chip thickness) (Chae et al., 2006)	113
Figure 4.1 Schematic of grinding process (N: Wheel rotational speed, rpm; V_f : Work table speed (or feed) mm/min)	118
Figure 4.2 Schematic of single grit grinding action (F_n : normal force; F_t : tangential force; N: rotational cutting speed, rpm; V_f : work table speed or feed, mm/min; a_p : undeformed chip thickness)	119
Figure 4.3 Simple schematic of research method	120
Figure 4.4 View from machining centre (Nanoform250 ultra grind)	121
Figure 4.5 Single grit grinding setup of Nanoform250 ultra grind machine centre	122
Figure 4.6 Picture of single grit grinding test with Inconel 718 workpiece	124
Figure 4.7 CBN grit (40/50 mesh size) used for single grit grinding tests	125
Figure 4.8 CBN grit (40/50 mesh size) glued onto the circumferential surface of the steel wheel	125
Figure 4.9 Schematic illustration of workpiece surface preparation before single grit grinding	128
Figure 4.10 Insitu surface grinding to improve flatness of the workpiece surface	129
Figure 4.11 En24T workpiece surface (a) after in-situ grinding and (b) after in-situ polishing process ($S_a = 90$ nm)	129
Figure 4.12 Schematic of longitudinal scratching	131
Figure 4.13 Longitudinal scratches on En8 steel	131
Figure 4.14 Traverse scratching on tilted surface	133

Figure 4.15 Scratches on Inconel 718 performed with traverse scratching method	133
Figure 4.16 Schematic of process monitoring setup	135
Figure 4.17 Photo of process monitoring devices	135
Figure 4.18 Signal/noise characteristics of AE and force/vibration sensors for different uncut chip thicknesses (Dornfield, 1999).	136
Figure 4.19 Pencil lead break test: (a) raw signal, (b) power spectrum (dB)	138
Figure 4.20 Force sensor calibration graphs for Labview and oscilloscope measurement	140
Figure 4.21 Labview block diagram for force acquisition	141
Figure 4.22 Forces recorded with Labview software ($V_c = 327.6$ m/min on En24T workpiece)	143
Figure 4.23 (a) Forces recorded with oscilloscope and (b) associated single grit scratches (not all scratches seen in the figure) performed at speed of 3000 rpm ($V_c = 327.6$ m/min on En24T workpiece) and table speed of 1250 mm/min	143
Figure 4.24 Force measurement and single grit scratch at low speed of 10 rpm on En24T steel workpiece	144
Figure 4.25 Three scratches after non-measured points filled. 1 st line shows longitudinal profile extraction direction to find deepest point, 2 nd line shows the section profile extraction direction using deepest point	148
Figure 4.26 (a) Longitudinal profile of the middle scratch shown in Figure 4.26 and (b) cross-section profile of scratches extracted by using deepest point coordinate in the direction of 2 nd line in Figure 4.25	148
Figure 4.27 Example of 3D profile of scratches using Talysurf CCI 3000	149
Figure 4.28 Cross-sectional profiles of single and multiple scratches produced with one pass of grit-workpiece interaction	150
Figure 4.29 Pile-up and groove section area for (a) one scratch at one pass, and (b) multiple scratches at one pass	151
Figure 4.30 Schematic view of a scratch cross-section profile	152
Figure 5.1 Procedures for finite element simulations performed in this study	157
Figure 5.2 Workpiece - tool FEM model schematic description	159
Figure 5.3 Illustration of cutting tools with different rake angles	159
Figure 5.4 Flow stress curves with temperature and strain rate data using Johnson-Cook flow stress model	162

Figure 5.5 Damage initiation during chip formation (JCCRT: Johnson-Cook damage initiation value or w in Equation (5.2))	164
Figure 5.6 Stress-strain curve illustrating damage evolution using progressive damage model	166
Figure 5.7 Crack toughness (K_{IC}) versus section size (Sisto et al., 1964)	168
Figure 5.8 Element degradation (SDEG) based on damage evolution during chip simulation	170
Figure 5.9 3D chip formation using Deform3D with cutting force and operating parameters	173
Figure 5.10 3D chip formation and JC flow stress properties used in the simulation	174
Figure 5.11 Cutting simulation attempt with 4 μm depth of cut using pyramid shape cutting tool	175
Figure 5.12 Cutting simulation with depth of cut of 16 μm using pyramid shape cutting tool	176
Figure 5.13 Cutting simulation using pyramid shape tool with depth of cut of 10 μm with cutting face consisting of the sharp edge at junction of two flat faces	178
Figure 5.14 Workpiece and grit body modelled in Abaqus/CAE	181
Figure 5.15 Grit trajectories used in FEM simulations	182
Figure 5.16 Longitudinal cross sectional profile of the single grit scratch at low speed ($V_c = 10.8$ m/min, $V_f=200$ mm/min)	183
Figure 5.17 Illustration of the multi pass grit simulation	184
Figure 5.18 Adaptive remeshing procedure in Abaqus/CAE	185
Figure 5.19 Remeshing rules defined for the single grit simulation	186
Figure 5.20 Remeshing the workpiece with iterative adaptive remeshing technique	187
Figure 5.21 Illustrative picture to show working and non-working zone of the FEM simulations	191
Figure 6.1 Variation of pile-up ratio with depth of cut (flat cutting edge)	195
Figure 6.2 Variation of pile-up ratio with groove area (flat cutting edge)	196
Figure 6.3 Chip removal strength versus depth of cut (flat cutting edge)	196
Figure 6.4 Variation of pile-up ratio with depth of cut (sharp cutting edge)	197
Figure 6.5 Variation of pile-up ratio with groove area (sharp cutting edge)	197
Figure 6.6 Chip removal strength versus depth of cut (sharp cutting edge)	199
Figure 6.7 Scratches with two different cutting edges (related to Figure 6.9)	200

Figure 6.8 Scratch form shape evolution (or grit cutting shape change because of grit wear) in a single grit scratch test (totally 28 scratches)	200
Figure 6.9 Variation in pile-up ratio with depth of cut (two different cutting edges)	201
Figure 6.10 Pile-up ratio variation with groove area (two different cutting edges)	201
Figure 6.11 Schematic illustration of multiple cutting edges causing high pile-up ratio	202
Figure 6.12 Chip removal strength versus depth of cut (two different cutting edges)	203
Figure 6.13 Variation in pile-up ratio with depth of cut (multiple cutting edges) at $V_c=327.6$ m/min	204
Figure 6.14 Variation in pile-up ratio with depth of cut (multiple cutting edges) at $V_c=109.2$ m/min	204
Figure 6.15 Variation in pile-up ratio with groove area (multiple cutting edges) at $V_c=109.2$ m/min	205
Figure 6.16 Pile-up ratio variation with depth of cut (Inconel 718 workpiece)	206
Figure 6.17 Pile-up ratio variation with groove area (Inconel 718 workpiece)	206
Figure 6.18 Chip removal strength versus depth of cut (Inconel 718 workpiece)	208
Figure 6.19 Pile-up ratio versus depth of cut (two scratches at every grit-workpiece interaction: one placed above the trend line acts sharper; another one placed below the trend line acts blunt)	210
Figure 6.20 Pile-up ratio versus groove area (two scratches at every grit-workpiece interaction: one placed above the trend line acts sharper; another one placed below the trend line acts blunt)	210
Figure 6.21 Pile-up ratio versus depth of cut (two scratches at every grit-workpiece interaction)	211
Figure 6.22 Pile-up ratio versus groove area (two scratches at every grit-workpiece interaction)	211
Figure 6.23 Pile-up ratio versus depth of cut (single edge scratches on En8 steel)	213
Figure 6.24 Pile-up ratio versus groove area (single edge scratches on En8 steel)	213
Figure 6.25 Chip removal strength versus depth of cut (single edge scratches on En8 steel)	214
Figure 6.26 3D view of a scratch with (a) lateral cross section, (b) longitudinal cross section	216
Figure 6.27 Variation of pile-up ratio along a scratch in the longitudinal direction	217
Figure 6.28 Pile-up ratio versus depth of cut along a single scratch	218

Figure 6.29 Chip removal strength versus depth of cut along a single scratch	219
Figure 6.30 3D view of single scratch (a) lateral cross-section, (b) longitudinal cross-section	220
Figure 6.31 Variation of pile-up ratio along scratch length	221
Figure 6.32 Pile-up ratio versus depth of cut along scratch length	221
Figure 6.33 Chip removal strength versus depth of cut along scratch path	223
Figure 6.34 Effective grit engaging radius for ideal sphere shape grit	224
Figure 6.35 Effective grit engaging radius variation with depth of cut (flat cutting edge)	226
Figure 6.36 Effective grit engaging radius versus groove area (flat cutting edge)	226
Figure 6.37 Pile-up ratio versus effective grit engaging radius (flat cutting edge)	227
Figure 6.38 Effective grit engaging radius versus depth of cut (sharp cutting edge)	227
Figure 6.39 Effective grit engaging radius versus groove area (sharp cutting edge)	228
Figure 6.40 Pile-up ratio versus effective grit engaging radius (sharp cutting edge)	228
Figure 6.41 Effective grit contact radius versus depth of cut (single and multiple cutting edges)	229
Figure 6.42 Pile-up ratio versus effective grit engaging radius (single and multiple cutting edges)	229
Figure 6.43 Cutting forces versus depths of cut measured using Labview software	231
Figure 6.44 Cutting forces versus groove area measured using Labview software	231
Figure 6.45 Force ratio (F_n/F_t) for Labview measurements	232
Figure 6.46 Cutting forces recorded with oscilloscope versus depth of cut	233
Figure 6.47 Cutting forces recorded with oscilloscope versus groove area	234
Figure 6.48 Cutting forces recorded with oscilloscope versus depth of cut for single and multiple edge scratches	235
Figure 6.49 Cutting forces recorded with oscilloscope versus groove area for single and multiple edge scratches	236
Figure 6.50 Force ratio (F_n/F_t) versus groove area for forces recorded with oscilloscope	237
Figure 6.51 Specific energy versus depth of cut (Labview data)	238
Figure 6.52 Specific energy versus groove area (Labview data)	238

Figure 6.53 Specific energy versus depth of cut (oscilloscope data)	239
Figure 6.54 Specific energy versus groove area (oscilloscope data)	239
Figure 6.55 Specific energy versus depth of cut with different cutting edges	240
Figure 6.56 Specific energy versus groove area with different cutting edges	241
Figure 7.1 Chip simulation with varying fracture energy	248
Figure 7.2 Chip formation with different depths of cut	249
Figure 7.3 Chip shape variation alteration with change of rake angle	250
Figure 7.4 Chip breakage during serrated chip formation ($G_f=1500$ N/m, $h=20$ μ m, $\gamma=0^\circ$, $V_c = 300$ m/min, material: Aluminium alloy)	251
Figure 7.5 Chip fracture development at high negative rake angle ($G_f=1500$ N/m, $h=20$ μ m)	253
Figure 7.6 Primary and secondary shear zone demonstration at negative rake angle cutting (a) stress demonstration (b) element degradation (SDEG) demonstration (Cont. in next page)	254
Figure 7.7 Temperature changes during chip formation ($G_f=1500$ N/m, $h=20$ μ m, temperature unit is in $^\circ$ C)	257
Figure 7.8 Temperature changes with fracture energy during chip formation (Rake angle= 22° , $h=20$ μ m, temperature is in $^\circ$ C)	258
Figure 7.9 Plastic strain rate (ER11) distribution ($G_f = 1500$ N/m, $h = 20$ μ m)	259
Figure 7.10 Equivalent plastic strain (PEEQ) distribution with various rake angles ($G_f= 1500$ N/m, $h=20$ μ m)	260
Figure 7.11 Grit and workpiece model for the set of simulations in this group	265
Figure 7.12 Single grit trajectory during simulation using five steps	265
Figure 7.13 Stress and elastic-plastic deformation state representation (frictionless simulation result longitudinal representation of scratch)	266
Figure 7.14 Rubbing phase demonstration using plastic strain contour as an indicator (frictionless simulation result)	268
Figure 7.15 Rubbing phase demonstration using heavily deformation region as an indicator (frictionless simulation result)	269
Figure 7.16 Simulated multiple pass surface creation	270
Figure 7.17 Deformation in the simulation of three parallel scratch passes 10 μ m apart.	271

Figure 7.18 Multi-pass scratch profiles	271
Figure 7.19 Scratches formed using different friction coefficients (sectional view from longitudinal direction)	272
Figure 7.20 Ploughing action profiles taken from the cross-section at the end of step-3	273
Figure 7.21 Scratch cross-section profiles (a) at the end of step-2 and (b) at the end of step-3 using different friction coefficient	275
Figure 7.22 Cross section profiles of the scratches using different friction coefficient	276
Figure 7.23 Pile-up ratio at the end of step-2 and step-3 using different friction coefficients	277
Figure 7.24 Single grit simulation path with depth and horizontal distance demonstration	278
Figure 7.25 Force components for multi pass simulation (frictionless condition)	279
Figure 7.26 Force components: frictionless and friction coefficient of 0.5	279
Figure 7.27 Variation in total force (absolute values) with friction coefficient and cross-pass scratching	280
Figure 7.28 Grit-workpiece model used in the second group simulations	281
Figure 7.29 A view during grit advancement showing accumulation of workpiece material in front and side of grit ($a_p = 2 \mu\text{m}$ and $\mu = 0$)	282
Figure 7.30 Simulation of grit progress at first indentation, middle and end of simulation (frictionless; $a_p = 5 \mu\text{m}$)	283
Figure 7.31 Deformation due to ploughing effects with single grit simulation (a_p : maximum depth)	284
Figure 7.32 Cross-section profiles of the simulations using CBN grit (see Figure 7.33 for the analyses of profiles)	285
Figure 7.33 Pile-up ratio along scratch length using different maximum depths and friction coefficients	287
Figure 7.34 Pile-up ratio versus groove area at different steps along scratch length	288
Figure 7.35 Variation in total force along grit simulation path	289
Figure 7.36 Total forces with respect to groove area (simulated frictionless condition)	290
Figure 7.37 Grit trajectory with three steps used in the simulation	292
Figure 7.38 First contact and deformation along scratch using grit with radius of $20 \mu\text{m}$ and horizontal speed of 300 m/min	292

Figure 7.39 Overlapped cross-section profiles at different grit speeds; at the end of step-1 (a), and at the end of step-2 (b)	293
Figure 7.40 Cross section profiles at the end of step-1 and step-2 using different speeds	295
Figure 7.41 Pile-up ratio versus grit horizontal speed, at the end of step-1 and step-2	296
Figure 7.42 Cross -section profiles obtained (a) at the end of step-1 and (b) at the end of step-2 with stress distribution (Grit radius=20 μm and horizontal speed= 300 m/min)	297
Figure 7.43 Forces along the scratch length at different speed (max. depth (a_p) was set to 1 μm disregarding the indentation due to grit asperity which is also around 0.4 μm)	299
Figure 7.44 Simulation model using grit radius of 250 μm and speed of 300 m/min	301
Figure 7.45 Cross section profiles (a) at the end of step-1 and (b) at the end of step-2 for the grit having radius of 250 μm and speed of 300 m/min	301
Figure 7.46 Force variation along grit trajectory for the grit having radius of 250 μm and speed of 300 m/min	302
Figure 7.47 Cross- section profiles obtained (a) at the end of step-1 and (b) at the end of step-2 with stress distribution (Grit radius=250 μm and horizontal speed= 300 m/min)	303
Figure 7.48 Comparison of some cutting forces (F_t and F_n) from FEM simulation, extrapolated data from FEM and experimental results (from single grit scratching tests)	306

List of Tables

Table 3.1 Examples of Johnson-Cook flow stress model (JCM) application in the literature	85
Table 3.2 Examples of application for flow stress models in the literature	90
Table 3.3 Friction models (Iqbal et al., 2008)	97
Table 4.1 Workpiece material typical properties	126
Table 4.2 Chemical compositions of the workpiece materials	126
Table 5.1 Aluminium alloy A2024-T351 material properties (Mabrouki et al., 2008)	161
Table 5.2 Damage parameter for aluminium alloy A2024-T351 (Mabrouki et al., 2008)	163
Table 7.1 Summary of cutting simulation condition and remarkable chip type	245
Table 7.2 Material properties of grit and workpiece for the first group of simulations	264
Table 7.3 Material properties used in the simulation set	291

Nomenclature

Symbol	Description
V_c	Cutting speed
N	Grinding wheel rotational speed
V_w and V_f	Work table speed and feed rate
a_p	Undeformed chip thickness in grinding
t and t_c	Undeformed and deformed chip thickness in orthogonal cutting
l_c or l_g	Contact length or geometric contact length
b_k	Width of grinding wheel
f_d	Dressing feed
b_d	Width of dressing tool
a_d	Dressing depth of cut
h	Depth of cut in orthogonal cutting
γ	Tool rake angle (degree)
α	Tool clearance (or flank) angle (degree)
ϕ	Shear angle (degree)
P	Grinding power
u	Specific energy
F_x, F_y, F_z	Force components in given direction
F_t, F_n	Tangential and normal force
A	Area of a finite element
$[K]_{\text{element}}$	Stiffness matrix
$[B]_{\text{element}}$	Known as B – matrix in FEM
$\sigma_1, \sigma_2, \sigma_3$	Principal stresses
$\varepsilon_{xx}, \varepsilon_{yy}, \gamma_{xy}$	Strain components
σ_m	Hydrostatic stress
σ'	Deviatoric stress

$\sigma, \bar{\sigma}$	von-Mises stress or equivalent stress
σ_h	Stress at the peak strain (in Rhim and Oh's model)
σ_s	Reduction stress function (in Rhim and Oh's model)
ε	Equivalent plastic strain
ε_c	Critical strain
ε_p	Peak strain
$\dot{\varepsilon}$	Strain rate
$\dot{\varepsilon}_0$	Reference strain rate
E	Elastic modulus of material
ν	Poisson's ratio
ρ	Mass density
C_p	Specific heat
α_d	Thermal expansion
A	Initial yield stress (in Johnson-Cook flow stress)
B	Hardening modulus (in Johnson-Cook flow stress)
C	Strain rate dependent coefficient (in Johnson-Cook flow stress)
m	Thermal softening coefficient (in Johnson-Cook flow stress)
n	Work hardening exponent (in Johnson-Cook flow stress)
T_{room}	Room temperature
T_{melt}	Melting temperature
T_c	Crystallization temperature
G_f	Fracture energy per unit area of a crack
u^{pl}	Equivalent plastic displacement
L	Characteristic length of a finite element
w	Damage initiation parameter
D	Overall damage variable (in damage evolution criterion)
σ_{y0}	Yield stress at onset of damage
ε_0^{pl}	Equivalent plastic strain at onset of damage
ε_f^{pl}	Equivalent plastic strain at failure
\tilde{E}	Elastic modulus after damage

G	Shear modulus
H'	Work hardening rate
K_{IC}	Fracture toughness
\dot{q}_w	Heat flux density
η	Inelastic heat fraction
η_f	Fraction of energy dissipation due to friction
J	Equivalent heat conversion factor
τ	Shear stress
$\dot{\gamma}$	Slip strain rate
μ	Friction coefficient
M^{NJ}	Mass matrix (in Explicit integration formulation)
P^J	Load vector (in Explicit integration formulation)
Γ^J	Internal force vector (in Explicit integration formulation)
$u_{i,j,k}$	Nodal displacement of a finite element
Sa	Average surface roughness in 3D
GA	Groove cross-section area (in scratch test)
P_1, P_2	Side pile up areas (in scratch test)

Abbreviations

FEM	Finite Element Method
FEA	Finite Element Analysis
MD	Molecular Dynamics
SHPB	Split Hopkinson Pressure Bar
SPH	Smooth Particles Hydrodynamics
SRG	Stock removal grinding
FFG	Form and finish grinding
HEDG	High efficiency deep grinding
JCM	Johnson-Cook flow stress model
JCCRT	Johnson-Cook damage initiation criterion in Abaqus
EGER	Effective grit engaging radius
CBN	Cubic Boron Nitride
Al ₂ O ₃	Aluminum Oxide
MRR	Material removal rate
HV	Hardness Vickers (Vickers Pyramid Number)
2D	Two-dimensional
3D	Three-dimensional

Acknowledgement

I wish to express my sincere gratitude to my supervisor Prof. Xun Chen for his endless support, encouragement and invaluable advice throughout the course of my PhD study. His professionalism and invaluable criticism inspired me to think deeply to overcome the difficulties which I encountered during my PhD study.

I also would like to thank Dr. Simon Barrans and Dr. Leigh Fleming for their criticisms and helpful suggestions on my first year and second year report.

I wish to thank manufacturing technical teams in the School of Computing and Engineering for their support and advice for manufacturing of some special parts which I used in my research. My special thanks are also for IT department in the School of Computing and Engineering for the technical support on computer systems.

I also wish to thank all my friends for their friendship and advice before and during PhD study.

I wish to thank my parents and also my brothers and sisters for their patience, endless support, and their lasting love.

Finally, I would like to gratefully acknowledge the University of Huddersfield for providing full scholarship throughout my PhD study.

Chapter 1 Introduction

1.1 Motivation

Grinding is a form of material removal applied to many metals and ceramics, especially hard-to-machine materials, to obtain smooth surfaces on products within a desired tight tolerance. The grinding process has been a key manufacturing process since ancient times, but then of course, it was not used as an engineering process (Malkin and Guo, 2008). Grinding was not understood scientifically until the mid-1940s when it was investigated as an engineering process (Malkin and Guo, 2008; Doman, 2008). Grinding mechanics and material removal mechanisms are complex and the processes are still not fully understood. In the manufacturing industry, almost 65% of machining firms use the grinding process (Doman, 2008) and a significant portion of production cost is due to grinding or related abrasive processes.

Minimizing the cost and energy consumption of the abrasive process, including reduction of labour costs and abrasive tool failure is a prominent reason for research into the abrasive process. In addition, with the rapid development of aerospace, automotive, and biomedical industries, there is continuously increasing demand for technological components with stringent requirements and tight tolerances. To meet these demands precision grinding plays a vital role in reducing surface roughness to the order of sub-micron level on difficult-to-machine materials such as ceramics and hardened metals. Research on precision grinding with relatively smaller abrasive tools is a crucial and promising area for research.

Study on grinding process mechanics has been on-going for several decades regarding different scales. Tönshoff et al., (1992) and Brinksmeier et al., (2006) summarized grinding models using analytical, kinematic, and numerical approaches. These works focused mainly on

the entire grinding wheel – workpiece interaction and were supported with experimental grinding tests. However, some experimental observations were difficult to explain theoretically due to the complex nature of the process mechanisms. Also, the determination of some of the mechanical characteristics, e.g., stresses, strains, and temperature distribution across the machined surface are difficult to obtain experimentally and grinding process analysis using experimental tests could be both costly owing to the high price of grinding tools and not generally valid as the results obtained might be valid only for certain machining condition. Thus, prediction of mechanical parameters such as forces, strains, stresses and surface deformations that occur during grinding using computer technology is a valuable means of getting additional insight into the final quality of machined surface and to reduce costly experiments.

Development in the technology of computers has enabled modelling and simulation of the grinding process in a digital environment. Some empirical models of the grinding process have been developed by researchers, including regression analysis models (Zhang, 1994; Kun and Liao, 1997) and neural network models (Sathyanarayanan et al., 1992; Maksoud et al., 2003). However, the validity of these models is constrained to specific circumstances and usually they do not give as much information as in the case of experimental tests. Finite element methods are the most widely accepted modelling techniques but computing technology is still not advanced enough to model all the details of the process. Some grinding processes such as the thermal process have been modelled by considering the grinding wheel as a heat source (Mahdi and Zhang, 2000; Moulik et al., 2001; Chuang et al., 2003). These models do not adequately represent the grinding process to obtain useful physical results about material removal phenomena, stresses, strains, etc. To overcome these problems the grinding process has been modelled using the single grit approach (Klocke et al., 2002; Doman et al., 2009^a; Anderson et al., 2011^a; Anderson et al., 2012), which considers single grit action on a workpiece to improve

understanding of the material removal mechanism, as well as physical quantities such as stress distribution, strain and cutting forces exerted during the process. Understanding the material removal mechanism in grinding is the main purpose behind the FEM modelling of single grit grinding. Since grinding has very complex material removal mechanisms comparing to other cutting processes such as turning, milling, etc., material removal in grinding can be completed in three dominant phases: rubbing, ploughing and cutting, first proposed by Hahn (1962). Accurate simulation of these material removal phases in the grinding process is important to predict grinding surface creation using abrasive grits and eventually the surface quality of machined parts, in a simulation environment.

1.2 Aim and objectives

Modelling of the grinding process numerically at the micro scale by considering grit-workpiece interaction is still at the development stage and thus far physical models which can represent grinding process at the micro scale has not been fully developed due to restrictions of computer technology. Nevertheless as computer technology has advanced, research on micro scale modelling and simulation of machining has increased and research on micro scale grinding by modelling and simulation supported by experimental tests appears very promising (Brinksmeier et al., 2006; Lai et al., 2008; Aurich et al., 2009).

The aim of this work was to develop an FEM model of single grit-workpiece interaction, supported by experimental tests, to improve the understanding of material removal mechanisms in the grinding process.

To achieve this aim the following objectives will be met;

- Development of FEM model for single grit – workpiece interaction which can represent the material removal mechanisms in grinding.
- Simulation of FEM model under different input conditions to explore the relational dependency between input and output parameters.
- Development of FEM model for chip formation model using the orthogonal cutting approach to determine the influential parameters in defining the different types of chips.
- Determining the material deformation tendency across a simulated single grit scratch.
- Development of the grinding surface creation model in FEM to capture material deformation and force variation by means of multi-pass scratches.
- Experimental analysis of single grit scratches under various conditions including speed, workpiece material, depth of cut, etc., to determine the influences of these parameters on material removal mechanisms in terms of rubbing, ploughing and cutting.
- Establishment of suitable metrology techniques for the analysis of experimentally generated scratches.
- Establishment of suitable process monitoring tools to capture process dynamics and to transfer experimental data into the computer environment.
- Comparison of finite element simulation results with experimental results.

1.3 Outline of the thesis

This thesis is composed of nine chapters with an introductory chapter.

Chapter-2 discusses the fundamentals of grinding process technology. It contains a description of the grinding process, abrasives, dressing, and a literature review on material removal mechanisms from the grinding process, particularly single grit grinding.

Chapter-3 presents modelling and simulation techniques used in machining processes, particularly in the grinding process. Fundamentals of finite element method are described together with constitutive models, failure models, meshing techniques and friction and heat generation models. The literature for finite element simulation of the grinding process is included, particularly wheel – workpiece and grit – workpiece interactions. Finite element modelling of the chip formation process is included when considering the orthogonal cutting concept.

Chapter 4 describes the materials and experimental methodology for the research carried out. It includes the single grit grinding experimental setup, definition of workpiece and grit materials and establishment of process monitoring system. Technique to analyse material removal mechanisms in single grit grinding are also described in this chapter.

Chapter 5 describes the development procedure of a finite element model (FEM) for chip formation and single grit grinding simulation.

Chapter 6 presents the experimental results of the single grit grinding tests. Scratches generated during single grit tests are analysed in terms of rubbing, ploughing and cutting. The influences of single grit grinding conditions are analysed using scratches on the workpiece surface.

Chapter 7 presents the finite element simulation results. Chip formation mechanisms for three common type of chip (continuous, serrated and discontinuous) under different conditions are presented in this chapter. Single grit grinding simulation results are also presented. Scratch formation is analysed using FEM in terms of ploughing and rubbing mechanisms. The chapter ends by presenting force variation under different simulation conditions.

Chapter 8 contains the overall discussion on the experimental and numerical results. Finally, conclusions and suggestions for future work are in chapter 9.

Chapter 2 Grinding Process Technology

2.1 Introduction

This chapter presents available knowledge concerning the fundamentals of the grinding process and grinding material removal mechanisms. The early stage of this chapter includes the background of metal cutting operations. A large number of journal papers and technical articles have been published on the grinding process and the huge volume of publications can be taken as proof of the importance of grinding process for manufacturing.

Here literature on single grit-workpiece interaction will be reviewed and the grinding process is described with its peripheral tools and material removal mechanism for wheel-workpiece interaction and single grit-workpiece interaction. The former is generally called the macro-scale approach where the process is investigated in terms of grinding wheel-workpiece interaction, whereas the latter is called the micro scale approach since it deals with the relatively small scale between individual abrasive grit and the workpiece material. The orthogonal cutting process is discussed since the chip formation phase of single grit grinding has similar features with types of chip formed obtained during various cutting conditions.

2.2 Fundamentals of machining process

Machining is a common name for removing unwanted material to manufacture a desired surface profile. Turning, milling, drilling and grinding operations are common machining processes which are used in the manufacturing industry. Unwanted material is removed in the form of small chips from the work material. A chip form will vary depending on kinematics of the removal mechanisms, which are affected by workpiece material properties, operational

parameters, cutting tool geometry, etc. Research on machining or metal cutting processes has been on-going for a long time though the research focus has changed from conventional macro scale machining to precision micro scale machining where the demands is for smaller size components with high surface quality. Some possible objectives into the machining process are to predict the shape of chip form, cutting forces, and machined surface quality; and to reduce manufacturing cost, tool wear and machining cycle time based on operational parameters and tool geometry. However, determining the influences of operational parameters on the machined surface in terms of machining deduced workpiece burn, chatter, residual stresses and surface integrity is also of concern for research on machining processes. The orthogonal cutting process model, first proposed by Merchant (1945), is one of the fundamental models of cutting used to predict the shear angle during chip formation. However, Merchant's model is oversimplified and calculated shear angles and cutting forces do not correspond to experimental results. Figure 2.1 schematically depicts the orthogonal cutting process model as proposed by Merchant (1945).

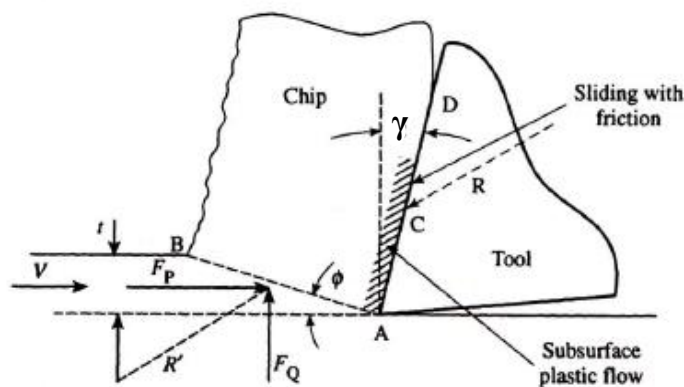


Figure 2.1 Merchant's orthogonal cutting model (Merchant, 1945)

Where V is a cutting speed, γ is a rake angle, ϕ is the shear angle, t is a undeformed chip thickness, F_p and F_q are the cutting and thrust forces respectively with R' as their resultant.

Chip formation is of major interest in metal cutting. Chips are formed due to excessive plastic deformation of material ahead of the cutting tool. During chip formation, plastic deformation is highly localized in two regions (Shaw, 1996): the first is the primary shear zone, which is shown by the dashed line AB in Figure 2.1. Plastic deformation in the primary shear zone occurs at high strain with varying strain rates, particularly, in high speed machining. Large plastic deformation in this zone is responsible for heat generation across the shear line. The second region is the secondary shear zone, which is shown by line AD in Figure 2.1. Plastic deformation occurs mainly because of severe friction between tool rake face and chip. Heat generation in the secondary shear zone is mainly because of friction and plastic deformation. There is also a tertiary deformation zone between the tool flank (or clearance face) and its interface with machined surface.

Formation of chips is governed by operational parameters such as feed rate, depth of cut, speed, material properties, tool shape, and rake angle. In metal cutting generally, chips are classified into three types; continuous chips, serrated or saw tooth chips and discontinuous chips as shown in Figure 2.2 (Childs et al., 2000). Material properties influence chip shape and formation but so do operational parameters such as cutting speed and rake angle (Childs et al., 2000; Günay et al., 2004; Mabrouki et al., 2008; Öpöz and Chen, 2012). Saw tooth shape chip is a general characteristic of hardened steels and titanium alloys at high cutting speeds (Childs et al., 2000; Sima and Özel, 2010). Shear bands become weaker due to decreasing yield strength with increasing temperature caused by plastic straining at high speed (Xie et al., 1996; Childs et al., 2000; Hortig and Svendsen, 2007). Highly deformed shear bands lead to material out flow from the chip front surface which forms a saw tooth shape chip. A continuous chip is produced under steady state cutting of ductile materials whereas discontinuous chips are produced by

fracture mechanism when the material has not sufficient ductility to form a continuous chip (Childs et al., 2000).

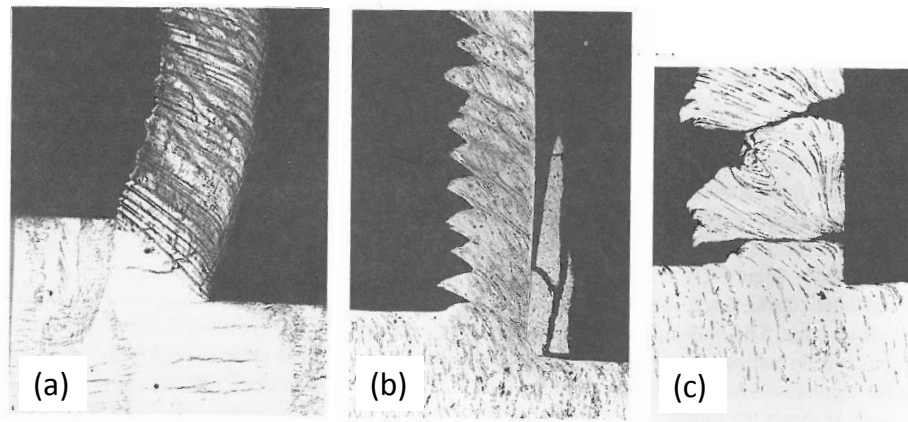


Figure 2.2 Three types of chips (a) continuous chips (b) serrated (or saw tooth) chips and (c) discontinuous chips obtained from different materials with different machining conditions (Childs et al., 2000)

In machining processes, determining chip shape is a significant challenge for cutting mechanics. Once chip shape is known, calculation of cutting forces is relatively simple; calculation of stresses and temperature in the work and tool, both of which affect the machined surface quality and tool condition, is slightly more difficult, but development of a FEM will help to calculate stresses, deformation, temperatures and other parameters.

Strain hardening of the material during chip formation has a significant influence on chip flow during chip formation (Childs et al., 2000; Childs, 2009; Sima and Özel, 2010). Lubrication is also an influential parameter in machining. Curled and thinner chips can be obtained by cutting with lubricant and thick and straight the chips were obtained by dry cutting (Childs et al., 2000). While there is no known laws governing chip curvature, factors which could affect the chip radius are variation in friction along the chip/tool contact length, roundness of cutting edge and also strain hardening behaviour and variations of strain hardening through the thickness of the

chip (Childs et al, 2000; Jaspers and Dautzenberg, 2002^a; Asad et al., 2008; Woon et al., 2008; Childs, 2010; Sima and Özel, 2010; Öpöz and Chen, 2012).

2.3 Background to the grinding process

The grinding process is a material removal process using a grinding wheel which is made up of a large number of randomly oriented abrasive particles. Grinding particles can be considered as refractory material since they have good resistance against the high temperatures to which they are exposed during the grinding operation (Shaw, 1996). Essential operational parameters are shown in the schematic drawing of up-cut surface grinding in Figure 2.3. Surface grinding operation is called up-cut grinding if the grinding wheel engages in opposite direction to the motion of the workpiece. Down-cut grinding is where direction of grinding wheel engagement point and movement of the workpiece are in the same direction. There are small differences between up-cut and down-cut grinding in terms of grinding energy, surface finish, tendency to burn, and wheel wear (Tawakoli, 1993).

The grinding operation is performed at relatively high speed and undeformed chip thickness is relatively small particularly in fine grinding operations compared to other machining processes. The grinding operation may be divided into two regimes: stock removal grinding (SRG) and form and finish grinding (FFG) (Shaw, 1996). The former is mainly used to remove unwanted material without regard to surface quality as with abrasive cut-off operation. In this case, undeformed chip thickness is relatively high and wheel wear is so fast that it is not necessary to dress the grinding wheel to remove wear flats and metal adhering to wheel surface. To obtain the desired surface finish, the wheel must usually be dressed periodically to provide sharp cutting edges that are relatively free of adhering metal and wear flats. The mean

undeformed chip thickness in FFG is relatively small, and this gives rise to important difference in the metal removal mechanism compared to that in metal cutting (Shaw, 1996).

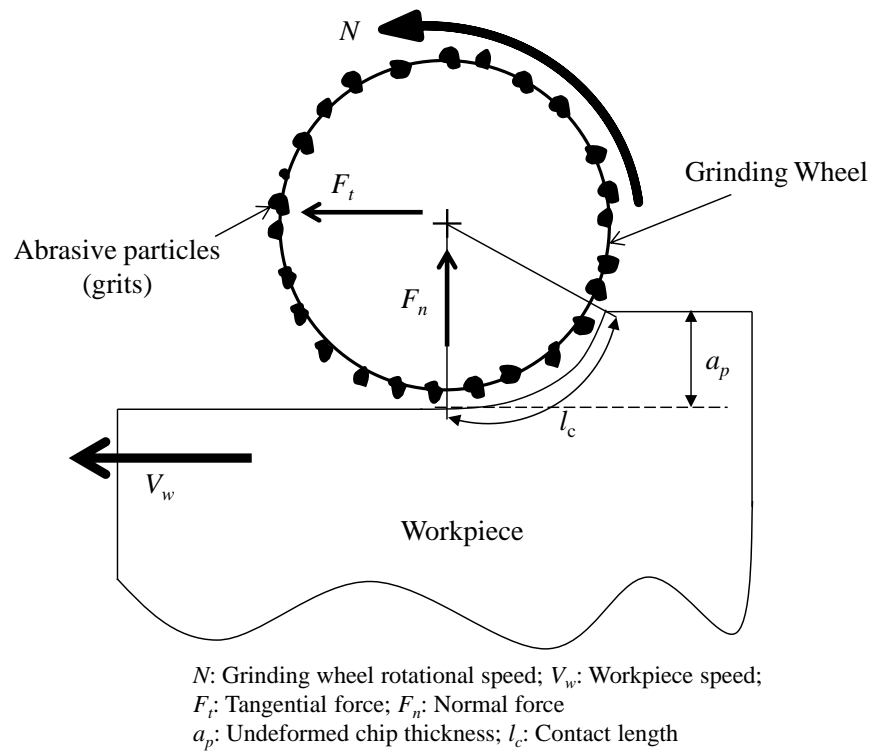


Figure 2.3 Schematic of up-cut surface grinding with important process parameters

To measure grinding performance, grinding system behaviour must be evaluated properly. The grinding system behaviour is mainly assessed by considering abrasive geometry, kinematics, mechanics, and energy and material properties. Overall grinding performance including finish surface quality is directly related to performance of the grinding wheel used during the grinding operation. The performance of a precision grinding wheel is usually determined by using the parameters such as grinding force, machining vibration, temperature in the cutting zone, and workpiece surface roughness. The grinding wheel must be correctly dressed to keep it in good

conditions to provide low force and temperature as well as good workpiece integrity and roughness (Chen and Rowe, 1996^a; Chen et al., 1996).

2.4 Abrasives

Abrasives tend to be hard refractory brittle particles that are crushed and sorted according to size and shape (Shaw, 1996), but may also be classified according to their hardness or chemistry. While all abrasives are hard (indentation hardness $> 2000 \text{ kg mm}^{-2}$), those that are unusually hard are often called super abrasive, Diamond (D) and cubic boron nitride (CBN), have hardness of about 6000 and 4500 kgmm^{-2} , respectively (Shaw, 1996). Hardness values of the most common abrasives are usually quoted as Knoop hardness (Rowe, 2009). Values of Knoop hardness with respect to temperature for some common abrasives are shown in Figure 2.4.

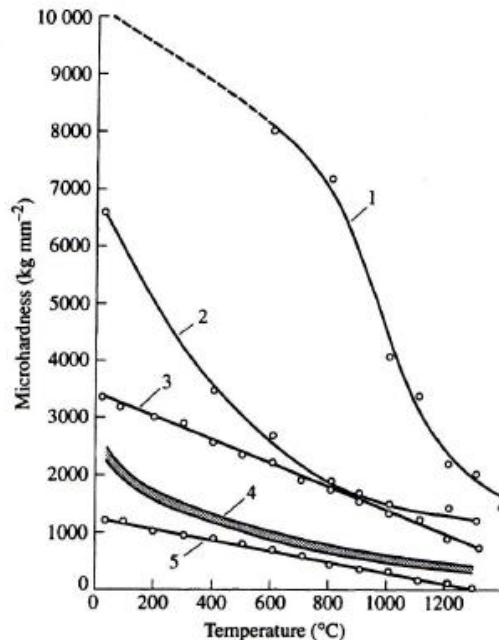


Figure 2.4 The variation of Knoop hardness with temperature for several hard materials: 1, diamond; 2, CBN; 3, SiC; 4, varieties of Al_2O_3 ; 5, tungsten carbide (92 w/o WC, 8 w/o Co) (after Loladze and Bockuchava 1972; Shaw, 1996)

Friability of an abrasive grain is the tendency for it to fracture under compression. Increasing the friability of grains would be better for low grinding forces as fracture of grains during grinding may be advantageous in providing fresh cutting edges; hence grains with higher friability tend to be better at maintaining grinding wheel cutting efficiency (Rowe, 2009).

Diamond is a super abrasive and often used in precision grinding applications, but has a limited ability with ferrous material because the high affinity between diamond and ferrous materials causes excessive wear, limiting its use to nonferrous materials (Rowe, 2009).

CBN is the second hardest material and it is widely used in grinding steels. CBN is increasingly replacing conventional abrasives for precision grinding of hardened steels due to its low rate of wear and the ability to provide and maintain close tolerances on the parts produced. The high thermal conductivity of CBN abrasives provides the advantage of cooler grinding compared with conventional aluminum oxide wheels or silicon carbide wheels. This allows much higher removal rates without thermal damage or tensile residual stress (Rowe, 2009).

2.5 Dressing

Dressing is a process to prepare a grinding wheel for grinding operation (Rowe, 2009). A grinding wheel is dressed to perform the following tasks;

- It is used as truing to eliminate deviation from specified form; generally a new grinding wheel must be dressed to provide better roundness by removing deviated parts.
- Dressing process is necessary to re-establish the surface of the grinding wheel when its grains lose their edges and break due to the wheel wear. So, regular dressing on the grinding wheel can provide a sharp cutting surface with uniform distribution of cutting edges.

The topography of the grinding wheel highly influences the grinding process performance and several wear factors can change the topography of the wheel during its life. After a certain period of use, the wheel must be dressed to introduce new grains to the cutting process and to re-establish its original shape (Hassui, 1998). An example of single point diamond dressing process is illustrated in Figure 2.5.

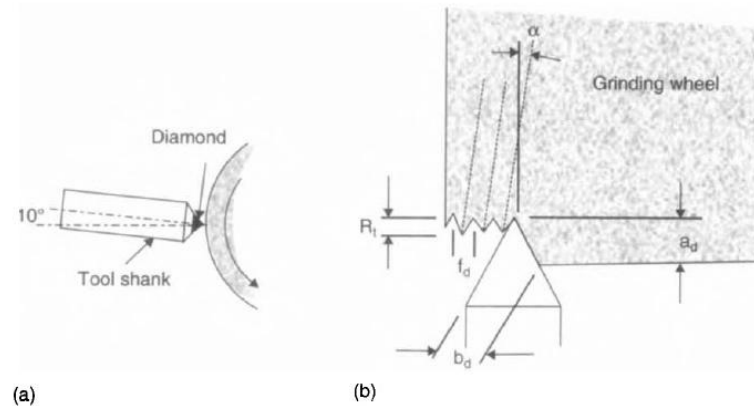


Figure 2.5 Single point dressing with a stationary non-rotating dressing tool (a) single point dressing tool and (b) single point traverse dressing, where f_d is a dressing feed per revolution of grinding wheel, b_d is a width of the dressing tool, a_d is a dressing depth of cut (Rowe, 2009)

The dressing tool is traversed across the surface of the grinding wheel as in Figure 2.5 to generate the required form and cutting surface. Figure 2.5-(b) illustrates how the dressing depth of cut a_d and the dressing feed per revolution of the grinding wheel f_d create a helical groove on the wheel surface (Rowe, 2009). It has been found that the effect of dressing depth on grinding power is stronger than that of dressing lead; however, the effect of dressing depth on surface roughness is weaker than that of dressing lead. It was experimentally demonstrated that the dressing conditions can significantly affect wheel redress life (Chen et al., 1996).

Effect on grinding performance of varying the dressing conditions were investigated by means of simulation supported with experimental tests (Chen et al., 1996). Investigation showed that a coarse dressing condition leads to low grinding force and grinding power but a high workpiece surface roughness. Also, grinding performance of the wheel in the dwell period for ‘spark-out’ was simulated by Chen et al., (1996). Simulation and experimental results demonstrated that grinding power in the dwell period decreases following an exponential decay function, but the reduction of surface roughness does not follow an exponential decay. Chen (2002) also explained the effect of sharpness of grinding wheels in terms of grinding wheel performance. To this, the effects of dressing conditions were investigated together with grinding conditions. It was found that a sharp wheel provide a low grinding force and fast material removal during grinding. It was suggested that the time constant of the grinding system became a good measure of wheel sharpness when system stiffness was kept constant.

Chen et al., (2002) reviewed the performance of CBN wheels and considering the advantages and difficulties met in the application of CBN wheels for internal grinding. It was concluded that the hardness of CBN grains potentially increases re-dress life and improves dimensional stability. The importance of touch dressing for improved dimensional stability, and other operational techniques to maintain an open surface topography of the wheel, were also highlighted.

2.6 Material removal mechanism in grinding

Material removal mechanisms for grinding can be categorized into two groups: (i) removal mechanisms during grinding wheel-workpiece interaction and here investigation will be at a macro scale, and (ii) removal mechanism considering single grit-workpiece interaction and investigation will be at a micro scale.

This thesis considers the removal mechanism at the micro scale, investigating the grit-workpiece interaction. After presenting a literature review which includes fundamental removal mechanisms that occur during grinding and details of single grit grinding performance (including material removal rate, force and energy variation with different process parameters) conclusions are drawn on the direction and content of the thesis. The literature review provided here excludes the finite element modelling and simulation given in the next chapter.

2.6.1 Material removal at the macro level for the grinding wheel working surface

Material removal during machining with grinding wheels must be considered in terms of wheel wear and material removal from the workpiece simultaneously. Here, a concise description is given of the fundamental wheel wear mechanism based on wheel topography and its influences on material removal from the workpiece.

Grinding wheel topography is one of the main factors determining grinding performance when considering the quality of the ground surface. So, understanding grinding wheel topography in conjunction with grinding process performance and material removal is crucial. Recently, Doman et al., (2006) reviewed the grinding wheel topography models to show the state of the art in this technology. Based on the previous work, a general modelling approach for grinding wheel using grain size, shape, arrangement, and wheel dressing strategy is recommended (Doman et al., 2006). Chen described the formation of grinding wheel topography in a series of papers (Chen and Rowe, 1996^a: Chen and Rowe, 1996^b: Chen et al., 1996: Chen et al., 1998) considering grinding mechanics and dressing conditions by means of simulation and experiment. Chen suggested how to select dressing conditions based on wheel wear and desired

grinding performance, but it was necessary to determine those parameters most influential for grinding wheel wear in order to get better performance over the entire grinding operation.

The grinding wheel wears with use and after a certain period needs to be dressed to generate fresh cutting edges. With the dressing operation, new grits protrude to re-establish the grinding wheel topography. Wheel wear occurring during grinding is generally composed of three major mechanisms; attrition wear, grain fracture and bond fracture (Chen et al., 1998; Malkin and Guo, 2008). Attrition wear is the dulling of abrasive grains and growth of wear flats due to rubbing against the workpiece. Grain fracture can be considered as removal of abrasive fragments by fracture within the grain. Bond fracture occurs by dislodging the abrasive from the bond. It occurs due to the friction between the chip and the wheel bond (Malkin and Guo, 2008). The attrition wear makes the smallest contribution to the decrease of the wheel volume, but is the most important for defining the end of the wheel life. With the increase of attrition wear, the cutting forces and temperature within the grinding zone increase and the quality and surface integrity of the workpiece could be reduced (Hassui, 1998). Bond fracture is the most important mechanism regarding the loss in the wheel radius (Hassui, 1998).

Earlier work performed by Kannappan and Malkin (1972) to reveal the effect of grain size and operating parameters on grinding found grinding force components increased linearly with attrition wheel wear as determined from the wear flat area, with a relatively slow growth rate up to a critical value of the wear flat area at workpiece burn, and thereafter the rate of increase is much greater. Larger grinding forces and wear flat areas were also obtained with harder wheels. Kannappan and Malkin (1972) also investigated the wheel condition with the number of active grains per unit area in the wheel surface and found more active grains with harder wheels, and the number of active grains increased up to burning and decreased thereafter.

One of the important parameters for determining grinding efficiency in terms of material removal is the G-ratio, which is commonly used in selection of a grinding wheel. Malkin and Guo (2008) define the G-ratio as the volume ratio of metal removed to wheel wear. In grinding wheel selection generally, a larger G-ratio is used subject to certain limits of surface roughness. Kannappan and Malkin's (1972) investigation on material removal mechanisms showed that the larger G-ratios were generally obtained with coarser grains, faster table speeds, harder wheels and smaller downfeeds. G-ratio is also associated with attrition wear on grains. Attrition wear rate decreases with coarser grains and consequently a larger G-ratio is obtained. In addition, there exist relatively less sliding between the wear flats and the workpiece for every grinding pass with increasing table speed and this might result in less attrition wear and a higher G-ratio.

Determination of the onset of workpiece burn, defined as a thermal damage on the workpiece surface, is another important parameter which is directly related to the grinding wheel tool life (Kannappan and Malkin, 1972). Grinding workpiece burn is characterized by increasing grinding forces, larger wheel wear rates, and deterioration in the workpiece surface quality. In Kannappan and Malkin's (1972) investigation, they found that the workpiece burn occurs where the critical wear flat area is bigger with finer grain size and larger table speeds and downfeeds. The grinding energy flux at burn also increases with downfeeds. The grinding wheel tool life, which is defined as the number of passes before burning occurs, is greater with coarser grains, softer abrasives, higher table speeds and smaller downfeeds.

2.6.2 Material removal at the micrometre scale due to single grit action

The first study on the mechanism of single grit action on the workpiece was conducted by Hahn (1962). Hahn proposed abrasive grit rubbing hypothesis. He proposed that the material removal at individual abrasive grit scale is composed of three phases (or stages), namely,

rubbing, ploughing and cutting. Three phases of the material removal mechanism occur during single grit-workpiece interaction as illustrated in Figure 2.6. These three phases begin with grit-workpiece engagement, where the grit slides over the workpiece within elastic limit of material up to the onset of plastic deformation, this stage is called rubbing, which has negligible contribution to the material removal process during grinding. The rubbing phase is followed by a ploughing stage, where the material is plastically deformed but no chip formation occurs at this stage. In the ploughing stage, material swells-up across both sides of the grit as well as material accumulated continuously in front of the grit until the ultimate material removal occurs with the formation of a chip. When pile-up material could not withstand the shearing stress generated in the bulged material ahead of the grit tip, the pile-up or bulged part is fractured from the workpiece in the form of a chip, and this stage is named as a chip formation or cutting stage. The transition from rubbing to ploughing and then ploughing to cutting depends on the depth of grit penetration into the workpiece (Rowe, 2009). Although rubbing and ploughing make negligible contribution to material removal, they can adversely contribute to the grinding process by producing an excessive rate of wheel wear and surface distortion due to increasing specific energy and friction, with a corresponding temperature rise. Specific energy is the energy required to remove a unit volume of material. The cutting process is the most influential phase for material removal and is where numerous tiny chips are removed from workpiece to produce the ground surface.

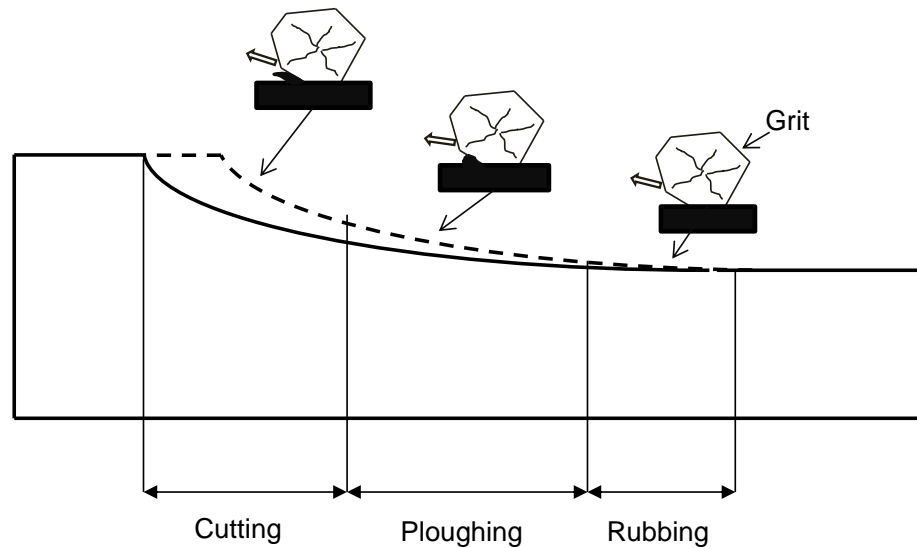


Figure 2.6 Rubbing, ploughing and cutting at different grain penetrations through the arc of contact

Early experimental research on single grit grinding was by Takenaka (1966) who used several grits with #24 mesh size on hardened steel and cast iron block as workpieces. Each groove produced consisted of many fine grooves and when the depth of cut was more than $1\ \mu\text{m}$ a spark was generated. He noted the three stages in material removal; rubbing, ploughing and chip formation and observed that the swelling up of workpiece material on both sides of the groove by the ploughing action of the grit was highly dependent on the shape of the grit. It was observed that the rate of ploughing increased with decrease of depth of cut and in the case of an extremely small depth of cut, the rubbing process was predominant although metal removal also occurred in the form of metal leaves torn from the workpiece surface.

Komanduri (1971) investigated grinding mechanics using highly negative rake angles (up to -85°) with a diamond tool and considered the individual grit interaction with the workpiece that occurred taking the grit geometry and grit wear into account. A schematic drawing of negative rake machining is shown in Figure 2.7. Komanduri did not use abrasive grit to perform

this investigation since it is difficult to measure the interaction angle. He simulated the grinding process by using cutting tools with large negative rake angles. He observed chip formations up to a rake angle of -75° at $10\ \mu\text{m}$ depth of cut; while the rake angle was -85° no chip formation was observed. He concluded: the possibility of chip formation depends on the thickness of the work material cut; that decreasing the thickness resulted in no chip formation but ploughing and side pile-up of material; the ratio of thrust force to the cutting force, for a positive rake angle is < 1 , while with highly negative rake angle this ratio is > 1 . Komanduri's work showed the flow of material ahead of the tool was divided into two directions as shown in Figure 2.7, material flowing towards the upper side of the stagnation point formed chips while material flowing under stagnation point was for ploughing and rubbing. The stagnation point changed with rake angle, depth of cut and width.

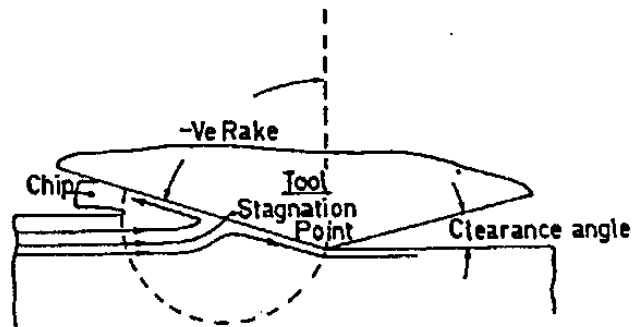


Figure 2.7 Machining with negative rake angle (Komanduri, 1971)

Shaw (1971) modelled the abrasive grit as a spherical body and described the chip formation by means of an extrusion-like mechanism during single grit interaction with the workpiece as illustrated in Figure 2.8. The undeformed chip thickness in grinding is quite small compared to that found in conventional cutting. So, the effective rake angle gets large negative values. Metal removal by grit due to concentrated shear was assumed to describe the extrusion-

like process. The force R (Figure 2.8-(a)) between the abrasive particle and the workpiece give rise to material in plastic zone, which is assumed to be similar to that produced in a Brinell hardness test. Figure 2.8-(b) shows a schematic of an active cutting edge with a radius of curvature ρ on the surface of abrasive particle. The dashed circle is the elastic-plastic boundary. The position of this is such that the resultant force R' has a small unconstrained region of the plastic zone in front of the abrasive particle. The chip is extruded through this unconstrained region (Shaw, 1996). The mechanism illustrated in Figure 2.8 leads to size effects which are more important than those encountered in cutting and could result in an increase of specific energy that means that a large volume of material must be deformed plastically to produce a small chip.

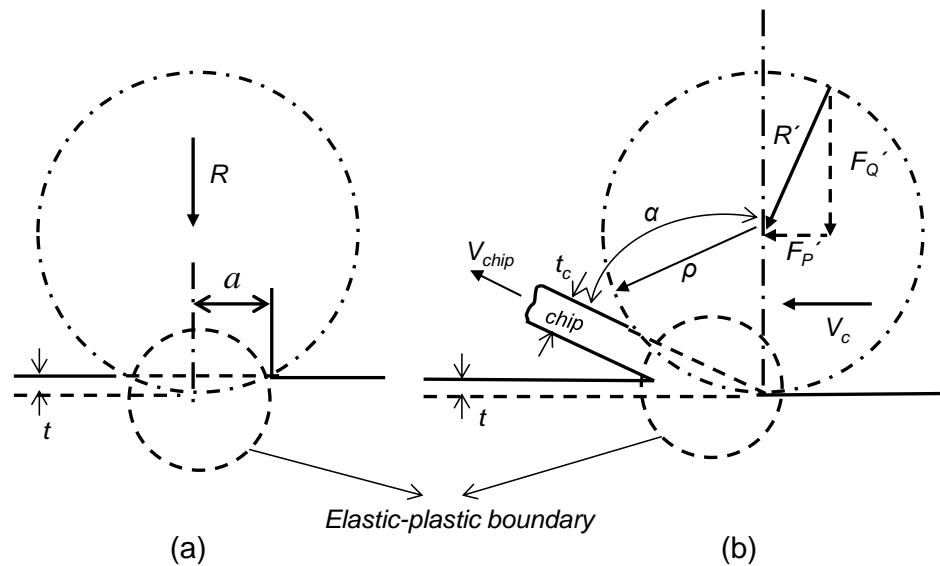


Figure 2.8 (a) Hardness indentation with a spherical indenter, a is the contact radius due hardness indentation, R indentation load, (b) indentation at the tip of an abrasive grit with a radius of curvature at the grit tip= ρ and resultant force R' inclined at angle α to the vertical. The deformed chip thickness is t_c and the cutting ratio is t/t_c , V_c is the cutting speed (Shaw, 1996)

Doyle (1973) investigated chip formation with single grit by using a quick-stop test to demonstrate material removal with abrasive particles having large negative rake angles. The quick-stop test is one of the most used techniques to obtain chip form under specified machining conditions. It provides the rapid disengagement of the tool from the workpiece during cutting and effectively freezes the chip forming process which allows investigation of the chip forming mechanism in more detail. Silicon carbide grits were used for the investigation with a machining system similar to that of overcut fly milling so that a continuous groove was produced on the workpiece. Very little side flow was observed indicating that most of the material that interacts with single grit is removed in the form of chips. The chip forms as a frontal bulge ahead of the grit. This type of chip is developed due to highly localized shear within a narrow region and is followed by chip fracture, which leads to the generation of discontinuous chips. This was the form of the chips collected in grinding test since the grit had a large negative rake angle.

Lal et al., (1973) investigated the wear characteristic of single abrasive grains where the dominant wear mechanisms were rubbing and friction. It was performed by using stationary grains loaded against a disk rotating at approximately 800 rpm. It was found that the mean wear volume increases linearly with grain's sliding distance, when the load on the grain and the sliding speed are maintained constant. Wear rates for soft steel were found to be greater than those for hard steel of the same composition. It was concluded that the friction coefficient was not so sensitive to the grain type but was affected by sliding speed. The friction coefficient was found to be about 0.3 at a sliding speed of 900 m/min, but was about 0.5 at a sliding speed of 300 m/min.

Buttery and Hamed (1977) investigated the parameters which most affect the efficiency of individual grits during grinding. They performed their experiments at high speeds of up to 2220 m/min using idealized cutters to simulate abrasive grits on different workpiece materials having

different values of hardness. It was found that cutting efficiency increases with increasing cutting speed and material hardness. No precise reason is given to explain the change in cutting efficiency with speed and hardness, but it was believed related to thermal effects and plastic straining rate in the workpiece material. Based on the change in grinding efficiency with speed, it was concluded that grinding forces would be lower at higher speeds at the same grit depth of cut with a given material; this observation was confirmed by experiment. It was also found that the surface roughness (R_a , defined as an average roughness) is lower with harder material because (1) hard materials produce less pile-up and (2) there is less elastic deformation with hard materials. Farmer et al., (1968) also suggested hard materials to obtain a good surface finish.

The wear and cutting efficiency of abrasive grits or grinding tools is highly influenced by the type of workpiece materials to be ground. König et al., (1985) found that different wear occurs on the abrasive grit during the scratching of carbon steel in different heat treatment conditions. The influence of coolant and friction coefficient in single grit scratching was also investigated. Investigation was performed by using a surface grinder with integrated scratch device. According to the results obtained, scratching on annealed steel leads to obvious loading on the grit surface which results in increase of cutting force and ultimately fracture of the grit sections. Grit wear was determined by using the scratched groove cross section; the changes in cross section could show the amount of wear from the grit during the time the scratches were made. An electron microscope and energy-dispersion x-ray analysis were used to categorize the type of wear (e.g. abrasion, stress created by high thermal changes, grit splintering, diffusion, etc.) to occur on the cutting edge of the abrasive grit. It was found that there is an increase in the rate of grit wear in the order of annealed, normalized and hardened steels. In addition, it was found that a high degree of hardness of the workpiece material resulted in high scratch forces.

König et al., (1985) found that better lubrication has the effect of reducing the force effect in scratch depths of 20 to 30 μm . With better lubrication the grit edge could penetrate further into the work material as the minimum depth of cut with lubrication is larger than that when dry. The presence of lubrication resulted in smaller tangential forces. According to König et al., (1985) the friction coefficient varied between 0.08 and 0.15; it decreased as temperature rose from 20 °C to 300 °C and then increased again until 600 °C, the maximum test temperature was reached.

Matsuo et al., (1989) investigated the effect of grit shape on cutting force in single grit cutting and grinding tests. Scratch tests were performed on steels and alumina using CBN and diamond grains (#14-20). For the single grit micro cutting tests cutting speed ranged from 14 to 30 m/min and the maximum depth of cut was around 25 μm . For the single grit grinding tests the cutting speed ranged from 762 m/min to 1800 m/min and maximum depth of cut was 100 μm . According to the test results, cutting forces increase linearly with increasing cross sectional area of the groove, independently of work material and grit type. Grit shape has greater effect on the normal force component than the tangential force component.

Pile-up material in single grit grinding was also investigated in Matsuo's work by changing the direction of the grit cutting face. It was found that pile-up material is largely dependent on the direction of the grit scratching face. Large pile-up was observed in diamond scratching, while the pile-up produced with CBN was smaller. However, in wet condition, CBN grit generated a pile-up as large as with a diamond grain. This was attributed to the low friction coefficient due to the wet condition which, in grinding, can generate high pile-up of material. In addition, the normal grinding force for a constant cutting cross sectional area was found much greater with grains which were less sharp compared to sharp grains.

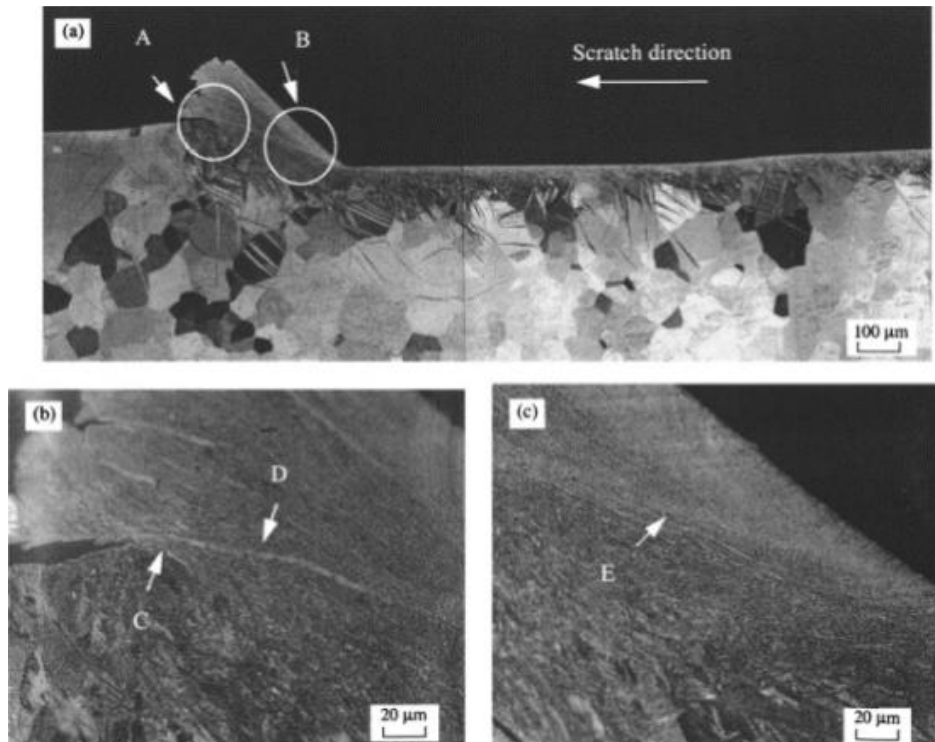
Ohbuchi and Matsuo (1991) used shaped CBN and diamond grits (#20/24) to investigate force and chip formation in single grit orthogonal cutting tests. Shaped grits allowed adjusting of

the rake angle with large negative values ranging between -45° and -75° . The shaped grits had cutting width of 200-300 μm and nose radius quite small compared to the depth of cut (less than 30 μm). They observed that variation in rake angle mostly influences the thrust force rather than the cutting force. Larger thrust force was observed with larger negative rake angle. The cutting force in a wet condition was less than for a dry condition, and less for a slow speed than a high, but there was no remarkable change at high speeds. A stagnant region in front of rake face was observed when the rake angle was between -30° and -60° , however, no stagnant region was observed at the rake angle of 0° . Ohbuchi and Matsuo concluded that the existence of a stagnant region in the cutting with large negative rake angle make chip generation easy. Besides, a large pressure normal to rake face is necessary to generate a stagnant region when the negative rake angle is large. A similar plastically deformed layer was observed both with diamond and CBN grains but the deformation with CBN was larger.

Feng and Cai (2001) investigated the effect of grinding speed and grinding sectional area on single grit grinding forces using titanium alloy TC4, superalloy GH4169 and aluminium oxide (10~15%ZrO₂) grain (#14). They demonstrated that the friction coefficient decreased with increase of grinding speed; that pile-up ratio decreased with increase in depth of cut, and that at high speed grinding (grinding speeds: 4020, 5400,7200 m/min) the pile-up ratio approached zero and cutting efficiency increased. They also observed that single grit grinding forces decreased with increasing grinding speed when the grinding sectional area remained constant.

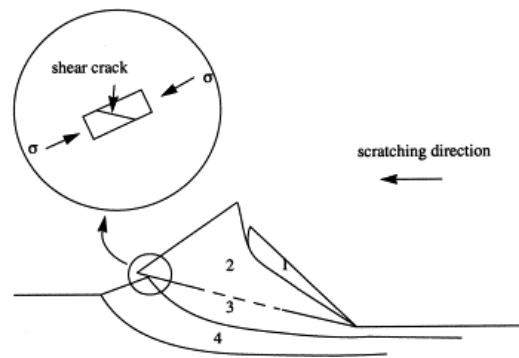
Wang et al., (2001) performed single grit scratching tests with a conical diamond tool on pure titanium to characterize the material removal mechanism. The scratches' depth of cut was around 60 μm and speed of cut was 32.4 m/min (which might not be considered within the micromachining range). They observed that a front-ridge formed during scratching, and divided the front ridge into four regions which depended on deformation characteristics as shown in

Figure 2.9: stagnant region, a lamella zone with shear bands, a hardened sublayer, and a propagating zone. The stagnant region is formed because of adhesion between tool and groove face and acts as built-up edge whose geometry is greatly affected by the adhesion characteristics between tool and the material. Specific energy variation was also investigated during scratching. It was observed that specific energy is determined by hardening when the groove size is small; when the groove size is larger the competition between hardening and softening dictates the specific energy. Finally, the scratch process was characterized by an overall friction coefficient, instantaneous specific energy, and instantaneous scratch hardness because instantaneous quantities are more sensitive to the depth of cut during scratching.



(A) (a) Optical micrograph of a partial scratch on annealed pure titanium, (b) details of cracking and shear bands in the toe of front-ridge and (c) shear band region at the heel of front-ridge

Figure 2.9 Micrograph in (A) and schematic in (B) representing material deformation characteristic in front-ridge formed during partial scratching (Wang et al., 2001) (Cont. in next page)



(B) Schematic of the zones developed in the front-ridge of scratch shown in above picture. (1) stagnant zone in contact with tool; (2) lamella extruded between two shear bands, (3) sublayer of shear surface with heavily hardened material, and (4) propagating zone full of plastic deformation.

Figure 2.9 (Cont.) Micrograph in (A) and schematic in (B) representing material deformation characteristic in front-ridge formed during partial scratching (Wang et al., 2001)

Ho and Komanduri (2003) investigated the material removal mechanisms of rubbing, ploughing and cutting which occur during grinding with a stochastic approach. They determined the various grinding process parameters analytically including the number of abrasive grits in actual contact, the number of actual cutting grits per unit area for a given depth of wheel indentation, the minimum diameter of the contacting and cutting grains, and the volume of chip removed per unit time. Their investigation proposed that a large number of grains on the surface of the wheel pass over the workpiece per second (~million or more per second), but only very small fraction of the grains rub or plough into the work material (~3.8% for FFG and ~1.8% for SRG) and even a smaller proportion (~0.14% for FFG and ~1.8% SRG) of participate in actual cutting. The results validated the rubbing hypothesis of Hahn (1962).

Brinksmeier and Glwierzew (2003) investigated chip formation mechanisms in grinding with a single grit scratching test at speeds ranging from 18 to 300 m/min. Synthetic diamond of FEPA grain size of D91 was used. Their results show that low cutting speed with small depth of cut leads to the increase of ploughing ratio and makes chip formation less efficient. Higher

values of cutting speed with higher depth of cut increases the efficiency of micro-cutting. It was suggested that high values of cutting speed in combination with maximum depth of cut should be used to achieve the most efficient chip formation.

Ohbuchi and Obikawa (2006) investigated the effect of grain shape and cutting speed in grinding with kinematic simulation of randomly generated grain shape. A statistical distribution of the effective rake angles of the abrasive grain was obtained by applying Usui's four models of kinematically admissible velocity fields. They proposed a grain cutting model to predict the surface generation in grinding considering upheaval, which is caused by the effect of grain shape and cutting speed, and effect of elastic deformation of the grain. The direction of chip flow in the simulation was predicted using the minimum energy method. The four models of kinematically admissible velocity field are: Model 1, complete chip formation; Model 2, incomplete chip formation; Model 4, wall of partial chip generation; Model 5, plastic upheaval generation. Model 3 was skipped since it was not achievable with the minimum energy model. By using the energy method and model type, direction of chip flow and effective rake angle were found. Ohbuchi and Obikawa found that lower cutting speed results in large side flow. The energy method was combined with FEM simulation to calculate three components of the cutting force. The effective rake angle calculated by the energy method was used in the FEM simulation to calculate the cutting forces. It was reported that the results were not satisfactorily good, since cutting speed and undeformed chip thickness influences were not considered in the model in order to simplify the calculation of the model.

Park et al., (2007) have developed an analytical model to predict the cutting and ploughing forces during single grit grinding. Grit-workpiece interaction was modelled as 2D material removal process with a defined critical rake angle; below this rake angle material deformation occurred only by plastic deformation rather than cutting. The ploughing forces were determined

considering the plastic deformation similar to that which takes place during the indentation of a spherical body. The model incorporated material properties such as strain, strain rate and temperature. Without including temperature effects the proposed model predicted that cutting forces are higher than found by experiment. When the temperature was included, better agreement with experimental data was obtained. Their results suggest that cutting action is more prominent than ploughing at large depth of cuts; but less when the depth of cut is smaller.

Barge et al., (2008) studied single grit scratching to better understand plastic deformation and failure phenomena induced by grinding processes. Experimental test consisted of scratching a soft flat surface (AISI4140 steel) using a cutting insert fixed on the periphery of a disc. The experimental setup allowed producing scratches at high cutting speeds up to 3000 m/min for depth of cut of 80 μm . From the experimental results, a normal and tangential force versus instantaneous depth of cut graph was drawn at various cutting speeds. The forces increased linearly with increasing depth of cut, however, interestingly, higher forces were obtained at higher cutting speed, which is contrary to some previous work (Feng and Cai, 2001). The reasons for this were not expressed clearly because the work was solely experimental and was associated with hardening and softening phenomena which could occur during material cutting.

Ghosh et al., (2010) studied grinding mechanics using the single grit test. They performed their tests on a soft ductile material (rolled aluminium) with a diamond abrasive grain (size 600 μm). The diamond grit was used in 4 different orientations to demonstrate the influence of grit geometry on the material removal mechanisms of grinding. It was observed that the orientation of the grit was an influential factor in determination grinding forces and material pile-up. Also, they observed that the pile-up sections were asymmetric which might indicate randomness of chip formation and the ploughing process. It was observed that the specific energy requirement decreased with increasing depth of cut irrespective of orientation of the grit. It was found that

both geometry of the ground groove and energy requirement were significantly influenced by orientation of the grit.

Recently, Anderson et al., (2011^b) studied the cutting effectiveness of grinding grits using a high speed scratch tester built on Blohm Planomat CNC grinding machine. A spherical diamond tool with a nose radius of 0.508 mm was used to produce scratches at cutting speed of 300 m/min to 1800 m/min at depths of cut ranging from 0.3 μm to 7.5 μm . The scratches were quite long, about 100 mm to capture the cutting force profile. The scratch length was kept long to overcome the insufficient natural frequency of the force sensor to capture force profile at smaller length scratches. Experimental results show that the normal forces increased with cutting speed, while the tangential forces decreased with cutting speed. The increase in normal forces with cutting speed was attributed to the strain rate hardening of the workpiece material since strain rate is a function of velocity. However, the decrease in the tangential force with cutting speed was attributed to the decrease in coefficient of friction between the cutting tool and the workpiece. Anderson et al suggested that the strain hardening effects due to strain rate were not sufficiently large so as to overcome the reduced friction and its effects on cutting mechanics. Scratch profiles were also investigated in this work and larger pile up height was observed at larger depths of cut. In addition, slight decrease in average pile up height was observed with the increase of the cutting speed.

2.6.3 Size effect in grinding

Size effect is one of the most significant characteristic of micro scale machining. It is also a well-known aspect of the grinding process. The size effect in machining is generally described as the increase of specific energy with decrease of undeformed chip thickness. The size effect phenomenon was first discussed by Backer et al., (1952). They found that the specific energy

became larger while the undeformed chip thickness was reduced in surface grinding. However, it is now considered that the increase of specific energy with decrease of undeformed chip thickness is due to the chip forming process being a special high-strain extrusion process that involves a rapidly increasing strain with decrease in undeformed chip thickness. Thus, it results in very large specific energy in the hot working regime existing in the FFG chip forming zone (Shaw, 1996).

Shaw (1971) proposed a theoretical explanation for the size effect using an idealized sphere as an abrasive grain as shown earlier in Figure 2.8. He determined that the specific force increases as the undeformed chip thickness is reduced. The force exerted by the grain was determined by using an analogy similar to that of the force obtained in the Brinell hardness test. Kannappan and Malkin (1972) attributed the specific energy increase to the growing portion of ploughing and rubbing energy when the undeformed chip thickness is reduced. Malkin and Guo (2008) proposed that the grinding power P , during material removal process, can be partitioned into chip formation, ploughing and sliding (rubbing) components. According to Malkin and Guo's suggestion, the chip formation component can be estimated based on constant specific energy of chip formation. The ploughing component P_p was assumed to be based on a constant ploughing force per unit width. The sliding power P_s was assumed to be proportional to the area of the wear flats on the surface of the wheel. Because of the critical grain depth of cut for the commencement of chip formation, the proportion of ploughing and sliding in grinding increases when the grain depth of cut decreases. This makes the specific energy high when the depth of cut is small.

Nakayama et al., (1977) attributed the high specific energy to inherent poor cutting ability of abrasive grits and proposed the following reasons for poor cutting ability of grits: (1) the bluntness of the grit tip as well as the cutting edges lead to rubbing action along the chip

formation and this requires high-specific energy; and (2) extremely small average chip thickness in grinding leads to a very high effective rake due to significant edge radius at the grit tips. Shaw (1995) also explained the size effect in single point diamond turning (SPDT) and ultra precision diamond grinding (UPDG) with regard to undeformed chip thickness involved in the processes. He stated that chip forming model shifts from concentrated shear to micro-extrusion with decreasing undeformed chip thickness. When the undeformed chip thickness is less than the radius at the tool or grit tip, the effective rake angle of the tool has a large negative value.

Rowe and Chen (1997) explained the size effect using the ‘sliced bread analogy’ which makes the assumption that the thinner a loaf is sliced the more energy is required to slice the complete loaf because a greater surface area is cut and deformed. Thus the greater the total surface area involved in cutting, ploughing and rubbing, the more energy is required. It is proposed that the cause of the size effect in grinding is that with smaller chips, a larger chip surface area is generated and the sliding and ploughing energy is increased. It has been shown that the variations of specific energy in grinding can be related comprehensively to a wide range of grinding and dressing parameters regarding the size effect. According to the size effect, specific energy can be controlled by changing the grinding conditions or the dressing conditions, so as to increase or reduce the size of the idealized undeformed chips.

It is also known that the specific energy requirement in grinding is high compared to machining. Ghosh et al., (2008) attributed this high specific energy requirement to the irregular and random geometry of the abrasive grits, which include a lot of rubbing and ploughing actions along with the chip formation by the shearing process. Also, the effective rake angle in grinding is highly negative which contributes to the high specific energy requirement in grinding. Ghosh et al., (2008) predicted the specific energy requirement analytically for high-efficiency deep grinding (HEDG) of bearing steel by a monolayer CBN wheel. Although energy observations

demonstrated a scattered distribution as shown in Figure 2.10, the developed analytical model was able to predict the specific energy within an acceptable limit. The grinding specific energy, both experimental and modelled as the contribution of ploughing and rubbing diminish at higher depth of grit cut.

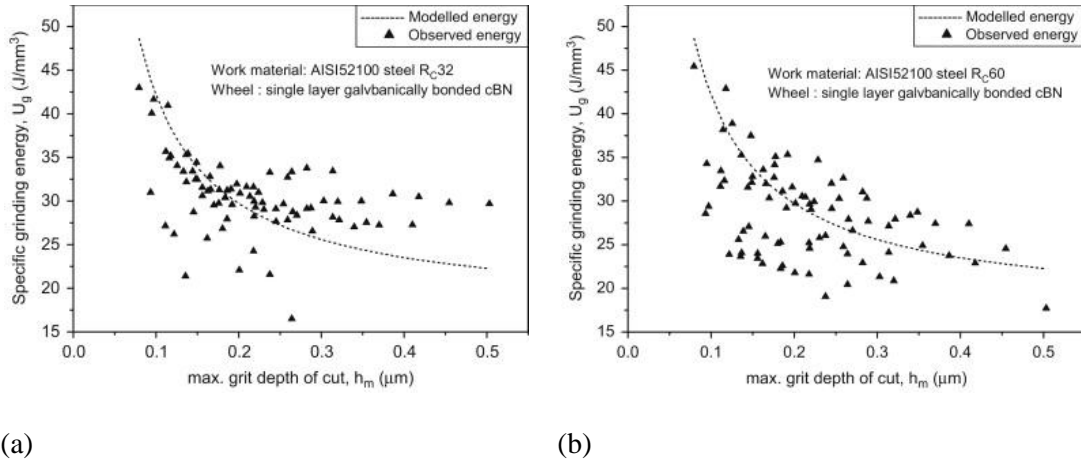


Figure 2.10 Variation of specific energy with maximum grit depth of cut into the workpiece (a) hardness R_C32 and (b) hardness R_C60 (Ghosh et al., 2008)

2.7 Summary

In this chapter, a fundamental understanding of grinding technology has been acquired from the available knowledge. Previous works on single grit grinding have been reviewed to reveal the importance of individual grit-workpiece interactions in terms of material removal mechanisms (rubbing, ploughing and cutting), cutting mechanics (cutting force, specific energy, etc.), material mechanics (workpiece material hardening or softening phenomena) and surface finish quality. So far the majority of research has been conducted to determine the influence of machining conditions (such as depth of cut, cutting speed, material properties, etc.) for micro-

scale grinding. Single grit grinding tests have been performed mainly using shaped tools (such as shaped diamond grains, conical indenter, shaped cutter or inserts, etc.).

However, in real grinding process, abrasive grains have irregular shapes and their shapes continuously change during interaction with the workpiece due to wear and fracture of the grains so that material removal mechanisms and cutting mechanics could show different characteristics at every moment of grit-workpiece engagement. For instance, an abrasive grit could produce scratches with a single edge groove when it has a fresh cutting edge, but, later on, it could start to produce scratches with multi-edges grooves due to multiple cutting edges generated by grain fractures it has experienced. The material removal mechanism in the single edge scratches and multi edge scratches shows completely different characteristics in all aspects (ploughing and cutting mechanisms, cutting forces, specific energies). Thus, micro scale grinding using shaped cutting tools cannot provide a detailed understanding of micro-grinding material removal mechanisms.

From previous researches on the single grit grinding, there exist some experimental investigations conducted by using abrasive grits rather than using shaped tools. These have failed to offer a detailed explanation of material removal mechanisms of micro grinding because of the narrow concentration of the research which has focused mainly on measuring cutting force as a function of cutting speed and depth of cut. Scratch profiles were not intensively investigated in these researches. However, in order to understand the material removal mechanisms, scratch profiles must be analysed in terms of rubbing, ploughing (side ploughing or material pile up and pile up ratio), and cutting mechanisms across the scratch length.

Looking at the state of the art grinding technology, the single grit grinding mechanism is not fully understood in terms of material removal mechanisms and cutting mechanics. It requires further research and this thesis aims to contribute to the detailed understanding of grinding

material removal mechanism by concentrating on those areas where insufficient information is available. To do this, the effects of abrasive grit shape on ploughing and cutting mechanisms is studied on different materials (with various hardness values). Changes in the abrasive grit shape with advances of grit scratching and its influences on the scratch form (profile) could be very useful to discover the unknown behaviour in the single grit grinding mechanism. Side ploughing (or pile-up) will be investigated by using pile up ratio definition (the ratio of the cross sectional pile-up area to the groove section area across the scratch form) to explore the cutting mechanics with the machining conditions (cutting speeds, depths of cut, material properties). Previously, the entire scratch form has never been investigated. Another novel approach in this study will be to show how material removal mechanisms during single grit scratching changes along the scratch. Further, a novel FEM approach for grinding surface creation (studied for the first time in this thesis) using single grit scratching technique will be studied in detail.

Chapter 3 Modelling and Simulation of the Grinding Process Using FEM

3.1 Introduction

Modelling dynamic machining processes by simplifying the real system and simulating the processes under prescribed conditions is the most popular technique for predicting machine behaviour and influences of the machining parameters on both tool and workpiece. Applications of modelling and simulation techniques to the grinding process have become very popular as the power of computer systems has increased to a level where it can solve complex problems such as abrasive grit-workpiece interaction. With a well-designed model, simulation of the grinding process could reduce costly experimental investigation to determine changes in grinding process behaviour on the quality of the machined part, tool failure, workpiece deformation characteristics and cutting mechanics. In addition, numerical simulations, such as finite element method (FEM) simulation, are able to determine some machining characteristics such as cutting mechanics and stresses, strains, strain rates, temperature gradients within the materials which are extremely difficult to determine by experimental tests alone.

Grinding is one of the most complex machining processes. Due to its complexity there is no universal model to comprehensively predict machining behaviour in terms of grinding forces, stresses, surface creation, surface finish and material removal. In the literature, the modelling techniques for grinding process have been subdivided into two groups: physical process models which contain fundamental analytical, finite element, kinematic and molecular dynamic models; and empirical process models including regression and neural network models (Tönshoff et al.,

1992; Brinksmeir et al., 2006). Additionally, heuristic models such as rule based models have been used occasionally for grinding process modelling (Brinksmeir et al., 2006). The state of the art in modelling and simulation of grinding process is highlighted in the review paper by Brinksmeier et al., (2006) and simulation models are categorized as shown in Figure 3.1.

A physical model is developed in conjunction with physical laws by using mathematical equations, while an empirical model is developed by using actual results obtained from experimental tests. To build an empirical model, grinding tests are performed and results are recorded together with machining conditions and then coefficients are calculated to link input (grinding conditions) and output (grinding test results) parameters. Finally, a developed model is validated by performing further grinding tests and experimental and predicted results are compared. In contrast to the empirical model, physical model cannot usually be easily implemented in a computer system, and its development requires much more effort compared to the empirical model. But physical model of the machining process can often be applied to different machining process by adjustment of the model whereas empirical models are only valid for prescribed conditions. This can be seen as a superiority of the physical model over the empirical model.

Physical models are generally used to predict the machining forces, stress-strain variation along machined surface, deformation on the tool and machine part, temperature rise along cutting edges etc., and in some cases, machined part geometry can be estimated by using well developed physical models. An essential aspect of physical and empirical models is an application scale. Since grinding processes can be modelled either at a macroscopic scale where the grinding wheel-workpiece interaction is of concern or at the microscopic scale of the single abrasive grit-workpiece interaction. Empirical models have been mostly used for grinding applications at the macroscopic scale and they can also be used for microscopic scale. Physical

models, however, can be applied to both macroscopic and microscopic scale grinding applications (Brinksmeier et al., 2006).

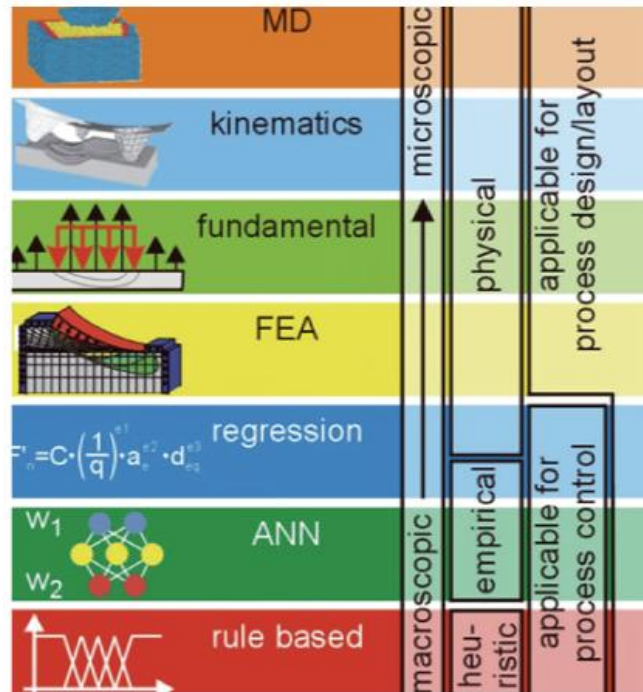


Figure 3.1 Simulation category of abrasive process (Brinksmeier et al., 2006)

Finite element analysis (FEA) and molecular dynamic (MD) analysis use physical laws for the modelling and simulation of abrasive grit-workpiece interaction. MD analysis is a good tool for atomistic level simulation but its computation can be cumbersome when its application reaches micrometre scale (Brinksmeier et al., 2006; Oluwajobi and Chen, 2010). FEA can be applied to macro and micro scale simulations. The one obstacle in the simulation of computational model such as FEA and MD has been the limited power of computer systems. However, with the rapid development in computer technology, even more complex FEA and MD analysis has become feasible to simulate advanced machining processes. FEA is the most frequently used method to model machining processes because there exist several powerful

software packages available for FEA application (such as Abaqus, Ansys, Deform, MSc. Marc, AdvantEdge, Forge, etc.) and also its application to machining processes is well understood comparing to other numerical methods (such as Smooth Particle Hydrodynamics (Ruttimann et al., 2010; Bağci, 2011)). Besides, advanced material removal mechanism can be simulated using the FEM by introducing elastoplastic material models (Doman et al., 2009^a). Unlike analytical and kinematical models, the FEM provides indispensable numerical solutions together with multi-physics analysis including thermo-elastoplastic material properties to solve the given problem (Doman et al., 2009^b). Material model definition is crucial for the accurate and reliable simulation of material removal mechanisms.

In the grinding process, the purpose of FEA is to predict the result of the metal cutting process in terms of the cutting forces, stresses, temperatures, chip geometry, etc. These parameters are used to evaluate the process performance taking into account energy consumption, grinding wheel failure, abrasive wear rate, possible abrasive fracture, workpiece burn, surface finish, chip-workpiece interaction caused surface deterioration, etc. Some of the FEA outputs such as strains, stresses and temperature distribution across the workpiece and tools are difficult to determine experimentally, hence, FEA is a useful computational tool which provides critical information about the workpiece and tool condition (Wu et al., 2005). In the last decade several models have been developed using FEA to simulate machining processes including cutting, milling, grinding at the macro scale (Mackerle, 2003; Soo et al., 2004; Brinksmeier, et al., 2006; Özel and Zeren, 2007; Lai et al., 2008; Calamaz et al., 2011). But some problems still exist at micro scale modelling of the grinding process when abrasive grit-workpiece interaction occurs at the level of a few micrometres (μm). In this chapter, up-to-date finite element simulations of the grinding process, especially for micro scale single grit-workpiece interaction, will be provided to demonstrate current knowledge. Fundamental of finite

element theory for machining applications, flow stress models, chip formation simulations and macro scale grinding process analysis are given to provide a clear picture in the state of the art of FEA technology.

3.2 Finite element method approach for modelling material removal

3.2.1 Fundamental of finite element method

FEA is a frequently used numerical method to find the approximate solution of complex problems such as metal forming and metal machining which are difficult to solve without a numerical approach. FEM uses partial differential and integral equations to evaluate the solution of a problem. A problem for FEA is an assembly of finite elements where the problem variables are calculated only at the nodes of the elements. The values of variables between nodes are determined by interpolation. In FEM, an exact solution of the problem is not sought; only approximate solution can be achievable at every node. Physical laws are applied to each finite element to obtain a solution; then the nodal solutions are assembled to describe the entire continuum. Eventually, the global solution of the entire continuum is evaluated numerically (Childs et al., 2000).

Figure 3.2 illustrates FEM discretization using triangular elements for a thin plate (thickness t_h) loaded elastically in its plane by three forces F1, F2 and F3.

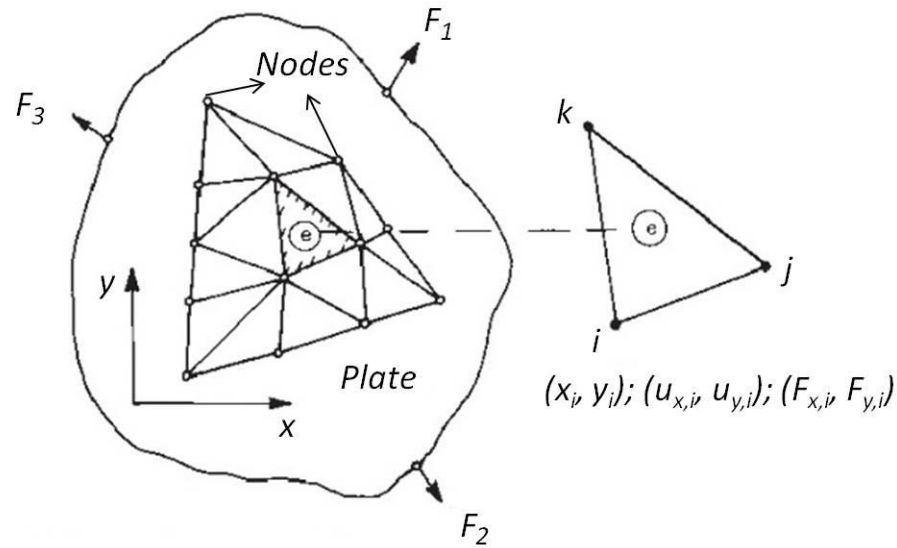


Figure 3.2 Finite element method illustration for a mechanical problem (Childs et al., 2000)

The vertices of the elements are the nodes for the problem. Each element (as identified by 'e') is defined in two dimensions by the position of its three nodes, (x_i, y_i) for node i and similarly for j and k . The external forces cause x and y displacements of the nodes, $(u_{x,i}, u_{y,i})$ at i and similarly at j and k . The adjacent elements transmit external forces to the sides of the element, equivalent to forces $(F_{x,i}, F_{y,i})$, $(F_{x,j}, F_{y,j})$ and $(F_{x,k}, F_{y,k})$ at the nodes.

It is useful to describe the fundamental of FEM approach to relate stresses, strains, displacements and forces with each other. These fundamental FEM equations can be found in Childs et al., (2000), and extended to metal machining. The most fundamental relation of FEM can be strain-displacement relations (Childs et al., 2000), where the strain represents the rate of displacement with position, and can be described as:

$$\varepsilon_{xx} = \frac{\partial u_x}{\partial x} = \frac{(y_j - y_k)u_{x,i} + (y_k - y_i)u_{x,j} + (y_i - y_j)u_{x,k}}{2\Delta} \quad 3.1$$

Where Δ is the area of the element; ε_{xx} , ε_{yy} and γ_{xy} are the strain components. Matrix algebra allows a compact expression of these results:

$$\begin{Bmatrix} \varepsilon_{xx} \\ \varepsilon_{yy} \\ \gamma_{xy} \end{Bmatrix} = \frac{1}{2\Delta} \begin{pmatrix} y_j - y_k & 0 & y_k - y_i & 0 & y_i - y_j & 0 \\ 0 & x_k - x_j & 0 & x_i - x_k & 0 & x_j - x_i \\ x_k - x_j & y_j - y_k & x_i - x_k & y_k - y_i & x_j - x_i & y_i - y_j \end{pmatrix} \begin{Bmatrix} u_{x,i} \\ u_{y,i} \\ u_{x,j} \\ u_{y,j} \\ u_{x,k} \\ u_{y,k} \end{Bmatrix} \quad 3.2$$

More compact still;

$$\{\varepsilon\}_{element} = [B]_{element} \{u\}_{element} \quad 3.3$$

Where $[B]_{element}$, known as the B- matrix, has the contents of Equation (3.2).

The second fundamental relation could be stress-strain relation which, in the elastic range, is described by Hooke's law. The stress tensor σ_{ij} has nine components (for 3D analysis) but, because $\sigma_{ij} = \sigma_{ji}$, only six are independent. The same rule applies to the strain tensor. The basis of the stress-strain relation in matrix form can be expressed as:

$$\begin{Bmatrix} \sigma_{xx} \\ \sigma_{yy} \\ \sigma_{zz} \\ \sigma_{xy} \\ \sigma_{yz} \\ \sigma_{zx} \end{Bmatrix} = \begin{bmatrix} & & & & & \\ & & & & & \\ & & & & & \\ & & & & & \\ & & & & & \\ & & & & & \end{bmatrix} \begin{Bmatrix} \varepsilon_{xx} \\ \varepsilon_{yy} \\ \varepsilon_{zz} \\ \varepsilon_{xy} \\ \varepsilon_{yz} \\ \varepsilon_{zx} \end{Bmatrix} \quad \text{or} \quad \{\sigma\} = [D]\{\varepsilon\} \quad 3.4$$

Here, $[D]$ is a 6x6 matrix. The content of this matrix changes depending on the whether the relation between stress-strain is elastic, elastic-plastic, or rigid-plastic as explained below.

For elastic condition;

$$\{\sigma\} = [D^e]\{\varepsilon\} \quad \text{or} \quad \{d\sigma\} = [D^e]\{d\varepsilon\} \quad 3.5$$

Where $[D^e]$ in explicit form is written as;

$$[D^e] = \frac{E}{1+\nu} \begin{bmatrix} \frac{1-\nu}{1-2\nu} & \frac{\nu}{1-2\nu} & \frac{\nu}{1-2\nu} & 0 & 0 & 0 \\ \frac{\nu}{1-2\nu} & \frac{1-\nu}{1-2\nu} & \frac{\nu}{1-2\nu} & 0 & 0 & 0 \\ \frac{\nu}{1-2\nu} & \frac{\nu}{1-2\nu} & \frac{1-\nu}{1-2\nu} & 0 & 0 & 0 \\ 0 & 0 & 0 & 1 & 0 & 0 \\ 0 & 0 & 0 & 0 & 1 & 0 \\ 0 & 0 & 0 & 0 & 0 & 1 \end{bmatrix} \quad 3.6$$

Where ν is Poisson's ratio.

For elastic-plastic condition;

First of all, it will be helpful to demonstrate the principal stresses and strain acting on a unit element, which will be used in the elastic-plastic flow definition. Figure 3.3 illustrates the principal stresses and strain increment on a unit element.

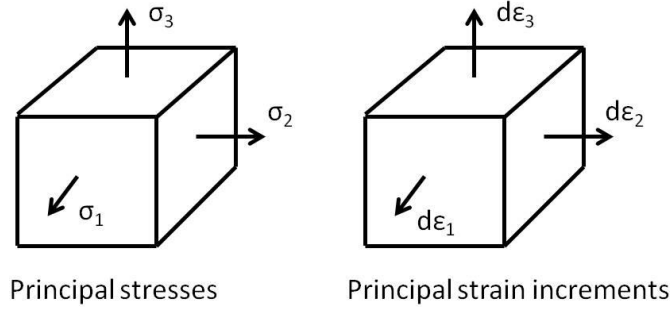


Figure 3.3 Illustration of principal stresses and principal strain increments (Childs et al., 2000)

Principal stress (σ_1, σ_2 and σ_3) acting on a unit element can be written in the form of hydrostatic stresses (σ_m) and the deviatoric stresses (σ') components:

$$\left. \begin{aligned} \sigma_m &= (\sigma_1 + \sigma_2 + \sigma_3)/3 \\ \sigma'_1 &= \sigma_1 - \sigma_m \\ \sigma'_2 &= \sigma_2 - \sigma_m \\ \sigma'_3 &= \sigma_3 - \sigma_m \end{aligned} \right\} \quad 3.7$$

The hydrostatic contribution has little influence on yielding. An acceptable yield criterion must be only function of the deviatoric stresses. The resultant deviatoric stress is defined as the RMS value of the individual values $\sigma'_r = \left(\sigma_1'^2 + \sigma_2'^2 + \sigma_3'^2 \right)^{1/2}$, which has been confirmed by

experiments to define the yield criteria. Material yielding occurs when the σ_r' reaches a critical value, commonly known as the von-Misses yield criterion. Von Misses yield criterion is also known as the equivalent stress criterion $\bar{\sigma}$ and determined as:

$$\bar{\sigma} = \sqrt{3/2}\sigma_r' \quad 3.8$$

Similarly, deviatoric strain needs to be determined since work hardening occurs with increasing yield stress beyond the critical value. A resultant deviatoric strain increment $d\varepsilon_r$ is determined as the RMS value of the individual principal strain increments;

$$d\varepsilon_r = (d\varepsilon_1^2 + d\varepsilon_2^2 + d\varepsilon_3^2)^{1/2} \quad 3.9$$

The equivalent strain increment $d\bar{\varepsilon}$ is defined as $d\bar{\varepsilon} = \sqrt{2/3}d\varepsilon_r$.

After defining deviatoric stresses and deviatoric strain, the stress and stress-strain relation for the elastic-plastic condition can be described using Equation 3.4 which is written in incremental or rate form;

$$\{d\sigma\} = [D^{e-p}]\{d\varepsilon\} \quad \text{or} \quad \{\dot{\sigma}\} = [D^{e-p}]\{\dot{\varepsilon}\} \quad 3.10$$

Where $[D^{e-p}]$ matrix has the content;

$$[D^{e-p}] = [D^e] - \frac{9G^2}{\bar{\sigma}^2(H' + 3G)} \begin{bmatrix} \sigma'_{xx}\sigma'_{xx} & \sigma'_{xx}\sigma'_{yy} & \sigma'_{xx}\sigma'_{zz} & 2\sigma'_{xx}\sigma'_{xy} & 2\sigma'_{xx}\sigma'_{yz} & 2\sigma'_{xx}\sigma'_{zx} \\ \sigma'_{yy}\sigma'_{xx} & \sigma'_{yy}\sigma'_{yy} & \sigma'_{yy}\sigma'_{zz} & 2\sigma'_{yy}\sigma'_{xy} & 2\sigma'_{yy}\sigma'_{yz} & 2\sigma'_{yy}\sigma'_{zx} \\ \sigma'_{zz}\sigma'_{xx} & \sigma'_{zz}\sigma'_{yy} & \sigma'_{zz}\sigma'_{zz} & 2\sigma'_{zz}\sigma'_{xy} & 2\sigma'_{zz}\sigma'_{yz} & 2\sigma'_{zz}\sigma'_{zx} \\ \sigma'_{xy}\sigma'_{xx} & \sigma'_{xy}\sigma'_{yy} & \sigma'_{xy}\sigma'_{zz} & 2\sigma'_{xy}\sigma'_{xy} & 2\sigma'_{xy}\sigma'_{yz} & 2\sigma'_{xy}\sigma'_{zx} \\ \sigma'_{yz}\sigma'_{xx} & \sigma'_{yz}\sigma'_{yy} & \sigma'_{yz}\sigma'_{zz} & 2\sigma'_{yz}\sigma'_{xy} & 2\sigma'_{yz}\sigma'_{yz} & 2\sigma'_{yz}\sigma'_{zx} \\ \sigma'_{zx}\sigma'_{xx} & \sigma'_{zx}\sigma'_{yy} & \sigma'_{zx}\sigma'_{zz} & 2\sigma'_{zx}\sigma'_{xy} & 2\sigma'_{zx}\sigma'_{yz} & 2\sigma'_{zx}\sigma'_{zx} \end{bmatrix} \quad 3.11$$

Where $G = 0.5E/(1+\nu)$ is the shear modulus, H' is the work hardening rate ($d\bar{\sigma}/d\bar{\epsilon}$), $\bar{\sigma}$ is the equivalent stress as given in Equation 3.8.

After describing the displacement-strain relation and stress-strain relation, the entire finite element formulation must be described. Forces at the nodes of each element and their global assembly are determined by using the finite element formulation. The force balance for a single finite element is described as,

$$\{F\}_{element} = t_h \Delta_{element} [B]_{element}^T [D][B]_{element} \{u\}_{element} \quad 3.12$$

In general, for any shape of finite element, $[K]_{element} = t_h \Delta_{element} [B]_{element}^T [D][B]_{element}$ is known as the stiffness matrix. By adding up individual finite element forces, a global force-displacement relation can be obtained for all element nodes,

$$\{F\} = [K]\{u\} \quad or \quad \{dF\} = [K]\{du\} \quad or \quad \{\dot{F}\} = [K]\{\dot{u}\} \quad 3.13$$

For the entire solution of the finite element continuum, it is necessary to integrate the incremental solution of Equation (3.13) across the elements beginning from its initial conditions to the required position. This operation would be performed by the FEM software. This section describes the fundamental FEM equations for elastic and elastic-plastic problems. Detailed information on FEM for metal cutting applications can be found in the Metal Machining Book (Childs et al., 2000). Specific elastic-plastic flow stress formulations used for FEM simulation in this thesis will be described in later sections.

3.2.2 Numerical formulation

In continuum mechanics, finite element motion can be described using three different algorithms: Eulerian (Raczy et al., 2004), Lagrangian (Soo et al., 2004; Özel, 2006), and Arbitrary Lagrangian Eulerian (ALE) (Movahhedy et al., 2000; Pantalé et al., 2004; Özel and Zeren, 2007). In addition, the entire finite element problem can, by considering boundary condition limitations, be divided into sub-regions in which different flows are applied, such as partly Eulerian motion and partly Lagrangian motion. Eulerian formulation is generally preferred in fluid mechanical problems, while Lagrangian formulation is more suitable for solid mechanical problems (Childs et al., 2000; Astakhov and Quteiro, 2008). In the Eulerian formulation, the mesh is fixed in space and constrained by creating control volume, thus material flows through a fixed mesh. On the other hand, in the Lagrangian formulation, finite element meshes are attached to work material and thus they flow together with deformation of the material. Figure 3.4 illustrates chip flow with these formulations (Eulerian and Lagrangian).

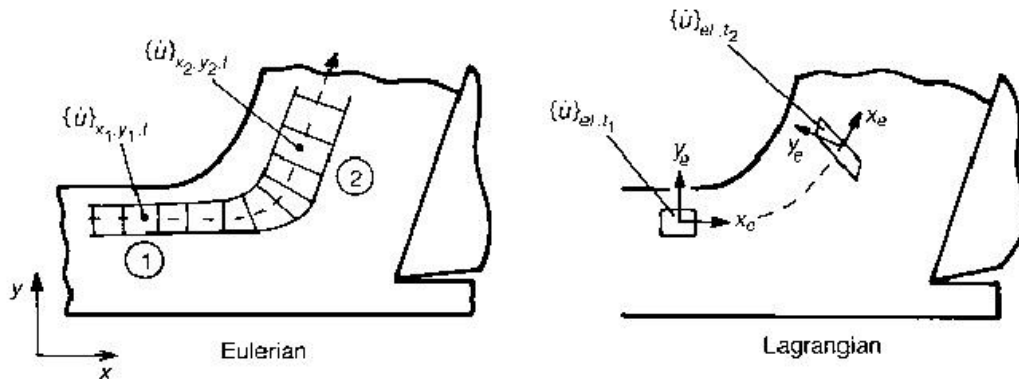


Figure 3.4 Eulerian and Lagrangian view of plastic flow (Childs et al., 2000)

Although both formulations have been used in metal machining application, each has advantages and drawback in terms of accuracy and capability as well as computational cost. In the Eulerian formulation, element shapes do not change with time, thus the coefficients of the [B] matrix, which is governed by the element shape, is computed only once. A common problem in finite element formulation is how to describe the effluxion of material property changes, such as strain hardening and thermal softening, from element to element throughout the entire mesh. This problem is faced mainly when the Eulerian formulation is used for FEM machining (Childs et al., 2000). The effluxion of material property changes from element to element is not a problem in the Lagrangian formulation, but [B] matrix must be updated continuously during material flow due to change in element shape. This results in geometrical non-linearity together with material nonlinearity in the finite element equations. Due to these nonlinearities, frequent remeshing is necessary to reduce element distortion during simulation. This could lead to extreme computational cost (Childs et al., 2000).

The one of the drawback of the Eulerian formulation is that only steady state metal cutting simulation can be performed whereas with the Lagrangian formulation metal machining such as chip generation can be formed based on cutting conditions. For example, saw tooth chip cannot be generated by using the Eulerian formulation but can by using the Lagrangian formulation. Another drawback of the Eulerian formulation in cutting simulation is the requirement of *a priori* known chip shape which must be defined before simulation - but in the case of Lagrangian formulation the chip shape need not be known *a priori*. Simulation using the Lagrangian formulation does have some drawbacks; due to severe plastic deformation during metal cutting some simulation elements are extremely distorted and new mesh generation is needed and well-defined remeshing method must be imported to reduce element distortion. Also, in Lagrangian formulation, a chip separation technique should be defined to allow chip separation from the

workpiece material. The chip separation technique such as node separation or fracture model with element deletion does not work efficiently in some machining conditions such as with a negative tool rake angle, or rounded cutting edge tools. Some of these problems can be reduced with frequent remeshing around the heavily deformed region, but frequent remeshing in the simulation bring other problems such as computational time (simulation can last for several days) or with the application of continuously remeshing some elements become extremely small and this may cause other problems since continuum mechanics may no longer be valid for extremely small elements of nano-scale size. These types of problems do not exist in the use of the Eulerian formulation, but Eulerian formulation has very limited capability for the metal machining because, for example, chip thickness should remain constant with *a priori* defined chip shape; this is not realistic for metal machining applications.

As it is clear from the above explanation, both the Lagrangian and the Eulerian formulations have drawbacks and limited capability for applications which involve heavy deformation and material properties dependent chip generation, as found in metal cutting. To reduce these drawbacks, formulation can be used which take advantage of both Lagrangian and Eulerian formulations (Movahhedy et al., 2000). The ALE adaptive meshing technique combines the features of pure Lagrangian analysis and pure Eulerian analysis. In ALE the mesh is neither attached to the material nor fixed in space. The mesh moves and material displacement is described as the sum of mesh displacement and relative displacement (Astakhov and Quteiro, 2008). ALE formulation can be applied to FEM model by using Eulerian and Lagrangian boundary conditions together (Figure 3.5– (a)) or pure Lagrangian boundary conditions (Figure 3.5– (b)). ALE adaptive meshing is a tool that makes it possible to maintain a high-quality mesh throughout an analysis, even when large deformation or loss of material occurs, by allowing the mesh to move independently of the material. ALE adaptive meshing does not alter the topology

(elements and connectivity) of the mesh, which implies some limitations on the capability of this method to maintain a high-quality mesh upon extreme deformation.

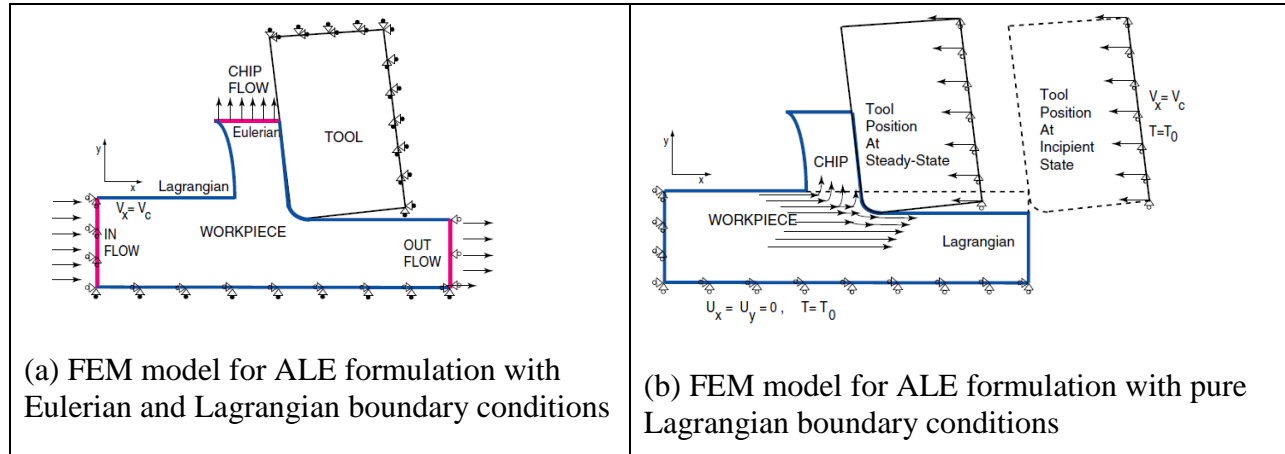


Figure 3.5 Finite element model boundary conditions for ALE formulation (Özel and Zeren, 2007)

Adaptive meshing can be achieved by creating a new mesh through a process called sweeping, and remapping solution variables from the old mesh to the new mesh with a process called advection. A new mesh can be created at a specified frequency by sweeping iteratively over the adaptive mesh domain. During each mesh sweep, nodes in the domain are relocated - based on the current positions of neighbouring nodes and elements - to reduce element distortion.

The new position, x_{i+1} , of a node is obtained as:

$$x_{i+1} = X + u_{i+1} = N^N x_i^N \quad 3.14$$

Where X is the original position of the node, u_{i+1} is the nodal displacement, x_i^N are the neighbouring nodal positions obtained during the previous mesh sweep, and N^N are the weight functions obtained from one or a weighted mixture of the smoothing methods. The displacements applied during sweeps are not associated with mechanical behaviour.

The node motion procedure is based on three smoothing methods, volume smoothing, Laplacian smoothing and equipotential smoothing (Abaqus user's manual, 2009). Smoothing methods can also be combined by using weighting factor between 0 and 1 to define the contribution of each method. The sum of the weighting factors should be 1. Smoothing methods are used to determine the new location of each node based on the location of neighbouring nodes and elements in the ALE domain (Pantalé et al., 2004; Abaqus user's manual, 2009). To demonstrate how the smoothing method works, volume smoothing is described here as an example, Volume smoothing relocates a node by computing a volume-weighted average of the element centres in the elements surrounding the node. In Figure 3.6, the new location of node M is determined by a volume-weighted average of the positions of the element centres, C, of the four surrounding elements. Eventually, the location of node M is forced to move towards the element centre C_3 by means of volume weighting to reduce the element distortion.

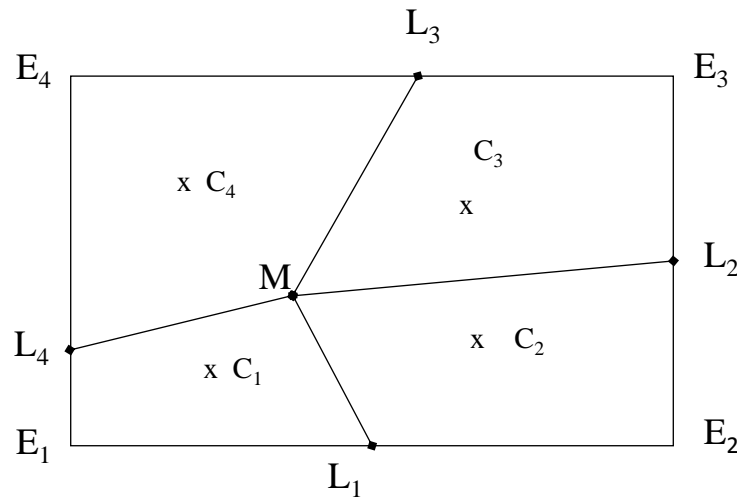


Figure 3.6 Relocation of a node during a mesh sweep

The ALE formulation has drawbacks. ALE formulation is sometimes not sufficient to replace the need for remeshing in machining simulation. It is necessary to have a tuning process for variables; this takes up a lot of time and is not guaranteed to work. Also, the history of material properties may not transfer properly during remapping and this may lead to increased inaccuracy in the model.

3.2.3 Newton-Raphson iteration method

The Newton-Raphson method (or simply Newton's method) is an iteration technique commonly used for the nonlinear finite element equations. Basic equations to be solved in nonlinear analysis, at time $t + \Delta t$, could be:

$${}^{t+\Delta t}R - {}^{t+\Delta t}F = 0 \quad 3.15$$

Where the vector ${}^{t+\Delta t}R$ stores the externally applied nodal loads and ${}^{t+\Delta t}F$ is the vector of nodal point forces that are equivalent to the element stresses. Both vectors in Equation (3.15) are determined by using the principle of virtual displacement. The nodal point forces ${}^{t+\Delta t}F$ are determined based on the nodal displacements, thus it is necessary to iterate to obtain the solution of Equation (3.15). The equations used in the Newton-Raphson iteration are, for $i=1, 2, 3\dots$

$${}^{t+\Delta t}K^{(i-1)}\Delta U^{(i)} = {}^{t+\Delta t}R - {}^{t+\Delta t}F^{(i-1)} \quad 3.16$$

$${}^{t+\Delta t}U^{(i)} = {}^{t+\Delta t}U^{(i-1)} + \Delta U^{(i)} \quad 3.17$$

With initial conditions

$${}^{t+\Delta t}U^{(0)} = {}^tU; \quad {}^{t+\Delta t}K^{(0)} = {}^tK; \quad {}^{t+\Delta t}F^{(0)} = {}^tF$$

The iteration will be terminated when the appropriate convergence criteria is satisfied (Bathe, 1996).

3.2.4 Time integration methods

FEAs for nonlinear dynamic problems are performed using either implicit or explicit time integration methods. Although both choices can be applicable to many FEM problems, both have particular advantages depending on the relevant equation of motion. The implicit solution is performed iteratively using Newton's method. Usage of an implicit model requires solving a set of equations concurrently for each time integration point. This leads to a large number of iterations with a prescribed increment to complete convergence, and that can incur huge computational cost depending on the size and complexity of the problem (Soo et al., 2004). The major advantage of implicit integration is to maintain unconditionally stable linear systems; the size of the time increment is not restricted to that used to integrate a linear system. Use of explicit time integration is computationally more efficient since no iteration or tangent stiffness matrix is required to solve the equations. Explicit integration uses the diagonal mass matrices, and the inversion of the mass matrix used in the computation of the acceleration vector is trivial so it increases computational efficiency of the explicit method (Pantalé et al., 2004). The explicit central difference integration rule, described below, is used to integrate the equations of motion of the entire system:

$$\dot{\mathbf{u}}^N_{\left(i+\frac{1}{2}\right)} = \dot{\mathbf{u}}^N_{\left(i-\frac{1}{2}\right)} + \frac{\Delta t_{(i+1)} + \Delta t_{(i)}}{2} \ddot{\mathbf{u}}^N_{(i)} \quad 3.18$$

$$\mathbf{u}_{(i+1)}^N = \mathbf{u}_{(i)}^N + \Delta t_{(i+1)} \dot{\mathbf{u}}_{\left(i+\frac{1}{2}\right)}^N \quad 3.19$$

Where u^N is a degree of freedom (a displacement or rotation component) and the subscript i refers to the increment number in an explicit dynamics step. The central-difference integration operator is explicit in the sense that the kinematic state is advanced using known values of $\dot{u}_{(i-1/2)}^N$ and $\ddot{u}_{(i)}^N$ from the previous increment.

The key to the computational efficiency of the explicit procedure is the use of diagonal element mass matrices because the accelerations at the beginning of the increment are computed by:

$$\ddot{u}_{(i)}^N = \left(M^{NJ}\right)^{-1} \left(P_{(i)}^J - I_{(i)}^J\right) \quad 3.20$$

Where M^{NJ} is the mass matrix, P^J is the applied load vector, and I^J is the internal force vector. A lumped mass matrix is used because its inverse is simple to compute and because the vector multiplication of the mass inverse by the internal force requires only n operations, where n is the number of degrees of the freedom in the model. The explicit modelling requires no iterations and no tangent stiffness matrix. The internal force vector, I^J , is assembled from the contributions of the individual elements such that a global stiffness matrix need not be formed (Abaqus user's manual, 2009).

In modelling metal cutting problems, the explicit integration method is mostly used since cutting processes are complex dynamic problems. The explicit method is guaranteed to converge, whereas an implicit code as an iterative solution is not guaranteed to converge. However, the choice of integration methods varies depending on the capability of the FEM software to compute the model. As is clearly seen from many publications, Deform software users such as

Özel (2006), Aurich and Bil (2006) and Özel (2009) use implicit integration methods whereas Abaqus software users such as Pantalé et al., (2004), Soo et al., (2004) and Mabrouki et al., (2008) prefer explicit integration methods depending on the capability of the software solver.

3.3 Finite element simulation of chip formation in literature

Finite element simulation of the machining processes is a very popular means of simulating chip formation. There are many publications on chip formation modelling and simulation via FEA (Marusich and Ortiz, 1995; Shet and Deng, 2000; Movahhedy et al., 2000; Mamalis et al., 2001; Mackerle, 2003; Bil et al., 2004; Belhadi et al., 2005; Aurich and Bil, 2006; Özel, 2009; Childs, 2009; Ambati and Yuan, 2010; Childs, 2010; Calamaz et al., 2011). The ultimate goal of all these researchers was to minimize cost and save time by reducing expensive experimental tests. To do so they had to estimate a number of physical parameters such as stress, strain and strain rate which are quite difficult to obtain by experimental tests. Besides, prediction of chip types and morphology under different operating conditions is one of the significant benefits provided by FEM simulations. This section presents some essential literature to give a clear picture of the state of the art of FEM simulation of chip formation; in particular what is possible or not with current technology. In the following sections, constitutive models to illustrate highly deformed material behaviour, influential factors in chip formation mechanism, and chip separation criteria are discussed together with an extensive literature review.

3.3.1 Commonly used constitutive material models for FEM cutting simulation

It is necessary to build a constitutive material model which realistically represents the flow strength (or yield strength) of the work material. The flow stress properties of work materials are

ideally obtained by empirical tests under varying strain, strain rate and temperature. For high speed machining applications where strain rates might increase to even 6000 s^{-1} or more, flow stress properties with its constitutive elements are estimated using the Split Hopkinson Pressure Bar (SHPB) test (Özel, 2006; Ramezani and Ripin, 2010). However, the level of strain and strain rate observed at shear zones during machining are much higher than those attained using the SHPB test which performs material tests at strain rates up to 10^4 s^{-1} (Jaspers and Dautzenberg, 2002^b; Ramezani and Ripin, 2010) and temperatures up to 600 °C (Özel, 2006). In the SHPB test range, the Johnson-Cook material flow stress constitutive model (JCM) has been frequently used by those researching metal machining applications where large deformation occurs at high strain rates (Mabrouki et al., 2008; Özel, 2009). However, the JCM may fail beyond the SHPB test range (Sima and Özel, 2010). To increase the material behaviour accuracy and reliability under very high strain rates beyond the SHPB, researchers have made modifications to the JCM and the parameters inserted into the model have been adopted by the numerical solution (Calamaz et al., 2008; Sima and Özel, 2010). In next section, the JCM, modified JCMs and other flow stress models are given.

3.3.1.1 Johnson-Cook material model

The Johnson-Cook material model (JCM) (Johnson and Cook, 1983) is widely used for analysis of material flow stress in metal machining simulation. It is much preferred for materials whose flow stress is highly influenced by strain rate and temperature changes due to plastic deformation caused by thermal softening. The JCM is described as:

$$\sigma = \underbrace{\left[A + B(\varepsilon)^n \right]}_{f_1} \underbrace{\left[1 + C \ln \left(\frac{\dot{\varepsilon}}{\dot{\varepsilon}_0} \right) \right]}_{f_2} \underbrace{\left[1 - \left(\frac{T - T_{room}}{T_{melt} - T_{room}} \right)^m \right]}_{f_3} \quad 3.21$$

f_1 components represents strain hardening behaviour
 f_2 components represents strain rate sensitivity behaviour
 f_3 components represents thermal softening behaviour of the metal

Where σ is the equivalent stress, ε the equivalent plastic strain, the strain rate $\dot{\varepsilon}$ is normalized with a reference strain rate $\dot{\varepsilon}_0 = 1 s^{-1}$, T_{room} room temperature, and T_{melt} is the melting temperature of the material, A is the initial yield stress, B the hardening modulus, n the work-hardening exponent, C the strain rate dependency coefficient, and m is the thermal softening coefficient. Several applications of the JCM are presented in Table 3.1.

Table 3.1 Examples of Johnson-Cook flow stress model (JCM) application in the literature

Reference	Software	Constitutive model	Separation criterion	Chip type	Material
Vaziri et al., (2011)	Abaqus/Explicit	JCM	ALE simulation and JC damage	Continuous chip but not mentioned about chip type	AISI1045
Özel (2009)	Deform 3D Implicit integration	JCM	Continuous remeshing	Continuous chip	AISI4340
Ambati and Yuan (2010)	Abaqus/Explicit 2D	JCM	JC damage	1-Segmented 2-Discontinuous with very low plastic displacement	AISI4340
Wang et al., (2009)	Deform 2D Implicit integration	JCM	No separation criterion, Automatic remeshing	Segmented chips	Al6061-T6
Mabrouki et al., (2008)	Abaqus/Explicit	JCM	JC damage	Segmented chip	Aluminium alloy (A2024-T351)
Özel and Eren (2007)	Abaqus/Explicit	JCM	No chip separation criterion, ALE formulation	Small chips	AISI4340
Arrazola et al., (2007)	Abaqus/Explicit	JCM	No separation criterion, ALE formulation	Serrated chips	AISI4140
Hortig and Svendsen (2007)	Abaqus/Explicit	JCM	Fracture strain based failure criterion	Serrated chips	Inconel 718
Belhadi et al., (2005)	Abaqus/Explicit 2D	JCM	JC damage	Serrated	AISI4340 Steel
Guo and Yen (2004)	Abaqus/Explicit	JCM	JC damage-ALE mesh	Discontinuous chip	AISI4340

3.3.1.2 Modified Johnson-Cook material model by Calamaz

Modification to the JCM was suggested by Calamaz et al., (2008) for finite element simulation of metal cutting. In Calamaz's model, flow softening is defined as a decrease in flow stress with increasing strain beyond a critical strain hardening.

$$\sigma = \left[A + B\varepsilon^n \left(\frac{1}{\exp(\varepsilon^a)} \right) \right] \left[1 + C \ln \left(\frac{\dot{\varepsilon}}{\dot{\varepsilon}_0} \right) \right] \left[\left(1 - \left(\frac{T - T_{room}}{T_{melt} - T_{room}} \right)^m \right) \left(D + (1 - D) \tanh \left(\frac{1}{(\varepsilon + S)^c} \right) \right) \right] \quad 3.22$$

Where $D = 1 - (T/T_{melt})^d$, and $S = (T/T_{melt})^b$.

The JCM was modified again by Calamaz et al., (2011) by improving the strain softening effect as shown by the following equation;

$$\sigma = \left[A + B\varepsilon^n \left(\frac{1}{\dot{\varepsilon}} \right)^a \varepsilon^{(n-0.12(\varepsilon\dot{\varepsilon}))^a} \right] \left[1 + C \ln \left(\frac{\dot{\varepsilon}}{\dot{\varepsilon}_0} \right) \right] \left[1 - \left(\frac{T - T_{room}}{T_{melt} - T_{room}} \right)^m \right] \quad 3.23$$

When parameter a is set to a non-zero value, the strain softening phenomenon is observed. The higher the value of a , the greater is the magnitude of the strain softening. A high value of friction coefficient together with introduced strain softening parameter a of 0.11 gave the best agreement for the chip formation in machining Ti-6Al-4V titanium alloy (Calamaz et al., 2011).

3.3.1.3 Modified Johnson-Cook material model by Sima and Özel

Sima and Özel (2010) have suggested further modification on the strain hardening part of the JCM by including flow softening at higher strain values which is almost identical to Calamaz' s model (Calamaz et al., 2008). Here a parameter s was introduced to further control the \tanh function for thermal softening.

$$\sigma = \left[A + B\varepsilon^n \left(\frac{1}{\exp(\varepsilon^a)} \right) \right] \left[1 + C \ln \left(\frac{\dot{\varepsilon}}{\dot{\varepsilon}_0} \right) \right] \left[\left(1 - \left(\frac{T - T_{room}}{T_{melt} - T_{room}} \right)^m \right) \left(D + (1 - D) \left[\tanh \left(\frac{1}{(\varepsilon + p)^r} \right) \right]^s \right) \right] \quad 3.24$$

Where $D = 1 - (T/T_{melt})^d$, and $p = (T/T_{melt})^b$

The effect of flow softening is more pronounced at low temperatures, and as temperature increases, both strain hardening and flow softening effects are reduced.

3.3.1.4 Flow stress model used by Childs

Childs (2010) used the material flow stress dependence on strain, strain rate and temperature to be of the form shown in the following equations,

$$\sigma = g(\varepsilon^p) \left(1 + \frac{\dot{\varepsilon}^p}{\dot{\varepsilon}_0^p} \right)^{1/m} \quad 3.25$$

$$g(\varepsilon^p) = \sigma_0 \Theta(T) \left(1 + \frac{\varepsilon^p}{\varepsilon_0^p} \right)^{1/n}, \quad \varepsilon^p \leq \varepsilon_c^p \quad 3.26$$

$$g(\varepsilon^p) = \sigma_0 \Theta(T) \left(1 + \frac{\varepsilon_c^p}{\varepsilon_0^p} \right)^{1/n}, \quad \varepsilon^p > \varepsilon_c^p \quad 3.27$$

$$\Theta(T) = \sum_{i=0}^5 c_i T^i, \quad T_0 \leq T \leq T_c \quad 3.28$$

$$\Theta(T) = \left(\frac{T_{\text{melt}} - T}{T_{\text{melt}} - T_c} \right) \sum_{i=0}^5 c_i T^i, \quad T_c < T \leq T_{\text{melt}} \quad 3.29$$

Where σ is the effective von Mises stress, g the flow stress, σ_0 is the yield stress at T_0 , ε^p the accumulated plastic strain, $\dot{\varepsilon}_0^p$ a reference plastic strain rate, m strain rate sensitivity exponent, n hardening exponent, $\Theta(T)$ is a function of a temperature in the flow stress model, T_0 a reference temperature, T_c crystallization temperature, c_i material constants for $i=1,2,..5$. This flow stress model was also used by Marusich and Ortiz (1995) with an adaption of the power hardening law with linear thermal softening.

3.3.1.5 Flow stress model of Rhim and Oh

Rhim and Oh (2006) proposed a new flow stress model based on assumptions concerning large deformation processes at very high speed and high temperature during cutting process and attempt to predict the serrated chip formation.

$$\sigma = \sigma_h \left[1 - \exp(-k_1 \varepsilon^{n_1}) u(T) \right]^{m_1} - \sigma_s \left[1 - \exp(-k_2 \varepsilon^{*n_2}) \right]^{m_2} u(T) \quad 3.30$$

Where σ_h is the flow stress at the peak strain (ε_p); σ_s is the reduction stress function of strain rate and temperature; k_1 , k_2 , n_1 , n_2 , m_1 and m_2 are material parameters. The Avrami type terms are used for the thermal softening effect of dynamic re-crystallization and $(\sigma_h - \sigma_s)$ is the stress reached in the steady state after annihilation of dislocations. $u(T)$ is a step function of temperature defined as $u(T) = 0$ for $\varepsilon < \varepsilon_c$ and $u(\varepsilon) = 1$ for $\varepsilon > \varepsilon_c$.

$$\sigma_h = (C_0 + C_1 \varepsilon^p) (1 + C_2 \ln \dot{\varepsilon}) (C_3 - C_4 T^{*q}) \quad 3.31$$

Where C_0 , C_1 , C_2 , C_3 , C_4 , p and q are the parameters determined to satisfy temperature rise over $0.5T_{melt}$ in the primary shear zone. The term T^* is calculated as,

$$T^* = \frac{T - T_{room}}{T_{melt} - T_{room}} \quad 3.32$$

$$\varepsilon^* = \left[\frac{\varepsilon - \varepsilon_c}{\varepsilon_p} \right] u(\varepsilon) \quad 3.33$$

Where $u(\varepsilon)$ is a step function in the strain defined as $u(\varepsilon) = 0$ for $\varepsilon < \varepsilon_c$ and $u(\varepsilon) = 1$ for $\varepsilon \geq \varepsilon_c$. The parameter ε_c represents the strain when orthogonal dynamic re-crystallization occurs and

ε_p is the peak strain at the peak stress of the flow curves. With this model, Rhim and Oh (2006) predicted the adiabatic shear localization band and performed serrated chip formation. But the model was proposed only for the situation where dynamic recrystallization occurs in large plastic deformation processes at high strain rates, it was not proposed to describe the complicated phenomena of adiabatic shear band formation during large deformation,

Applications of these models (modified JCM, model used by Childs, and Rhim and Oh's flow stress model) will be presented with a review of appropriate literature in later sections and a list can be found in Table 3.2. However, flow stress models used for machining are not limited to these models, there are also some other flow stress models have been used occasionally for machining simulations. They are Oxley flow stress model (1989) that used power law strain hardening to represent material behaviour; the Andrade-Meyers modified JCM model (Andrade and Meyers, 1994) accounts for phase transformation effects in flow stress behaviour of a material above the material recrystallization temperature; Zerilli-Armstrong (1987) have developed material constitutive model taking into account the dislocation dynamics, each material structure type (face centred cubic and body centred cubic) will have its own flow stress model dependent on the dislocation characteristic of the particular material structure. Furthermore, the flow stress models proposed by El-Magd al., (2003) and Maekawa et al., (1983) have been occasionally used for carbon steels (Iqbal et al., 2007).

Table 3.2 Examples of application for flow stress models in the literature

Reference	Software	Constitutive model	Separation criterion	Chip type	Material
Calamaz et al (2011)	Forge 2005 2D	JCM and Modified JCM,	Material separation by automatic remeshing	Serrated chips	Ti-6Al-4V
Sima and Özel (2010)	Deform-2D	Modified JC plastic model	Chip separation achieved with continuous remeshing	Serrated chips	Ti-6Al-4V
Childs (2010, 2009)	AdvantEdge-2D	As given in Eqn. (3.25)	Adaptive remeshing	Continuous chips	Normalised medium carbon steels (mild steel)
Lorentzon et al., (2009)	MSC. Marc 2D Implicit	Isotropic rate independent piecewise linear plasticity model	1- Cockroft-Latham fracture model 2- Plastic strain fracture criterion 3- With periodic remeshing	1- Segmented chip 2- Continuous chip 3- Discontinuous chip	Alloy 718
Aurich and Bil (2006)	Deform-3D	1-JCM for Temperature below $0.5T_m$ 2-JC-Avrami model for temperature above $0.5T_m$	1- Continuous remeshing 2- Cockroft-Latham damage	1-Continuous chip 2-Serrated chips	Not mentioned
Bil et al., (2004)	1-MSC. Marc/implicit 2-Deform 2D/implicit 3-AdvantEdge/explicit	1- and 2- strain, strain rate and temperature dependent flow stress data used 3- Eqn. similar to Eqn.(3.30)	1- No separation criterion, via remeshing 2-No separation criterion , remeshing 3-Cockroft-Latham damage criterion	Continuous chip	C15 steel
Soo et al., (2004)	Abaqus Explicit 3D model	Elastic plastic isotropic hardening, and flow stress defined as a function of strain, strain rate and temperature	Chip formation was achieved by using a shear failure criterion where the equivalent plastic strain was taken as the failure measure	Continuous chip simulated	Inconel 718
Bäker et al., (2002)	Abaqus/Standard 2D	Plastic flow curves based on experiment	Predefine separation line and then separate nodes on this line. and pure deformation method	Continuous and segmented chips	Ti6Al4V
Mamalis et al., (2001)	MARC-2D Implicit FEM	Isotropic hardening using flow stress as a function of strain, strain rate, temperature	Geometrical shape separation criterion based on a critical distance at the tool tip regime.	Continuous chip without segment	Not mentioned
Shet and Deng (2000)	Abaqus/explicit 2D	An over-stress rate dependent, elastic-visco-plastic constitute law was employed.	Chip separation based on critical stress criterion and a nodal release technique	Continuous chips	AISI4340
Marusich and Ortiz (1995)	Pronto2D explicit dynamic code	Slightly different from Eqn. (3.25)	Continuous remeshing.	Continuous, Segmented and discontinuous chips	AISI4340

3.3.2 Influential factors in chip formation

In metal cutting processes, three types of chip formation often occur: continuous, serrated and discontinuous. The continuous chip is not appreciated in automated machining since it interferes with the machining process and may cause unpredictable flaws and damage on the machined surface, cutting tool or machine tool, or even injuries to the operator. To overcome such problems, the serrated chip (also called the saw tooth or continuous segmented chip), which is easier to break and to dispose of, is considered a relatively ideal chip for the machining process (Xie et al., 1996). Being able to predict the cutting conditions which lead to the formation of serrated chips is increasingly important. Increasing segmentation on continuous chips eventually leads to serrated chips. Segmentation during chip formation is triggered by two phenomena: formation of an adiabatic shear band and crack initiation mechanism in a primary shear zone (Sima and Özel, 2010). Adiabatic shear banding refers to the localization of the deformation into narrow bands of intense plastic deformation that usually form during high-rate plastic deformation and often precede shear fracture (Batra et al., 1990). In addition to adiabatic shear band induced segmentation, serrated chips are formed when a chip fractures at the primary deformation zone due to overstrain and the interfaces of the chip segments are welded immediately after the fracture by compression and high level of chemical activity. Then, a crack is generated according to a predefined criterion and propagates in the direction of the shear zone into the chip, which enables segmentation (Aurich and Bil, 2006). The simulated generation of segmentation is achieved by employing either failure criterion or a modified constitutive model regarding strain, strain rate and temperature as a function of flow stress into the FEM. Deployment of flow stress is highly desired in couplings with continuous adaptive remeshing to mitigate the distortion of the element that takes place due to high plastic deformation at the

primary and secondary deformation zones. It is expected that, ultimately, adaptive remeshing will enable processing to a complete solution without termination of the model due to excessive element distortion. Aurich and Bil (2006) developed a 3D chip formation model by introducing Rhim's flow stress equations to account for thermal softening, and used adaptive remeshing to deal with element distortion and fracture mechanism based chip separation criterion. They observed significant influence of the applied method on predicted chip shape; adaptive remeshing alone resulted in continuous chips, thermal softening generated brief segmentation and fracture mechanism causing severe segmentation. Calamaz et al., (2011) studied the influence of strain softening phenomenon and the friction law on the shear location generating serrated chips. Bäker et al., (2002) developed a 2D orthogonal cutting process considering adiabatic shearing effects and generated segmented chips by applying a remeshing technique to the model.

Segmentation of chips is also dependent on operating parameters; segmented continuous chips are often produced at high cutting speeds and the degree of segmentation increases with increasing feed or uncut chip thickness (Sima and Özel, 2010, Öpöz and Chen, 2012). Tendency to form segmented chips is smaller at lower cutting speeds (Calamaz et al., 2011).

Tool rake angle might also be an influential parameter on chip type formation. In experimental tests Komanduri (1971) observed curled chip formation until a rake angle of -75° . He noticed that the side flow increase with increasing negative rake angle. Ohbuchi and Obikawa (2003) developed a thermo-elastic-plastic finite element model of orthogonal cutting with a large negative rake angle to reveal the mechanisms and thermal aspects of the grinding process. Serrated chips were observed with single grit grinding with a rake angle of -45° and -60° . Recently, Öpöz and Chen (2012) have demonstrated the formation of a continuous chip (at 22° rake angle), serrated chip (at 0° rake angle) and discontinuous chip (at -30° rake angle).

3.3.3 Chip separation criteria

The earliest FEM simulation of chip formation was by Strenkowski and Carroll (1985) and they achieved serrated chip by using chip separation criteria. To date, chip separation has been achieved either by *a priori* defined separation criteria, such as using critical stress and damage model (Shet and Deng, 2000; Mabrouki et al., 2008; Ambati and Yuan, 2010), or by fully plastic flow of material by means of adaptive remeshing technique employed in the FEM model (Özel, 2006; Sima and Özel, 2010). Finite element analysis of chip formation can be modelled either by using Eulerian formulation or Lagrangian formulation (as explained in Section of 3.2.2). In the Eulerian based model, there is no need to define chip separation criterion, cutting is simulated from the steady state but it is necessary to define the initial chip shape, so it is not very realistic for machining purpose. Conversely, Lagrangian formulation allows simulation of chip formation without defining initial chip shape from incipient of chip formation to the steady state. It gives more realistic results when predicting chip geometry and other machining parameters such as stress, strain, and force. However, the Lagrangian formulation needs a chip separation criterion to enable chip separation from the workpiece (Mamalis et al., 2001). Huang and Black (1996) evaluated chip separation criteria and divided them into two main categories: physical criteria such as effective plastic strain and strain energy density; and geometrical criteria such as distance tolerance. They concluded that neither geometrical nor physical criteria simulated the machining process correctly and suggested a FEM simulation based on a combination of geometric and physical criteria. Often, parting lines, or sacrificial layer, are used together with a failure criterion to allow chip separation from the workpiece when an updated Lagrangian formulation is used (Mabrouki et al., 2008). In early FEM models of chip formation, node release techniques based on distance tolerance, effective plastic strain and strain energy density were employed in the

model (Mamalis et al., 2001; Bil et al., 2004). According to the node release technique, an element in front of the tool is separated following nodal release when the defined criterion is satisfied. Recently, three methods have been used to generate chips;

1. Material failure (damage) models based on fracture which consider crack initiation followed by crack growth to form a chip according to a specified degradation criterion mechanics (Mabrouki et al., 2008; Lorentzon et al., 2009).

2. Flow stress models which take thermal softening and strain hardening into account and chips are produced due to plastic flow of material over the tool tip without crack formation, such models use continuous adaptive remeshing (Sima and Özel, 2010; Childs, 2009; Childs, 2010),.

3. Plastic flow of material by means of Arbitrary - Lagrangian - Eulerian (ALE) adaptive meshing (Guo and Yen, 2004; Özel and Zeren, 2007).

Moreover, material failure models and adaptive remeshing are combined to give further improvement on chip formation (Guo and Yen, 2004; Lorentzon et al., 2009). For the formation of serrated chips, in particular, combination of a material failure model with adaptive remeshing methods into a FEM model is crucial.

Explicit FEM analysis is generally preferred in cutting simulation since explicit analysis is guaranteed to converge. Large deformation was prevented by an updated Lagrangian formulation. Movahhedy et al., (2000) developed an orthogonal cutting model using the ALE approach to solve the equations derived by considering strain rate and temperature dependencies. Özel and Zeren (2007) developed a model where the chip was generated by plastic flow of workpiece material, and solved the developed equations with a FEM using ALE adaptive meshing without using chip separation criteria. Sima and Özel (2010) simulated serrated chips without using damage or failure models by adiabatic shearing due to temperature – dependent flow softening with continuous remeshing in Deform 2D.

Cutting simulations have been performed more realistically by introducing a progressive failure model with chip separation criteria (Huang et al., 1996) and adaptive meshing such as ALE has been used in the FEM (Özel and Zeren, 2007). To date, many models based on plasticity and fracture have been developed, their solution has involved different meshing techniques and implicit or explicit FEA software packages such as Deform (Jinsheng et al., 2009; Özel, 2009), Abaqus (Özel and Zeren, 2007; Mabrouki et al., 2008), MSC. Marc (Lorentzon et al., 2009) and Forge (Calamaz et al., 2011).

Use of a progressive failure model is a crucial factor when modelling cutting simulation in machining processes. One of the key features in failure progression is a properly introduced damage evolution criterion into the model. Damage evolution in the Abaqus software can be performed in two ways either by defining equivalent plastic displacement or by defining fracture energy dissipation (Abaqus user's manual, 2009). Ambati and Yuan (2010) studied the mesh-dependence in the simulation of cutting by introducing a progressive damage model coupled with a plastic displacement damage evolution criterion. They produced various shapes of chips by changing the plastic displacement value and showed that chip transition took place from continuous to segmented with increasing depth. Mabrouki et al., (2008) studied the dry cutting of aeronautical aluminium alloy and used a numerical model based on Johnson-Cook law incorporating material damage evolution by using a fracture energy model. They simulated a variable feed rate and cutting velocity with constant fracture energy. Their results showed that higher cutting speeds resulted in higher segmentation in the chip. A summary of chip separation criterion can be found in Table 3.1 and Table 3.2 together with corresponding chip type formation under different conditions.

3.3.4 Friction scheme in FEM simulation

Predicted results from FEM simulation of machining are highly influenced by two factors; the first one is the flow stress models which define the material deformation behaviour under high straining and thermal changes; and the second one is friction characteristics between the tool-chip interfaces (Özel, 2006). Friction conditions at the tool-chip interface (tool-chip contact length) strongly influence heat generation in this region (secondary shear zone) (Iqbal et al., 2008). In order to define friction scheme between tool-chip interfaces, the tool-chip contact length should be determined. Iqbal et al., (2008) reviewed the tool-chip contact length model and used friction models for chip formation mechanism. The contact length and friction parameters between the tool and chip are influenced by many factors, such as, undeformed and deformed chip thickness, rake angle, cutting speed, feed rate, etc., (Özel, 2006; and Iqbal et al., 2008). Characterization of friction at the tool-chip interface is difficult and complicated in machining. To capture the friction characteristics at the tool-chip interface, the best way is to measure the normal and frictional stresses by actual machining process experimentally. Well-known Coulomb friction model has been often used in the modelling of machining processes. According to Coulomb friction model ($\tau_f = \mu\sigma_n$), frictional stresses, τ_f , is proportional to normal force, σ_n , with a coefficient of friction, μ . However, in high speed machining, the Coulomb friction may not represent the tool-chip contact behaviour appropriately because interaction between tool face and chip become more complicated with increasing cutting speed. Zorev (1963) proposed a friction model for complex friction regime in high speed machining, his model consider sticking and sliding region between tool and chip interface separately. According to Zorev's model, the normal and shear stresses are represented as,

$$\tau_f(x) = \tau_p \quad \text{and} \quad \text{when} \quad \mu\sigma_n(x) \geq \tau_p \quad \text{while} \quad (x) \text{ within sticking region} \quad 3.34$$

$$\tau_f(x) = \mu\sigma_n(x) \quad \text{and} \quad \text{when} \quad \mu\sigma_n(x) < \tau_p \quad \text{while} \quad (x) \text{ within sliding region}$$

Where τ_f is a frictional shearing stress, τ_p is an average shear flow stress at the tool-chip interfaces. Some other friction models can be found in Table 3.3, which is from Iqbal et al., (2008) review.

Table 3.3 Friction models (Iqbal et al., 2008)

No	Friction model	Mathematical equation
1	Constant Coulomb friction law	$\tau_f = \mu\sigma_n$
2	Constant shear friction law (Wanheim and Bay, 1978)	$\tau_f = mk_p$
3	Variable Coulomb friction law	$\mu = f(\sigma_n) = \tau_f / \sigma_n$
4	Variable shear friction law (Usui and Shirakashi, 1982)	$m = \frac{\tau_f}{k_p} \left[1 - e^{\left\{ -(\sigma_n / \tau_f) \right\}} \right]$
5	Constant shear friction in sticking region and constant Coulomb friction in sliding region	$\tau_f = mk_p, \therefore 0 < x \leq l_{st}$ $\tau_f = \mu\sigma_n, \therefore 0 < x \leq l_{sl}$

Where τ_f = Frictional stress, σ_n = Normal stress, m = shear friction factor, k_p = Shear flow stress of the chip in the primary shear deformation zone, μ = Coefficient of friction, l_{st} = Sticking contact length, l_{sl} = Sliding contact length.

3.3.5 Chip generation based on FEM models in the literature

The results found in the literature on chip formation with software, constitutive models, and chip separation criterion and corresponding chip type were given in Table 3.1 and Table 3.2. According to Table 3.1 and Table 3.2, the JCM is the most popular model for simulation of chip formation where large deformation occurs at high strain rate. The JCM also takes into account

strain hardening and thermal softening phenomena up to certain limits. The main difficulty in chip formation simulation is insufficient flow stress data at high strain rates and temperatures to characterize the material deformation during the FEM simulation. However, these are experimentally evaluated data and the current SHPB has a limiting strain rate of up to 10^4 s^{-1} (Ramezani and Ripin, 2010). To reduce the deficiencies of available test information, the JCM has been modified by e.g., Sima and Özel (2010) who increased the flow stress behaviour capability to encompass more complicated situations (higher strain rate, hardening, softening, etc.). However, the problem is not only the flow stress model, to simulate the chip more realistically other criteria are also vital, these include chip separation criterion and the remeshing method. To date, chip formation has been simulated using adaptive remeshing (chip formed due to plastic flow), which is unable to demonstrate discontinuous chip and crack growth, or using a material failure model without damage evolution, which cannot correctly demonstrate material behaviour after damage initiation, or using sacrificial layers which allow chip separation exactly from the defined line but this is not acceptable for realistic chip formation since chips could include cracks even within itself.

Thus, a model is needed which can consider damage mechanics and damage evolution until ultimate chip formation, which considers adaptive remeshing to reduce element distortion and uses a flow stress model which should demonstrate material yielding at large deformation under high strain rate. Flow stress is dependent on experimental material data and is needed so that damage mechanics can be coupled with damage evolution to develop a more realistic chip formation model. Considering this necessary point, in this thesis a FEM model is developed that takes into account adaptive meshing, damage mechanics and damage evolution criterion in conjunction with the JCM. This will help to further understanding of chip simulation in the grinding process.

3.4 Finite element simulation of grinding process in literature

Grinding is a complex material removal process due to the large number of abrasive grains with an unknown geometry which varies with time. A better understanding of the physical processes of grinding can help to produce a more promising model and simulation. A model for grinding should describe the complex relationships between process and machine parameters, and work results. The interaction is modelled to predict grinding forces, temperatures, grinding energies, surface integrity, in ways that depend on the model used. Recent papers have reviewed both macro scale and micro scale FEA of the grinding process, and the different objectives pursued by modelling and simulation (Klocke, 2003; Brinksmeier et al., 2006; Doman et al., 2009^b). It was generally concluded that understanding of the simulation of the grinding process should be increased so that it will be possible to better predict process behaviour and component quality and to determine optimum process parameters prior to the manufacturing process. It should also allow complex preliminary investigations and development time to be reduced. Studies have shown that substantial time and cost saving can be obtained by the integration of process simulation within the development and planning phases (Klocke, 2003).

3.4.1 Wheel-workpiece interaction approach

Finite element simulation of the grinding process considering grinding wheel-workpiece interaction (the macro scale approach) is usually applied to calculate the influences of heat and mechanical surface pressure on the complete workpiece in terms of temperature distribution or form deviation. Thermal analysis of the grinding process has significant importance for this type of model (Rowe et al., 1997; Malkin and Guo, 2007). The grinding wheel is modelled as a moving heat source and the investigation is generally focused on thermal effects in the grinding

zone. The plastic material behaviour and the chip formation are not considered in the macro scale approach. Here, relevant literature regarding macroscopic simulation of the grinding process is reported together with a general simulation procedure.

In most macroscopic models the grinding wheel is represented as a combined source of heat and surface pressure, which is moved over the workpiece with feed speed. The exact distribution of the heat source within contact zone, between the workpiece and the grinding wheel, must be ascertained in order to provide realistic input parameters, in particular the heat flux distribution. Simplified profiles of the heat source were often idealized by assuming a rectangular, triangular, parabolic or trapezoidal shape. A general macro scale thermal model setup is shown in Figure 3.7. To model even a simplified heat source, it is essential to know the heat flux density \dot{q}_w which flows from the heat source into the workpiece. Most temperature models are based on the theory of Carslaw and Jaeger (1959) and this has been extended to take into account the cooling lubricant in front of and behind the contact zone of the workpiece (Figure 3.7(a)) and the constant temperature of the clamped areas (approximated as ambient temperature). The calculated uniform heat flux density is shown in Equation (3.35).

$$\dot{q}_w = K_v K_w \frac{V_c F_t}{l_g b_k} \quad 3.35$$

Where contact length is l_g , contact width of grinding wheel is b_k , cutting speed V_c , K_v and K_w are the energy dissipation (percentage) and heat distribution factors (percentage) respectively, and F_t is the tangential force during the process.

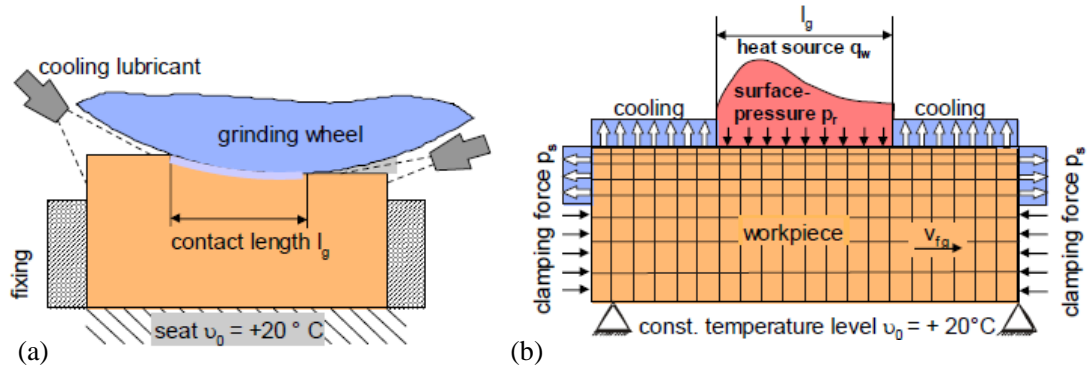


Figure 3.7 Macro scale FEM model description (a) illustration of grinding wheel-workpiece interaction (b) illustration of FEM model (c) different heat flux distribution used as heat source in the FEM model (Klocke, 2003)

The tangential force F_t can be measured using a dynamometer during grinding process. The factor K_v indicates the percentage of mechanical energy which is transformed into heat and can be set to $K_v=1$, because almost total grinding power is transformed into heat in the primary deformation zone. The heat distribution factor K_w corresponds to the percentage of heat energy entering into the workpiece (Brinksmeier et al., 2006). Calculation of K_w is shown with a diagram in Brinksmeier et al., (2006) using experimental and statistical method.

Mahdi and Zhang (1995) developed a 2D FEM model to predict the phase transformation that occurs during the grinding process. The model used temperature dependent thermal properties for the steel alloy (En23). A moving heat source with a triangular profile was used in the FEM. The relative peak location of the heat flux was found to be a critical parameter for material phase transformation during grinding. Mahdi and Zhang (2000) also investigated the residual stress caused by phase transformation and thermal deformation by using the similar

model in Mahdi and Zhang (1995). Hamdi et al., (2004) investigated the grinding induced residual stresses by using a thermo-mechanical FEM for a steel material (AISI52100). In the model, heat input is taken to be a function of such grinding parameters as wheel speed, workpiece speed and depth of cut. It was found that the temperature inside the workpiece changes proportional to the wheel speed.

Moulik et al., (2001) developed a FEM model to calculate the temperatures and stresses arising due to a moving heat source with a rectangular profile for the grinding of elastic and elastic-plastic workpiece materials. This FEM model was applied to calculate the surface and sub-surface residual stress induced in an elastic-plastic solid by such sources of heat when convection heat transfer is assumed to occur at the solid surface. The finite element calculations show that the near surface residual stresses produced by moving sources of heat are generally tensile and the magnitude of this stress increases with increasing heat flux values.

Chuang et al., (2003) investigated grinding forces and the associated stress and deformation fields generated in a ceramic workpiece during plunge surface grinding. They designed a 2D FEM with the grinding parameters and the mechanical properties of the workpiece as input variables. According to the results the depth of the subsurface shear failure zone increases with an increase in maximum undeformed chip thickness or the wheel depth of cut. The resulting local grinding force vector, maximum stress and damage zone sizes were predicted as a function of maximum undeformed chip thickness.

Mamalis et al., (2003) developed a FEM to predict the temperature field of the grinding zone. The FEM was developed based on Jaeger's model (Jaeger, 1942), where the grinding wheel is considered to be a moving heat source using the implicit finite element code Marc. Distribution of temperature fields in the workpiece was successfully calculated by the proposed model when the power exerted during grinding was a known parameter. The heat affected zone

can also be extracted from the temperature field of the workpiece by considering the critical temperature for tempering, and martensitic and austenitic transformation.

Liu et al., (2002) reported a finite element analysis on grinding and lapping of wire-sawn silicon wafers. An FEA model was first developed to simulate the waviness of the deformation of wire-sawn wafers in grinding and lapping processes. FEA simulations shed light on why conventional grinding cannot remove waviness effectively and why lapping was more effective than grinding in removing waviness.

3.4.2 Single grit-workpiece interaction approach

The investigation of the modelling and simulation of single grit-workpiece interaction was first initiated by Hahn (1962). According to Hahn, interaction between an abrasive grit and workpiece has three stages or phases in achieving material removal in the form of chips. These three stages of material removal mechanism performed by a single grit are illustrated in Figure 3.8.

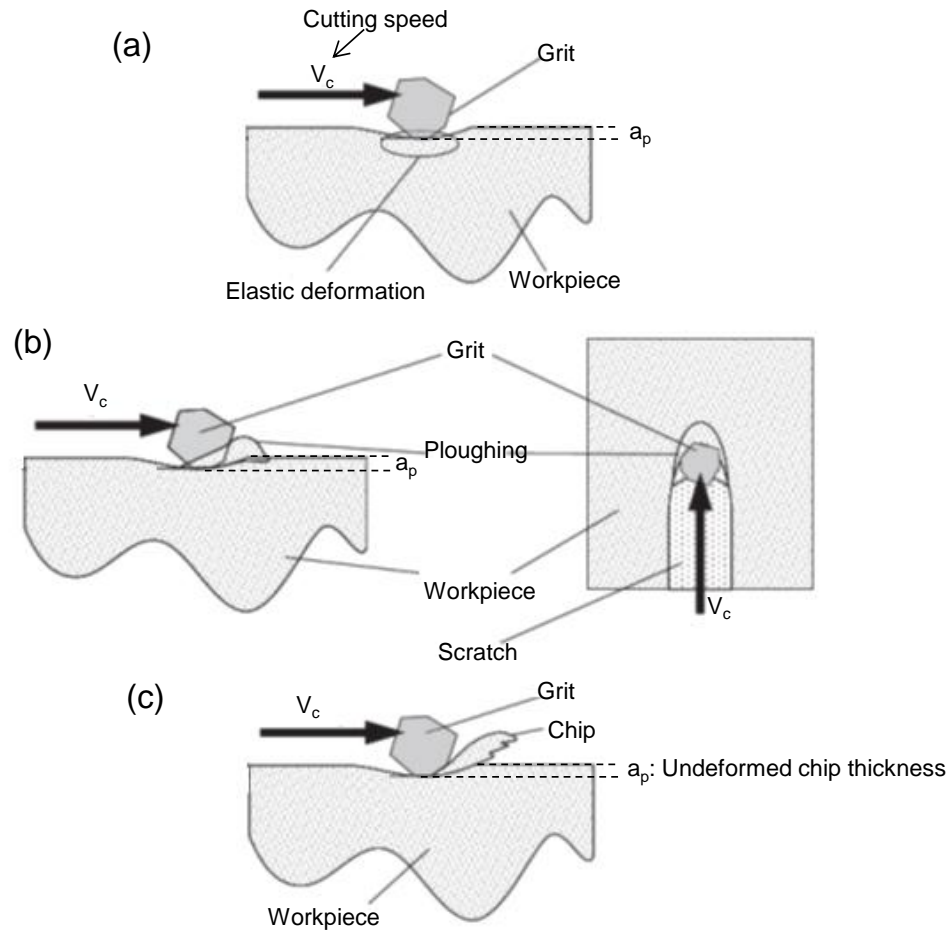


Figure 3.8 Illustration of (a) rubbing, (b) ploughing, and (c) chip formation phases of material removal by an individual grit (Doman et al., 2009^a)

The chip formation with abrasive grit differs in many ways from chip formation that occurs during conventional cutting. These can be listed as;

- **Cutting tool geometry effect:** Cutting tools in grinding are abrasive grits which have a geometrical shape that might continuously change during the cutting process depending on the operating conditions, whereas cutting tools in other cutting processes such as turning have a properly defined tool shape and chips are formed according to this shape and the operating conditions.

- **Size effect:** The cutting edge size and undeformed chip thickness are remarkably small in grinding compared to those in conventional cutting processes.
- **Number of cutting tools effect:** Numerous abrasive grits are involved in material removal processes during grinding each having a different geometry and different size, whereas generally single tools used for other cutting processes have a defined size and shape.
- **Material plastic flow direction effect:** Material might flow across both sides and ahead of the abrasive grit in different proportions depending on the grit shape and undeformed chip thickness, whereas with a shaped cutting tool material side flow is not large, material flow occurs predominantly ahead of the tool with more stable conditions compared to those occurs during grinding.
- **Cutting tool attack angle effect:** This is also known as the tool rake angle effect, where the rake angle is the angle between the cutting tool's front face and the material in front the cutting tool. This angle is highly negative during abrasive grit cutting but it cannot be known exactly, whereas the rake angle is one of the specifications of conventional machining and can be defined exactly before machining begins.

Material removal mechanisms as stated above mean that simulation of single grit action is difficult which is not the same for normal cutting processes, even though in the literature some researchers have proposed a simple similarity between abrasive grit cutting and shaped tool cutting which can be achieved by using a large negative tool rake angle (Ohbuchi and Obikawa, 2003). In addition to differences between single grit action and conventional cutting, single grit action on the workpiece requires 3D modelling rather than 2D simulation. Because abrasive grits

have irregular shapes which engage with the workpiece at large negative rake angles, the interaction occurs on both sides of the abrasive grit and also at the front face of the grit during grinding. So, cutting action (chip formation) occurs not only ahead of the grit but also in both side of the grit. This phenomenon is dissimilar to the chip formation that occurs during other machining processes, especially when a shaped cutting tool is used. Another crucial action with abrasive grit is the ploughing action, abrasive grit creates a groove and residual ploughed material is left on both side of the groove. This residual ploughed material and side chips can be modelled only in 3D. Therefore, three main challenges (3D model requirements, size effect and shape effects) remained to be solved for the modelling and simulation of the single grit cutting mechanism. There does not yet exist any FEM model of the single grit process which can successfully simulate these three actions (rubbing, ploughing and cutting) of the workpiece.

In the open literature physical descriptions of the sliding action in contact mechanics, surface friction and ploughing action by scratching and indentation are available, but none of them are capable of describing chip formation. Some FEM simulations have been attempted for the single grit grinding process together with some closely related areas such as sliding simulation and scratch simulation using an indenter are reviewed to demonstrate the state of the art technology in this field.

Lambropoulos et al., (1996) developed an axisymmetric FEM of indentation for the grinding of a glass surface which was modelled as an elastic-perfectly plastic material, by using rigid indenters having a radius of curvature and conical shape at the tip. This model was used to investigate compressive stresses in the plastic zone generated by an abrasive grit. However, this model was only capable of demonstrating the material pile-up around contact regions and stress distribution caused by indentation. As the indenter was not moving there was no material removal with this model.

To predict the grinding damage of ceramics Zhang and Peng (2000) developed a 3D FEM model which considered single grit grinding, where the grit was modelled with a spherical tip. Grinding damage was described as any form of strength degradation and surface deterioration that appeared during grinding. This model did not demonstrate chip formation. The damage zone was determined using effective von Mises stress distribution. Ceramic material modelling can be counted as different from other materials in terms of damage and elastic-plastic behaviour. The proposed model showed good agreement with experimental results. It is a useful innovation for damage prediction of grinding ceramics.

Klocke et al., (2002) developed a 2D FEM model by using Deform software to simulate the single grit cutting process where the grit is passing through the workpiece material. The grit was modelled with a cutting edge radius of 50 μm , scratching depth of cut was 20 μm , grit speed was 2700 m/min and table speed was 180 mm/min. A picture obtained from 2D FEM simulation is shown in Figure 3.9. The simulation predicted the maximum temperature would be around 1700 °C which was within the same band as previous analytical calculations. Klocke et al., (2002) also noted that there were many unknown parameters in the use of FEM simulation of cutting with a single grit. These parameters are associated with material properties which are not available for high speed grinding because conventional flow curves do not represent material behaviour at high strain and high strain rates which happen during the grinding process.

Simulation of single grit grinding was attempted at the RWTH Aachen University and at the IWT of the University of Bremen (Klocke, 2003). 2D and 3D simulations performed at these research centres are shown in Figure 3.10. The 3D model was obtained using an inelastic grit model which has tip radius and depth of cut of 5 μm . With a single grit FEM model, chip formation could not be properly achieved because of some problems which are not explained in

the paper. But single grit FEM simulation is very promising for the understanding of grinding process mechanisms.

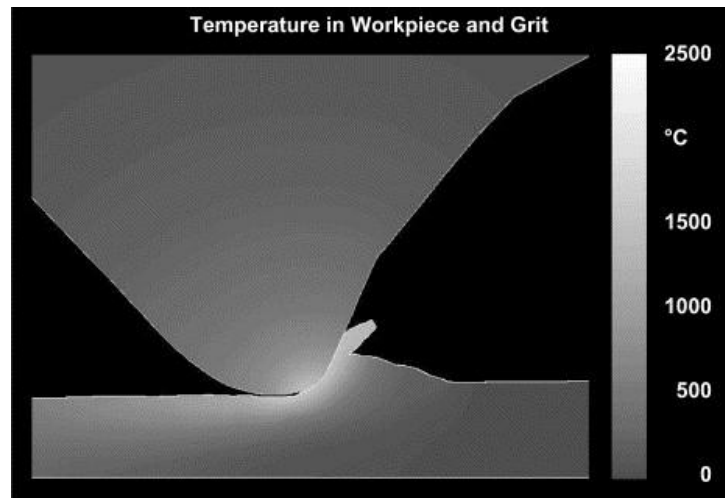


Figure 3.9 Temperature distribution during chip formation of single grit scratching (Klocke et al., 2002)

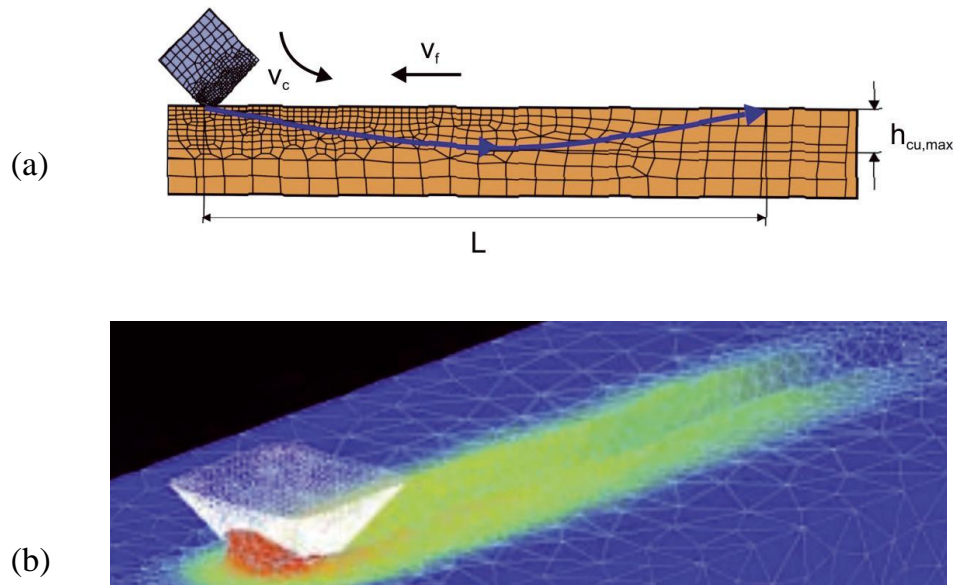


Figure 3.10 Single grit grinding simulation (a) 2D and (b) 3D model (Klocke, 2003)

Ohbuchi and Obikawa (2003) developed a finite element model of orthogonal cutting with a highly negative rake angle to provide more understanding of the mechanisms and thermal

aspects of grinding. A large rake angle was used since cutting with abrasive grit resembles the orthogonal cutting with large negative rake angle. Material behaviour was described by using thermo-elastic-plastic material properties. A stagnant chip region was observed during simulation and was removed by changing the cutting tool model to one where the model had a front nose which had the shape of the stagnant region. According to the results, chips are formed unconditionally with higher rake angles, whilst grinding with abrasive grit is in a lower range of rake angles where chip formation is restricted by the critical cutting speed and critical undeformed chip thickness. They found the critical cutting speed and uncut chip thicknesses for efficient material removal, but these parameters are affected by tool rake angle which suggests that high speed grinding is preferable to micro cutting with abrasives. Serrated chips and front bulging were obtained from the simulation and which strongly depends on the cutting speed, depth of cut and rake angle. When the cutting speed or the depth of cut decreases, chip shape diverges from serrated to bulging type flow.

Park et al., (2007) used finite element simulation to predict the shear angle developed during negative rake cutting by considering single grit interaction during grinding. A FEM model based on Merchant's model was solved using Deform 2D, and coefficients determined to predict the forces which occur during the micro grinding process. The cutting tool was assumed as perfectly sharp with negative rake angle of -20° , -40° , -60° and -80° , the cutting speed was 0.167 m/min and depth of cut was set to 250 μm . Park et al., (2007) also studied ploughing forces during micro scale grinding. In their model, ploughing action was simplified into the spherical indentation problem using FEM simulation. Thus, the ploughing force was directly determined from the indentation force. The proposed model without considering thermal effects predicts higher forces compared to experiment. When the thermal effects are included, better results were obtained which agreed with experimental results.

Doman et al., (2009^a) investigated the rubbing and ploughing stages of single grit grinding by using 3D finite element model performed in LS-DYNA software. In the FEM model, the size of the mesh element at the contact zone (grit-workpiece contact) was around 10 μm but much larger elements were used outside the contact zone. Elements sizes were too big for chip formation but chip formation was not the interest of the study. Only rubbing and ploughing stages during single grit grinding were investigated. Depth of cut for the simulation ranged from 1 μm to 20 μm . The rubbing to ploughing transition was observed at a depth of cut around 3 μm in the simulation, although in the real tests ploughing was observed at lower depth than that. The experimental verification was performed by using an alumina sphere indenter with a diameter of 2 mm. Simulation and experimental results demonstrated a good agreement for force prediction.

Chong et al., (2011) developed a cutting process for a single abrasive grit by using a multiscale modelling technique which combines FEM with a meshless method (Smooth Particle Hydrodynamics, SPH). The meshless method was suggested since finite element simulation often could not produce chips because of element distortion at small scale and remeshing problems. In the model, chip formation zone was modelled by using the SPH method but the outer region of chipping zone and cutting tool were modelled using FEM. To form chips, a 10 μm of depth of cut was used. It was concluded that the cutting capability of the abrasive grit (shaped grit was used in the model) increases with the increase of grit rake angle.

Anderson et al., (2011^a and 2012) investigated the single abrasive grain mechanism by experiment and FEM simulation. Unlike previous work, they used a combined Eulerian and Lagrangian formulation for the FEM model. The 3D FEM model was performed in LS-DYNA hydrocode using explicit time integration. The workpiece mesh and simulation results are shown in Figure 3.11. They used Eulerian element for the large deformation region and Lagrangian element for the small deformation region in the workpiece mesh. Void space was used to capture

the expanding Eulerian element; without it, expanding Eulerian material would be removed from the simulation. Simulation with a spherical tool only demonstrated ploughing material in front and side of the tool, whereas, a flat nose cutting tool (similar to negative rake angle cutting) produced chips at 4 μm depth of cut. Transition from rubbing to ploughing was not captured, and it was concluded that the three phases of material removal (rubbing, ploughing, and cutting) during abrasive grain cutting seems to occur simultaneously but in different proportion depending on the machining (or simulation) conditions. According to these results, normal forces increased with cutting speed due to strain rate hardening of the workpiece, and tangential forces decreased with cutting speed due to reduction in the coefficient of friction between cutting tool and workpiece. It is clear from the above description this workpiece model was too complicated to adapt the single grain grinding process to different conditions, and the model was unable to demonstrate chip formation with a spherical tool. Chip was obtained using negative rake angle cutting which is similar to the 3D cutting.

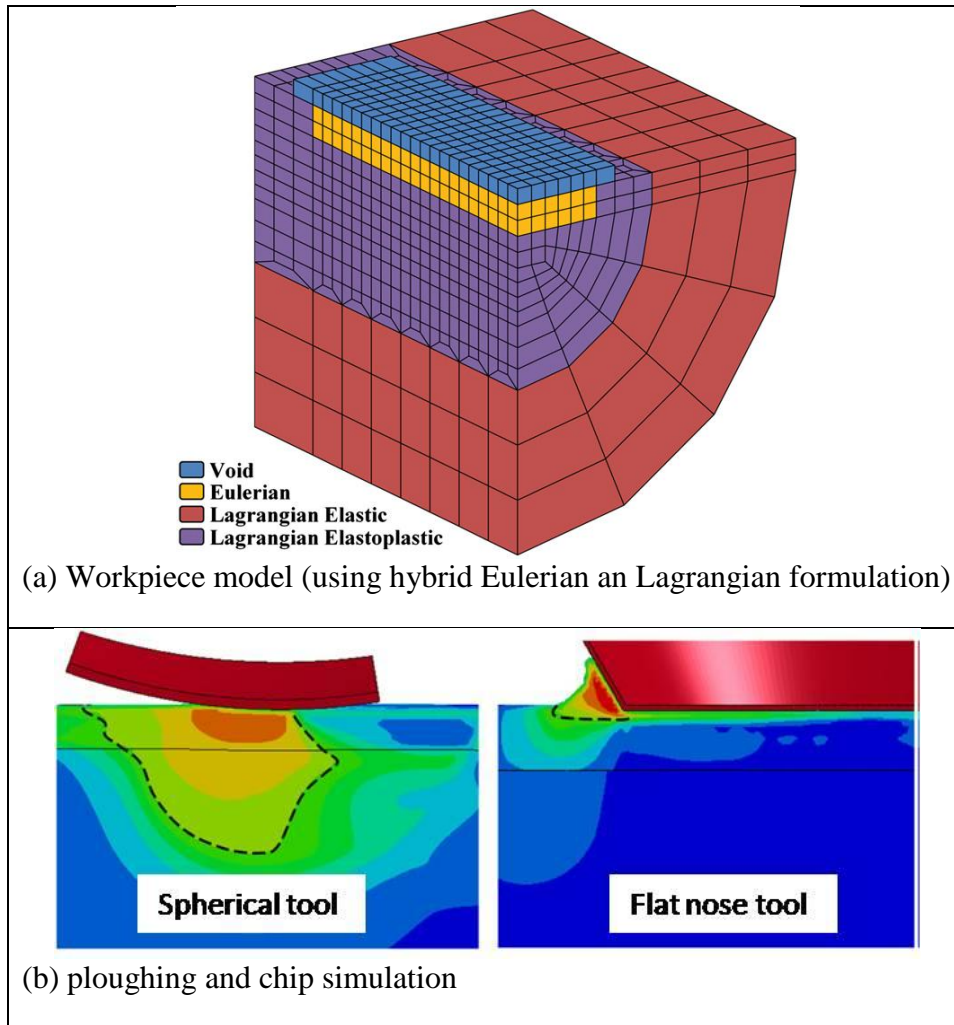


Figure 3.11 (a) Workpiece mesh and (b) simulation results (Anderson et al., 2012).

The micro milling process produces similar chip shapes to the grinding process. In micro milling, depth of cut and the feed rate per tooth are very small and no chips are formed below a value called minimum chip thickness. Chae et al., (2006) define it as the critical undeformed chip thickness (between 5% and 38% of the tool edge radius) below which no chip can be formed. Three different cases happen in micro-chip formation, as shown in Figure 3.12.

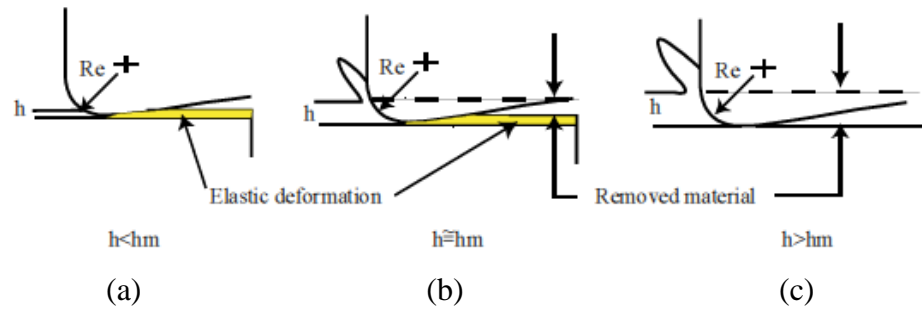


Figure 3.12 Schematic of the effect of the minimum chip thickness (R_e , radius of cutting tool; h , undeformed chip thickness; h_m , minimum chip thickness) (Chae et al., 2006)

Other useful and relevant investigations that would contribute to the understanding of single abrasive grit FEM simulation would include contact problems between two rough surfaces, scratching simulation with a shaped indenter for coating material surfaces, material stress distribution under small shaped spherical indenter loading. There are some works available regarding these issues, Ram et al., (2003) investigated the elastic stresses developed during sliding of abrasive grit on the workpiece material by using an implicit 2D FEM model performed in LS-DYNA software. The material was modelled using only elastic properties and contact between abrasive grit and workpiece as described by Hertzian contact theory. Abrasive grit was modelled as a Hertzian pressure loading onto the workpiece. Simulated elastic stresses were in close agreement with the theoretical results. Similarly, Yao et al., (2004) also investigated elastic contact between two rough surfaces using Hertzian theory to describe the contact. Determination of real contact area after deformation was studied and it was found that Hertzian contact theory did not give realistic results when surface asperities were taken into account. Hegadekatte et al., (2005) investigated sliding wear mechanisms using a finite element model developed in Abaqus. For this investigation, a wear model based on Archard's law (1953) was introduced into the FE model to solve general deformable-deformable body contact problems. The wear on both

surfaces was calculated using the contact pressure obtained from 2D and 3D FEM simulation. These investigations did not demonstrate single grit grinding removal mechanisms in terms of rubbing, ploughing and chip formation, they only included stress distribution based on defined contact between two bodies.

Bucaille et al., (2001) investigated elastic-plastic behaviour of thin coating materials with a scratch test by using 3D FEM simulation. The work material was modelled as elastic-perfectly plastic material interacting with a rigid indenter with no friction between the surfaces. The simulation was performed in Forge3D software. With high elastic modulus, deformation was found to be mainly plastic, material behaviour was similar to the behaviour of metal. Frontal and side pile-up was observed during scratching. Similarly, Li and Beres (2006) used 3D FEM model of a sliding scratch test to investigate the failures occur in coating materials. They used a rigid Rockwell C indenter for scratching a TiN/Ti-6Al-4V coating system. The FEM software of MSC Patran and MSC Marc were used for the analysis, as well as Abaqus/Standard and the results compared. The finite element results showed significant residual deformation remained after the indenter was moved away from the test location. With this model, three modes of contact between indenter and coating materials were observed; static, sliding and ploughing modes. Compressive stresses and tensile stresses were investigated and depended on the indenter movement. But numerical investigation has not been proved by experimental test in Li and Beres's study, it remains for future research.

Barge et al., (2003) investigated the ploughing process and associated deformation during abrasive wear by using finite element simulation and experimental tests. The work material was modelled by using large deformation and elastoplastic theory. A rigid sphere was used as an indenter for the simulation which was performed in Systus software. Residual depth and side pile-up were analyzed together with ploughing force. Larger residual depth was found with this

simulation and was attributed to elastic deformation of the indenter. The side pile-up was found smaller in experiment compared to the simulation results. Fang et al., (2005) investigated groove ridge formation using FEA. To produce a groove with a ridge, an indenter with sphere tip was used and simulation was performed in Ansys software. Bilinear elastic-plastic material behaviour with hardening characteristic was used for the workpiece material model. This study investigated mainly ridge morphology with different indentation depth obtained by using different materials.

3.5 Summary

The state of the art in modelling and simulation of machining processes particularly by FEA is summarized in this chapter. Chip formation simulation for orthogonal cutting is reviewed in order to understand the FEM model and simulation mechanisms for possible application to grinding mechanisms. The current state of the art in modelling chip formation is to use the fracture mechanism together with well-defined material behaviour at large deformation and high strain rates.

Recently the JCM or modified JCM have been very popular in machining simulation because the JCM takes into account strain rate dependent material properties which are measured using the Split Hopkinson Pressure Bar (SHPB) test. Although the SHPB test can measure material properties only up to a certain level of strain rate, it is currently accepted as the most reliable flow stress device. FEM simulation of the grinding process using the macro scale approach, where the grinding wheel is modelled using applied pressure and heat source, cannot achieve detailed mechanical characteristics of material removal. This approach has investigated general residual stress distribution or thermal hardening behaviour on the ground surface or subsurface. However, with the micro scale approach where the individual grit-workpiece interaction is analysed, detail information about material removal characteristic during rubbing,

ploughing, and chip formation stages can be analysed, and also grinding force, stress conditions and surface creation with geometrical analysis can be investigated.

Simulation with single abrasive grit is still in its developmental stage and there is insufficient information to adequately describe it. In the last decade there have been some attempts to perform this kind of FEM simulation but cutting mechanisms (e.g. chip formation) have not yet been simulated successfully at the micro scale (~1-3 μm depth of cut). Research has taken place on ploughing phenomenon during abrasive grit-workpiece interaction, sliding mechanisms and sliding-deduced stress distribution on the surface.

This thesis aims to contribute to FEM simulation of single grit grinding material removal mechanisms by considering the rubbing, ploughing, and cutting phases at a micro level, and provide a new perspective on the modelling and simulation techniques for machining technology using abrasive grits.

Chapter 4 Methodology of Single Grit Grinding

Investigation

4.1 Introduction

The grinding process has extremely complex material removal mechanisms because of the numerous irregularly shaped and sized abrasive grits bonded onto the grinding wheel, as illustrated schematically in Figure 4.1. Since a grinding process can be modelled as a cumulative process and the result of several single grit actions over the workpiece, the single grit interaction with the workpiece is of essential importance. With an understanding of individual grit-workpiece interaction mechanisms, the material removal phenomena could be extrapolated to the entire grinding wheel-workpiece interaction.

In this chapter, a methodological approach is presented in respect of the single grit test setup and workpiece sample preparation. In addition, methods of single grit grinding including traverse and longitudinal scratching are presented. Furthermore, a force sensor and Acoustic Emission (AE) monitoring system setup and scratch surface measurement technique are described. Finally, strategy to analyse scratches produced by single grit actions in terms of material removal mechanism is presented.

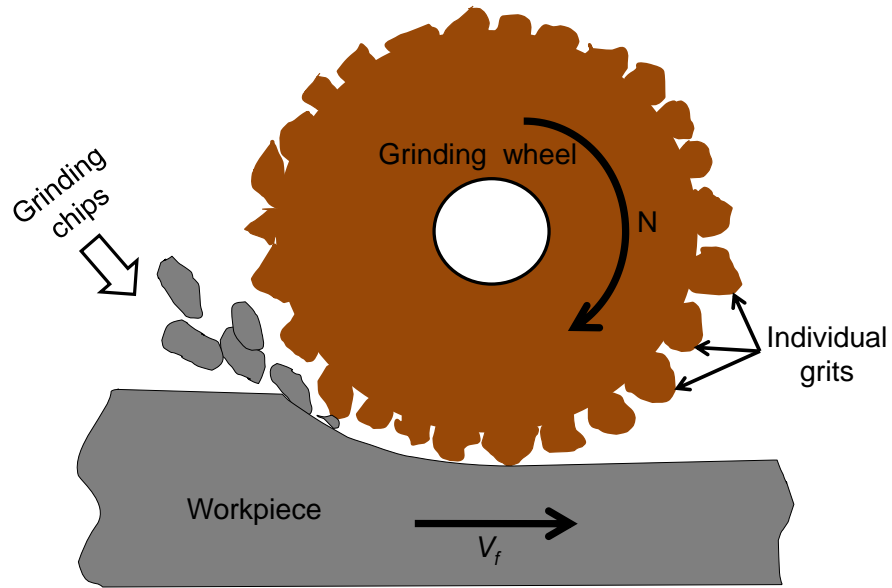


Figure 4.1 Schematic of grinding process (N: Wheel rotational speed, rpm; V_f : Work table speed (or feed) mm/min)

4.2 Single grit grinding approach

In order to understand the complexity of the grinding material removal process, the single grit grinding process can be considered as an elementary part of the grinding process of the grinding wheel, and the grinding process as the integration of numerous actions performed by individual grit. Thus, understanding of single grit action performed on a workpiece is important to model the overall grinding phenomena. Single grit action on the workpiece contains rubbing, ploughing and cutting (chip formation) phases. The schematic representation of single grit action with the three material removal phases is given in Figure 4.2.

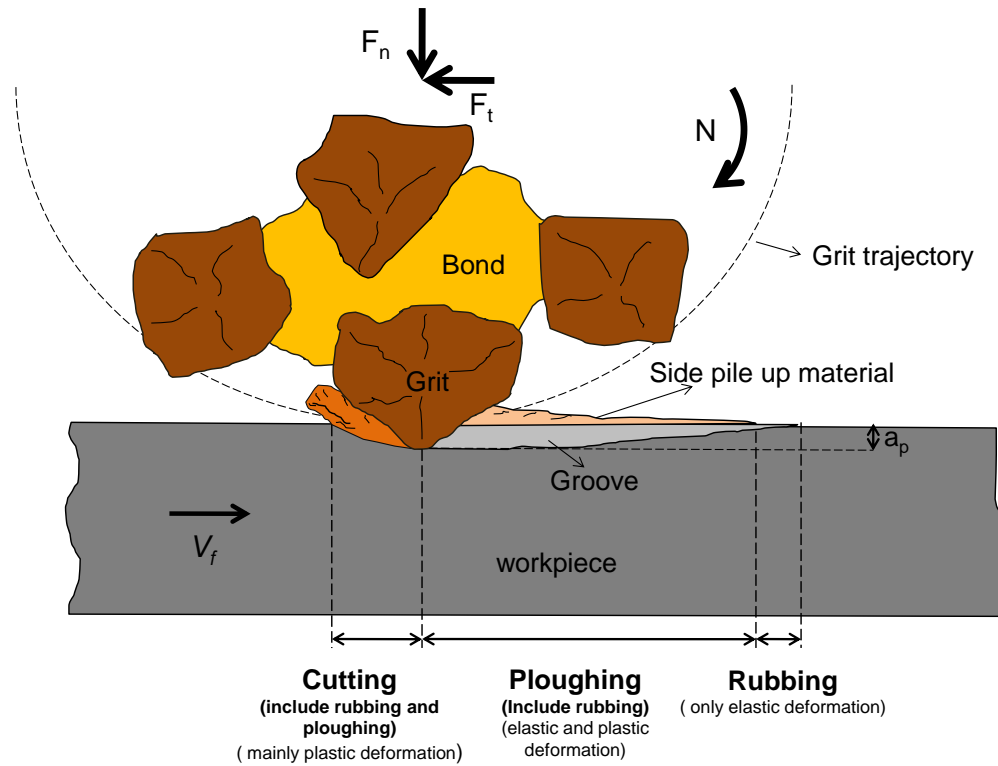


Figure 4.2 Schematic of single grit grinding action (F_n : normal force; F_t : tangential force; N : rotational cutting speed, rpm; V_f : work table speed or feed, mm/min; a_p : undeformed chip thickness)

The contribution of each phase to material removal varies depending on the size, geometry and sharpness of the grit, the hardness of workpiece and grinding kinematic conditions, such as depth of cut and scratching speed, etc. For instance, with smaller depth of cut, rubbing and ploughing processes are more prominent while with greater depth of cut chip formation would be prominent. In this investigation, single grit grinding tests were performed on different workpiece materials with different hardness including EN24T steel, Inconel 718, and En8 steel. Scratch grooves were cut by single grit action performed at different speeds and with gradually increasing depth. AE signals were used to detect initial contact. A force sensor was used during the single grit grinding process to record the force exerted during scratching. Single grit grinding

tests have been performed with different operational conditions and compared with numerical FEM simulation. A schematic of the investigation work flow is illustrated in Figure 4.3.

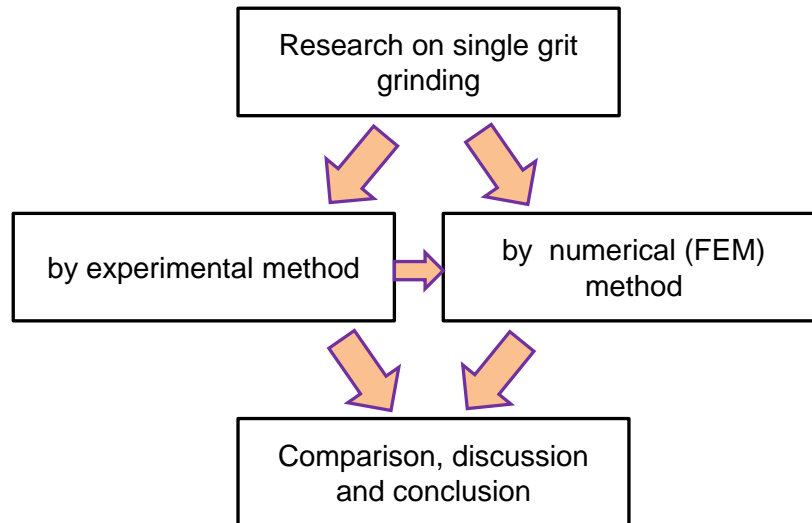


Figure 4.3 Simple schematic of research method

4.3 Establishment of single grit grinding test setup

4.3.1 Description of machining centre used for single grit grinding tests

The experiments for this research were mainly performed on a Precitech Nanoform 250 Ultragrind machining centre. The machine performs precision grinding and single point diamond turning and is capable of machining 3D free-form complex surfaces with a surface roughness to 1 nm and form accuracy to better than 100 μm . The machine has high precision motion control driven by a linear actuator of resolution 0.1 nm level for programming. It has two axis linear movements; one is worktable movement in the longitudinal Z direction and the other is spindle

movement in the lateral X direction. The overall view from the machining centre is shown in Figure 4.4.

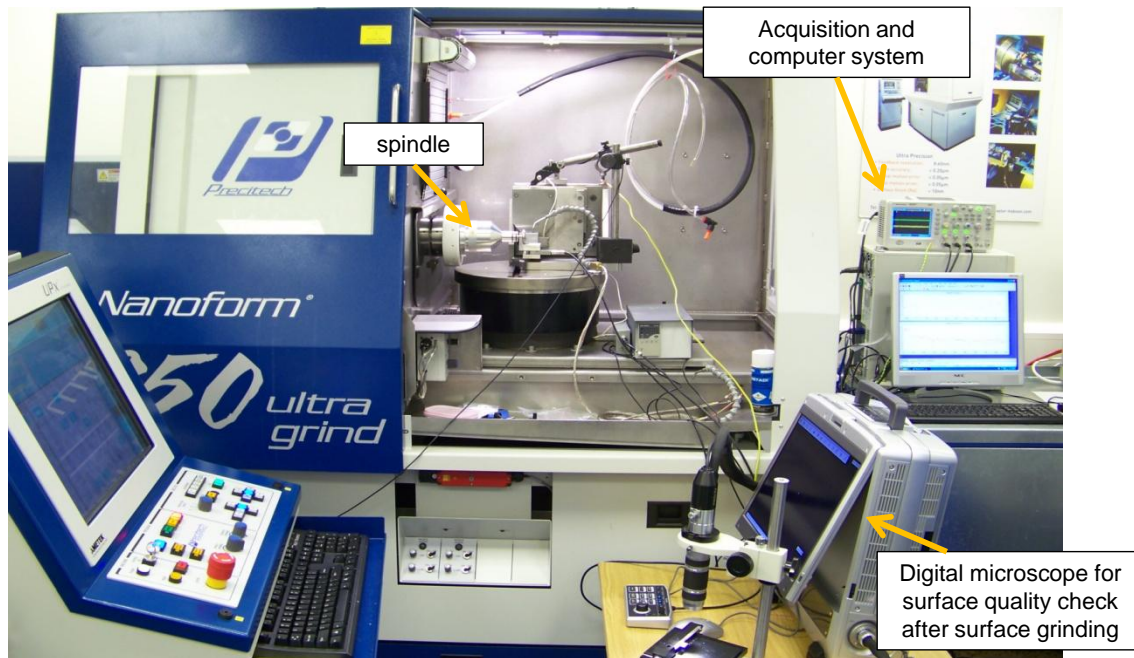
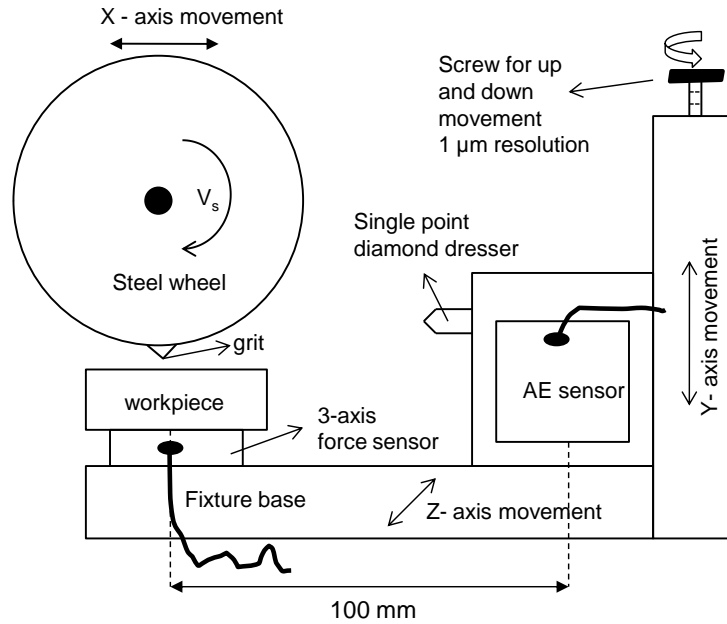


Figure 4.4 View from machining centre (Nanoform250 ultra grind)

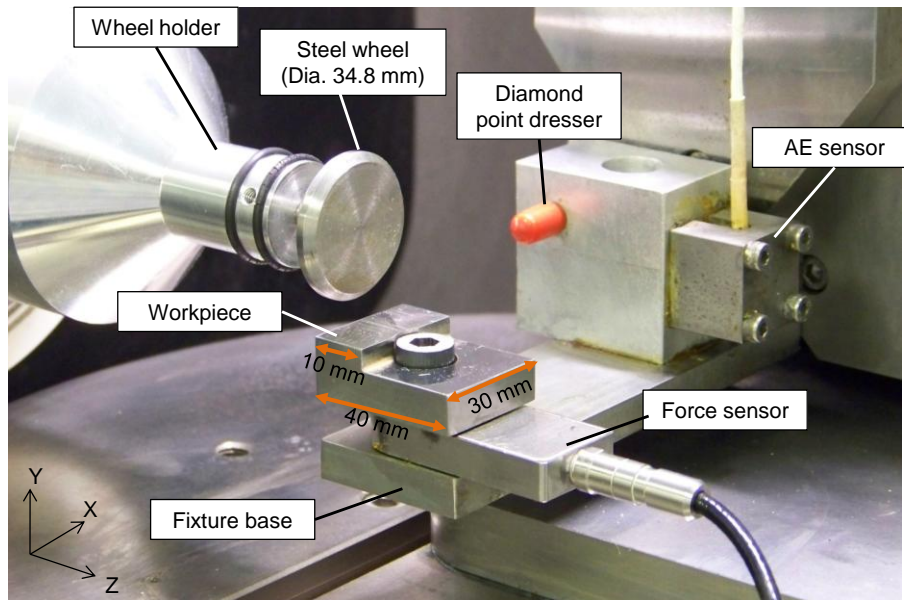
4.3.2 Single grit grinding test setup

The original machine was not designed to perform single grit measurements. A steel test rig was designed and made to enable the single grit grinding test. The single grit test setup is shown in Figure 4.5. The vertical movement was driven by a screw with a 1 μm resolution (see Figure 4.5 - (a)) for grit and workpiece touch point adjustment and depth of cut setting. The workpiece was mounted onto the designed test rig as shown in Figure 4.5 – (b). A Kistler 3-axis force sensor was mounted under the workpiece to measure forces during single grit scratching and an AE sensor was mounted near the workpiece to acquire the AE signal during machining.

The AE sensor could not be installed on the workpiece because of space restrictions but the mounting position still allows the AE sensor to acquire AE signal.



(a) Schematic of single grit grinding test setup



(b) View of single grit grinding test setup

Figure 4.5 Single grit grinding setup of Nanoform250 ultra grind machine centre

4.4 Establishment of single grit grinding tests

Single grit grinding experiments were conducted on three different workpiece materials. Firstly, some preliminary experiments were performed on En8 steel to check the feasibility of single grit grinding process using a test setup. Basically, the first experiment was performed to improve the test setup and to develop a strategy to obtain acceptable results for further single grit grinding processes. The first tests on En8 steel showed how to improve grinding parameters such as rotational speed of the wheel and table speed to improve surface flatness, surface finishing, process monitoring tool installation and data collection from sensors. The second set of single grit experiments was performed on the Inconel 718 workpiece for comparison with the steel. But due to the difficulty of identifying the data logging datum point during process monitoring, the data collected from the AE and force sensors could not be matched for individual scratches so that data was inconclusive. Figure 4.6 shows single grit grinding setup with the Inconel 718 workpiece. In this setup the wheel stops moving forward half way along the workpiece before the wheel finally stops rotating and the data logging loses its datum point.

The third set of single grit grinding experiments was performed on En24T steel (AISI4340) which was used in some of the FEM simulations in this thesis. For the experiment on En24T steel, the problem of data logging was solved by cutting-off the workpiece material (see Figure 4.5 – (b)) to avoid any grit-workpiece interaction during the transient rotations when the wheel was stopping.

Individual machining conditions are given with the results of the experiments in Chapter 6. These provide a detailed view of research conditions for which results were obtained. Briefly, cutting speed, work table speed, workpiece materials, and depth of cut are primary variables which were considered during experiment design.

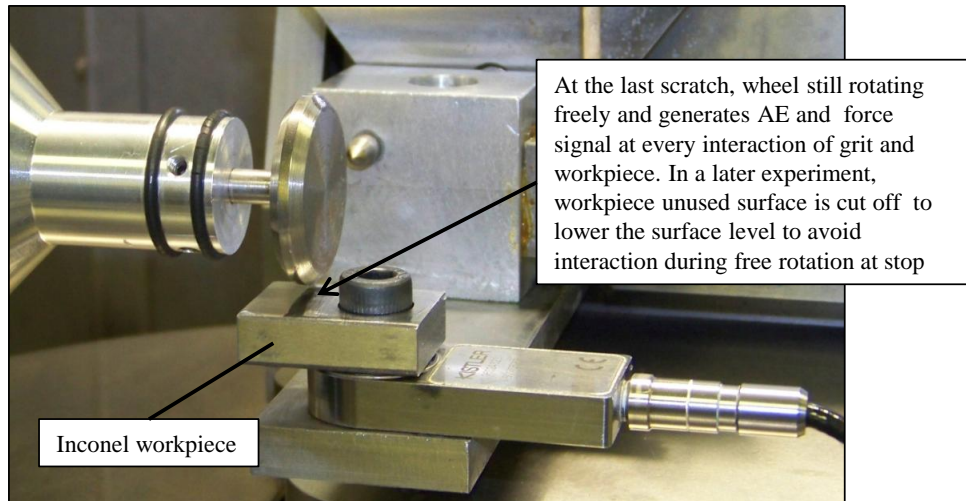


Figure 4.6 Picture of single grit grinding test with Inconel 718 workpiece

4.4.1 Abrasive grit material

CBN grits having a 40/50 mesh size (Figure 4.7) were used as the single grit abrasive throughout the experiments. CBN abrasive has significantly higher toughness, endurance, abrasive ability, thermal conductivity and chemical stability compared to standard abrasive materials such as Al_2O_3 and SiC. CBN also has a significantly bigger modulus of elasticity (706 GPa or more) than conventional abrasives (296-365 GPa). The specific heat capacity of CBN (670 J/kg \cdot °C) is lower than that of Al_2O_3 (<http://www.harisdiamond.com/cbn.html>). Some important characteristics of CBN and other abrasives were detailed in Chapter 2.

To perform single grit grinding tests, the circumferential surface of the steel wheel was ground by high speed spindle grinding (20000 rpm or $V_c = 502.2$ m/min) in-situ to reduce roundness error to less than 1 μm . After this process, CBN grit was glued onto the circumferential surface of the steel wheel using super glue (Loctite super glue) as shown in

Figure 4.8. The steel wheel was never taken out of its holder to maintain calibration settings throughout the experiments.

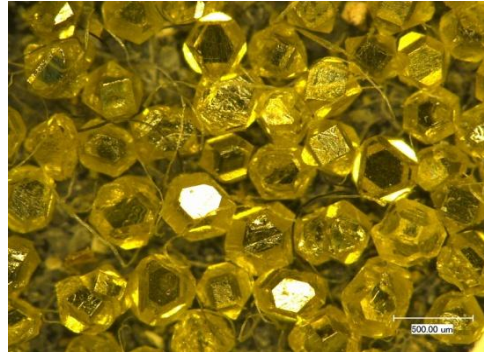


Figure 4.7 CBN grit (40/50 mesh size) used for single grit grinding tests

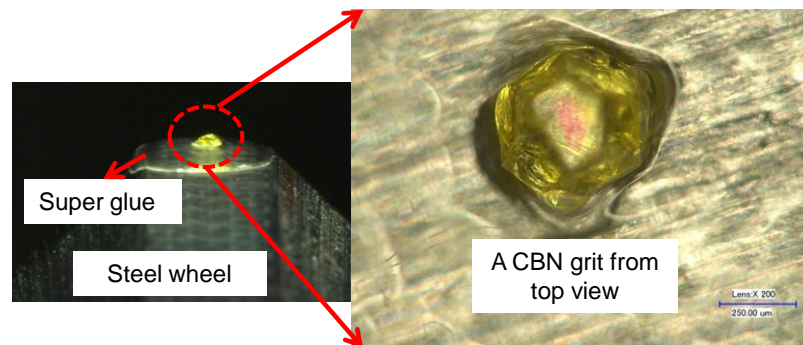


Figure 4.8 CBN grit (40/50 mesh size) glued onto the circumferential surface of the steel wheel

4.4.2 Workpiece material properties

Material properties and chemical composition of the three workpiece materials (En8 steel, Inconel 718 and EN24T steel) are given in Table 4.1 and Table 4.2. En8 steel was used for the preliminary single grit grinding test and to improve the test setup and conditions. EN24T steel has similar material properties to AISI4340 steel and was used for some FEM simulations. AISI

4340 steel was preferred for the FEM simulations since there is sufficient information about its plastic properties at different strain rates and reports in the literature available for comparisons. The Inconel 718 workpiece was used for single grit scratching (grinding) to investigate the variation of material removal mechanism with different materials.

Table 4.1 Workpiece material typical properties

Material properties	Inconel 718 (Ref1) at 25 °C	En8 steel (Ref2:AISI 1040) at 25 °C	En24T steel (Ref2:AISI 4340) at 25 °C
Density (kg/m ³)	8190	7845	7700-8003
Hardness (HV at 1 kg load)*	355	222.2	289.2
Tensile strength (UTS) (MPa)	1240	518.8	744.6
Yield strength (MPa)	1036	353.4	472.3
Elastic Modulus (GPa)	211	190-210	190-210
Poisson's ratio	0.284	0.27-0.3	0.27-0.3
Melting point (°C)	1260-1336	1520	1427

Ref1: <http://www.aviationmetals.net>; Ref2: <http://www.efunda.com>; *Measured values

Table 4.2 Chemical compositions of the workpiece materials

Material	C	Si	Mn	S	P	Cr	Mo	Ni	Al	B	Cu	Fe	Nb	Ti
In718 (Wt, %) (Ref3)	17- 21	<= 0.35	<=0.35	<=0.015	<=0.015	<=1	2.8 - 3.3	50 - 55	0.2 - 0.8	<=0.006	<=0.3	17	4.75 - 5.5	0.65 - 1.15
En8 (Wt, %) (Ref4)	0.36 - 0.44	0.10 - 0.40	0.60- 1.00	0.050 Max	0.050 Max	-	-	-	-	-	-	-	-	-
En24T (Wt, %) (Ref4)	0.36 - 0.44	0.10 - 0.35	0.45 - 0.70	0.040 Max	0.035 Max	1.00 - 1.40	0.20 - 0.35	1.30 - 1.70	-	-	-	-	-	-

Ref3: <http://www.matweb.com>, Ref4: <http://www.kvsteel.co.uk/>

4.4.3 Workpiece surface preparation

Before commencing single grit grinding experiments, the workpiece surface had to be prepared in terms of surface flatness and surface roughness. Workpiece surface was already ground with a conventional surface grinder after being cut as a test sample. Although workpiece surfaces were ground, after mounting the workpiece onto the test rig the flatness was not good

(higher than 100 μm between two ends of the workpiece surface) with respect to machine spindle. Also the surface roughness ($S_a = \sim 0.5 \mu\text{m}$) was very high due to the rough grinding process. Thus, the workpiece surface roughness and flatness needed further improvement in-situ to assure surface condition was good enough (with a flatness between two ends of the workpiece surface less than 2~3 μm and surface roughness S_a less than 0.1 μm) to carry out the single grit grinding experiment with a depth of cut accurate to an order of a few micron. The workpiece surface preparation procedure is illustrated in Figure 4.9; first of all the workpiece was installed into single grit test rig, then the workpiece surface was ground in situ to improve the surface flatness and surface finish, see Figure 4.10. After surface finish grinding, surface flatness was measured using a LVDT probe. If the flatness was around 1~2 μm level and then the surface was polished using polishing felt with 6 μm and 1 μm particle diamond spray applied consecutively to the surface while the polishing felt was rotating and moving over the workpiece surface. At this stage surface roughness could not be measured until the single grit grinding tests had been completed, because any movement of the workpiece would have ruined the alignment between the wheel and the workpiece. After experiments were completed, surface roughness was measured with a Talysurf CCI 3000 interferometer. An example of microscope pictures obtained of the surface after in-situ grinding and polishing is shown in Figure 4.11. The roughness after polishing was around $S_a = 90 \text{ nm}$ for the En24T steel workpiece. However, it is not easy to keep the roughness value around same level for each sample because the process was extremely complex and affected by several parameters. Measured surface roughness of the En8 workpiece was around $S_a = 50 \text{ nm}$ and for the Inconel 718 was around $S_a = 40 \text{ nm}$.

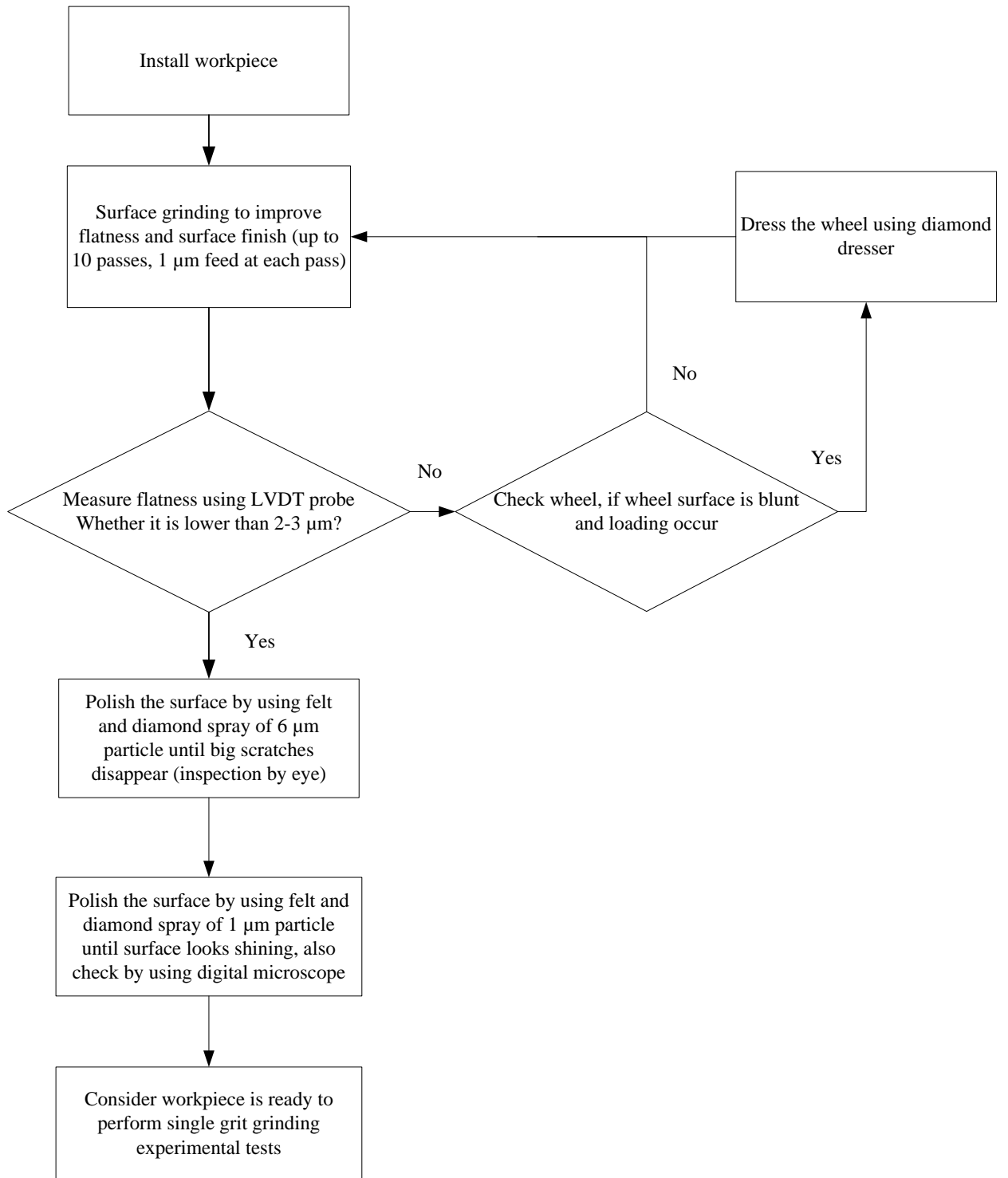


Figure 4.9 Schematic illustration of workpiece surface preparation before single grit grinding

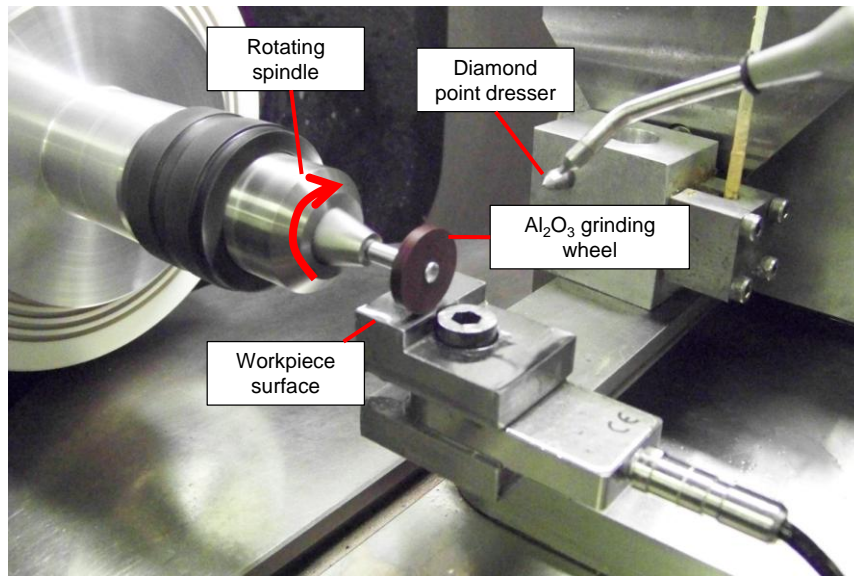


Figure 4.10 In-situ surface grinding to improve flatness of the workpiece surface

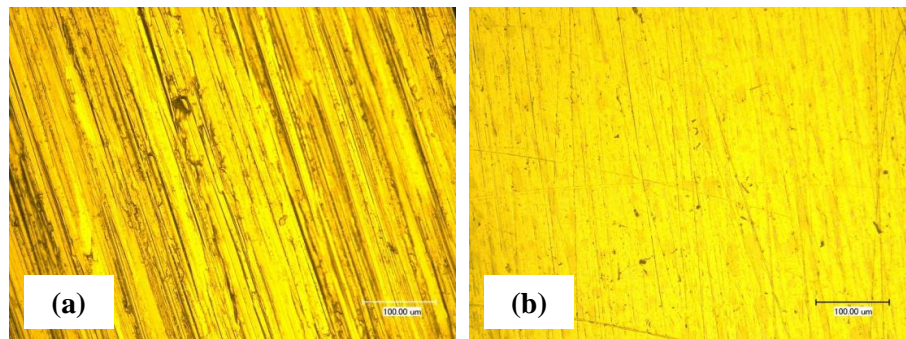


Figure 4.11 En24T workpiece surface (a) after in-situ grinding and (b) after in-situ polishing process ($S_a = 90 \text{ nm}$)

4.5 Single grit grinding methods

Single grit grinding was performed using two different methods. The first one was longitudinal scratching, which was applied in the first set of experiment with En8 steel. It was realized that this method has limited capability to produce scratches at higher speeds and varying

depth of cut. The traverse scratching method was used for the remaining parts of the experiments.

4.5.1 Longitudinal scratching

A set of single grit grinding experiment was performed in the longitudinal direction to create similar scratches with one pass of the single grit wheel over the workpiece surface. During longitudinal scratching, the steel wheel was rotating and moving forward whilst the work table was stationary. Longitudinal scratching was performed at comparatively low cutting speed ($N = 100$ rpm or $V_c = 10.8$ m/min) since the single grit wheel needs to travel a distance at least that of the preceding scratch length to generate a subsequent scratch and avoid scratches overlapping each other. Depth of cut was set by adjusting workpiece position in the Y axis. The single grit wheel was moved down until it touched the workpiece surface. This was controlled by the AE signal monitor (step-1 in Figure 4.12). After touching was detected, the single grit wheel was offset relative to the workpiece, outwards in the X direction (step-2 in Figure 4.12). After setting spindle translational speed and single grit wheel speed, the scratches were made as shown in step-3 in Figure 4.12. There was no relative movement between work table and single grit spindle since the work table stayed still and the only movement was that of the single grit wheel. Different values of depth of cut could be set by the grit being lowered into the workpiece by moving the workpiece up along the Y-axis using a screw slider mechanism. After one pass of the single grit wheel, the process was repeated by shifting the work table position (1-2 mm) in the Z direction to generate new passes of scratches. An example of scratches performed on En8 steel using longitudinal scratching method is shown in Figure 4.13.

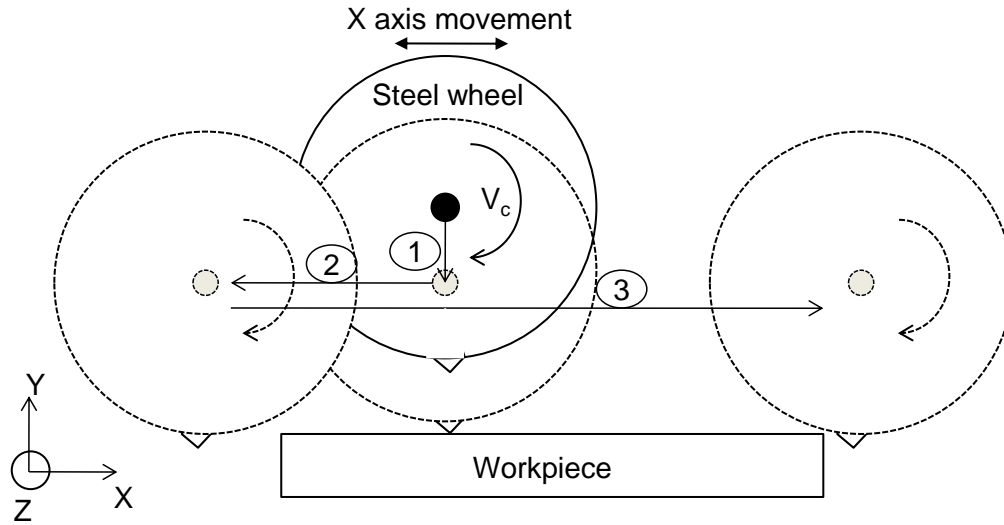


Figure 4.12 Schematic of longitudinal scratching

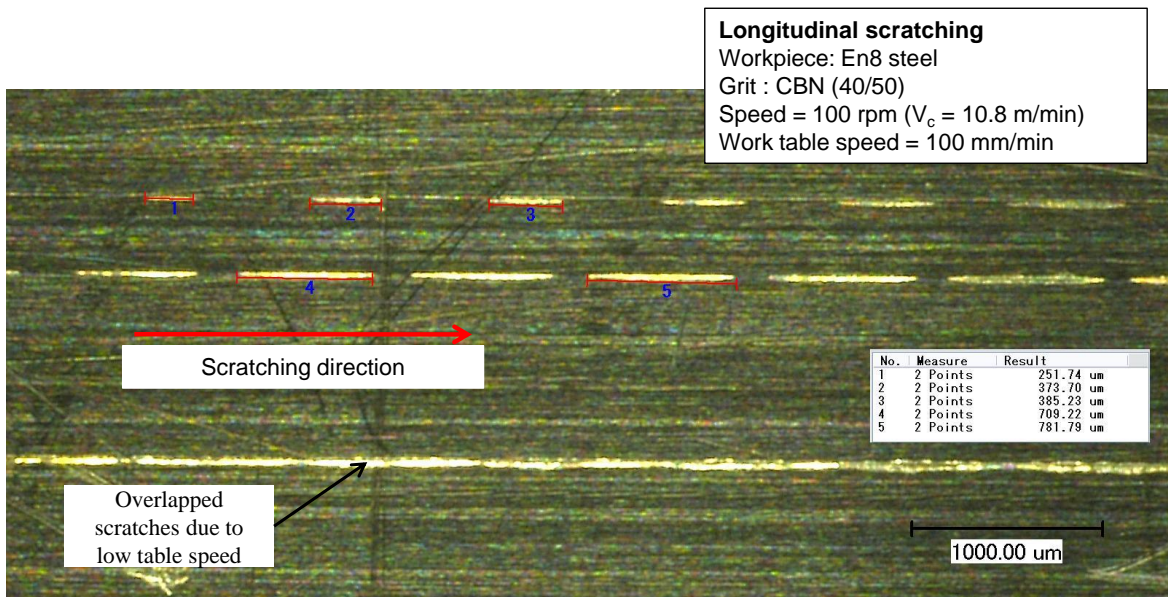


Figure 4.13 Longitudinal scratches on En8 steel

4.5.2 Traverse scratching

Traverse single grit grinding experiments were performed when the worktable was moving towards the wheel spindle and the steel wheel was rotating with relatively high speed of up to 5000 rpm ($V_c = 546.6$ m/min). Speeds exceeding 5000 rpm are not suitable because a high work table speed is needed to separate the scratch marks. The speed of the work table was limited to 3000 mm/min and machining length was around 10 mm. Force acquisition was also not feasible at higher speeds with the available sensor.

The most critical point during the single grit scratching experiment was setting the desired depth of cut and obtaining scratches with a minimum depth of cut. Depending on the workpiece surface, two methods could be applied to provide the desired depth of cut. If the polished workpiece surface flatness was good enough to obtain scratches of different depths of cut, the grit can be fed into workpiece using the vertical movement of the grit wheel to set depth of cut. If the polished workpiece surface is tilted at a small angle (height difference between two ends of the workpiece surface was less than $5 \mu\text{m}$), the procedure to provide different depth of cut is as illustrated in Figure 4.14 which shows the steel wheel with grit was moved to the middle of the workpiece surface, and then moved down until the grit gently touched the workpiece (step-1 in Figure 4.14), as detected by AE signal. After that the steel wheel was offset to the outside of the workpiece lower side edge (step-2 in Figure 4.14). At this point, the rotation of the single grit wheel was set to the desired speed, after waiting a few seconds to allow the speed to stabilise the single grit scratching movement shown in step-3 in Figure 4.14 commenced. On completion of this process, several scratches with gradually increasing depth of cuts from a few hundred nanometres to a few micrometres deep could be achieved (see Figure 4.15). Then, the process was repeated by shifting the position along the X-axis to generate new series of scratches with

the desired wheel speeds. This process can be continued until the entire area of the test surface was scratched by single grit.

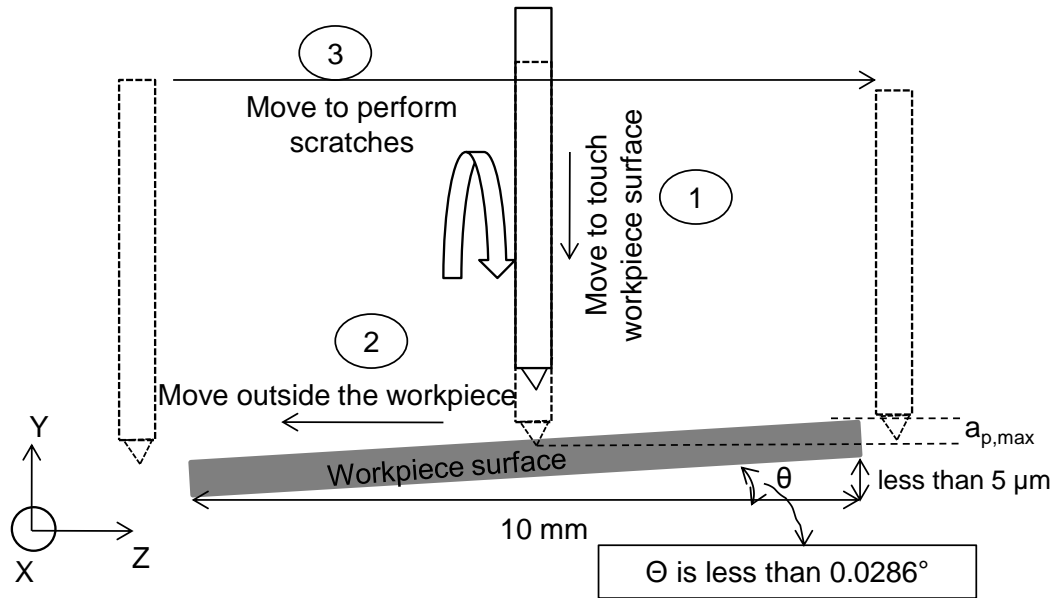


Figure 4.14 Traverse scratching on tilted surface

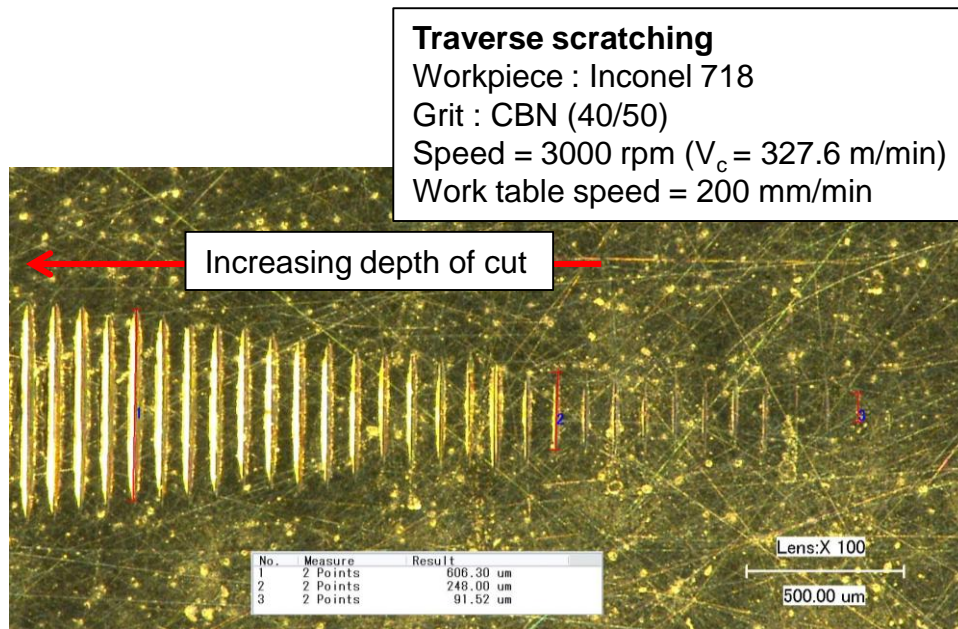


Figure 4.15 Scratches on Inconel 718 performed with traverse scratching method

4.6 Process monitoring setup

Process monitoring in machining processes is crucial to assess process performance. During machining, real-time and in-process monitoring systems can give relevant information of tool condition and part quality – knowledge of which are essential for the effectiveness of the process. Real-time and in-process monitoring system can also be used to protect the machine from such unexpected events as high speed grinding wheel failure that would cause significant damage to high speed systems (Hwang et al., 2000). However, selection of sensors, where to place them, and how to process the data and extract information are issues that need to be decided by the researchers. In machining, power sensors, force sensors, accelerometers, and AE sensors are all used for process monitoring. It is generally agreed that AE monitoring during machining offers a real time sensory input which could provide the needed information on such parameters as tool condition, machine dynamics and part quality (Hwang et al., 2000). In this thesis, AE was used to monitor contact detection between single grit and workpiece surface. The AE signal generated when the grit contacted the workpiece was collected by the AE sensor and transferred to a computer environment where it was analysed and stored. A Kistler piezoelectric force sensor (9602A3201) was used to measure the cutting force exerted during the single grit grinding process. A schematic drawing of the process monitoring system used in this research is illustrated in Figure 4.16. Figure 4.17 shows the data acquisition environment including computer, data acquisition cards, oscilloscope and software which were used during single grit grinding process monitoring and recording.

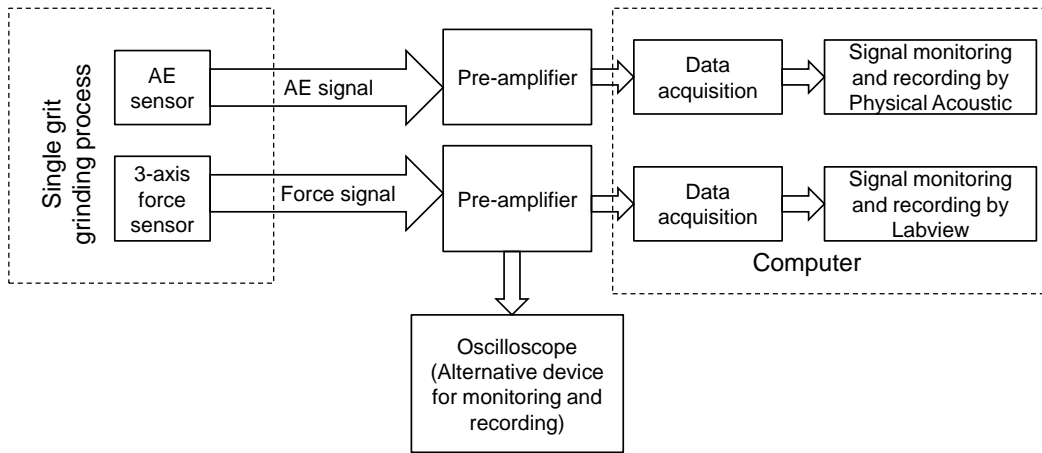


Figure 4.16 Schematic of process monitoring setup

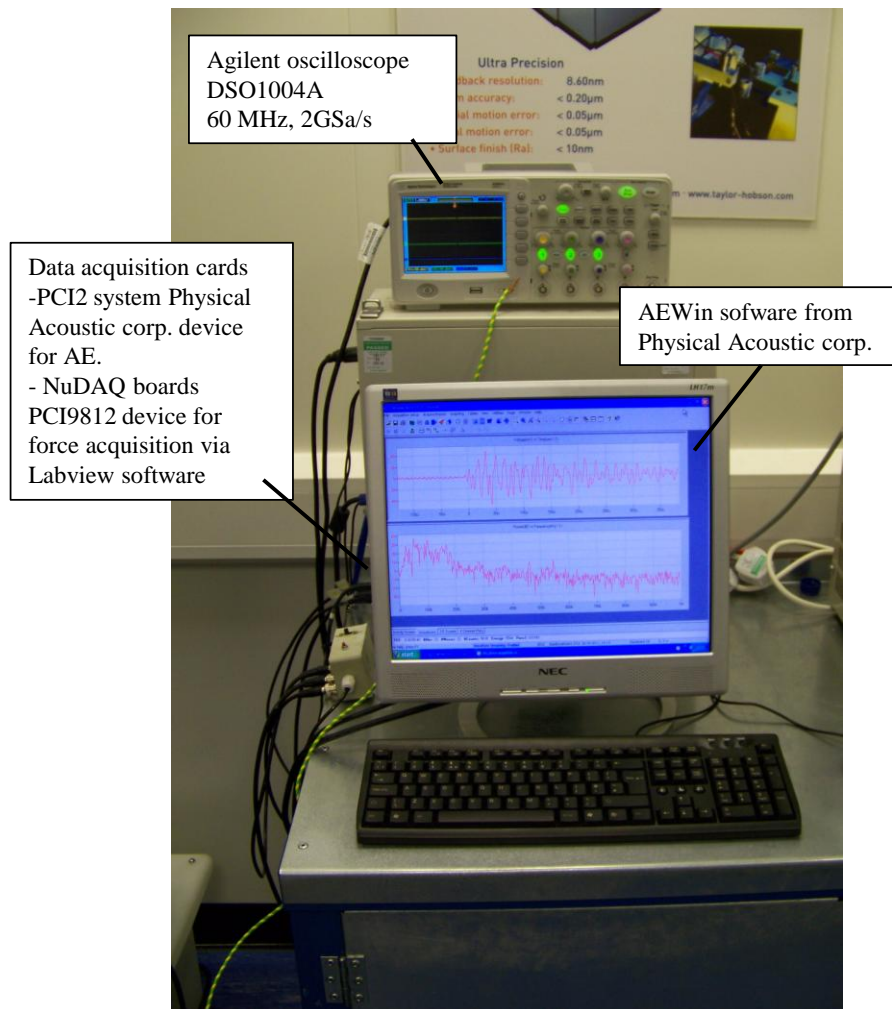


Figure 4.17 Photo of process monitoring devices

4.6.1 Acoustic emission

AE is transient elastic waves, from about 25 kHz to several MHz, generated by the release of energy from localised sources within or on the surface of materials which are subject to permanent alteration in their structure (Itturospe et al., 2005; Lee et al., 2006). AE is a useful monitoring tool in machining applications since plastic deformation is a strong source of AE. Fracture is also a source of AE since the propagation of micro cracks releases elastic energy due to the generation of new surfaces. Friction or rubbing between two surfaces is another potential source of AE; surface asperities come into contact and are plastically deformed, generating AE (Lee et al., 2006). One important reason for using AE is due to the superiority of AE sensors over other sensor such as force and vibration whilst acquiring high Signal/Noise ratio (S/N) at precision machining scale see Figure 4.18 (Dornfield, 1999).

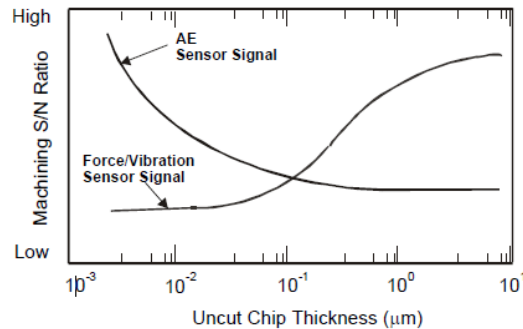


Figure 4.18 Signal/noise characteristics of AE and force/vibration sensors for different uncut chip thicknesses (Dornfield, 1999).

In this research the AE signal was monitored to detect contact between single grit and workpiece before commencing the experiment. The AE sensor is sensitive enough to detect contact point between the two surfaces. Knowing the contact position could facilitate depth of cut setting conditions. However contact detection was in order of few hundred nanometres

(sometimes micrometre) because up and down workpiece movement is driven by a screw -based slider mechanism. The slider mechanism resolution is around 1 μm and manually controlled.

Before commencing use of the AE system it was calibrated using the well-established Hsu-Nielsen pencil lead break test which also verified the sensitivity of the AE sensors (BS EN 1330-9:2009 Non-destructive testing (HMSO, London)). This procedure also gave a check on whether the AE acquisition systems were functioning properly. The test can be performed by using a 2H pencil lead with a 0.5 mm diameter and approximately 3 mm length from its tip, lead break occurs by pressing it against surface of the workpiece. This generates an intense AE signal that the sensor detects as a strong burst (Hsu and Breckenridge, 1981). The emitted AE signal from the pencil lead break test is shown in Figure 4.19. Signal intensity shows whether the location of the sensor is close enough to the source to detect the required AE signals strength and there exist no saturation due to setting the sensitivity of the sensor too high and whether it may saturate during grinding (single grit grinding).

The AE sensor (model: WD from Physical Acoustic Corp.) has an operating frequency range between 100 kHz to 900 kHz and operating temperature range between $-65\text{ }^{\circ}\text{C}$ to $177\text{ }^{\circ}\text{C}$. The sensor was confined inside housing and grease was used to guarantee good contact between surfaces and to improve acoustic energy transfer from source to sensor. The AE signal from the sensor was pre-amplified (Physical Acoustic Corp. 2/4/6 with differential signal input) with a gain of 40 dB before reaching the data acquisition card (PCI2 Physical acoustic device). AEwin software was used to monitor and record the AE signal. The software can allow setting of some acquisition values such as waveform sampling; which was set at 2×10^6 samples/second. The raw signal was recorded in time domain; it can be transformed into frequency domain to obtain the power spectrum of the signal. The software Waveviewer was used for this transformation in this research.

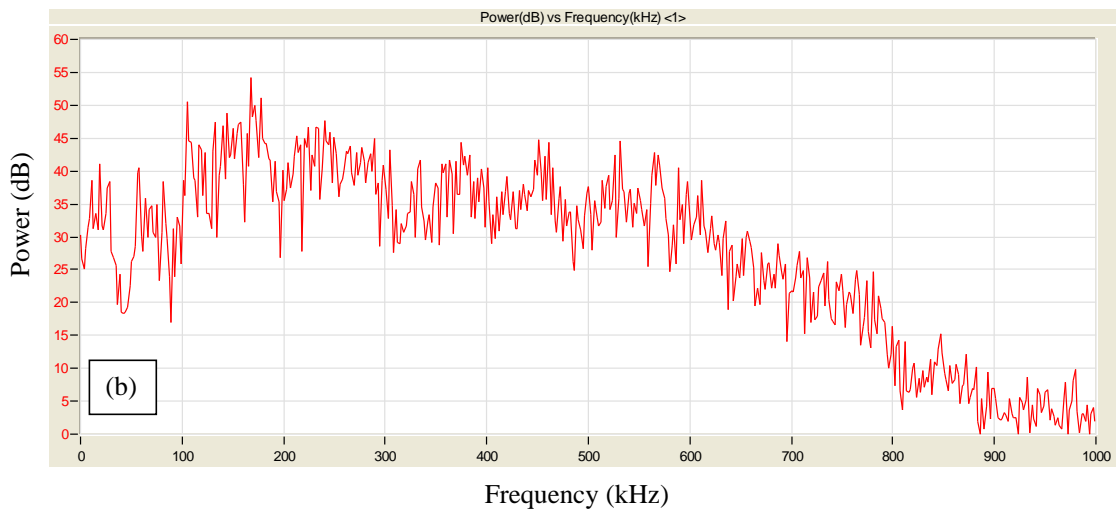
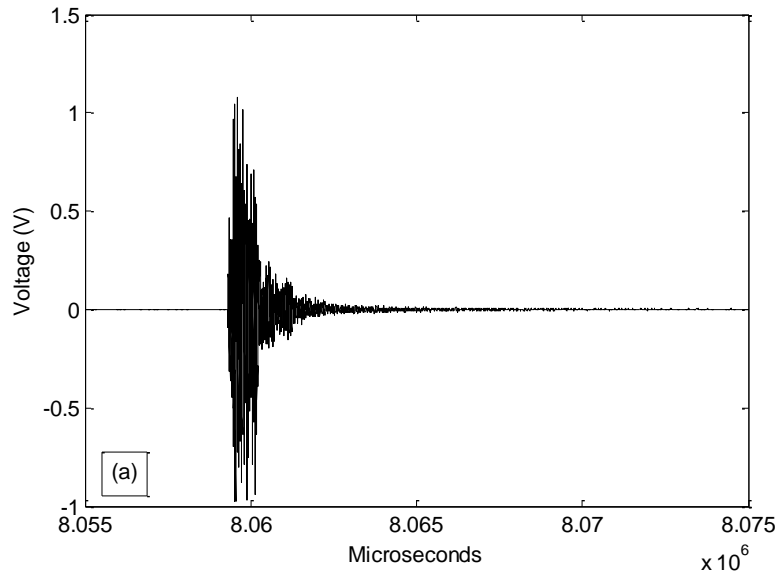


Figure 4.19 Pencil lead break test: (a) raw signal, (b) power spectrum (dB)

4.6.2 Cutting force measurement

Force measurement is one of the most important process monitoring methods in machining applications because machining performance and machined surface quality are directly related to the forces exerted during machining. Machining forces play a key role in determining tool life, tool or workpiece damage, surface quality parameters such as residual stresses, surface hardness and elastic-plastic deformation of the workpiece material. Machining forces for grit grinding are of interest of this research. Single grit grinding is the elementary action of grinding process; the machining force measured during single grit action could provide a better understanding of grinding mechanics and can be compared to finite element simulation results. The Kistler force sensor used in the experiments has two measurement ranges; high range with low sensitivity is between ± 5 kN for Fz component, and ± 2.5 kN for Fx and Fy components; low range with high sensitivity is between ± 1 kN for Fz and ± 500 N for Fx and Fy measurements. In this research, the sensor was set for the low range with high sensitivity setting since small value of forces were expected for small depth of cut with the workpiece. For accurate measurement the sensor needed to be calibrated in situ after installation. Calibration was performed by applying masses (50, 100, 200, 500, 1000 and 2000 gram) to the X, Y and Z directions for Labview software reading and oscilloscope reading separately, since output voltage readings were different for both systems as shown in Figure 4.20. Labview readings were always higher than oscilloscope readings due to different processing units (such as preamplifier) used for signal acquisition. The sensor was calibrated for 3 three axes, this was similar to the single axis calibration procedure but measurement of *cross talk* needed consideration. Cross talk is the effect of a calibration force applied along one axis on another axis, for example the output on the X-axis transducer caused

by a Y-component force (<http://www.npl.co.uk>). The effect of cross talk was measured as less than 2-3% and was ignored during force calculation.

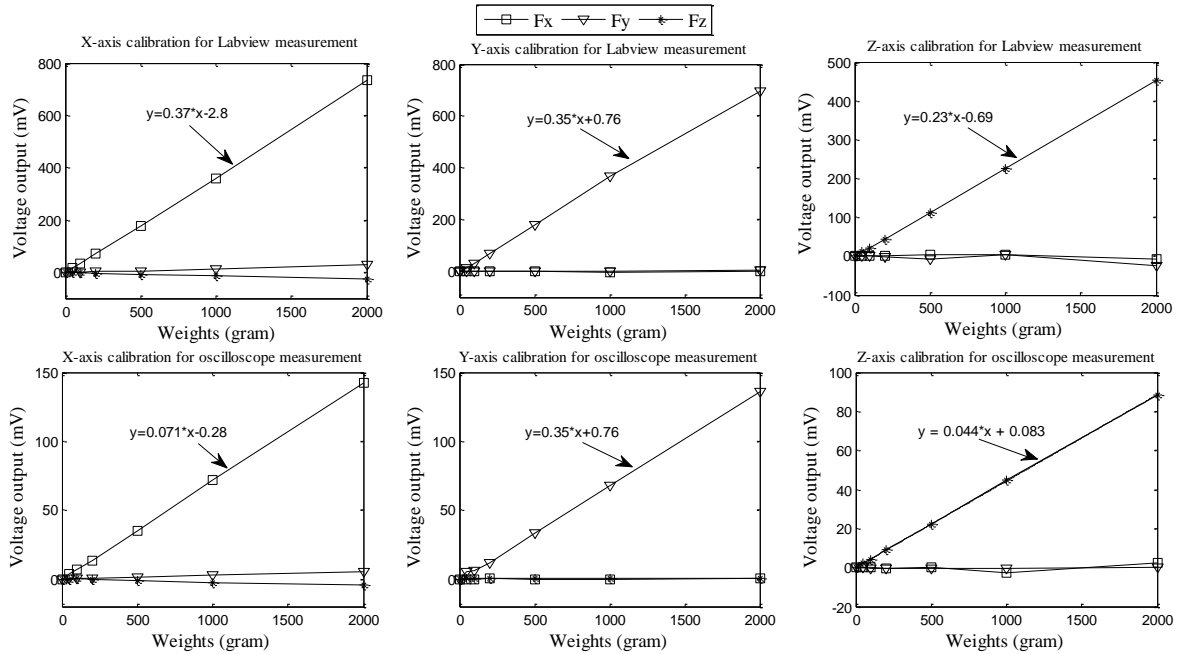


Figure 4.20 Force sensor calibration graphs for Labview and oscilloscope measurement

Labview software package and oscilloscope were used to monitor and to record the force sensor measurement. The block diagram of the Labview program for force acquisition is shown in Figure 4.21. Sampling rate was 10×10^3 Samples/sec. Cutting force components captured by Labview software are seen in Figure 4.22. The oscilloscope could not capture the signals for high speed machining because of the limit on the samples in the on-screen shot. Although the oscilloscope (Agilent, DSO1004A 60 MHz) has a sampling rate of 2×10^9 Samples/sec for one channel use with minimum time division setting (5 ns/ division), the sampling rate reduced to 8.553×10^6 Samples/sec when three channels were in use and when the time division set to 100 ms. In addition, the oscilloscope saved the captured data by re-sampling all the screen graph into 600 data points to take out from oscilloscope to excel spreadsheets, this made the accuracy of

measurement lower at relatively high speed machining. Figure 4.23 shows the single grit scratches with corresponding cutting force profiles which were recorded using oscilloscope.

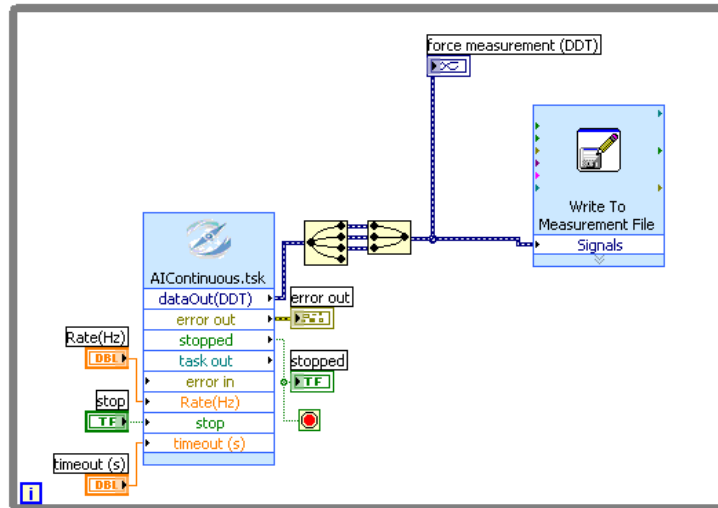


Figure 4.21 Labview block diagram for force acquisition

Forces exerted due to the grinding process contain important information on surface integrity and overall grinding process performance. Normal and tangential forces were recorded during single grit scratching to obtain possible relations between the material removal mechanism and other parameters such as cutting speed. Forces were recorded by using both the Labview based program and the oscilloscope. At relatively high speeds such as 3000 rpm ($V_c = 327.6$ m/min) the forces recorded by Labview were sampled at a rate of 10000 Samples/sec while the oscilloscope sampled at a rate of less than 1000 Samples/sec. This was because the oscilloscope sampling rate depends on the setting of the time axis, higher time division settings result in lower sampling rates. So at high speeds, Labview recorded the force signal much more accurately than the oscilloscope (Labview took 200 samples per revolution but the oscilloscope

took only 20 samples per revolution for 3000 rpm speed). At lower speeds, the oscilloscope took many more samples per revolution and the sensitivity and accuracy of the signal increased.

The force profile shown in Figure 4.24 was extracted for a very low speed ($N=10$ rpm or $V_c= 1.08$ m/min), which was performed to show obvious differences at extreme conditions (very low and relatively high speeds). Force profile extraction is an essential measurement to investigate variation of grit-workpiece interaction forces during the creation of a single scratch. Normal force variation throughout the scratch formation shows a quite symmetric distribution, in other words, the normal force increases from the first grit penetration into workpiece up to the scratch's deepest point, and then decreases during second part of the scratch formation until the grit leaves the workpiece. However, tangential force does not show a similar symmetry; the tangential force increases continuously due to accumulation of ploughed material ahead of the grit while the grit is advancing towards the end of scratch. Tangential force increases until almost the middle of the grit exit side of the scratch then start decreasing sharply as shown in Figure 4.24.

In fact, force acquisition at high speed and low depth of cut is a major concern. Some of the results include very high noise levels although a low pass filter was used during data transfer. At high speed, force signal oscillation is much higher than for low speed for both Labview and oscilloscope measurements. Thus the machining forces from single grit grinding were not accurately measured for all scratching tests due to these limitations. However, there are valid measurements available for analysis on the effect of cutting forces on scratches.

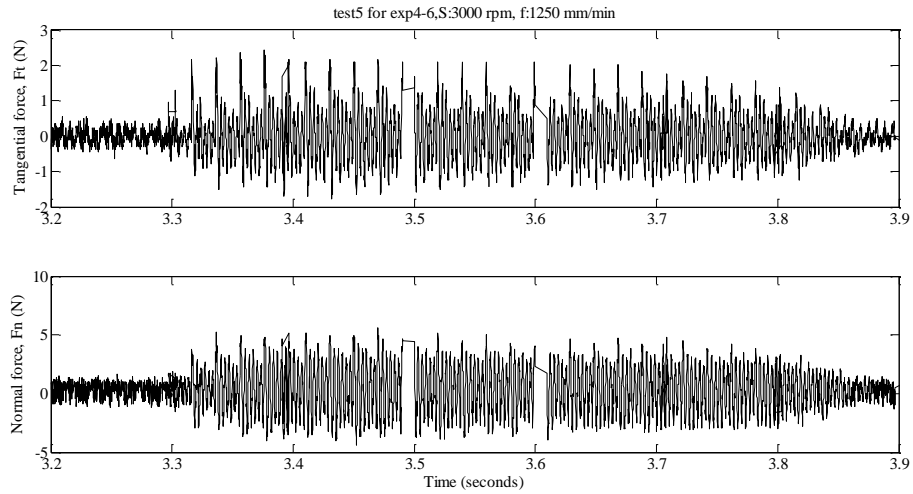
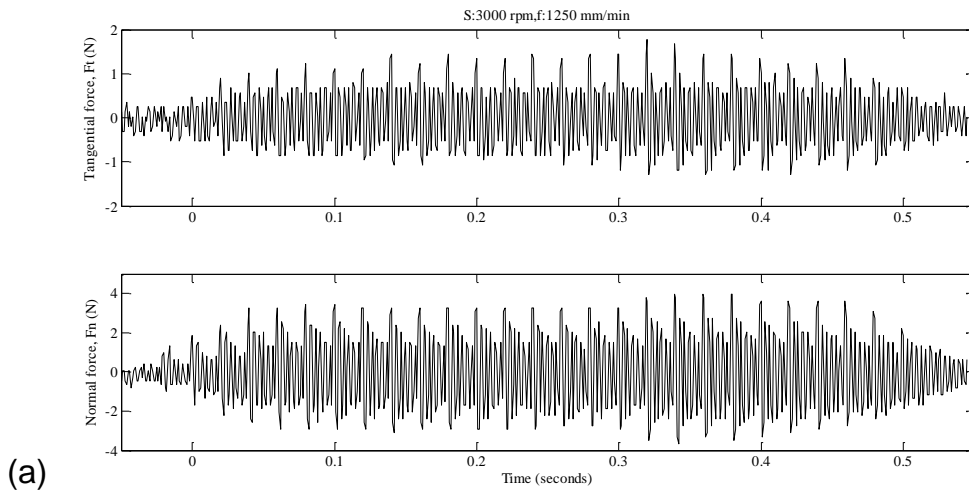
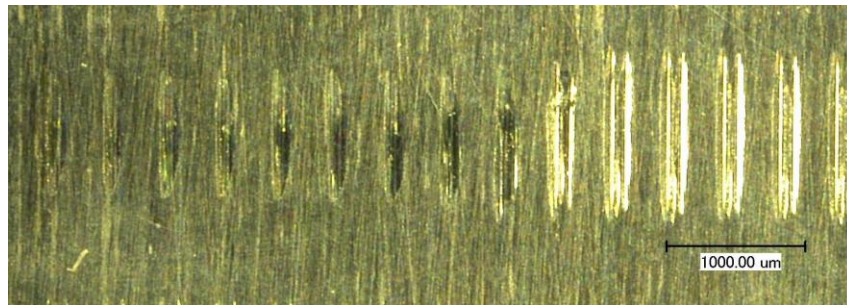


Figure 4.22 Forces recorded with Labview software ($V_c = 327.6$ m/min on En24T workpiece)



(a)



(b)

Figure 4.23 (a) Forces recorded with oscilloscope and (b) associated single grit scratches (not all scratches seen in the figure) performed at speed of 3000 rpm ($V_c = 327.6$ m/min on En24T workpiece) and table speed of 1250 mm/min

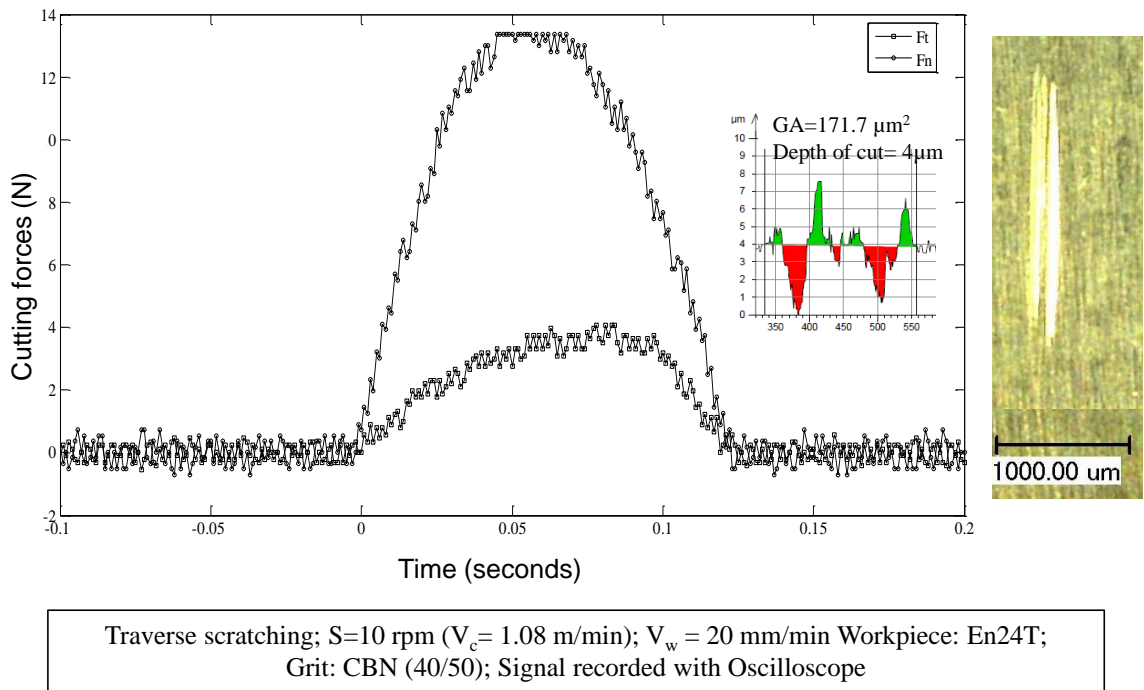


Figure 4.24 Force measurement and single grit scratch at low speed of 10 rpm on En24T steel workpiece

4.6.3 Specific energy calculation

Specific energy can be defined as the energy required to remove unit volume of material. According to Rowe and Chen, (1997) there existed a common consensus that specific energy increased with decreasing depth of cut. However, it is not so easy to explain specific energy variation simply when such dynamic parameters as shape factor, sharpness, number of cutting edges, depth of cut, speed, etc., are involved in the grinding process. Contrary to common knowledge concerning size effect phenomena in grinding, Doman (2008) found that specific energy increases with depth of cut, or material removal rate. Thus, specific energy will not always show the same trend.

The specific energy (u) for the single grit grinding process can be expressed as;

$$u = \frac{F_t}{GA} \quad 4.1$$

Where F_t is the tangential force, GA is the groove cross sectional area. This equation is a concise form of specific energy used in this thesis derived from grinding power (P) and material removal rate (MRR);

$$u = \frac{P}{MRR} = \frac{F_t \cdot V_x}{GA \cdot V_x} \quad 4.2$$

The specific energy in single grit grinding was calculated as the ratio of tangential force to cross-section area of the groove in early research (Brinksmeier and Glwierzew, 2003; Ghosh et al., 2010) and this definition is used in this thesis, as well.

The forces taken for consideration in this thesis are the maximum forces occurring during scratching process. The normal force generally reaches to its maximum value at the middle of scratch or deepest point of scratch; however, the tangential force may not reach its maximum value at the maximum depth of scratch, see Figure 4.24. Tangential force continues to increase after passing maximum depth due to continued accumulation of ploughed material in front of the grit while the grit is moving upward towards leaving the workpiece. In the current investigation it is difficult to find out the exact position where the tangential force reaches to its maximum value and it is assumed that the maximum forces occur at the deepest point of the scratch. For the investigation, the maximum value of normal and tangential forces was taken and scratch cross-

section was extracted from the approximate deepest point of the ground grooves. This was necessary assumption to make this investigation feasible.

4.7 Single grit scratch measurement method

The surface created by single grit scratches can be measured either by Taylor Hobson CCI interferometer or Taylor Hobson PGI stylus instrument. In this research, the CCI interferometer was selected as a main instrument to avoid possible damage caused by a stylus.

4.7.1 White light interferometer

Scratches produced by single grit grinding were measured using the Taylor Hobson Talysurf CCI 3000 that uses coherence correlation interferometer technology. “An interferometer is an optical device that splits a beam of light from a single source into two separate beams. Each of these beams travel separate paths, one onto a reference surface and the other onto the surface to be measured. The beams are then recombined resulting in an interference pattern. An imaging device, usually a CCD array, is used to collect this information. The Talysurf CCI 3000 is an advanced 3-dimensional non-contact optical metrology tool used for advanced surface characterization such as surface roughness, step-heights, form, shape, angular and critical dimension results” (Taylor Hobson precision, 2006). Due to its non-contact measurement technique an interferometer can give better feature information and extraction for scratches and pile-up than obtained by Stylus type instruments.

4.7.2 Scratch profile extraction by using CCI interferometer

The procedure for scratch measurements using the Talysurf CCI 3000 emphasises reliable. The instrument’s settings such as light intensity must be properly adjusted to obtain the best

scratch features including groove profile and details of material pile-up. Instrument limitations meant some points could not be measured at sharp edges and where there was thin swelling of the material section. However, these points can be treated by filling using a smooth shape calculated from neighbouring points. Before filling non-measured points, dilation - a basic morphological operation – is undertaken; it is performed by adding pixels to the boundaries of objects in an image. In dilation the value of the output pixel is set to the *maximum* value of all the pixels in the input pixel's neighbourhood (Gonzalez et al., 2004). After filling the non-measured points, an approximate scratch profile can be generated as shown in Figure 4.25. After 3D profiles of the scratches were obtained, 2D profile sections from the deepest point of scratches are extracted to measure the depth of groove, groove area, pile-up area and other relevant information. The deepest point is generally around the middle of scratches but sometimes due to imperfect form of the workpiece surface, the deepest point of the groove may not be at the middle of the scratch. To make sure the coordinates of the approximate deepest point are extracted, the longitudinal 2D profile of the scratches (in the direction of 1st line in Figure 4.25) is collected, see Figure 4.26-(a). Cross-section profiles of the scratches (in the direction of 2nd line in Figure 4.25) through the coordinates of the groove's deepest point are extracted as shown in Figure 4.26-(b). An example of a 3D view of scratches measured by Talysurf CCI 3000 is shown in Figure 4.27.

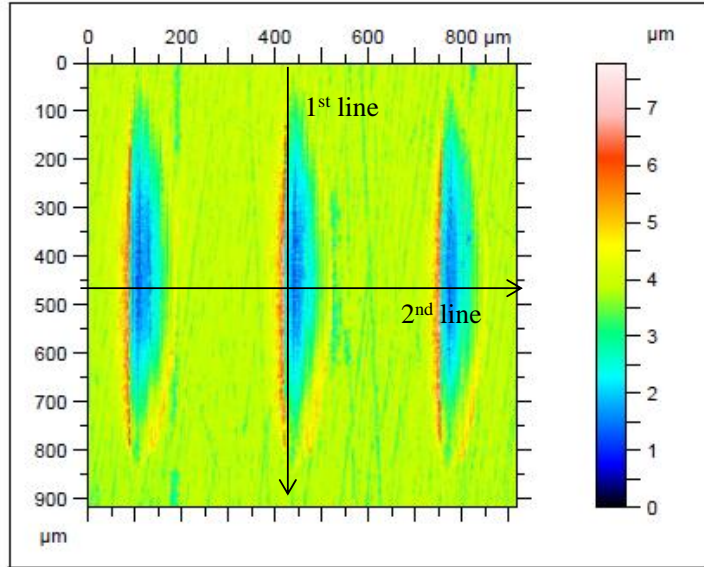


Figure 4.25 Three scratches after non-measured points filled. 1st line shows longitudinal profile extraction direction to find deepest point, 2nd line shows the section profile extraction direction using deepest point

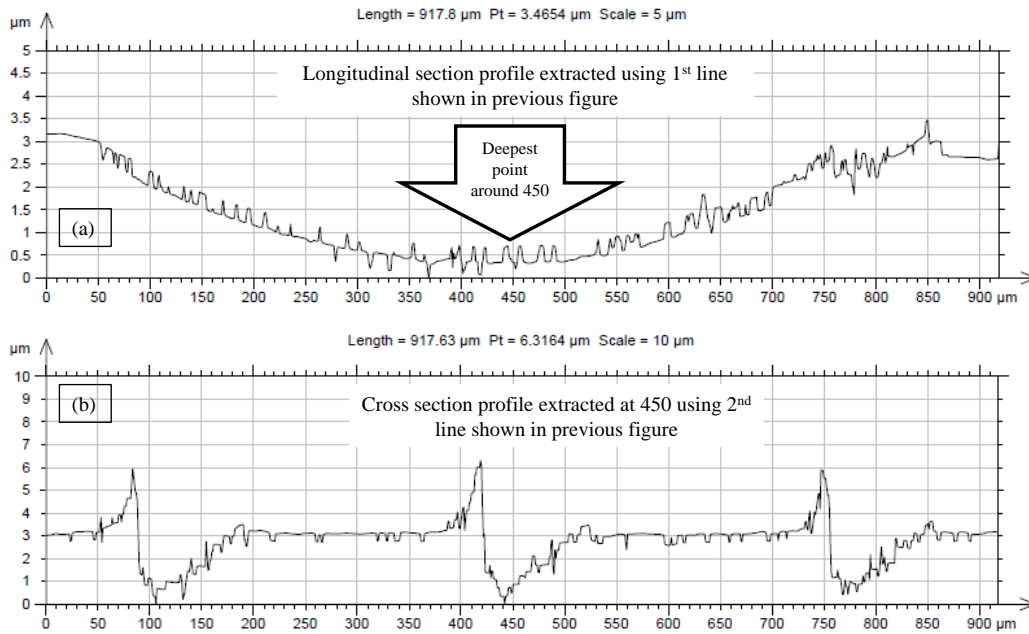


Figure 4.26 (a) Longitudinal profile of the middle scratch shown in Figure 4.26 and (b) cross-section profile of scratches extracted by using deepest point coordinate in the direction of 2nd line in Figure 4.25

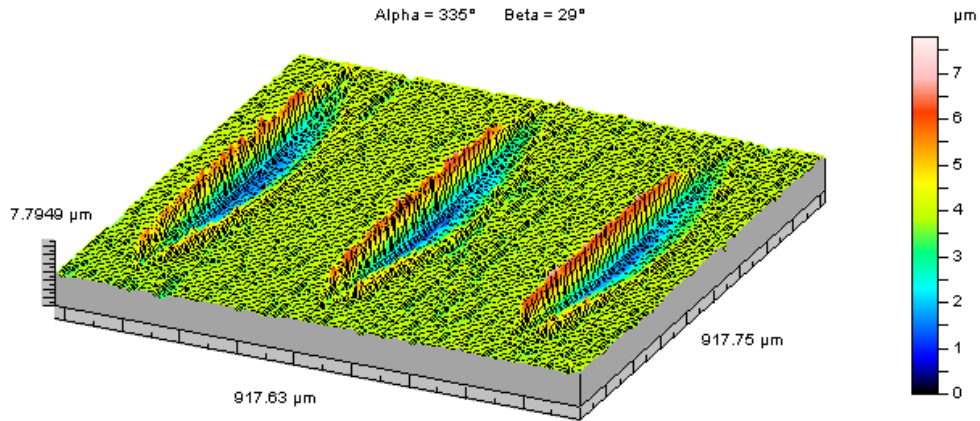


Figure 4.27 Example of 3D profile of scratches using Talysurf CCI 3000

Various types of scratches were obtained with different speeds and depth of cuts in a series of single grit grinding experiments. In the first instance, a single scratch is supposed to be generated as a result of grit-workpiece engagement at each pass of grit with wheel rotation. In our experiment, CBN grit was used as long as the grit sat on the circumference of the wheel. Sometimes grit dropped or separated due to insufficient adhesion of the super glue. Sometimes sudden fracture occurred during scratching at extreme depth of cut and grit was broken away from the wheel. In the latter case, broken grit was replaced by new grit in order to continue the experiment. If the same grit continued to produce many scratches without being separated from the wheel, after some time it becomes worn and the grit produces large (wide) scratches. When a new cutting edge appeared as the result of self-sharpening, multiple scratches would appear in one pass rather than just a single scratch as in the early stage of scratching (see Figure 4.28). According to experiments, single scratch and multiple scratches show some differences in terms of material removal mechanism.

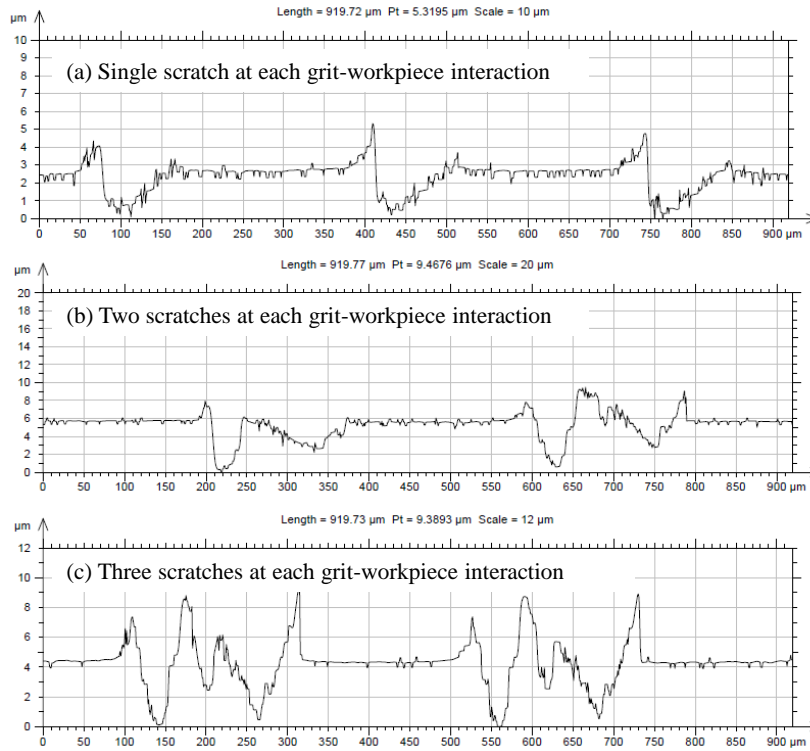


Figure 4.28 Cross-sectional profiles of single and multiple scratches produced with one pass of grit-workpiece interaction

In this work the material removal mechanism in single grit grinding was investigated to explore relational dependency between such parameters as depth of cut, speeds, pile-up ratio, etc. To perform this investigation, the pile-up areas of scratches and groove section area at the deepest point were calculated using Mountains software (TalyMap Universal version 3.1.9). The ratio of pile-up area to groove section area is a good method to demonstrate plough material variation depending on depth of cut, groove area, and effective grit engaging radius. Schematic representation of single grit ground scratch, pile-up and groove area notations are given in Figure 4.29.

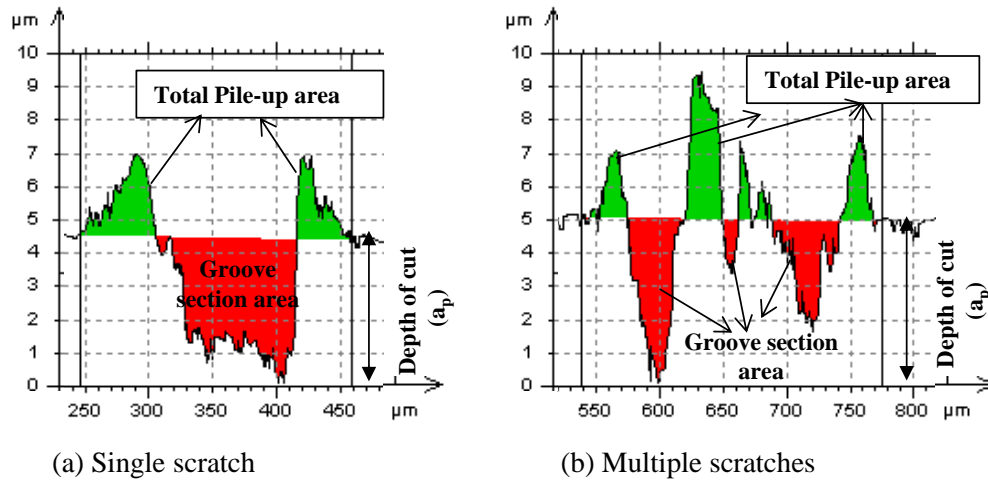


Figure 4.29 Pile-up and groove section area for (a) one scratch at one pass, and (b) multiple scratches at one pass

4.8 Methodology of material removal mechanisms in single grit scratching

In terms of material behaviour rubbing action occurs due to elastic deformation, ploughing action occurs due to a combination of elastic and plastic deformation and cutting occur due to plastic deformation with material separation. In practical, however, it is not easy to distinguish these three cases. It is necessary to perform single grit grinding tests to understand these three actions rather than grinding using an ordinary grinding wheel where several grits act simultaneously making it difficult to investigate material removal phenomena.

To understand the single grit grinding in practice, process monitoring tools such as AE signal have been used (Griffin, 2007). Some researchers have studied the scratch form and chips produced using a microscope to reveal the different phases of material removal mechanism (Takenaka, 1966; Brinksmeir and Glwerzew, 2003). But to date, no research has been published that demonstrates any clear transitions between these three actions. In this thesis, scratch form measured with a Talysurf CCI 3000 interferometer is used to interpret single grit grinding

results in terms of material removal mechanisms. The material removal phases seem to be difficult to distinguish exactly but can be expressed as an influence on the contribution of material removal. If we assume that the cross-section profile of the scratch is kept constant along the scratch length (see schematic cross sectional view of a scratch profile in Figure 4.30). In ideal rubbing action, there should be no scratches on the surface ($P1+P2=0$, $GA=0$). In ideal ploughing action, pile-up unit volume must be equal to the groove unit volume ($GA=P1+P2$), thus no material removal takes place with this action. In case of ideal cutting, the groove unit volume must equal to the removed material volume ($P1+P2=0$, $GA>0$), there should not exist pile-up material in the side of ground groove. However, in actual grinding these ideal approaches are not valid because the phases mix together and contribute to each other in terms of material deformation.

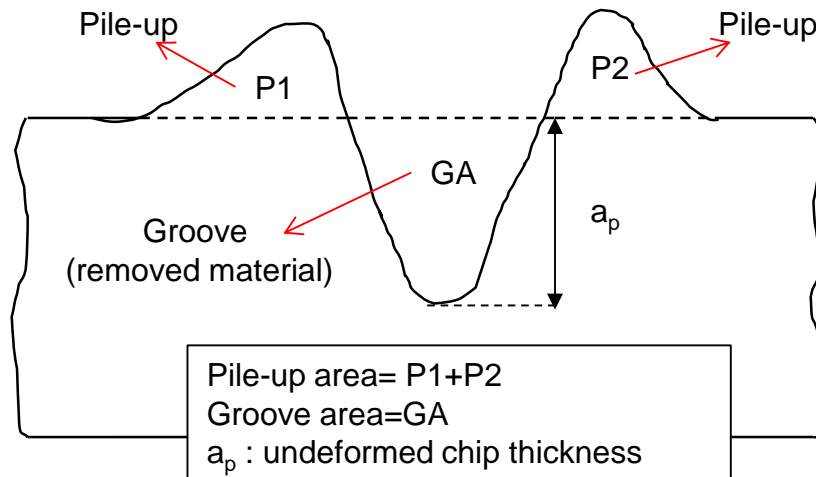


Figure 4.30 Schematic view of a scratch cross-section profile

In this thesis, material removal mechanism is investigated by considering the pile-up ratio variation at scratch cross sections. Higher pile-up ratio would demonstrate the process was

dominated by ploughing action while lower pile-up ratio would demonstrate the process was dominated by cutting action. The pile-up ratio can be calculated as;

$$\text{Pile-up ratio} = \frac{\text{Total pileup area}}{\text{Total groove area}} = \frac{P1 + P2}{GA} \quad 4.3$$

4.9 Summary

In this chapter, the methodology followed during the research programme has been introduced: in particular the experimental setup for the single grit grinding process. The single grit grinding procedure has been described in terms of longitudinal and traverses scratching. The sensors used for monitoring and recording process signals – an AE system and force sensor - are described for single grit grinding. The scratch form measurement methods to analyse material removal mechanisms in single grit grinding is described.

Chapter 5 will present and explain the methodology and strategy of developing a FEM simulation for cutting and single grit grinding action.

Chapter 5 FEM Simulation Development

5.1 Introduction

Finite element simulation of machining processes in this thesis refers to simulation of single grit grinding at the micro/submicron scale, where the depth of cut is in order of few micrometres or few hundred nanometres. This is not a straight-forward simulation and is dissimilar to conventional machining simulation which has a deeper cut. At the micrometre scale (generally higher than 10 μm) FEM simulation techniques have been widely used for cutting simulation, especially chip formation in turning and milling operations, where the simulations have been performed by utilizing cutting tools whose geometry is dissimilar to that of abrasive grit in the case of the grinding process. Abrasive grits in grinding have complex geometries and cannot be described as conventional shaped tools. During the grinding process numerous abrasive grits which are bonded onto the grinding wheel with an arbitrary orientation interact with the workpiece material, so the interactions of workpiece and grit during grinding can be considered as having a different geometry of interaction at every grit-workpiece engagement. Thus there are two obstacles which need to be overcome to simulate single grit-workpiece interaction; the first is the difficulty of using a micro/sub-micrometer scale necessitated by the shallow depths of cut (less than 5 microns), and the second one is the irregular abrasive grit geometry. Furthermore, material removal mechanism with abrasive grit shifts from concentrated shear, which is the main material removal mechanism in orthogonal cutting when the rake angle is higher than zero, to extrusion-like mechanism (Shaw, 1996). Thus, modelling of cutting process with negative rake angle (less than zero) using orthogonal cutting principles would also help to understand the differences between concentrated shear and extrusion-like material

removal mechanism. Here, a strategy is developed to form the FEM model for single grit-workpiece interaction at the micro/submicron scale. It begins with an understanding of the cutting simulation technique and implementation of chip formation using orthogonal cutting principles at relatively large scale in 2D Abaqus/Explicit, and then implementation at a micro/submicron scale of a single grit FEM simulation using a 3D model in Abaqus/Standard.

5.2 Framework of the FEM simulation

Single grit grinding simulation should consist of rubbing, ploughing and cutting phenomena, because three material removal phases occur at every grit-workpiece interaction in grinding, consecutively or simultaneously. There does not exist any FEM model to simulate these three actions at micro/submicron scale. Modelling and simulation of these actions using the finite element method will be challenging, however, prediction of cutting forces and ground surface creation would be invaluable outputs to extract from a FEM simulation. Finite element simulation could provide information about parameters such as stresses, residuals, strains, temperatures in the machined materials as a result of the grinding process, and these parameters are difficult to estimate by experimental work. In the context of this research, single grit grinding FEM model will be developed using simplified grit-workpiece interaction. Cutting simulation in grinding was previously modelled by using orthogonal cutting principles with negative rake angles (Ohbuchi and Obikawa, 2003). Cutting with negative rake angle could be considered as the only resemblance between the grinding and orthogonal cutting processes. However, orthogonal cutting with negative rake angles in 2D FEM models does not fully represent the material removal mechanism because in grinding chips are formed not only in front of the abrasive grit but also along both sides of the abrasive grit. Besides, ploughing (material swelling

up on both sides of the grit) can only be modelled with a 3D approach, which is not present in 2D orthogonal cutting processes.

It is necessary to make some assumptions to simplify the grit-workpiece interaction in the FEM model. Initially the abrasive grit is assumed spherical, and the other assumptions will be introduced in forthcoming sections. Preliminary FEM simulation attempts with a spherical grit show that single grit simulation of a shallow cut (few microns) is very demanding of CPU time (e.g. more than 100 hours). Also during simulations meshing problems arose which meant the model needed reconsideration to improve simulation results. Chip formation was not obtained in the preliminary single grit FEM simulations though ploughing did occur due to plastic deformation of the material. It was concluded that it was difficult to simulate within a single grinding model the three actions of cutting, ploughing and rubbing. The strategy was decided upon to start with cutting simulation using orthogonal cutting principles and varying parameters such as rake angles and depth of cuts. This would give important results to aid understand the general cutting mechanism and reconsideration of constitutive models, failure models and the meshing problems that frequently occur in FEM cutting simulations. Besides, 2D cutting simulation did not consume much time to investigate influence of the parameters on the model. After completion of the 2D cutting simulation, the best parameters found in 2D cutting simulation were applied to the 3D grit-workpiece model to mitigate difficulties caused by simulation cost (computational time) and aid formation of a model structure with plastic behaviour, contact methods, failure mechanism, remeshing scheme, etc. Therefore, the finite element simulations performed in this thesis was divided into groups as shown Figure 5.1, where the different material deformation states can be observed and analysed during single grit grinding and cutting.

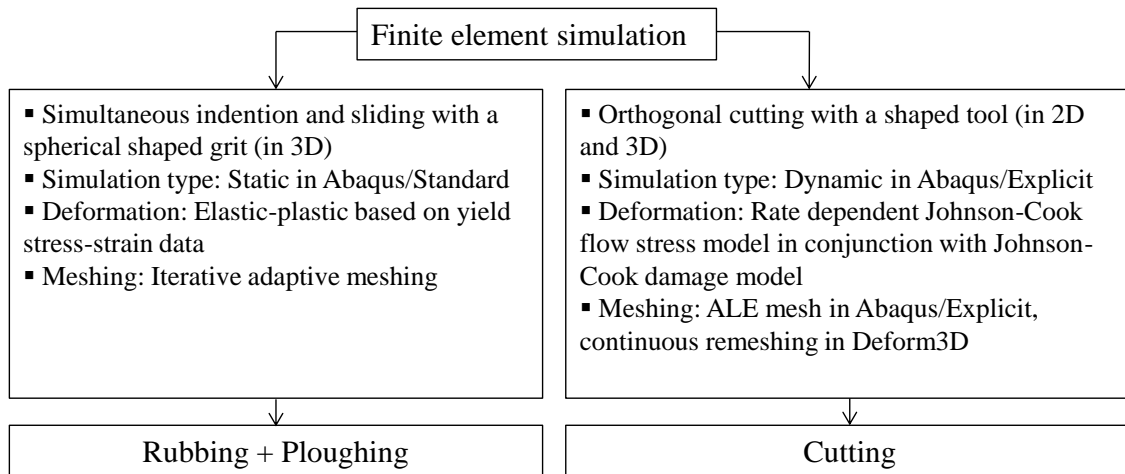


Figure 5.1 Procedures for finite element simulations performed in this study

5.3 Finite element model of cutting regarding orthogonal cutting mechanism

Orthogonal cutting simulations have been performed in Abaqus/Explicit to help understand the material behaviour under different machining conditions. Machining is a highly dynamic process where high plastic deformation occurs with high strain rates and temperatures. Material failure mechanisms are important behaviour characteristics during machining, which need to be considered during development of a FEM model. So, it is necessary to model appropriately to represent material behaviour under these conditions. Besides, knowledge of cutting tool geometry is required for the further investigation to reveal the influence of these parameters on cutting mechanisms under different conditions.

5.3.1 Material selection

A set of 2D finite element simulations have been performed to reveal the influences of machining conditions on chip formation during orthogonal cutting. Materials used for the cutting

FEM simulation were selected from the literature according to the availability of Johnson-Cook model (JCM) flows stress properties and Johnson-Cook (JC) damage parameters. A wide range of application and simulation results were considered during material selection to provide comparisons. Aluminium alloy (A2024-T351), which is widely used in the aerospace industry, was selected for a set of cutting simulations. Additional cutting simulations using different material properties were also performed in 2D and 3D during simulation development; however, these simulations are not included in the results chapter since the aim here was to find out the best simulation strategy. Material properties will be given in Sections 5.3.4 and 5.3.5.

5.3.2 Workpiece, cutting tool model and boundary conditions

A typical workpiece-cutting tool model is illustrated in Figure 5.2. The cutting tool was constrained as a rigid body. Tool speed was set to 300 m/min in a direction parallel to the workpiece in this study. The workpiece was fixed on the bottom left and held rigid against vertical and horizontal movement as shown in Figure 5.2. Chip formation simulations were performed with different rake angles and depth of cut to show the relational dependency of generated chip and operational parameters. Also, the influence of fracture energy during chip separation was investigated for continuous, serrated and discontinuous chips. Figure 5.3 demonstrates the some tool shape with different rake angles, which were used in this research.

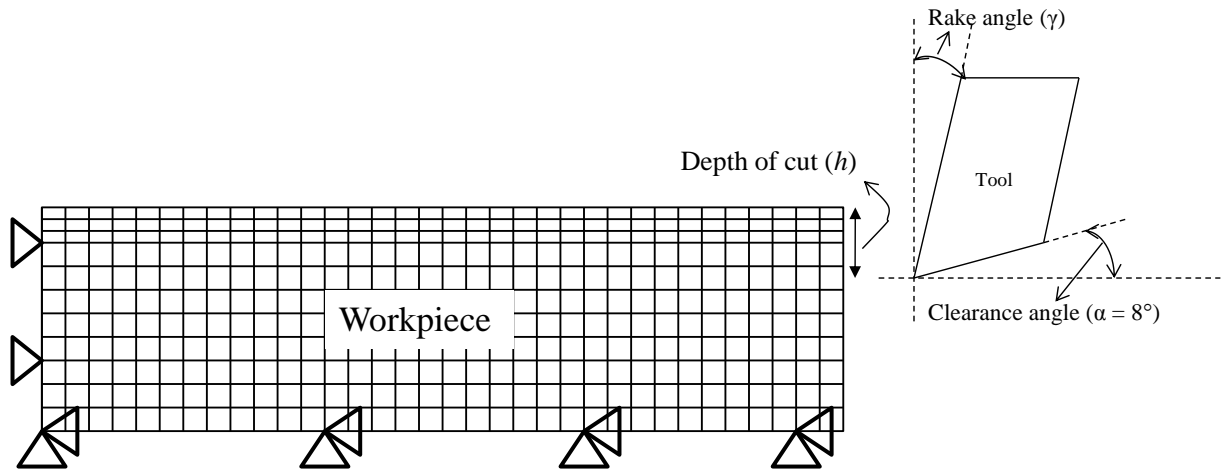


Figure 5.2 Workpiece - tool FEM model schematic description

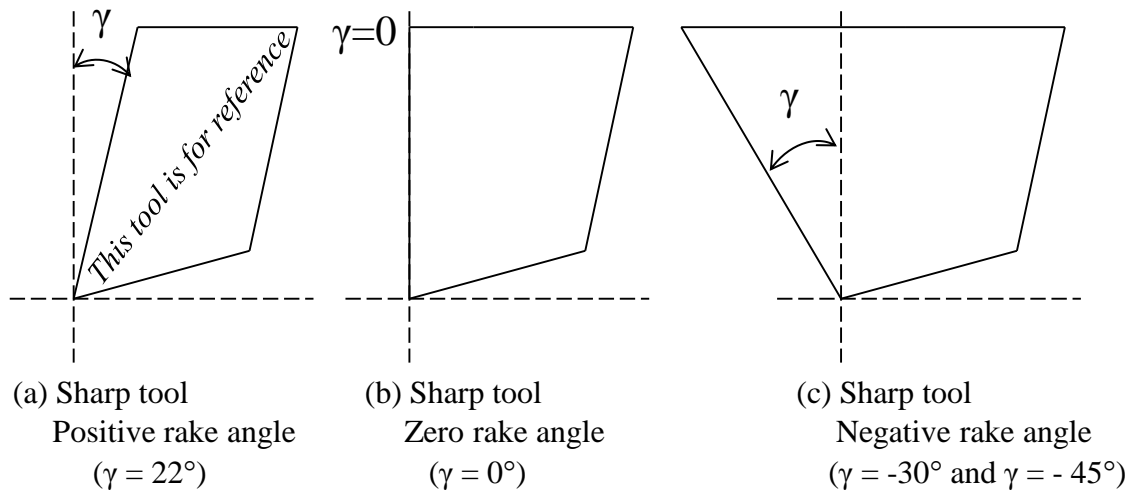


Figure 5.3 Illustration of cutting tools with different rake angles

For chip removal, 2D orthogonal cutting simulation was performed to provide more understanding of chip formation mechanism under various conditions. A damage evolution model was used to simulate fracture propagation commencing with damage initiation. The fracture energy model proposed by Hillerborg (1976) was included in the material model to determine damage evolution. Element deletion technique was used to remove the mesh element

when the element can no longer withstand shearing stress and material failure occurs. The element deletion technique was applied to the entire workpiece contrary to many previous works where element deletion was only applied to the sacrificial layer defined for chip separation from the workpiece (Mabrouki et al., 2008). Because chip fracture and cutting action do not only occur in a define section of workpiece material under the tool tip in the real cutting or grinding process, they can also occur even within chip itself, discontinuous chip formation mechanism could be good example which can explain fracture mechanism in different part of the material or chip.

5.3.3 Element shape and meshing

A 4-node bilinear plane strain quadrilateral, reduced integration, hourglass control element was used for the workpiece mesh. Throughout the FEM simulation ALE adaptive meshing was used for the mesh applied to the workpiece material (see Chapter 3). ALE mesh has generally been used to maintain a high quality mesh with extreme deformation but it can also be used with a fracture model as in this thesis. Formation of chips cannot be properly simulated without inclusion of a fracture model since ALE mesh technique is not good enough to create a chip by means only of plastic flow behaviour of material (Özel and Zeren, 2007). Several ALE meshing parameters (meshing frequency, smoothing, etc.) which are difficult to select in advance need to be tuned by trial and error based on simulation performance (Özel and Zeren, 2007). This makes the ALE mesh cumbersome to use in chip formation simulation. The literature review presented in Chapter 3 indicated that the continuous remeshing technique (available in Deform, MSC. Marc, Forge, AdvantEdge software, etc.) provides a better solution for chip formation compared to the ALE adaptive meshing; however, this is not available in the Abaqus software.

5.3.4 Material flow behaviour

JCM flow stress formulation (see Chapter 3) is used for all cutting simulation. JCM describes the flow stress of a material as the product of strain, strain rate and temperature effects, see Equation 3.21. The material properties and JCM parameters are given in Table 5.1. The corresponding JCM flow stress curves with respect to effective strains are illustrated for different strain rates and temperatures in Figure 5.4.

Table 5.1 Aluminium alloy A2024-T351 material properties (Mabrouki et al., 2008)

Parameters	Values for A2024-T351
A [MPa]	352
B [MPa]	440
n	0.42
C	0.0083
m	1
Density, ρ [kg/m ³]	2700
Elastic modulus, E [GPa]	73
Poisson's ratio, ν	0.33
*Specific heat, C_p [J/Kg/°C]	1000 for 220 °C from $C_p = 0.557T + 877.6$
*Expansion, α_d [$\mu\text{m.m}/^\circ\text{C}$]	22 estimated from $\alpha_d = 8.9 \times 10^{-3}T + 22.2$
T_{melt} [°C]	520
T_{room} [°C]	25
Heat fraction coefficient	0.9
* Single value estimated roughly from the given equations in order to simplify the material model since the scope of the thesis is mainly on single grit modelling rather than orthogonal cutting. Orthogonal cutting simulations performed for understanding of computational procedure for FEM and chip shape variation with a rake angle and depth of cut.	

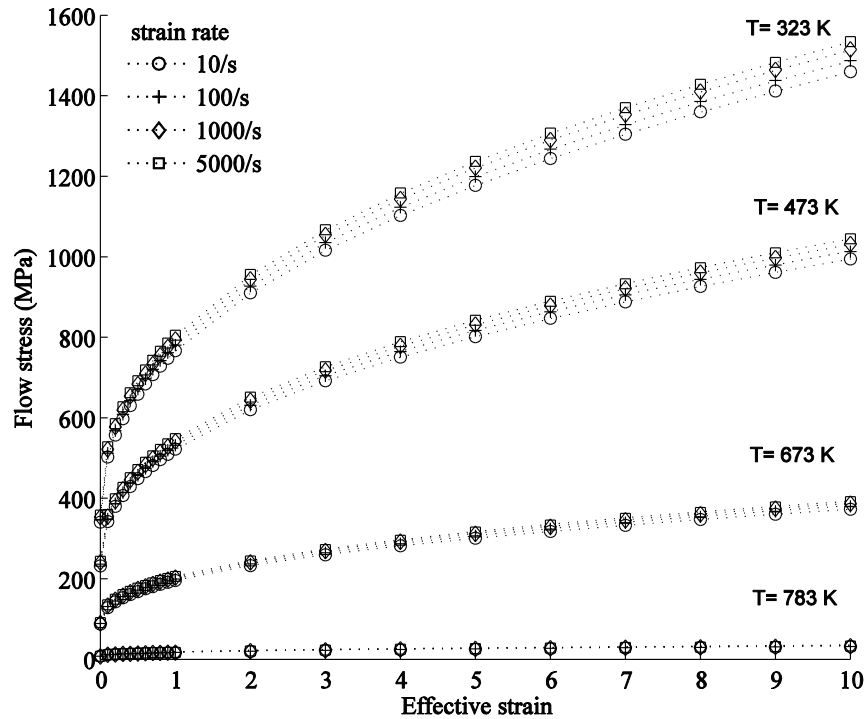


Figure 5.4 Flow stress curves with temperature and strain rate data using Johnson-Cook flow stress model

5.3.5 Material damage model

The damage model of Johnson and Cook (1985) is used in conjunction with the JCM flow stress model. The JC damage model is suitable for high strain rate deformation, such as high speed machining (Mabrouki et al., 2008). Teng and Wierzbicki (2006) claim the JC damage model gives more realistic simulations than other models (e.g. Wilkins, maximum shear stress, modified Cockcroft-Latham, constant fracture strain, and Bao-Wierzbicki fracture models). The JC damage model describes the general expression for the equivalent strain to fracture $\bar{\epsilon}^f$ is;

$$\bar{\varepsilon}^{-f} = \left(D_1 + D_2 \exp D_3 \frac{\sigma_m}{\sigma} \right) \left(1 + D_4 \ln \frac{\dot{\varepsilon}}{\dot{\varepsilon}_0} \right) \left[1 - D_5 \left(\frac{T - T_{\text{room}}}{T_{\text{melt}} - T_{\text{room}}} \right)^m \right] \quad 5.1$$

Where the Johnson-Cook damage parameters represent;

- D₁: Initial failure strain,
- D₂: Exponential factor,
- D₃: Triaxiality factor,
- D₄: Strain rate factor,
- D₅: Temperature factor, and

σ_m is the average of the three normal stresses and $\bar{\sigma}$ is the von Mises equivalent stress, $\dot{\varepsilon}$ is the strain rate which is normalized with a reference strain rate $\dot{\varepsilon}_0 = 1 \text{ s}^{-1}$.

The JC damage parameters for aluminium alloy (A2024-T351) used in the simulations are given in Table 5.2.

Table 5.2 Damage parameter for aluminium alloy A2024-T351 (Mabrouki et al., 2008)

D1	D2	D3	D4	D5
0.13	0.13	-1.5	0.011	0

Damage initiation begins according to the classical damage law (Mabrouki et al., 2008; Abaqus user's manual, 2009),

$$w = \sum \frac{\Delta \bar{\varepsilon}}{\bar{\varepsilon}^{-f}} \quad 5.2$$

Where $\Delta \bar{\varepsilon}$ is the increment of equivalent plastic strain during an integration step, w is damage parameter to initiate failure when it equals 1.

Here it is assumed that damage initiation is followed by damage evolution, and the damage evolution criterion governs the propagation of damage until ultimate failure. Damage initiation is represented in Abaqus as JCCRT (Johnson-Cook damage initiation criterion) calculated using

Equation (5.2). Figure 5.5 shows the damage initiation during chip formation. When the JCCRT or w value = 1, damage initiation begins on the element and progressive damage evaluation is determined via the damage evolution criterion which is given in the next section.

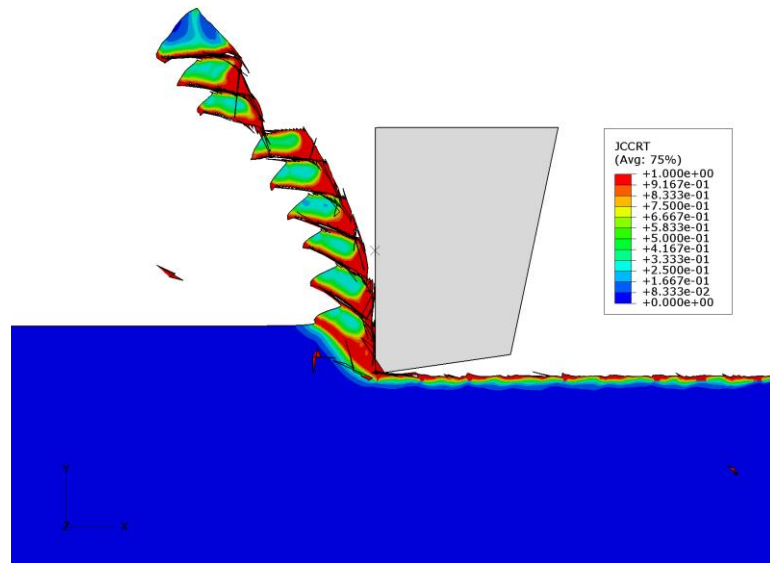


Figure 5.5 Damage initiation during chip formation (JCCRT: Johnson-Cook damage initiation value or w in Equation (5.2))

Stress-strain relationship as defined in material properties tables do not accurately represent the material's behaviour after initiation of damage. Due to strain localization, use of stress-strain to model damage propagation results in significant mesh dependency. To mitigate this mesh dependency, Abaqus offers two different damage evolution criteria, one based on plastic displacement and the other on fracture energy dissipation. Damage evolution with linear softening based on the fracture energy model of Hillerborg (Hillerborg, 1976; Mabrouki et al., 2008; Abaqus user's manual, 2009) was used in this study in order to show material toughness (K_{IC}) influences on chip formation, since the fracture energy can be evaluated as a function of K_{IC} . Hillerborg defined the fracture energy, G_f , required to obtain a unit area of crack as a

material parameter which governs the softening of the material after damage initiation as a stress-displacement response rather than a stress-strain response. To determine the stress-displacement response, a characteristic length (L), which is the typical length of line in the first order element associated with an integration point, is defined. Then Hillerborg's fracture energy is;

$$G_f = \int_{\bar{\varepsilon}_0^{-pl}}^{\bar{\varepsilon}_f^{-pl}} L \sigma_y d\bar{\varepsilon}^{-pl} = \int_0^{\bar{u}_f^{-pl}} \sigma_y d\bar{u}^{-pl} \quad 5.3$$

Where, \bar{u}^{pl} is the equivalent plastic displacement after onset of damage. A linear progression of the damage is assumed. Before damage initiation $\bar{u}^{pl} = 0$; after damage initiation $\bar{u}^{pl} = L\bar{\varepsilon}^{pl}$. In a FEM model, fracture energy is an input parameter which must be known before simulation begins. Following damage initiation, the damage variable increases according to;

$$D = \frac{L\bar{\varepsilon}^{-pl}}{\bar{u}_f^{-pl}} = \frac{\bar{u}^{-pl}}{\bar{u}_f^{-pl}} \quad 5.4$$

Where the equivalent plastic displacement at failure is computed as;

$$\bar{u}_f^{-pl} = \frac{2G_f}{\sigma_{y0}} \quad 5.5$$

Where σ_{y0} is the value of the yield stress at the moment when the failure criterion is reached.

Stress-strain behaviour of a material undergoing damage is illustrated in Figure 5.6. The solid curve in the figure represents the damaged stress-strain response, while the dashed curve is the response in the absence of damage. In the Figure 5.6 σ_{y0} and $\bar{\varepsilon}_0^{pl}$ are the yield stress and

equivalent plastic strain at the onset of damage respectively. $\bar{\epsilon}_f^{pl}$ is the equivalent plastic strain at failure, when the overall damage variable reaches the value $D = 1$. The relevant element is removed from the computation whenever $D = 1$ at an integration point, using the element deletion technique provided by the Abaqus software. Overall damage variable, D , can be obtained from the simulation output as a degradation variable, $SDEG$, and can be set to a value lower than unity considering the course of simulation.

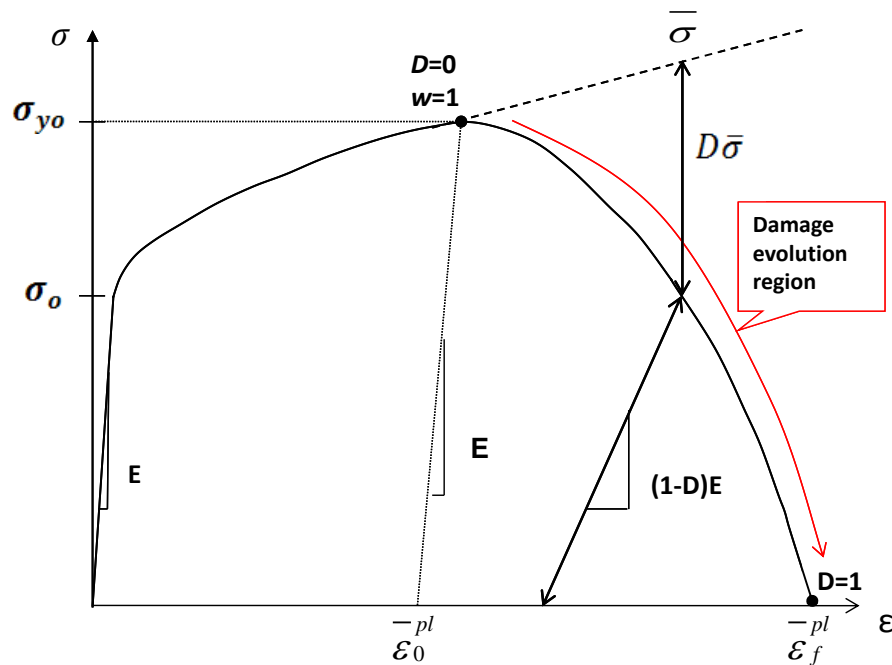


Figure 5.6 Stress-strain curve illustrating damage evolution using progressive damage model

Strength of the material along the curve can be calculated by

$$\sigma = (1 - D)\bar{\sigma} \tag{5.6}$$

Where σ and $\bar{\sigma}$ are the effective and apparent stress and D is the accumulated damage.

The elastic modulus after damage, \tilde{E} , is decreased but can be calculated by (He and Li, 2010);

$$\tilde{E} = (1 - D)E \quad 5.7$$

The difficulty in damage evolution is having to know *a priori* fracture energy value as an input parameter. Fracture energy required for the damage evolution can be determined from the equation below (Mabrouki et al., 2008);

$$G_f = K_{IC}^2 \left(\frac{1 - \nu^2}{E} \right) \quad (\text{Plane strain}) \quad 5.8$$

It can be seen that G_f calculated in this way is a function of the Poisson's ratio, ν , is proportional to the square of the fracture toughness, K_{IC} , and inversely proportional to Young's modulus, E . Importantly the fracture toughness (K_{IC}) indicates the resistance to crack growth and can be used to predict fracture initiation. High plastic deformation in machining processes causes variation in fracture toughness. He and Li (2010) investigated the influences of fracture toughness on aspects of strengthening and degrading. With increasing numbers of defects (micro-cracks and growths), some physical characteristic of materials also change; these include elastic modulus (which can be calculated using Equation 5.7) and toughness.

Measurements of K_{IC} are made using specimens containing very sharp fatigue pre-cracks. However, there are constraints on specimen dimension and crack length. Experimental evidence shows that the fracture toughness of metals is dependent on size of specimen during test; with the bigger the size of test specimen the more stable the value of fracture toughness, and with small test specimens the value is dramatically decreased as shown in Figure 5.7. These limitations make it difficult to obtain valid values of K_{IC} for materials (Garrison, 1987; Xiaozhi, 2011). So it is not realistic to use K_{IC} values measured at nominal test specimen size which is larger than that required for chip formation. If K_{IC} dependent fracture energy (G_f) applied to chip formation

simulation as a chip separation criterion, chip size is relatively small where the fracture is initiated and propagates. In addition, K_{IC} is not a constant property; it varies depending on the fracture mode of the material including micro-crack formation, element dislocation and subsequent crack growth along fracture lines. Mabrouki et al., (2008) introduced fracture energy method into the FEM model by using K_{IC} values measured at a nominal size to estimate the fracture energy required as a damage evolution criterion. In this thesis, fracture energy required for damage evolution was not determined from K_{IC} values; and is varied from 250 N/m to 20000 N/m to demonstrate its influences on chip type and morphology. Significant changes have been observed in chip morphology.

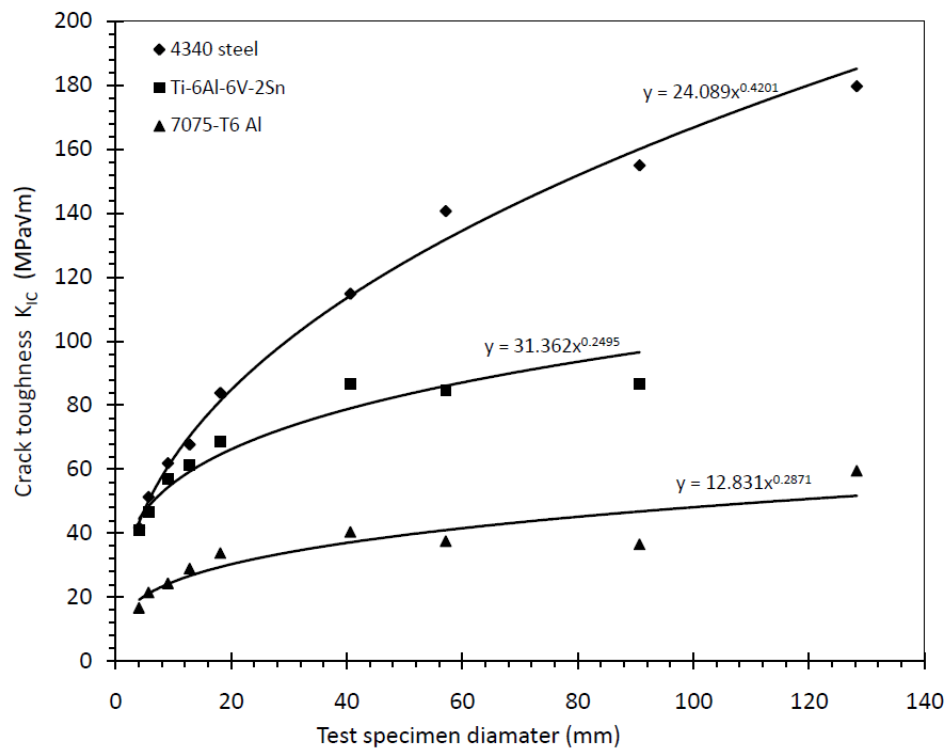


Figure 5.7 Crack toughness (K_{IC}) versus section size (Sisto et al., 1964)

5.3.6 Application of element deletion technique

Element distortion during simulation generally leads to the termination of program but a heavily distorted element can be removed from the mesh by setting the damage variables so as to reduce the possibility of termination. Highly distorted elements in Abaqus are deleted and kept out of computation. In the cutting simulation using Abaqus/Explicit, a sacrificial layer has been used to allow chip separation as described in the literature. Below a possible chip region there is a very thin layer defined in such a way that if the damage criterion is applied to that layer then the mesh elements in that region are removed from the computation using the element deletion method supported by Abaqus. Element deletion occurs when the degradation value (SDEG) calculated at a specified increment meets a specified value (default value 0.99) but can be set at any value less than unity to ease element deletion. Figure 5.8 demonstrates the element degradation (SDEG) distribution during chip formation. SDEG values are higher in the high deformation region e.g. primary shear zone and tool tip-workpiece contact zone in the chip. When the SDEG value reaches 1, ultimate element failure occurs via element deletion technique.

In the present study, no sacrificial layer is used to allow chip separation, damage criterion and element deletion is applied to entire workpiece to simulate crack initiation along the chip primary shear region. However, there is one drawback without a sacrificial layer, simulation can be terminated if element distortions increase excessively due to inconvenient damage parameters. In addition, without a sacrificial layer, some elements in the chip separation region, where tool comes into contact with workpiece, can extend too much.

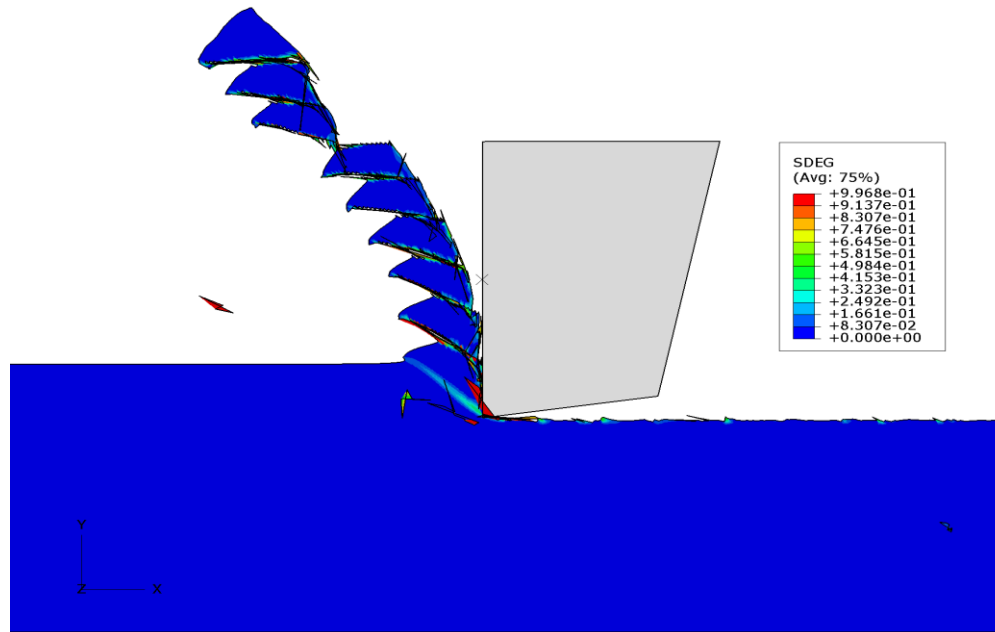


Figure 5.8 Element degradation (SDEG) based on damage evolution during chip simulation

5.3.7 Contact, friction and heat generation

Contact between tool and workpiece is defined by using the penalty contact model. Penalty friction formulation is used with a friction coefficient of 0.2 (assumed for Aluminium alloy (A2024-T351)) to define contact behaviour. In high speed machining, heat generated by local energy dissipation does not have sufficient time to diffuse away and local heating will occur in the active plastic zones and sliding frictional interface. Thus, temperature in the chip will rise and can be approximated as adiabatic heating. The temperature increase is calculated directly at the material integration points according to the adiabatic thermal energy increases caused by inelastic deformation (Shet and Deng, 2000; Belhadi et al., 2005). Heat conduction makes no contribution in an adiabatic analysis, thus the volumetric heat flux due to plastic straining can be calculated by;

$$\dot{q}_p = \eta \sigma \dot{\epsilon}^p \quad 5.9$$

Where \dot{q}_p is the heat flux added into the thermal energy balance, η is the inelastic heat fraction which is the proportion of work dissipated into heat (assumed constant at a default value of 0.9 in Abaqus), σ is the effective stress, and $\dot{\epsilon}^p$ is the plastic strain rate. The heat equation solved at each integration point is;

$$\rho C_p \frac{\Delta T_p}{\Delta t} = \dot{q}_p \quad 5.10$$

Where ρ is the density and C_p is the specific heat of the material. Considering Equations 5.9 and 5.10, local temperature rise due to plastic deformation is given by;

$$\Delta T_p = \eta \frac{\sigma \dot{\epsilon}^p \Delta t}{\rho C_p} \quad 5.11$$

Similarly, heat generated by friction forces lead to rise in temperature ΔT_f during a period of time Δt .

$$\dot{q}_f = \eta_f J \tau \dot{\gamma} = \rho C_p \frac{\Delta T_f}{\Delta t} \quad 5.12$$

Then temperature rise due to sliding friction between tool and chip interfaces,

$$\Delta T_f = \eta_f \frac{J\tau\dot{\gamma}\Delta t}{\rho C_p} \quad 5.13$$

Where, η_f is the fraction of dissipated energy caused by friction that contributes to the heating effect (assumed 0.9), J the equivalent heat conversion factor, τ shear stress computed by Coulomb's law and $\dot{\gamma}$ slip strain rate.

5.3.8 Summary of cutting FEM simulation procedure

Regarding cutting simulations performed in Abaqus/Explicit to help understanding chip formation mechanisms, the following investigations have been performed and detail results are given in the Chapter 7.

- Influence of rake angle,
- Influence of depth of cut,
- Variation of chip type and shape with operational parameters,
- Continuous, discontinuous and serrated chip formation,
- Fracture energy influence on chip shape,
- Primary and secondary shear zone development, and
- Force variation with depth of cut and rake angle.

5.4 Some cutting simulations using Deform3D

Some finite element simulations have been attempted by using Deform3D software to determine whether chip formation can be achievable or not at a shallower depth of cut less than 5 μm with a continuous remeshing method not available in Abaqus. First of all, chip simulation was performed for greater depth of cut, such as 0.1 mm, with the simulation parameters shown in

Figure 5.9. Tangential cutting force in +Y direction was gradually increasing with advance of chip formation while the tool was moving in +Y direction. JC constitutive material model was used in all simulations in this section by using JC parameters for AISI4340 steel, see Figure 5.10. The simulations were performed using a pyramid shape cutting tool (see Figure 5.11) with which to illustrate single grit grinding action with different cutting faces. With this pyramid shape cutting tool, simulations were performed for 3 different cases, which demonstrated some essential facts concerned with single grit FEM simulation.

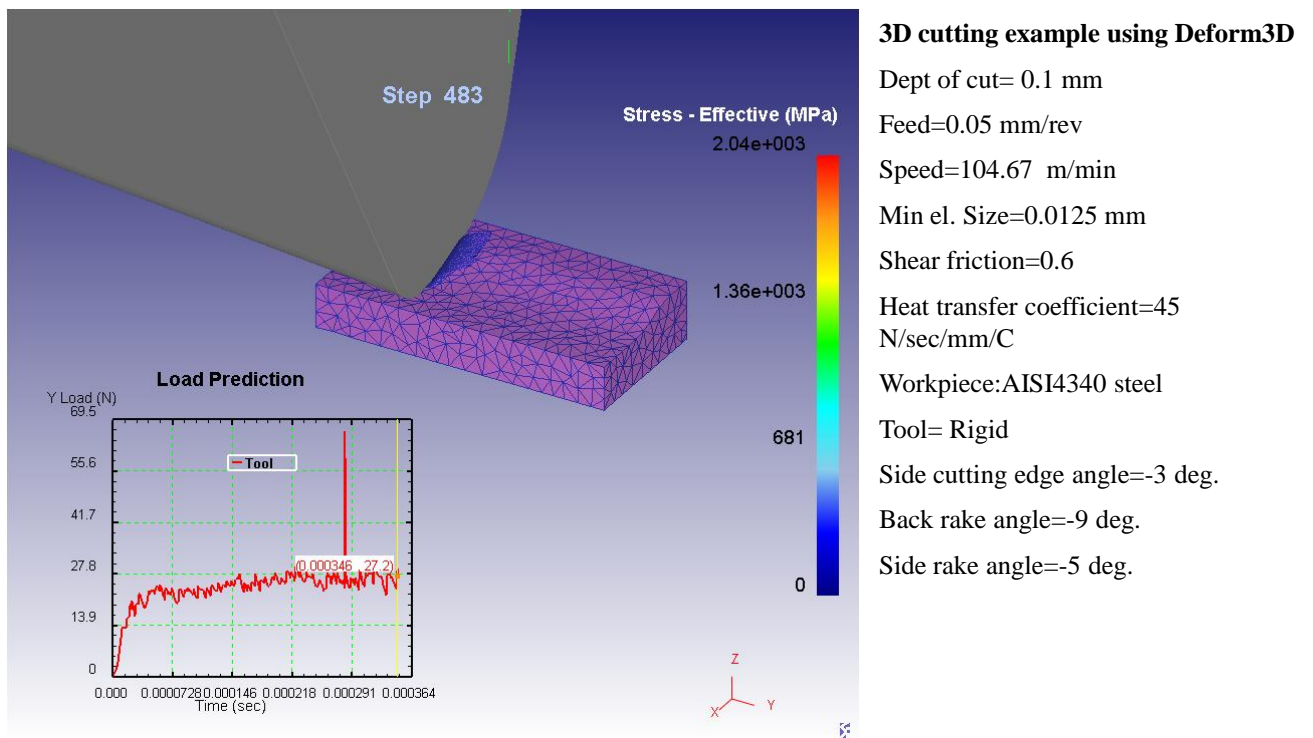


Figure 5.9 3D chip formation using Deform3D with cutting force and operating parameters

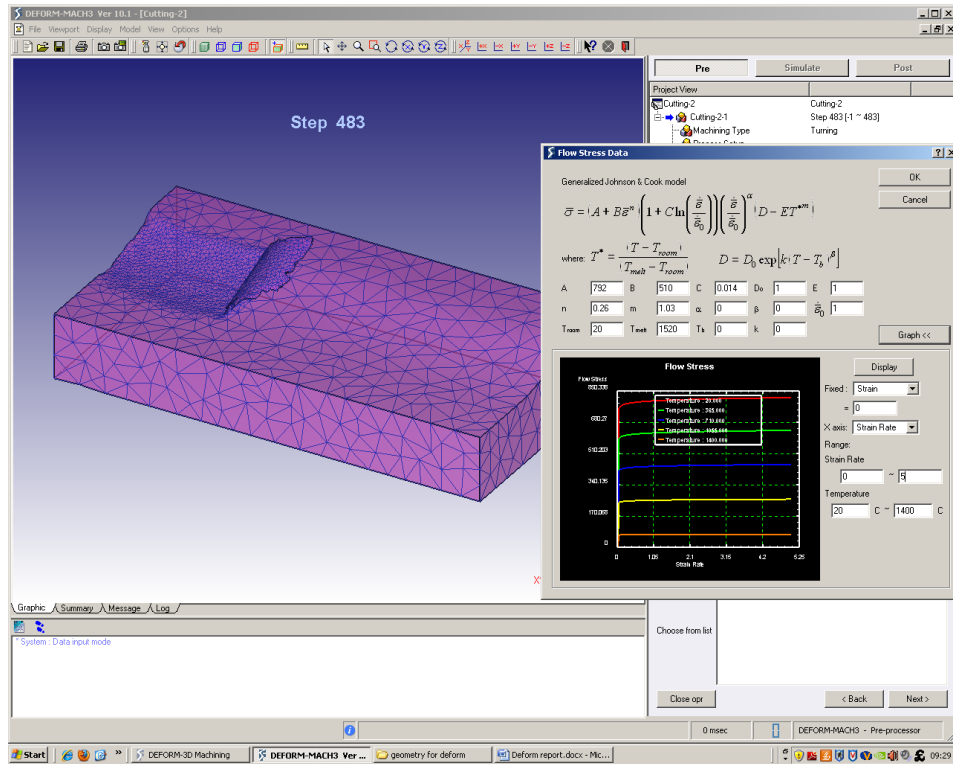


Figure 5.10 3D chip formation and JC flow stress properties used in the simulation

5.4.1 Case-1

FEM simulation was attempted with depths of cut 2 μm and 4 μm . Simulation with 2 μm depth did not work, it continuously gave memory error caused by the remeshing procedure and required a very small element size to produce chips. The simulation with 4 μm gave results as shown in Figure 5.11, but the remeshing process did not work properly and the cutting tool just ploughed the workpiece and deteriorated the surface, no proper chip formation was achieved.

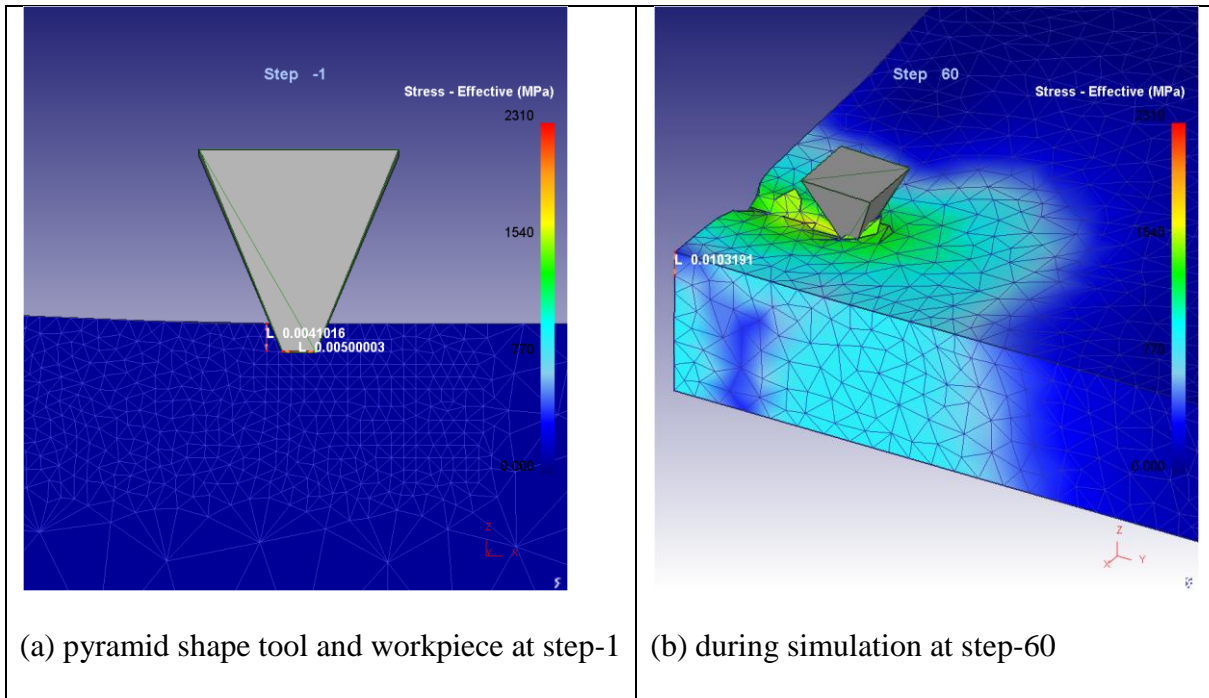


Figure 5.11 Cutting simulation attempt with 4 μm depth of cut using pyramid shape cutting tool

5.4.2 Case-2

A simulation with a 16 μm depth of cut was performed using the pyramid shape tool. The simulation performed acceptably and a chip was achieved. The cutting face of the tool was the side flat face of the pyramid and material accumulated ahead of the tool to form a chip but side pile-up of material was not efficient. Tangential and normal cutting forces increased gradually with increase of cutting length. This can be attributed to chip material accumulation before the cutting tool, see Figure 5.12 for pictures of different aspects of the simulation.

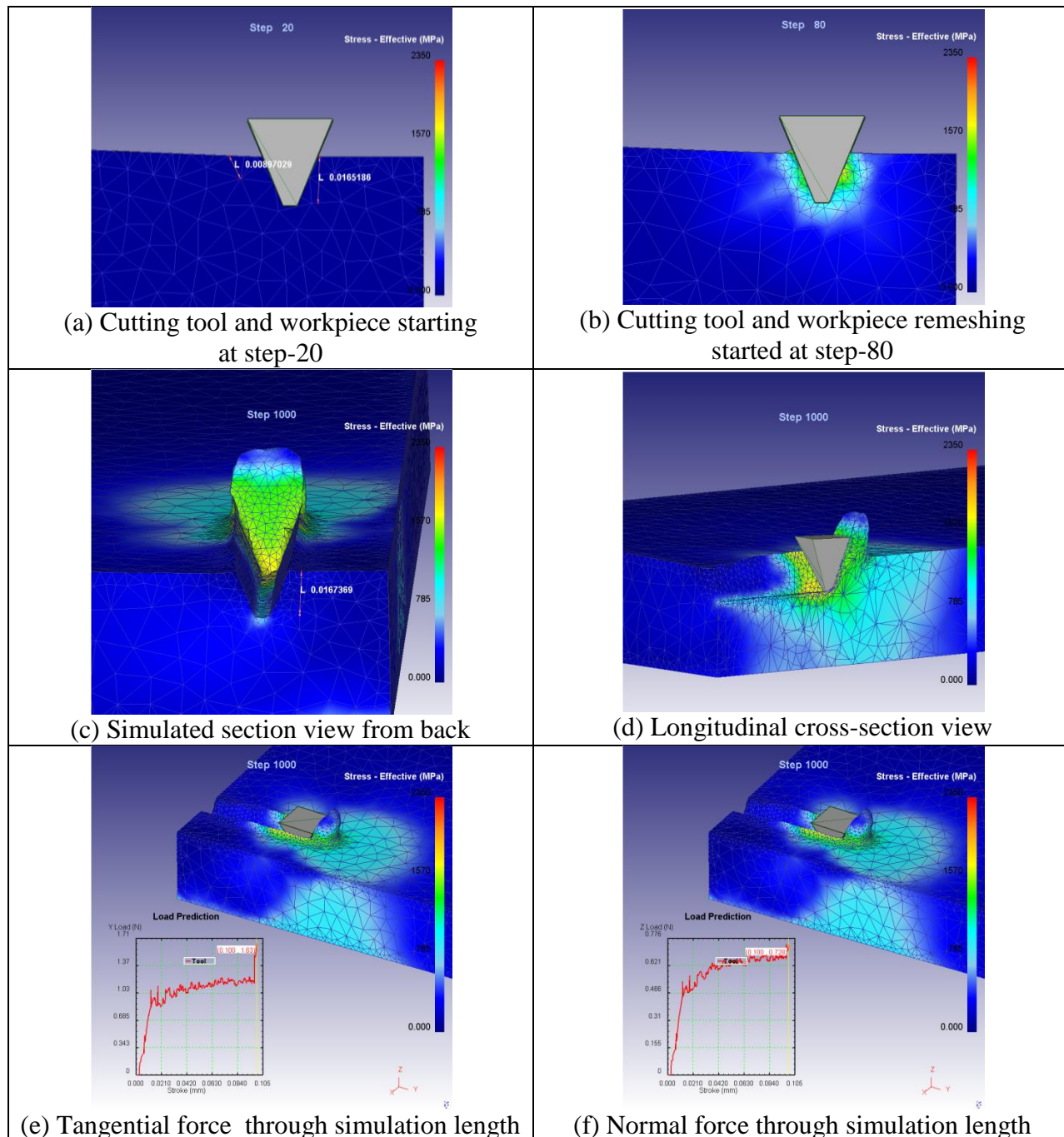


Figure 5.12 Cutting simulation with depth of cut of 16 μm using pyramid shape cutting tool

5.4.3 Case-3

A simulation with depth of cut of 10 μm was performed using a pyramid shape cutting tool with tool cutting face oriented as shown in Figure 5.13. The cutting face is a sharp edge consisting of the junction of two flat faces, which is dissimilar to Case-2. With the simulation working properly chips were not generated in front of the tool because sharp edge at the cutting face tears through workpiece material without material accumulating in front as shown in Figure 5.13(c) and (d). Thus, the tendency is for chips to form at the side rather than in front as in Case-2 or as typical chip formation in orthogonal cutting operations. This example shows that tool shape and orientation is effective in chip formation. Thus side flow and side chip formation can be attributed to cutting tool shape and geometric effects during grinding and irregular shape abrasive grits will generate both front and side chips during grinding. The tangential and normal cutting forces do not gradually increase after reaching a stable level, which is dissimilar to the forces acting in Case-2, since there is no material accumulation due to front chip formation ahead of the cutting tool.

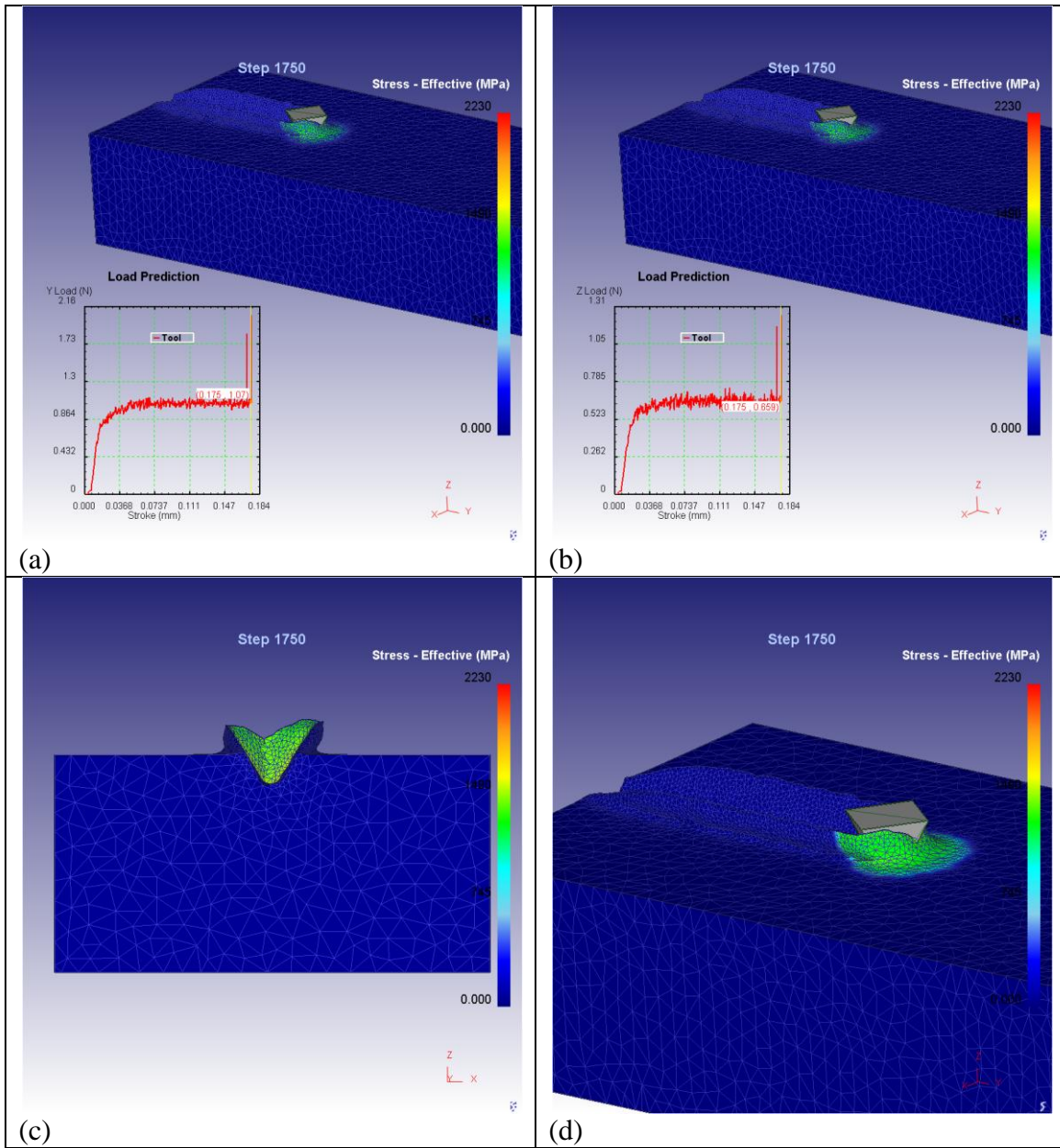


Figure 5.13 Cutting simulation using pyramid shape tool with depth of cut of 10 μm with cutting face consisting of the sharp edge at junction of two flat faces

5.4.4 Summary of the Deform3D simulations

These simulations were performed in Deform3D software, which was provided by WildeAnalysis™ for a one month evaluation period. A 2 μm depth of cut simulation was tried

but not successfully achieved which confirm that simulation of cutting very small depths of cut in the order of 1-2 μm is currently still not feasible using FEM but rubbing and ploughing mechanism can be studied at that level using FEM. The reason cannot be attributed to one thing; it is a combination of reasons such as computational power, remeshing issues, and continuum mechanics failure when the element size is at the nanometre level. A 3D chip formation was successfully achieved at depth of cuts of 10 μm or higher. A small number of simulations also show the effect of cutting tool shape on chip formation and cutting force variation during the cutting process.

5.5 Single grit grinding finite element model

Rubbing is the first action to occur during the grinding process when the abrasive grit starts to penetrate into the workpiece. As grit penetration increases workpiece material is deformed plastically and the ploughing process occurs until material is separated from the workpiece in the form of a chip. Modelling the exact abrasive trajectory during grinding is not an easy process, thus the single grit action is simplified by making some assumptions regarding material deformation characteristics during the process. The numerical results are intended to demonstrate the likely material deformation during single grit grinding, rather than representing quantified results which are exactly consistent with the real single grit grinding process. Therefore, the single grit scratching model presented here is only to demonstrate elastic-plastic deformation (rubbing and ploughing) and not chip formation. Thus a simplified model was developed for static conditions in Abaqus/Standard, subject to limitations (remeshing, element shape, etc.) which are explained in later sections. Various grit simulation paths (or trajectories), along which the grit moves have been designed to show rubbing and ploughing effects under different conditions. The rubbing region is more the difficult stage to represent in this process. Different

size grit, various depths (grit indentation depth into the workpiece during sliding), friction coefficient effects, different materials properties are considered in a set of simulations to see the influences on material deformation. The procedure and conditions to create the model are described below.

5.5.1 Computational method

Single grit scratching simulations under static conditions were performed in Abaqus/Standard which can be used when inertia effects and time-dependent material effects, such as creep, can be ignored for linear and nonlinear analysis but rate-dependent plasticity behaviour is taken into account. Static analysis was used due to the limitations of adaptive remeshing in other solutions such as the dynamic/implicit solution in Abaqus/Standard or the explicit solution in Abaqus/Explicit. Static analysis in Abaqus/Standard used the Newton iteration method similar to that used in the dynamic/implicit solution.

5.5.2 Grit geometry and workpiece design

Abrasive grit is modelled as a semi spherical shaped solid body. Real abrasive grit is not exactly spherical but grits are sorted according to their nominal diameters and may be considering as having a spherical body shape (Shaw, 1996; Doman et al., 2009^a; Anderson et al., 2011^a). In practice real abrasive grit might have several undefined cutting edges; at the grit tip some might be sharp while others might be round, but in any case will be continuously changing during grinding. Thus, it is required to make assumption to model the grit body, here, a spherical shape is chosen instead of a sharp cutting edge to provide easy sliding over the workpiece and reduce distortion of the element which would lead to termination of the program, see Figure 5.14. The size of the sphere (grit) used in the simulations was relatively smaller than the abrasive

grit used in the experimental tests because grit-workpiece engagement occurred over a very small portion of the abrasive grit tip which would not be the same as the nominal grit diameter. It could be greater when wear flats occurred or it could be very much smaller when fresh grit was used or fracture occurred. However, various size of grit (obtained by changing radius, R) was used in the simulation to observe the effect on material deformation at very small size grit. For this purpose, sphere radius (R) of $20\ \mu\text{m}$, $50\ \mu\text{m}$ and $250\ \mu\text{m}$ were used.

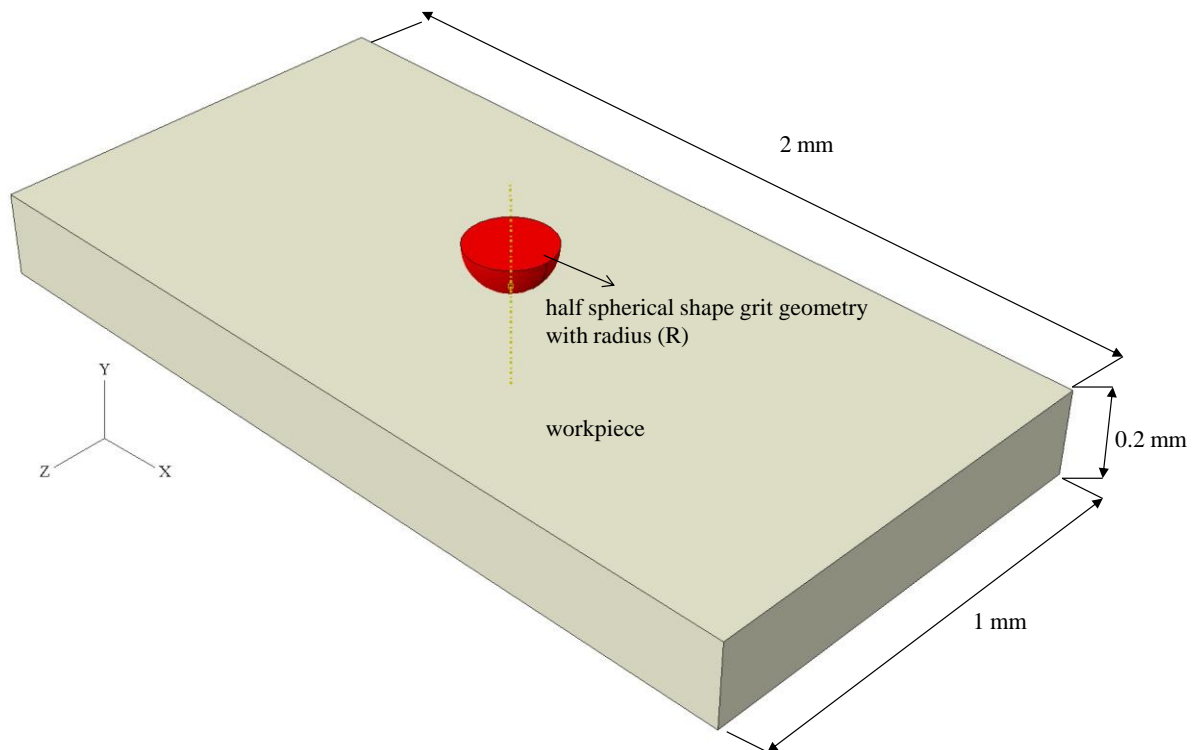


Figure 5.14 Workpiece and grit body modelled in Abaqus/CAE

5.5.3 Design of simulation to represent single and multiple grit scratching

A single grit scratch was simulated using different scratch trajectories to simulate rubbing and ploughing actions. At the first attempt of simulation, trajectory 'A' was used as shown in

Figure 5.15. Trajectory ‘A’ consisted of five steps. In step 1 the grit moves down onto the workpiece until contact occurred, and then in step 2 the grit continues to move down and penetrate the workpiece while moving in a horizontal direction until reaching maximum depth. In step 3 the grit then moves horizontally keeping penetration constant. In step 4 the grit begins to move upwards as shown in Figure 5.15 and finally reach to the stop position at step-5. This grit trajectory ‘A’ is suitable for very low speed scratching experiments, since with very low speed longitudinal scratching the middle of the scratched groove is flatter than the trochoidal groove obtained in actual grinding operations, see Figure 5.16. However, there is a problem with trajectory ‘A’, when the grit come into contact with workpiece, there exist a small penetration due to grit asperities caused by the grit element mesh. This small penetration is not convenient to detect the rubbing simulation. Since plastic deformation already occurs at the beginning of scratching even before the grit moves horizontally on the workpiece trajectory ‘B’ is defined, where the grit can move along the trajectory and penetrate into the workpiece using a tilted path. In trajectory ‘B’, the steps 1 and 5 in trajectory ‘A’ were omitted and steps 2 and 4 extended at the beginning and at the end, respectively, so trajectory ‘B’ is composed of 3 steps instead of 5. Detail dimension of each grit trajectory will be given in the analysis chapter.

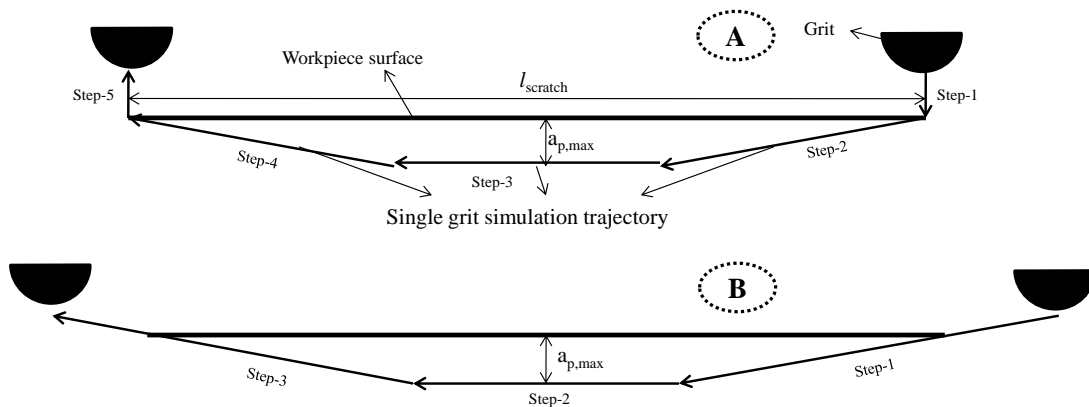


Figure 5.15 Grit trajectories used in FEM simulations

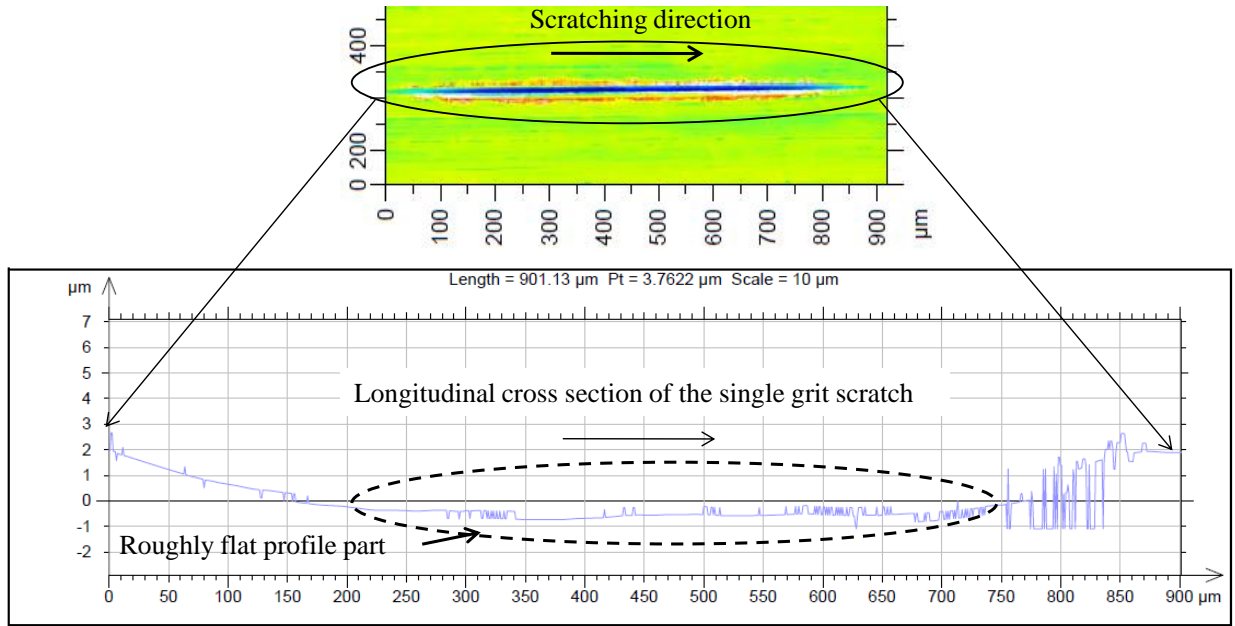


Figure 5.16 Longitudinal cross sectional profile of the single grit scratch at low speed ($V_c = 10.8$ m/min, $V_f=200$ mm/min)

In addition to the simulations performed using the grit trajectories described, multiple pass simulations were also performed to investigate ground surface creation using numerical analysis. For this purpose, multi-pass simulation was performed by shifting the grit $10\ \mu\text{m}$ in traverse direction (or $-Z$ direction in Figure 5.14) from the initial position then performing a second pass, then repeating the operation for a third pass of the simulation. The action is illustrated in Figure 5.17. For each pass of the simulation trajectory 'A' is used (Figure 5.15). Prediction of the ground surface created by single grit grinding simulation will be helpful to the understanding of how ploughed material effects the surface formation.

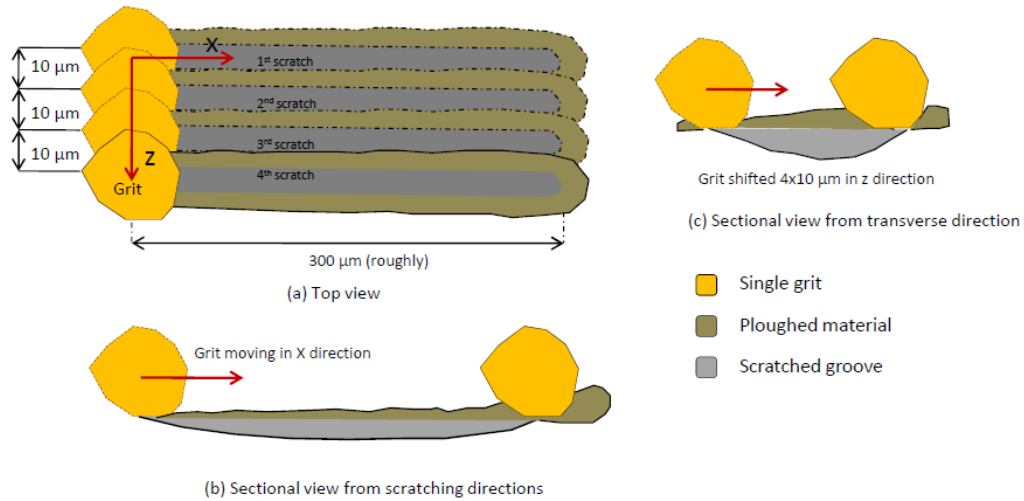


Figure 5.17 Illustration of the multi pass grit simulation

5.5.4 Element shape and adaptive remeshing

A typical mesh of the grain and workpiece is the C3D4 element, a four node linear tetrahedron element used to mesh both single grain and workpiece. A C3D4 type element is necessarily because of the element shape limitations of adaptive remeshing, in 3D analysis its application is only possible with the use of tetrahedral shaped elements.

The accuracy of the FEM analyses requires a fine mesh in the contact region and the capability to deal with stick-slip behaviour in multiple three-dimensional contact surfaces. Fine meshes over the contact area provide better conformity of contact between grain and workpiece. Coarse meshing may results in poor conformity of simulation due to the relatively large stress gradients in the grinding contact zone. In the FEM model, adaptive remeshing technique (Abaqus user's manual, 2009) is used to control distortion of the element due to dramatically increasing strain rate with large plastic deformation. Adaptive remeshing is an iterative technique

which is dissimilar to continuous remeshing used in general cutting simulation with software such as Deform3D. The general procedure for adaptive remeshing is described in Figure 5.18.

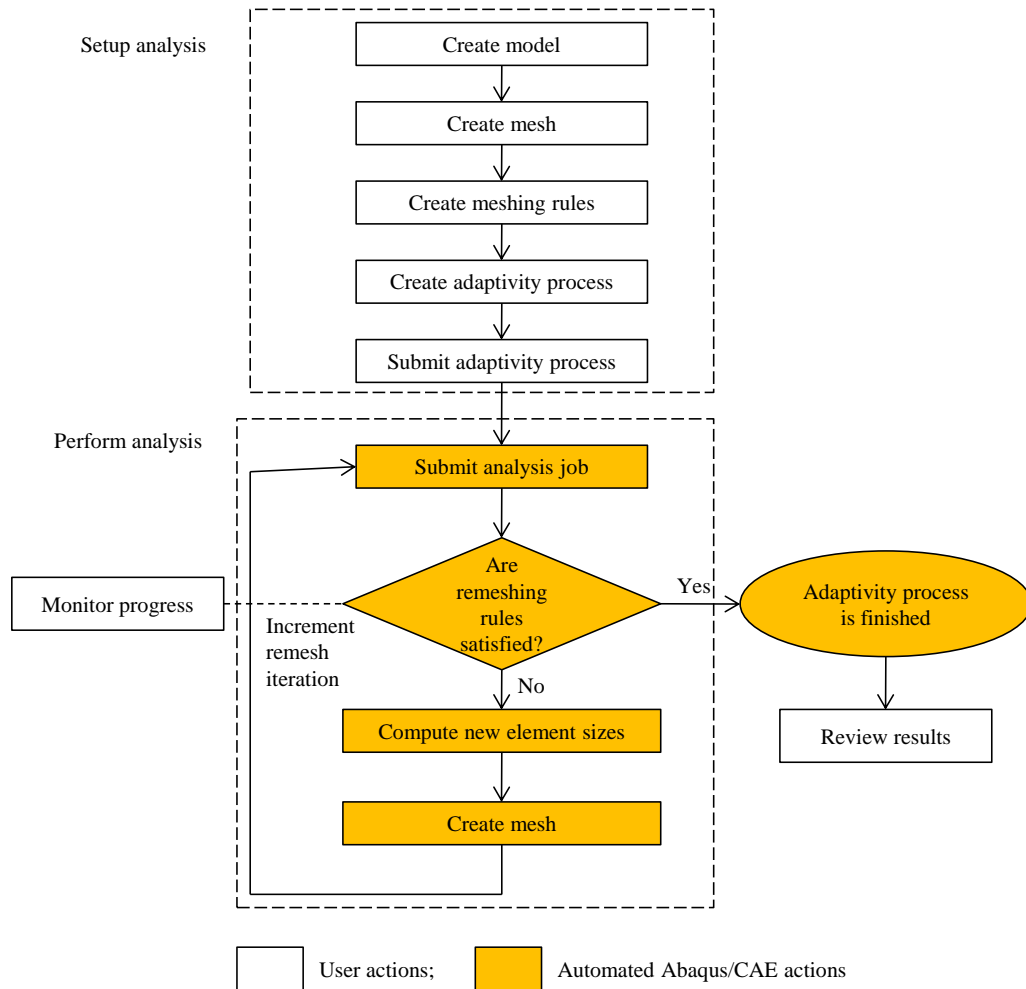


Figure 5.18 Adaptive remeshing procedure in Abaqus/CAE

The remeshing technique used here avoids remeshing the entire workpiece (Abaqus user’s manual, 2009). The remeshing is governed by mesh element size and average plastic strain error indicator is used to make decisions about element geometry and contact conformity at the interaction area. Remeshing rules needed to be defined to deal with the remeshing procedures.

Remeshing rules enable Abaqus/CAE to adapt the model's mesh iteratively to meet error indicator goals that have been specified. Remeshing rules defined for the single grit simulation is shown in Figure 5.19.

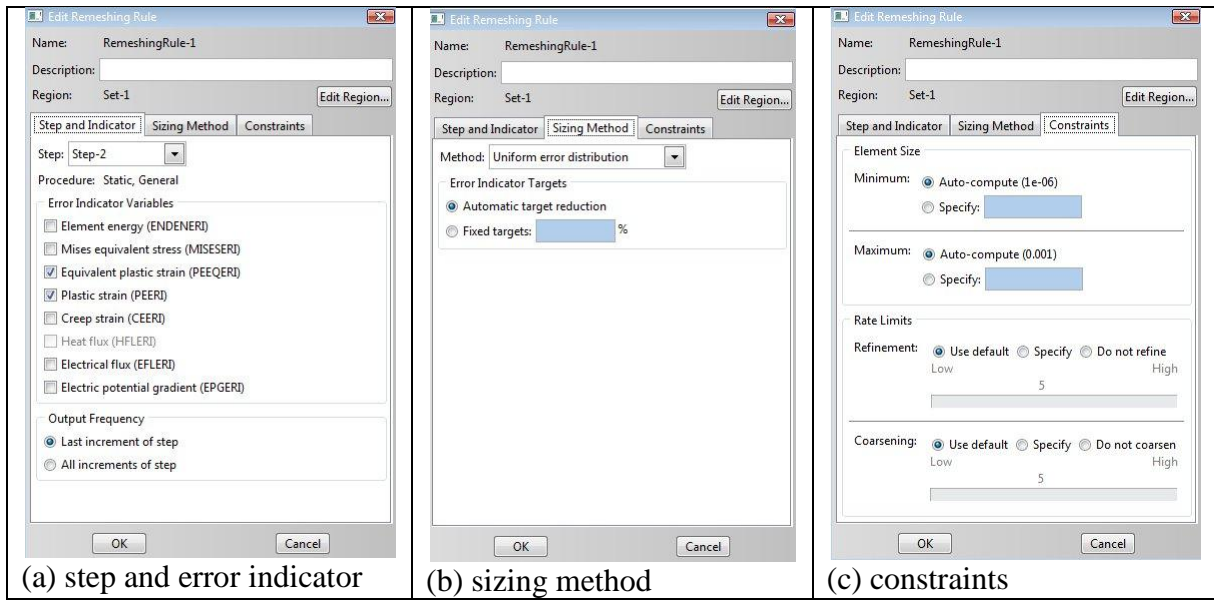


Figure 5.19 Remeshing rules defined for the single grit simulation

The remeshing rule had no effect on the mesh during the first simulation (Figure 5.20 (a)). However, during the first simulation Abaqus used the remeshing rule to calculate the error indicator output variables. In subsequent adaptive remeshing iterations the remeshing rule augmented the mesh size specification to produce a mesh that attempted to optimize element size and placement to achieve the error indicator goals described in the rule. Figure 5.20 shows three iterations of the mesh. The minimum element size in the last iteration was measured at around 200 nm, see Figure 5.20 (c). Three iterations were performed and a smaller element size was generated but the simulation did not work with this very small element. Simulations throughout this study were performed by using mesh sizes similar to the ones in Figure 5.20.

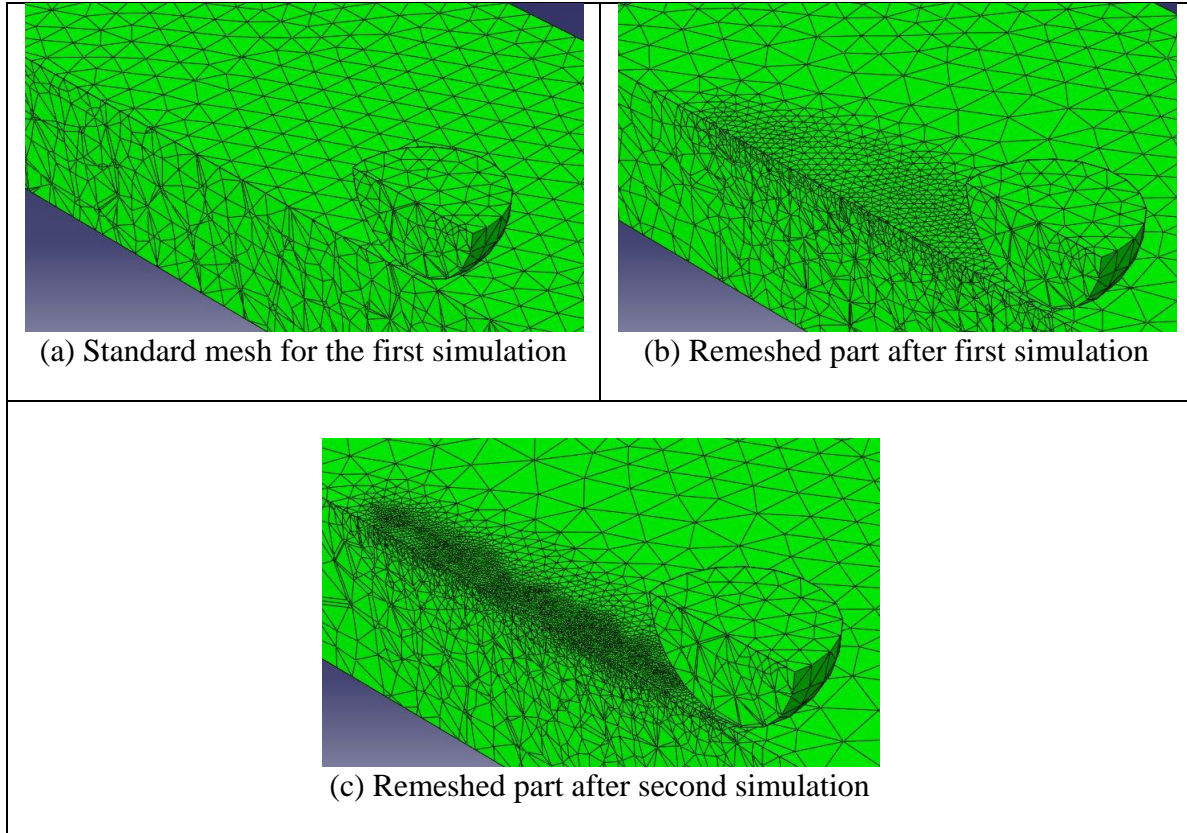


Figure 5.20 Remeshing the workpiece with iterative adaptive remeshing technique

5.5.5 Materials and elastic-plastic behaviour

Elastic-plastic material behaviour during single grit scratching simulation is governed by yield stress-strain curve based on yield stress-strain data (Shet and Deng, 2000). Material hardening was assumed to be isotropic. For the simulation, different material properties were used to observe variation of the deformation. In some simulations, material properties such as yield stress-strain data were generated artificially and represent a relatively softer material than mild steel. This provided an easy understanding of phenomena during grit sliding by observing elastic-plastic deformation. With hard material properties which were used in the later

simulations the elastic and plastic deformation was less obvious. The grit material was defined using two different properties. Material properties of the workpiece and the grits used in the simulations will be provided in Chapter 7 together with corresponding results to demonstrate the influence of material on the deformation.

5.5.6 Friction and contact description

In the FEM simulations, two bodies come into contact and in the interaction the harder material deforms the softer material. To allow contact between these two bodies, surface to surface type contact definition was used with a penalty contact algorithm. The harder material surface (grit body) was set as a master surface while softer material surface (workpiece) was set as a slave surface. To define the tangential behaviour of the contact interaction, both frictionless and with various friction coefficients, simulations were performed to see the effect on material deformation. In some simulations the friction coefficient was kept at $\mu=0.2$ and the deformation behaviour of different materials was investigated.

5.5.7 Analysis strategy of the results

Several single grit simulations have been performed using the grit trajectories shown in Figure 5.15. To extract essential information about material behaviour and deformation state, the following were carried out by the FEM. An attempt was made to separate the rubbing and ploughing stages by considering plastic strain distribution over the deformed material, but it was difficult to determine the exact elastic and elastic-plastic deformation zone because each element node shows plastic straining even at very small indentation. Actually, the elastic deformation state is supposed to be influential within very small length region which cannot be measured exactly in experimental tests. Stress and strain distributions along the grit sliding path with

increasing depth of cut will be discussed in the FEM result (in Chapter-7). Pile-up ratio at some locations along the scratched groove was calculated and will be compared with experimental results. However, experimental scratches include cutting phenomenon but in simulation this was ignored and this must be allowed for when explaining the pile-up ratios. Force variation through the simulation trajectories will be discussed, and friction effect on material deformation was also considered. Ground surface creation with single grit simulation was attempted and some good results obtained which shows how material deformation tends to form a surface as the groove geometry changes with the multi-pass grit simulation. This could provide a novel perspective for the single grit simulation at microscopic scale.

5.6 Working and non-working zone of the FEM simulations

It should be useful for a clear picture which can show the working and non-working zone of the FEM simulation under different conditions. Several simulations including 2D and 3D cutting using Abaqus/Explicit and Deform3D were performed as well as single grit simulations without cutting using Abaqus/Standard to determine the difficulties faced during FEM simulation of machining and single grit grinding. Working and non-working zones of the simulations performed throughout this study are illustrated in Figure 5.21. The difficulties in simulating cutting are generally due to mesh element size caused by small depth of cut. The non-working zone does not represent only the non-working condition but also represents the zone where the simulation has not been fully completed due to program termination. The non-working zone contains the zone(s) where the simulations are prone to be aborted due to high element distortion.

It was found that for orthogonal cutting simulations, the difficulties were generally the 3D simulation using Abaqus and Deform3D software were at small depth of cuts since small depth

of cut requires smaller element size in mesh to form a chip. For example, to perform a 3D cutting simulation with 2 μm depth of cut, the element size to obtain good chip morphology should be around a few hundred nanometres ($\sim 200\text{ nm}$). With this setting, 3D cutting simulation seems to be working (since simulation continuously running without termination) but actually it is impractical in terms of computational time. It was experienced that with this simulation setting 1 nm tool advancement took more than 24 hours, that means 1 mm tool advancement to form a chip would take more than 24000 hours. Computational time in working conditions with 50 μm depth of cut can complete 0.5 mm length cutting within 24 hours. Thus, computational time does not increase or decrease linearly with depth of cut, but is related to element size and increases with decreasing element size and depth of cut. 3D cutting simulations performed using Deform3D also allow some remarkable conclusions to be drawn about FEM cutting simulations of working and non-working zones. Section 5-4 introduced simulations using Deform3D, for working and non-working zone of the simulations using Deform3D, see also Figure 5.21 where the continuous thick black line in the chip formation side of the graph demonstrates working and non-working ranges of simulations using Deform3D. Simulation of effect of rake angle also had some difficulties – though this was more related to increase of element distortion when lowering the rake angle from positive to negative values. The simulations performed with spherical shape grit geometry show different behaviour because of the modelling conditions (Abaqus/Standard, iterative remeshing, no damage model used to allow element fracture, only elastic-plastic deformation). Single grit simulation works well at low depth of cut but with increase of depth of cut the simulation struggles to continue and it is terminated due to extreme element distortion. Element distortion in cutting was reduced by applying ALE meshing and damage model and element deletion techniques, but these are not applicable in a single grit simulation environment (static analysis in Abaqus/Standard). Grit radius also affects simulation working conditions. The

smaller the grit radius with increasing depth of cut leads to termination of the program due to heavily element distortion because this model does not include both the damage model and element deletion technique. Thus, when the simulation of the smaller radius grit with high depth of cut is run, after a certain time grit can no longer slide easily over the workpiece due to material accumulation ahead of the grit body. This accumulated material needs to be removed in the form of chips to allow to the grit to move along the designed path but it could not be removed due to FEM model limitations. However, spherical grit with high radius can slide easily even at relatively high depth of cut along the designed path without program termination.

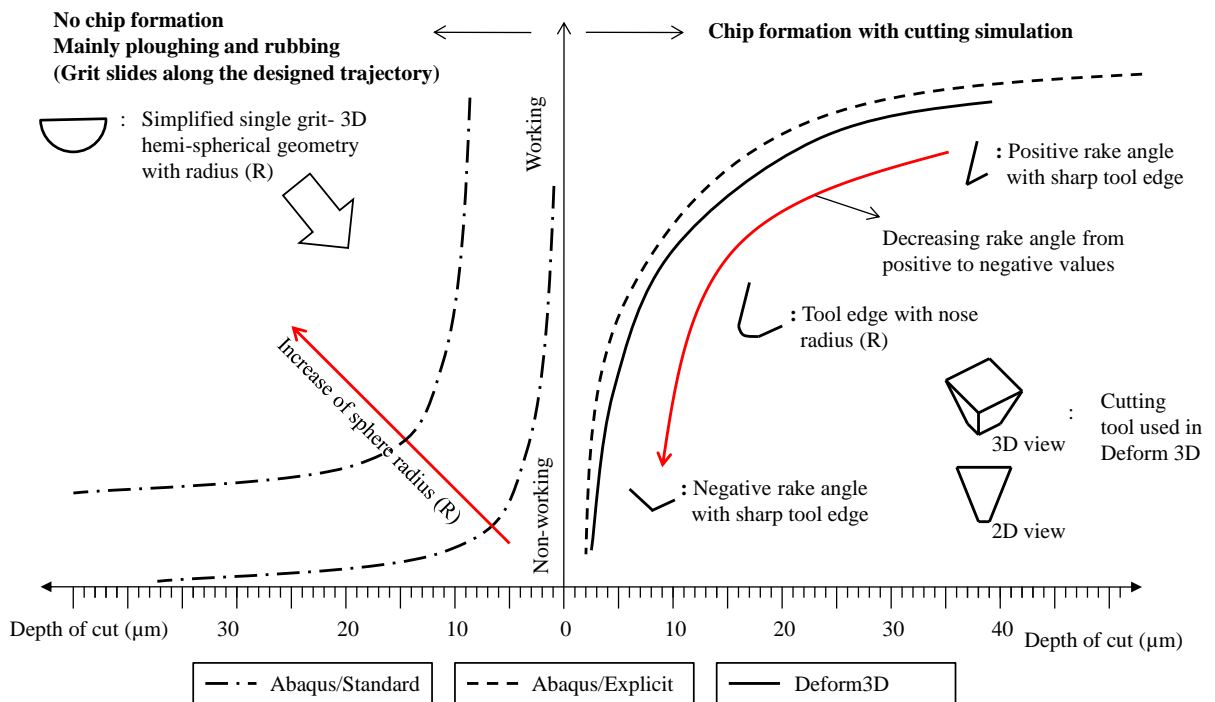


Figure 5.21 Illustrative picture to show working and non-working zone of the FEM simulations

5.7 Summary

In this chapter, FEM simulation procedure has been developed to perform single grit simulation at small scales down to $1\mu\text{m}$. The FEM models have been developed to perform the cutting, ploughing, and rubbing actions that take place during grinding. Because of the scale factor, accurate single grit grinding simulation could not be achieved and different simulations were designed to perform cutting and ploughing under different conditions. Cutting simulations were performed mainly by using orthogonal cutting principles whereas ploughing and rubbing simulations were performed by using simultaneous sliding and indentation action of spherical grit over the workpiece. Cutting simulations were performed mainly in 2D by using Abaqus/Explicit but some 3D simulation using Deform3D was also performed to investigate the feasibility of cutting at a small scale. In addition, an attempt was made to extract working and non-working conditions based on the simulations to obtain a clear picture about the conditions in which simulations do not work.

Chapter 6 Experimental Investigation of Single Grit Grinding

6.1 Introduction

Single grit grinding experiments were performed to uncover fundamental grinding process mechanisms at the micro scale. Such investigation on single grit interaction with a workpiece is crucial for providing more insight into the mechanics of grinding because wheel grinding process can be conceived of as the integration of numerous single grit actions on the workpiece surface. Experimental methodology regarding experimental conditions and setup has been described in Chapter 4. In this chapter, experimental results obtained from single grit grinding (scratching) of three different workpiece materials are presented. En8 steel, En24T steel and Inconel 718 were used as workpieces for the experiments. Single grit grinding scratches were investigated with respect to pile-up ratio (pile-up area to groove area ratio) for different depths of cut and groove areas, as well as cutting force variation and specific energy exerted during scratching. Cutting speed was included as a factor in the investigation of material removal mechanisms. Scratches were performed at speeds varying between 10 rpm ($V_c = 1.08$ m/min) to 5000 rpm ($V_c = 546.6$ m/min). Geometrical shape of the grit and cutting edge sharpness, as determined from the scratch profile were also considered as part of the investigation of material removal mechanisms.

6.2 Material removal mechanisms in terms of pile-up ratio and chip removal strength

Pile-up ratio (as defined in Equation 4.3), chip removal strength (or material removal strength) and effective grit engage radius are used as indicators to describe the behaviour of material removal under different grit cutting edge shapes. The chip removal strength is defined as a measure of rate of removal of material over the cross-sectional area of the scratch and is calculated by subtracting the total pile-up area from the total groove area. Pile-up ratio can provide information about the material removal phases (rubbing, ploughing and cutting) that occur during grinding. Higher pile-up ratio would mean less cutting while lower pile-up ratio would mean cutting is more prominent than rubbing and ploughing. Here, for the analysis the pile-up ratio was used for three different workpiece materials. Pile-up ratio was measured at the deepest point of the scratches and generally found around the middle of the scratches.

6.2.1 En24T steel

Grit cutting edges were changed through the course of scratching due to wear of the CBN grit cutting edges. According to experimental observation, fresh grit started with a single cutting edge and then with increase of number of scratches performed the grit cutting edge shape was altered, and sometimes multiple cutting edges were formed on a single grit. The scratches produced by single and multiple cutting edges show different characteristics in terms of material removal mechanism.

Figure 6.1 shows that the pile-up ratio gradually increases with increasing depth of cut. Scratch cross-section profiles are also given in Figure 6.1, and it is clear that the scratch profile is flat at the bottom of the groove. This shape also represents the grit cutting edge profile

interaction with the workpiece. Thus, scratching with a flat cutting edge results in slowly increasing pile-up ratio with increasing depth of cut.

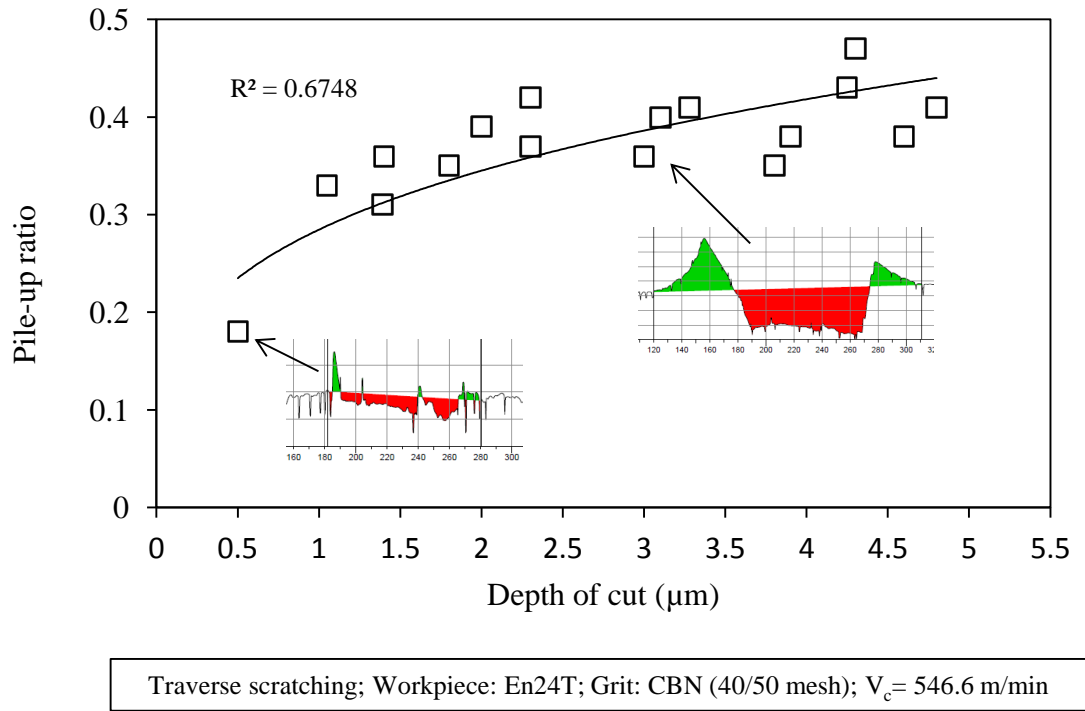


Figure 6.1 Variation of pile-up ratio with depth of cut (flat cutting edge)

Pile-up ratio versus groove area (Figure 6.2) shows a similar trend, as would be expected if the cut width remained more or less constant. The trend obtained with the given cutting edge, which has quite a flat bottom and walls of the cut which remain sharp, is such that it is not a blunt cutting edge. Chip removal strength shows a linear relation with depth of cut as shown in Figure 6.3.

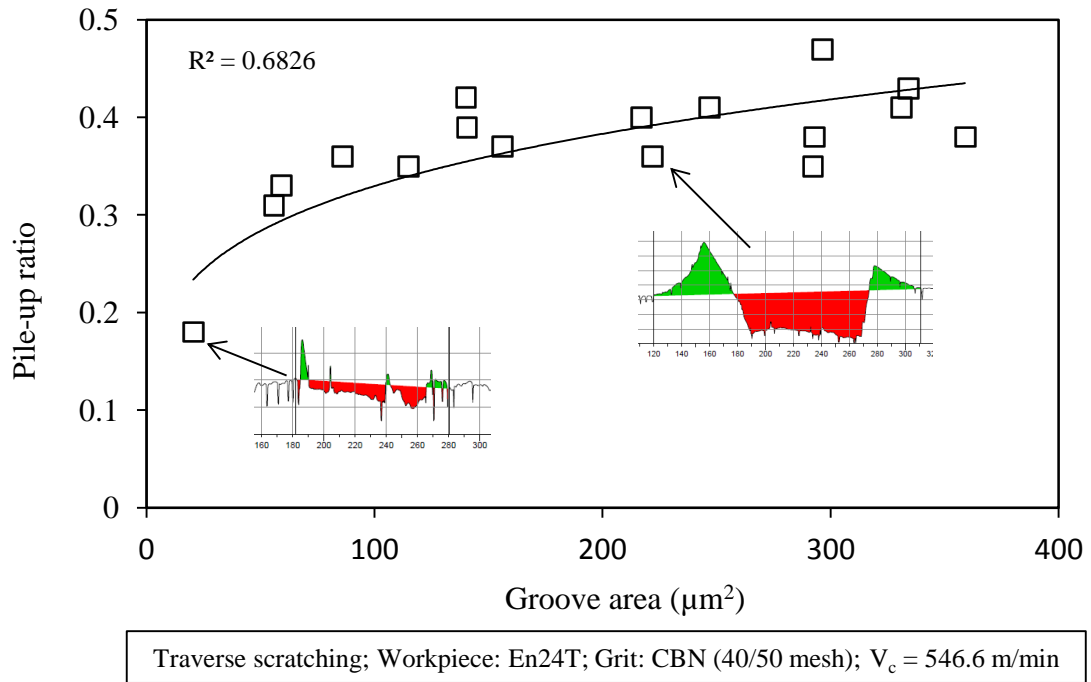


Figure 6.2 Variation of pile-up ratio with groove area (flat cutting edge)

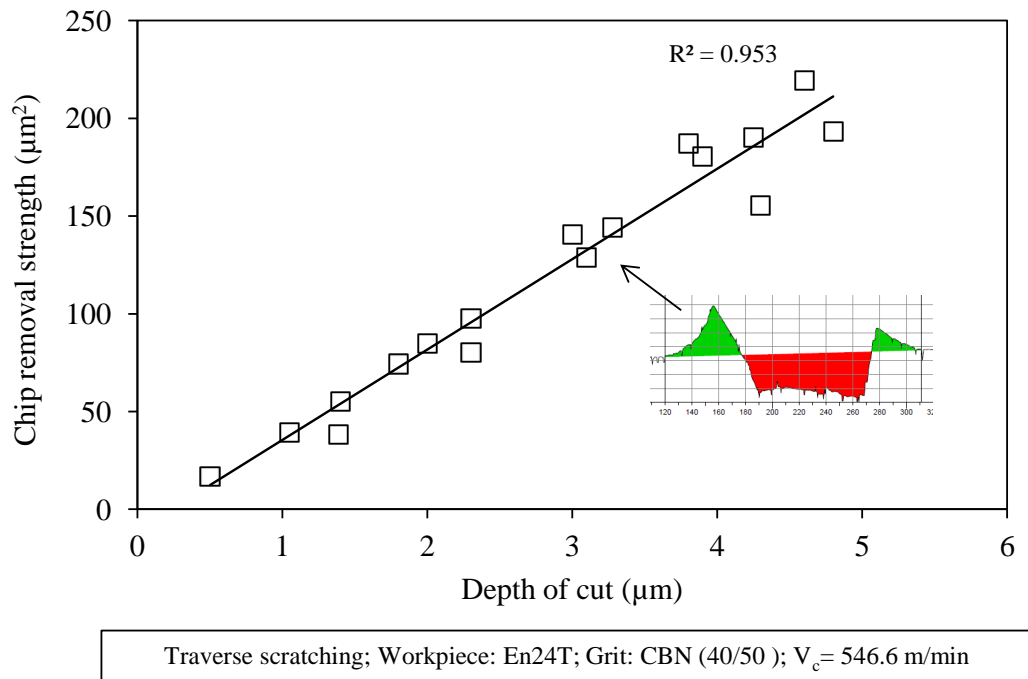


Figure 6.3 Chip removal strength versus depth of cut (flat cutting edge)

However, when the grit had a relatively sharper cutting edge, material removal behaviour as shown in Figure 6.4 to Figure 6.6 was quite the reverse to the results shown in Figure 6.1 to Figure 6.3.

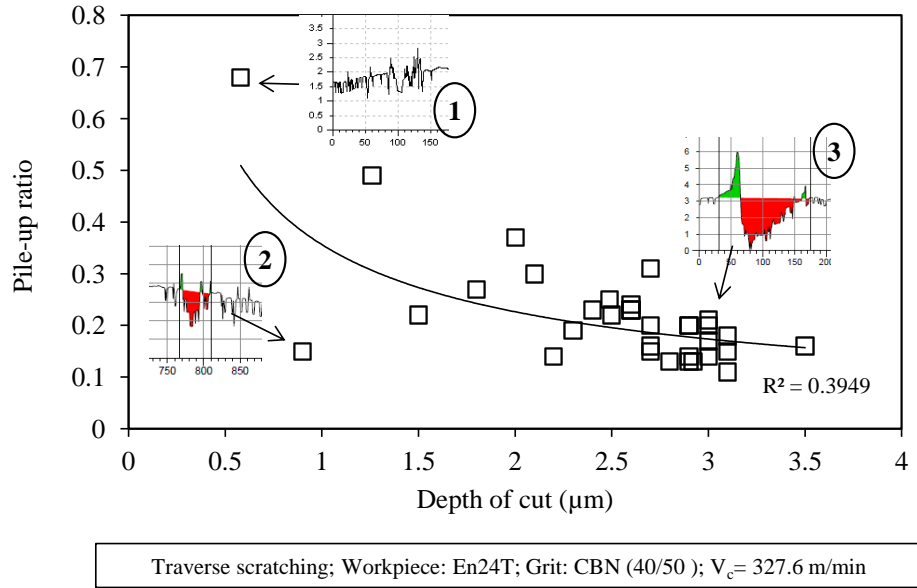


Figure 6.4 Variation of pile-up ratio with depth of cut (sharp cutting edge)

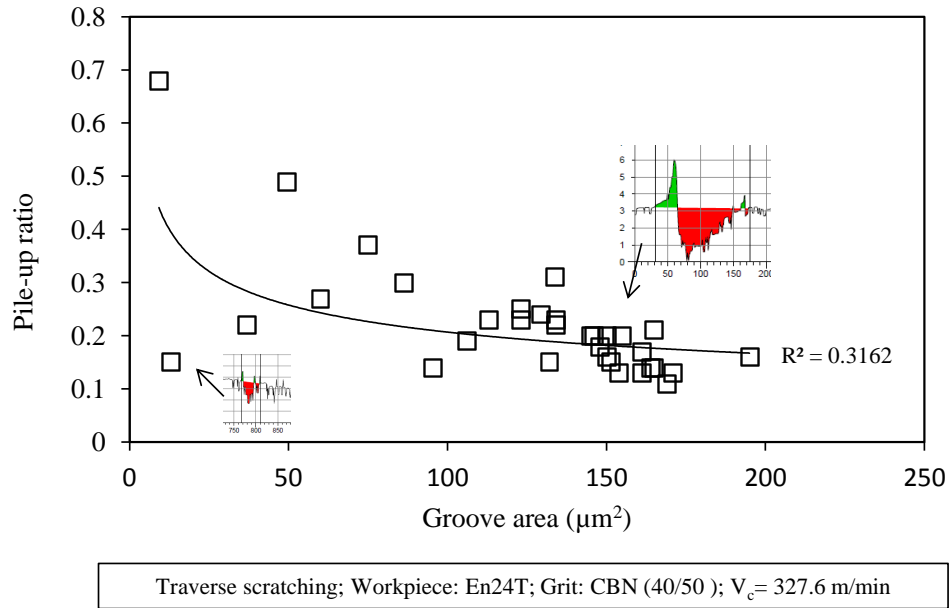


Figure 6.5 Variation of pile-up ratio with groove area (sharp cutting edge)

With a sharp cutting edge, pile-up ratio decreases with increasing depth of cut and groove area as shown in Figure 6.4 and Figure 6.5, respectively. Although data for the pile-up ratio might seem very scattered for smaller depths of cut this phenomenon is common and due to the difficulty of measurement under those circumstances. The scatter at shallow depths of cut could demonstrate that the material removal mechanism may vary between ploughing and cutting.

The grinding process is extremely dynamic and influenced by many parameters. Although cutting speed, material and table speed remained constant for the scratches in Figure 6.4 to Figure 6.6, dynamic parameters such as grit cutting edge shape, cutting edge sharpness and workpiece surface flatness changed throughout the process. The scratch profile marked as **1** in Figure 6.4 has a depth of cut of about 0.6 μm and the workpiece surface appears inclined upwards resulting in a high pile-up ratio. Scratch profile marked **2** in Figure 6.4 has a depth of cut of about 0.9 μm and the workpiece surface is inclined downwards which results in low pile-up ratio. Scratch profile marked as **3** in Figure 6.4 has a greater depth of cut, roughly 3 μm , and the workpiece surface looks flatter than for either scratch-1 or scratch-2, and the pile-up ratio is relatively low. From this comparison, it can be concluded that the pile-up ratio is dependent on interaction angle between grit cutting edge and workpiece surface. This interaction angle is directly dependent on workpiece surface flatness and direction of surface inclination. This relation between grit shape and workpiece surface flatness has never been mentioned in earlier research even though the influence of grit orientation on grinding mechanism was studied by e.g. Matsuo et al, (1989) and Ohbuchi and Obikawa, (2006).

Another reason for the scatter observed in the pile-up ratio could be due to measurement error of pile-up area and/or groove area. It is quite difficult to measure these quantities for scratches where the depth of cut is of the same scale as the original surface roughness. For such a

situation, the definition of pile-up ratio may not be appropriate; this will be a topic for future study.

Figure 6.6 shows that the rate of increase of chip removal strength increases with increasing depth of cut (parabolic curve), in contrast to Figure 6.3 where the chip removal strength increases linearly with depth of cut. The cutting edge of the grit was sharper for Figure 6.6 causing greater material removal with increasing depth of cut compared to the flat grit cutting edge for Figure 6.3. Thus, it can be inferred that chip removal strength is dependent on the grit cutting edge shape (including sharpness and bluntness).

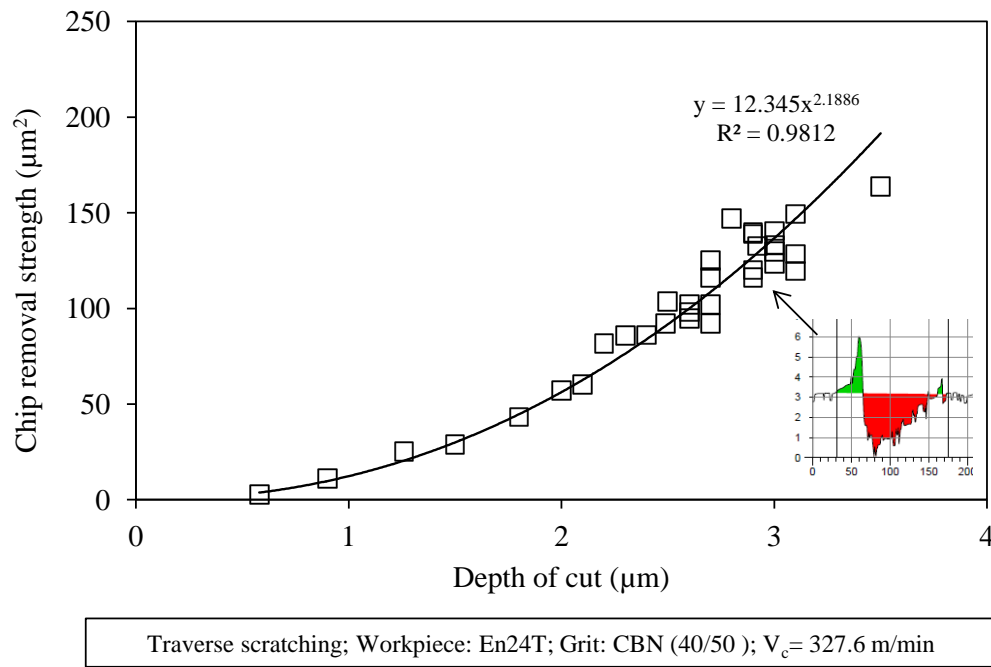


Figure 6.6 Chip removal strength versus depth of cut (sharp cutting edge)

A microscopic picture of the scratches from single cutting edges and multiple cutting edges in the same test is shown in Figure 6.7. Scratch form shape evaluation, i.e. change in grit cutting shape due to grit wear, for single edge and multiple edge scratches is shown in

Figure 6.8. During scratching, a single edge grit can suddenly start to produce multiple edge scratches which can look like separate scratches due to the distance between them, or they can be so close that their pile-up material overlaps. Multiple cutting edges are probably due to a worn single cutting edge breaking into many small cutting edges and these new cutting edges producing multiple scratches.

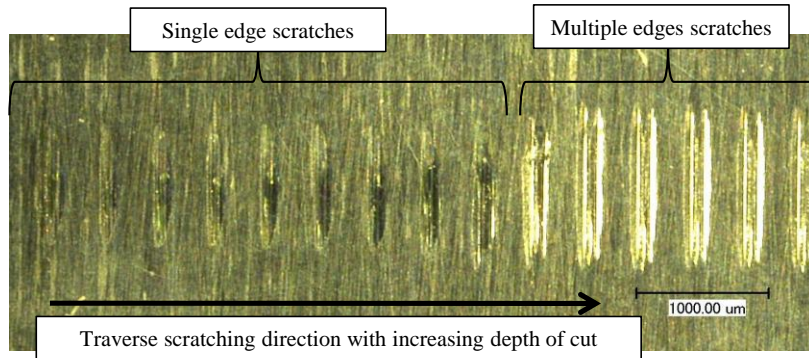


Figure 6.7 Scratches with two different cutting edges (related to Figure 6.9)

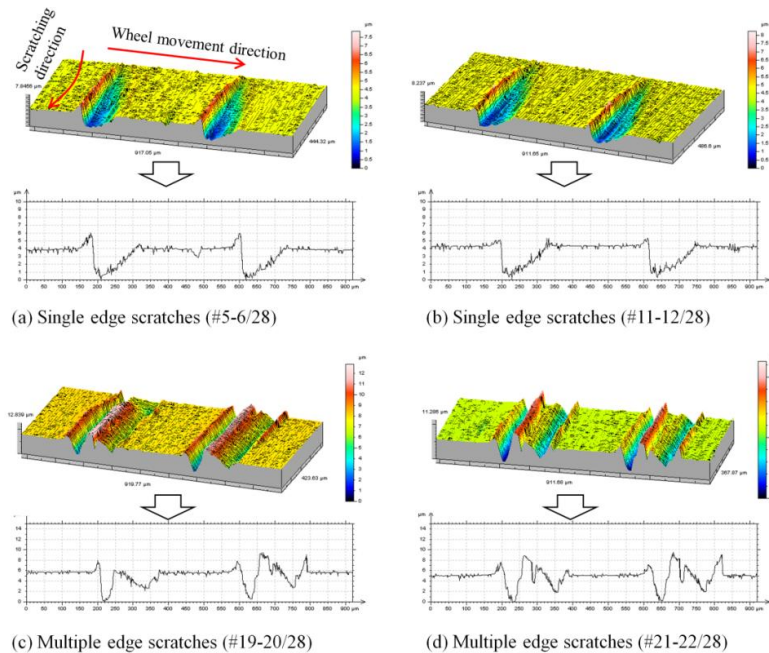


Figure 6.8 Scratch form shape evolution (or grit cutting shape change because of grit wear) in a single grit scratch test (totally 28 scratches)

According to Figure 6.9 the pile-up ratio decreases with increase in depth of cut for both single and multiple edge scratches. However, the pile-up ratio for single edge scratches is obviously less than that of the multiple edges scratches. For instance, for a depth of cut of around 4 μm the pile-up ratio for a single cutting edge scratch is around 0.1, whereas for the multiple cutting edge scratches it is around 0.8, see Figure 6.9.

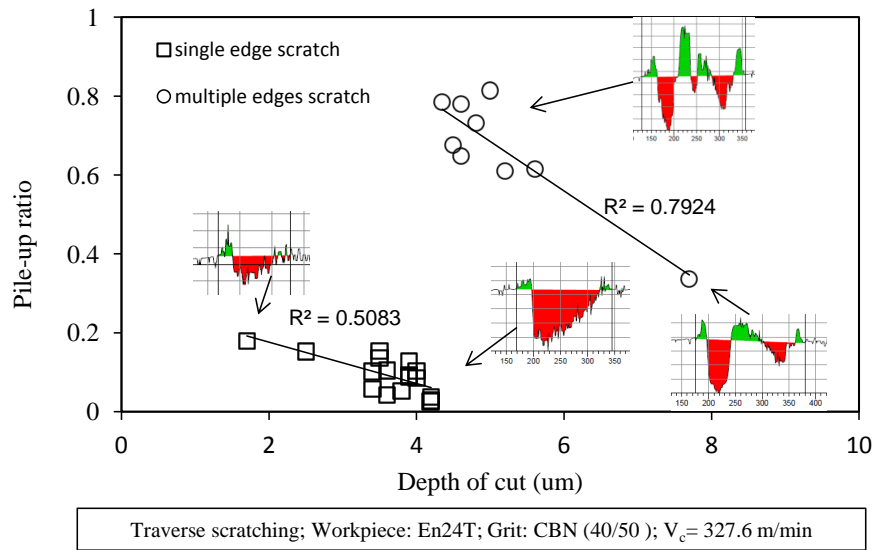


Figure 6.9 Variation in pile-up ratio with depth of cut (two different cutting edges)

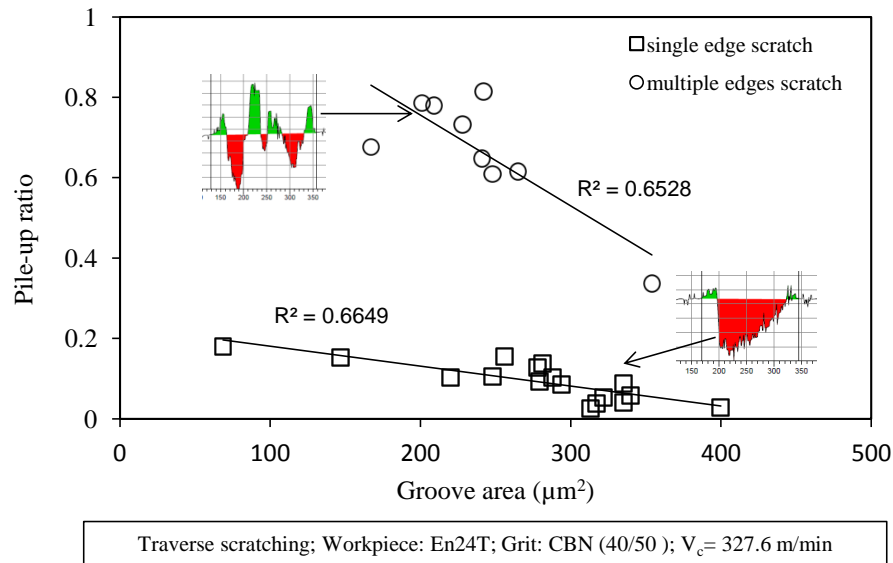


Figure 6.10 Pile-up ratio variation with groove area (two different cutting edges)

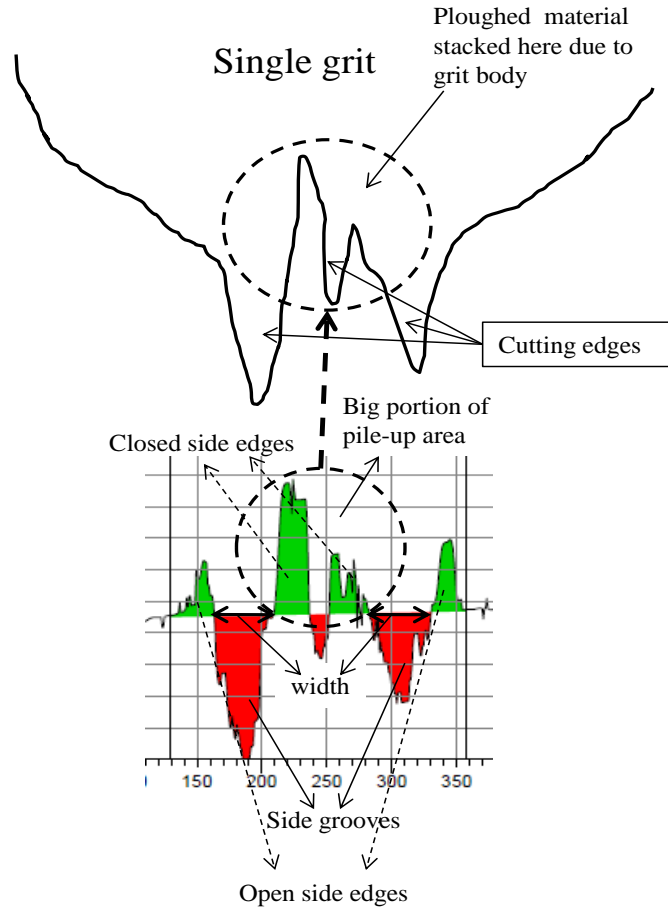


Figure 6.11 Schematic illustration of multiple cutting edges causing high pile-up ratio

The plot of pile-up ratio versus groove area, see Figure 6.10, shows a similar trend to that shown in Figure 6.9. The high pile-up ratio with multiple cutting edge grit can be attributed to individual cutting edge sharpness. With a single grit, multiple edge scratches will each have a smaller cutting edge width than the single edge scratching - these cutting edges may have a similar depth of cut but will be sharper. Considering the profile of multiple edge scratches, Figure 6.11 shows that a large portion of pile-up area can be in the middle of the scratches and cannot be removed as a chip due to the grit body. Material removal in terms of chip formation can only occur at the front of the cutting edges. Therefore, there seems to be two reasons for the

high pile-up ratio with multiple edge scratching: firstly each cutting edge of the grit is sharper due to a smaller width of engagement compared with the whole grit and the secondly material trapped in the middle of the grit will not be removed. Consequently, chip removal strength is lower with multiple cutting edges compared to a single cutting edge as shown in Figure 6.12.

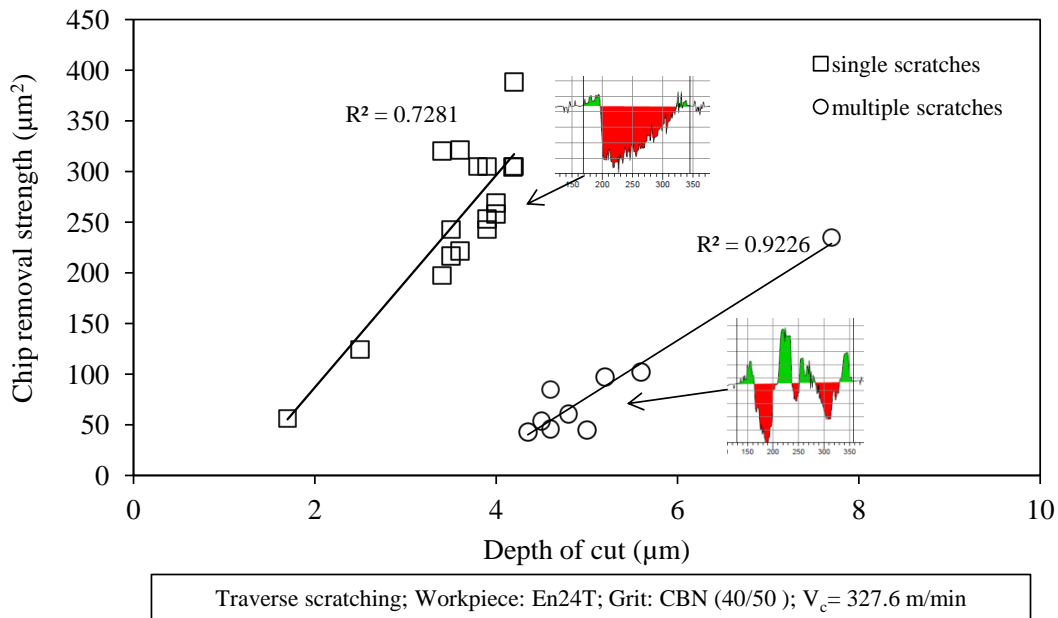


Figure 6.12 Chip removal strength versus depth of cut (two different cutting edges)

Figure 6.13 and Figure 6.14 show variation of pile-up ratio with depth of cut for two different speeds 1000 rpm and 3000 rpm, respectively. The trend for the pile-up ratio is similar to that seen in Figure 6.9, decreasing with increase of depth of cut. Furthermore, the values for the pile-up ratio are within a similar range, for instance for the depth of cut $4 \mu\text{m}$ the pile-up ratio was about 0.6 - 0.7. The one data point for a single edge scratch, shown in Figure 6.13, for a $0.5 \mu\text{m}$ depth of cut has high value of the pile-up ratio (>1.2) because of the very small depth of cut. For the deeper cuts the trend for pile-up ratio to decrease with depth of cut can be assumed linear within acceptable limits, but this assumption cannot be applied to depths of cut less than $1 \mu\text{m}$.

This variation in trend line will be better demonstrated in the forthcoming section of pile-up ratio variation with the Inconel 718 workpiece. Figure 6.15 shows variation of pile-up ratio with groove area, and a similar trend is seen as for Figure 6.14 (pile-up ratio versus depth of cut).

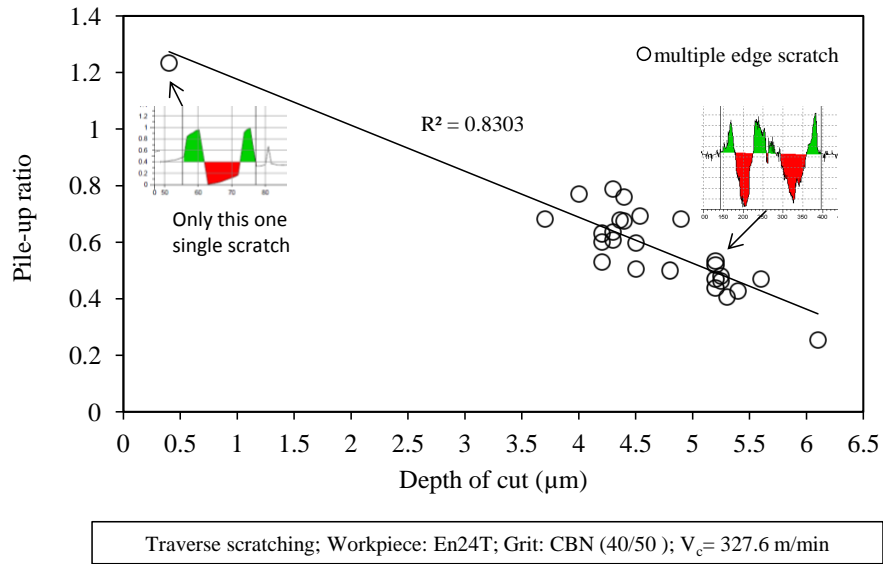


Figure 6.13 Variation in pile-up ratio with depth of cut (multiple cutting edges) at V_c= 327.6 m/min

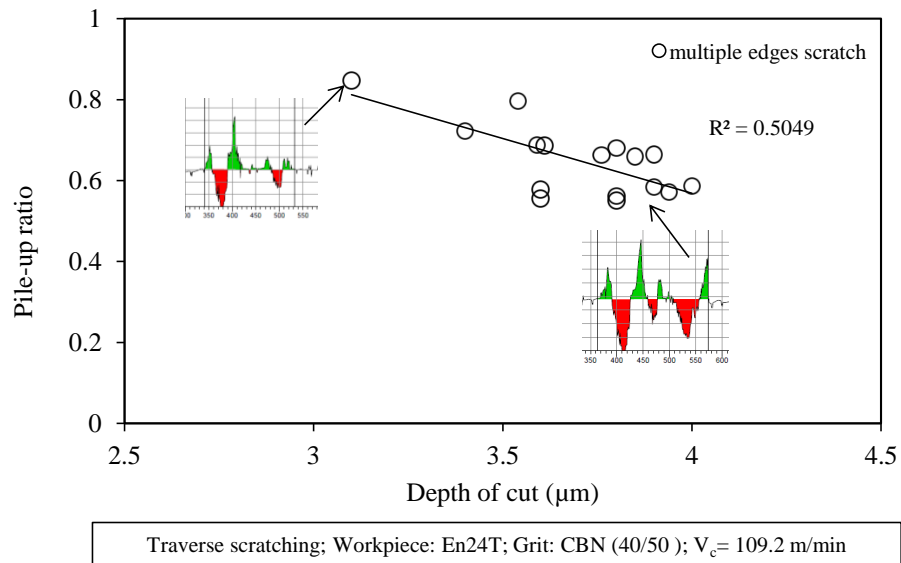


Figure 6.14 Variation in pile-up ratio with depth of cut (multiple cutting edges) at V_c=109.2 m/min

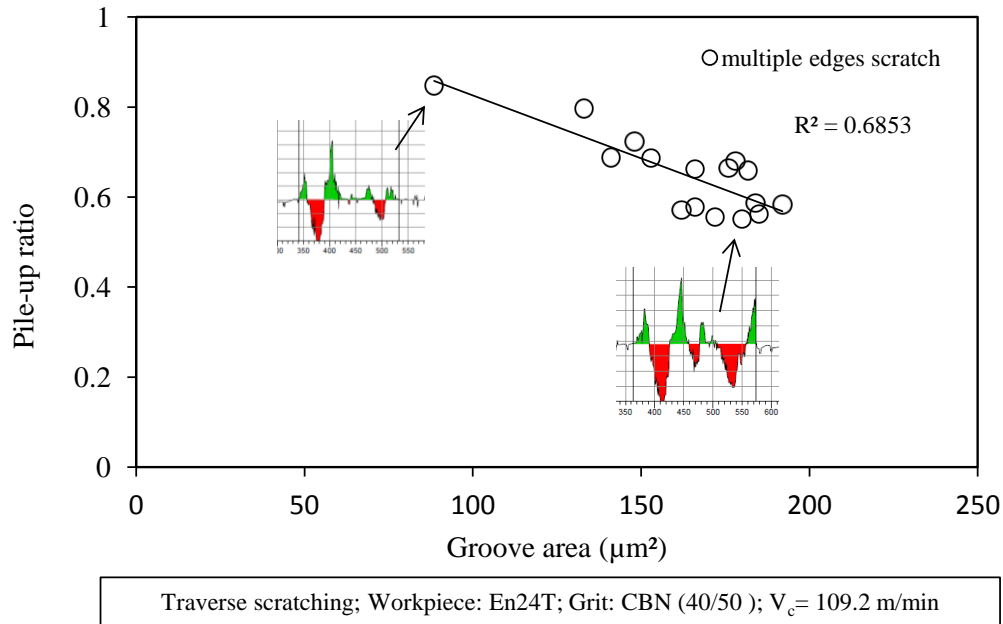


Figure 6.15 Variation in pile-up ratio with groove area (multiple cutting edges) at $V_c= 109.2$ m/min

6.2.2 Inconel alloy 718

The variation of pile-up ratio with depth of cut and groove area is well demonstrated with the Inconel 718 workpiece because experimental tests with multiple scratches ranged from a shallow depth of cut, around $0.5 \mu\text{m}$ to $6 \mu\text{m}$. Figure 6.16 shows the pile-up ratio against depth of cut. The graph shows that for depth of cut less than $1.5 \mu\text{m}$ there is steep decrease in pile-up ratio as the depth of cut increased. At depths of cut greater than about $1.5 \mu\text{m}$ the trend has a much shallower gradient but pile-up continues to decrease with depth of cut. The trend for pile-up ratio versus groove area, Figure 6.17 is similar.

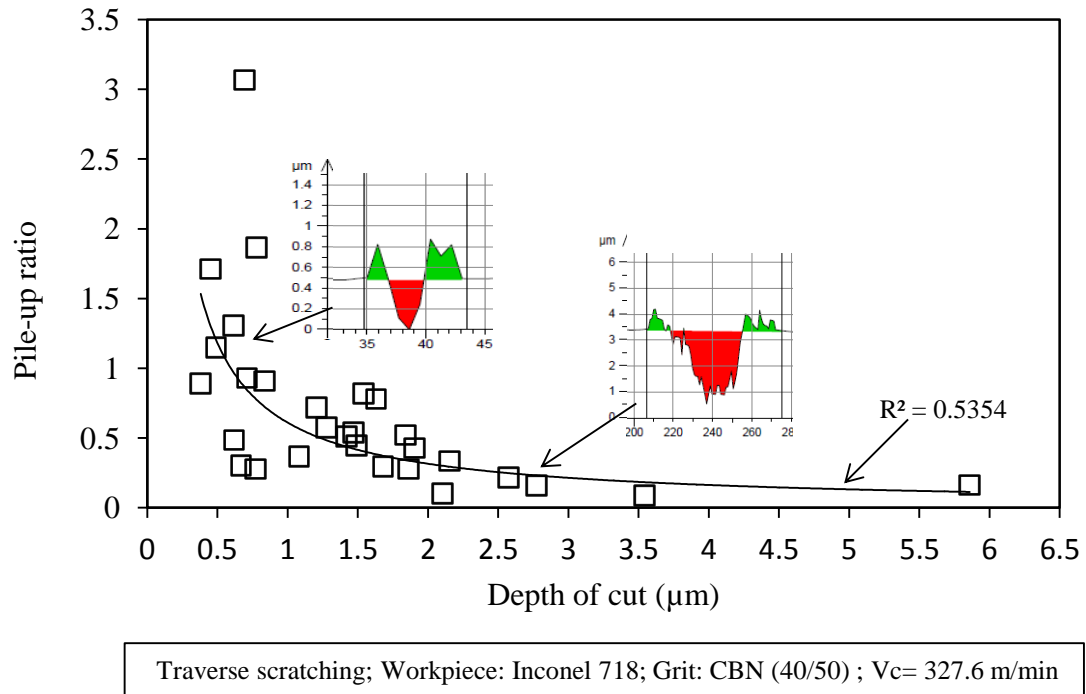


Figure 6.16 Pile-up ratio variation with depth of cut (Inconel 718 workpiece)

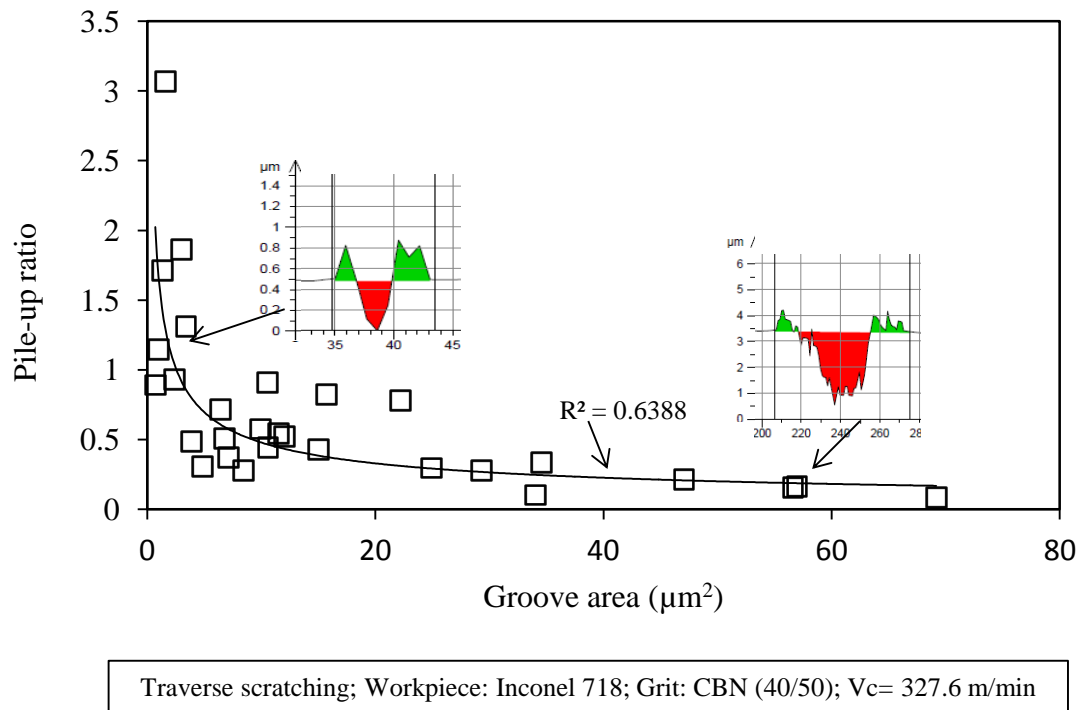


Figure 6.17 Pile-up ratio variation with groove area (Inconel 718 workpiece)

Figure 6.18 shows variation in chip removal strength with depth of cut using the same data set as in Figure 6.16. According to Figure 6.18, a transition point is obtained at around 1.5 μm depth of cut. Up to the transition point, the trend line which shows the chip removal strength against depth of cut has a lower gradient than when the depth of cut is greater than 1.5 μm . Up to the transition point the increase in chip removal strength could be attributed to the ploughing mechanism, but a depth of cut greater than 1.5 μm results in higher chip removal so the cutting action is more prominent in this region. The negative values in Figure 6.18 represent the scratch section where the pile-up ratio is higher than 1 due to efficient ploughing and material accumulation with advancement of grit body. The transition point is not as clear with pile-up ratio as it is with chip removal strength because with the pile-up ratio the data is more scattered. However, it is not easy to obtain the transition point for every set of measurements; the measured data set must include as wide a range of depth of cut as possible. In Figure 6.18, depth of cut varies from 0.5 μm to 3.5 μm and a sufficient number of measurements was taken to obtain the transition point for the chip removal trend line. This range of measurements was not available for every measurement set in the preceding or later sections.

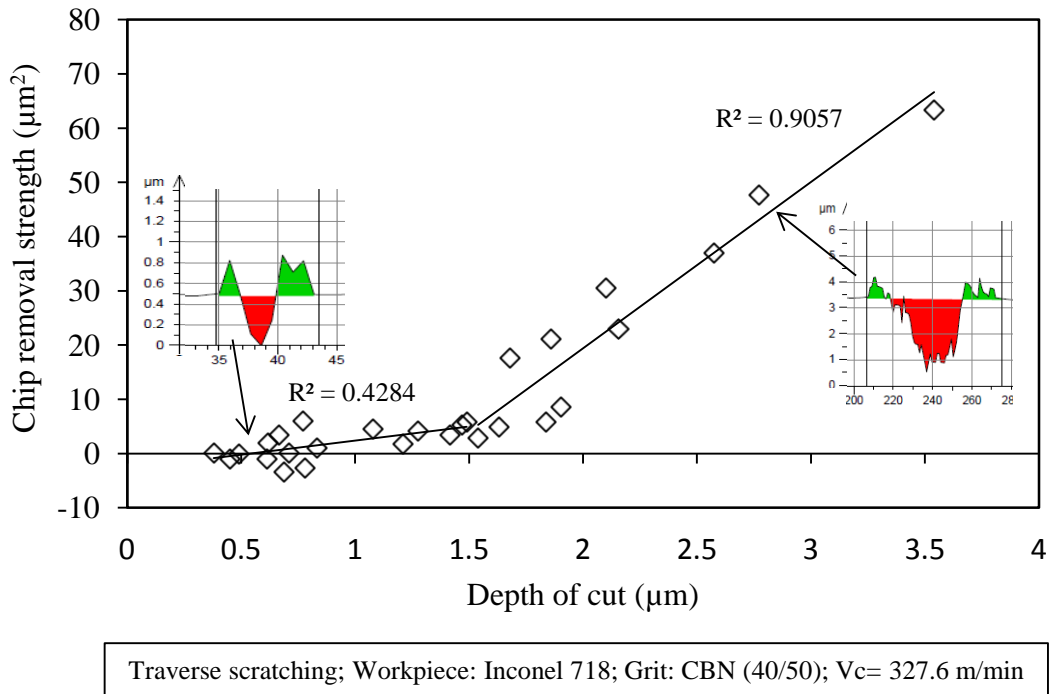


Figure 6.18 Chip removal strength versus depth of cut (Inconel 718 workpiece)

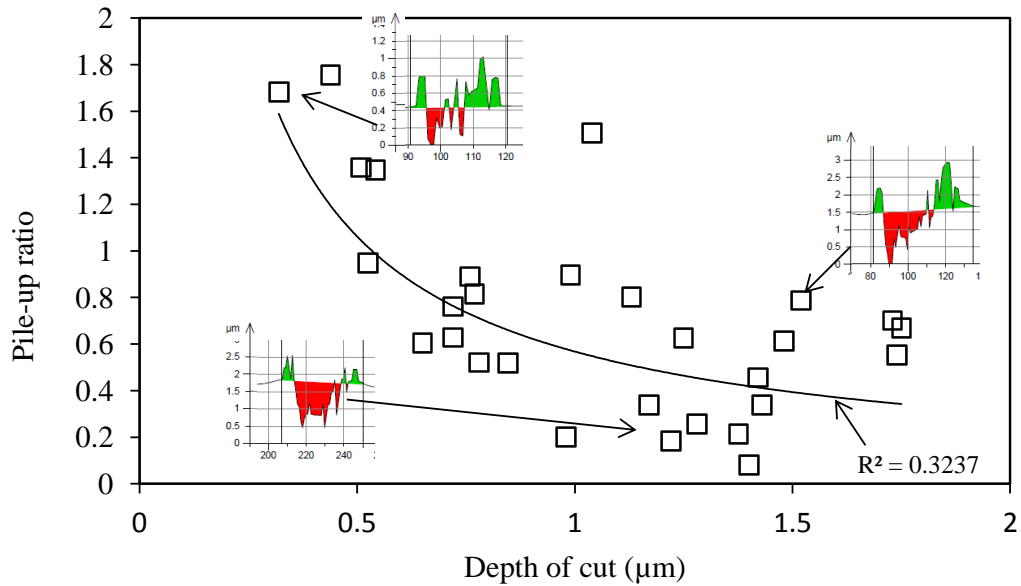
It should be pointed out that the pile-up ratio can have a value larger than unity when the depth of cut is very small (e.g. $< \mu\text{m}$) as shown in Figure 6.16, this can be attributed to three reasons. The first one is a less efficient cutting mechanism at small depth of cut with material ploughing more prominent. The second one could be the position of the cross-sectional scratch profile; it was attempted to consistently take the cross-section from the middle of the scratch path (because pile-up ratio is highly dependent on where along the scratch path the cross-section profile is extracted) but this was not always possible (this will be explained in Section 6.2.4). The third reason is material accumulation with the advance of the grit. A single grit starts to push ploughed material forward in the direction of the scratch path and when the cutting is not efficient during this process the pile-up ratio become larger than unity. Here, the larger pile-up ratio cannot be attributed not only to the smaller depth of cut but also to the position of the cross-

section profile along the scratch path and material accumulation ahead of the grit along the scratch path.

Figure 6.19 and Figure 6.20 show the variation in pile-up ratio with depth of cut and groove area, respectively. Grit has two cutting edges at every interaction but the measurements are not done separately. The trend line look generally similar to previous graphs, but the pile-up ratio looks to be highly scattered – this is due to the generation of two separate scratches at each grit-workpiece interaction. In Figure 6.19, at a depth of cut of about 1.5 μm it can be seen that the scratch profile above the trend line is sharper than the one below the trend line. This different behaviour of cutting edges can be explained by the influence of cutting edge sharpness (or bluntness) on material removal.

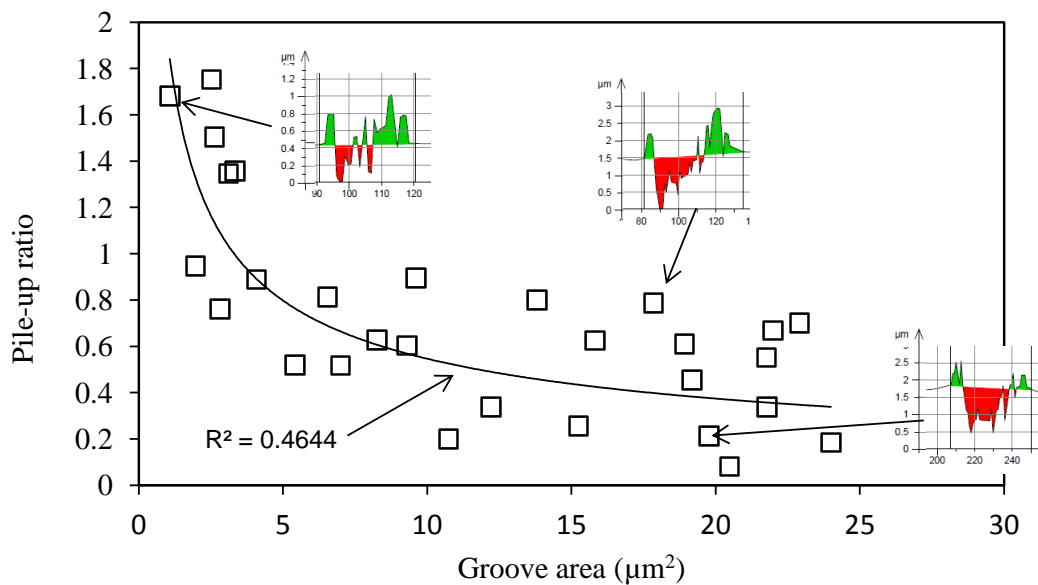
Figure 6.21 and Figure 6.22 show the variation of pile-up ratio with depth of cut and groove area, respectively; with rotational speed of 2000 rpm (or $V_c = 218.4$ m/min). Multiple cutting edges interact with the workpiece at every pass of the grit. So, two separate grooves were formed at each pass. The first cutting edge was sharper while the second one less sharp. The sharper cutting edge has a narrower width compared to the blunter, as shown in the right side of Figure 6.21 and Figure 6.22. Thus, the sharper the grit cutting edge (narrower the width) the higher the pile-up ratio while wider the cutting edges (blunter) results in a lower pile-up ratio.

Although the cutting speed was different during each set of single grit experiments, see Figure 6.16, Figure 6.19 and Figure 6.21, grit cutting edge shape was much more influential in material removal than the cutting speed. Thus, cutting speed effect on material removal is not discussed in these experiments.



Traverse scratching; Workpiece: Inconel 718; Grit: CBN (40/50 mesh), $V_c = 10.8$ m/min

Figure 6.19 Pile-up ratio versus depth of cut (two scratches at every grit-workpiece interaction: one placed above the trend line acts sharper; another one placed below the trend line acts blunt)



Traverse scratching; Workpiece: Inconel 718; Grit: CBN (40/50 mesh), $V_c = 10.8$ m/min

Figure 6.20 Pile-up ratio versus groove area (two scratches at every grit-workpiece interaction: one placed above the trend line acts sharper; another one placed below the trend line acts blunt)

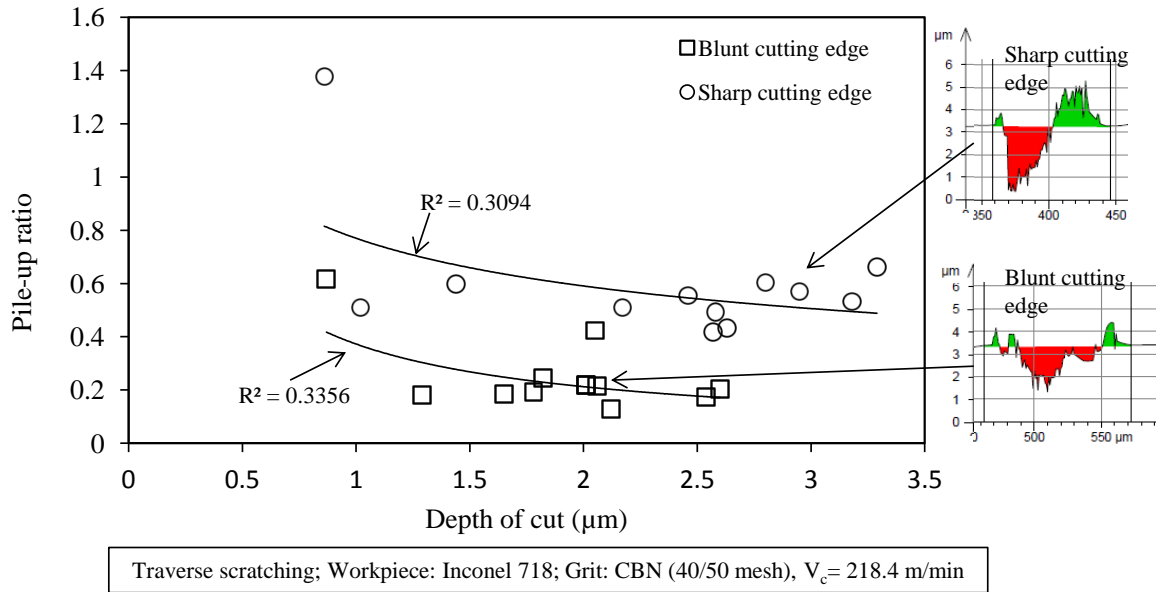


Figure 6.21 Pile-up ratio versus depth of cut (two scratches at every grit-workpiece interaction)

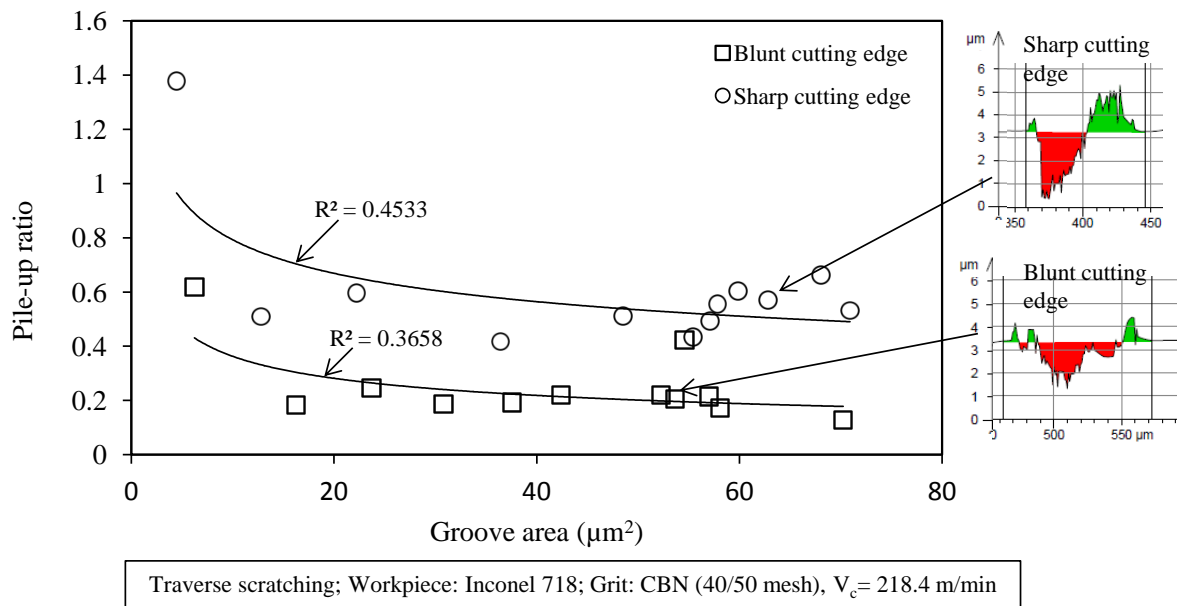


Figure 6.22 Pile-up ratio versus groove area (two scratches at every grit-workpiece interaction)

6.2.3 En8 steel

The single grit scratching test was also performed on En8 steel which has a lower hardness value (222.2 HV) than En24T steel (289.2 HV) or Inconel 718 (355 HV) because the material removal mechanism might show some alterations in terms of pile-up ratio or chip removal strength. Figure 6.23 and Figure 6.24 show variations in pile-up ratio with depth of cut and groove area, respectively. The less the depth of cut or groove area the higher the pile-up ratio. Figure 6.25 shows chip removal strength with respect to depth of cut, and a transition point can be seen at about 2.5 μm depth compared to the 1.5 μm for Inconel. Up to 2.5 μm depth, chip removal strength increases slowly with depth of cut, but when the depth of cut increases beyond the 2.5 μm , the chip removal strength increases rapidly with depth of cut. This means that after certain depth of cut, the chip removal mechanism becomes more influential than the ploughing mechanism.

Although the pile-up ratio trend with En8 steel is similar to those of En24T steel and Inconel 718, the magnitude of the pile-up ratio is greater for En8 than either En24T or Inconel 718 at similar depths of cut. For instance, at 2 μm depth of cut the pile-up ratio is around unity (0.8-1) for the En8 steel (Figure 6.23), but was measured at around 0.3 for En24T (Figure 6.4) and 0.2-0.3 for Inconel 718 (Figure 6.16). Thus, it can be claimed that softer material increases the tendency to obtain a higher pile-up ratio compared to harder material. But, the change in pile-up ratio is not only influenced by material properties or hardness but is also influenced by grit cutting edge shapes (sharpness or bluntness). So, the higher pile-up ratio found with En8 steel cannot be totally attributed to the material's lower hardness. The grit cutting edge used to scratch the En8 steel was much sharper than those used for the En24T and Inconel, and the influence of a sharper cutting edge pile-up ratio has already been mentioned in earlier sections. Thus, high

pile-up ratios are influenced by both grit cutting edge sharpness and material properties but the relative contribution of each factor could not be estimated from these experiments.

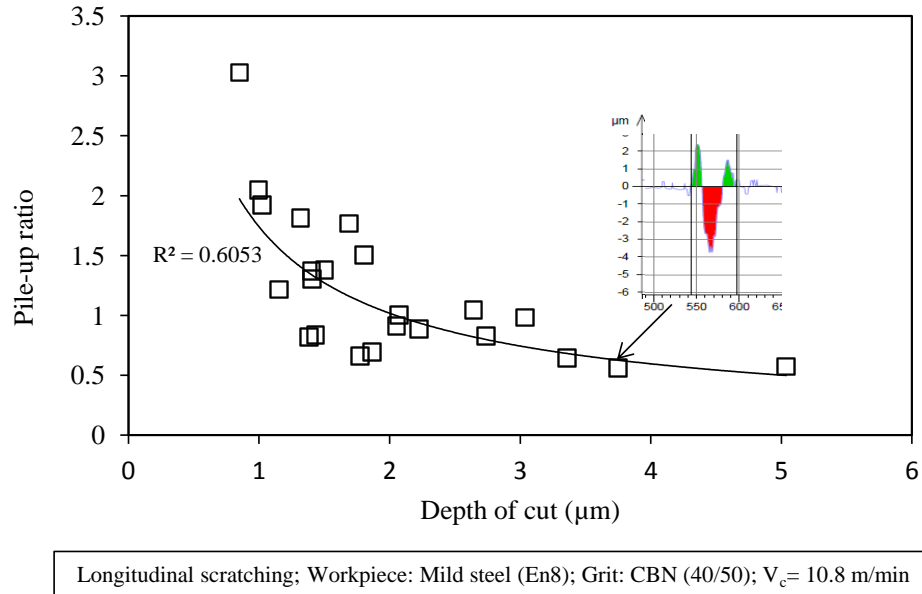


Figure 6.23 Pile-up ratio versus depth of cut (single edge scratches on En8 steel)

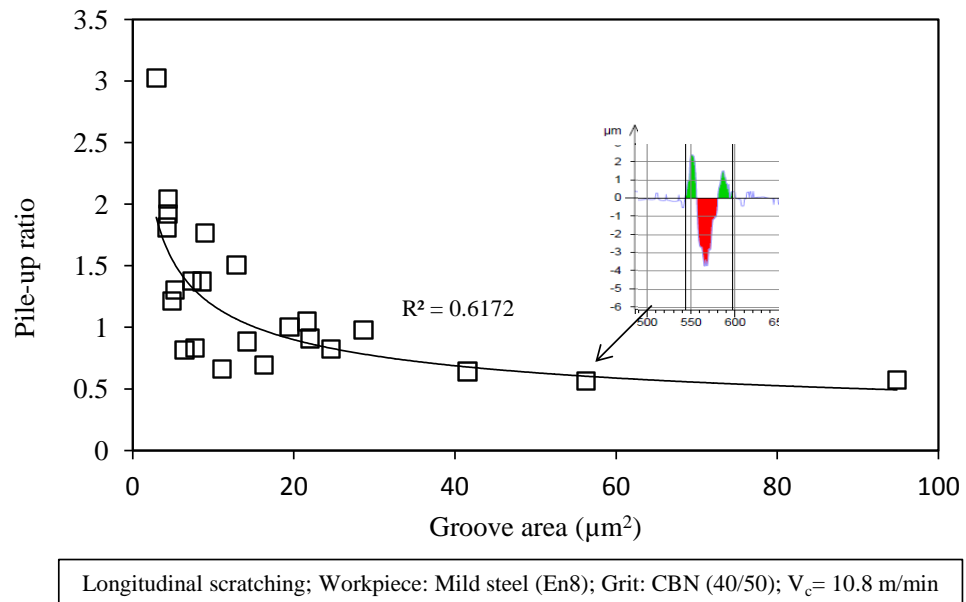


Figure 6.24 Pile-up ratio versus groove area (single edge scratches on En8 steel)

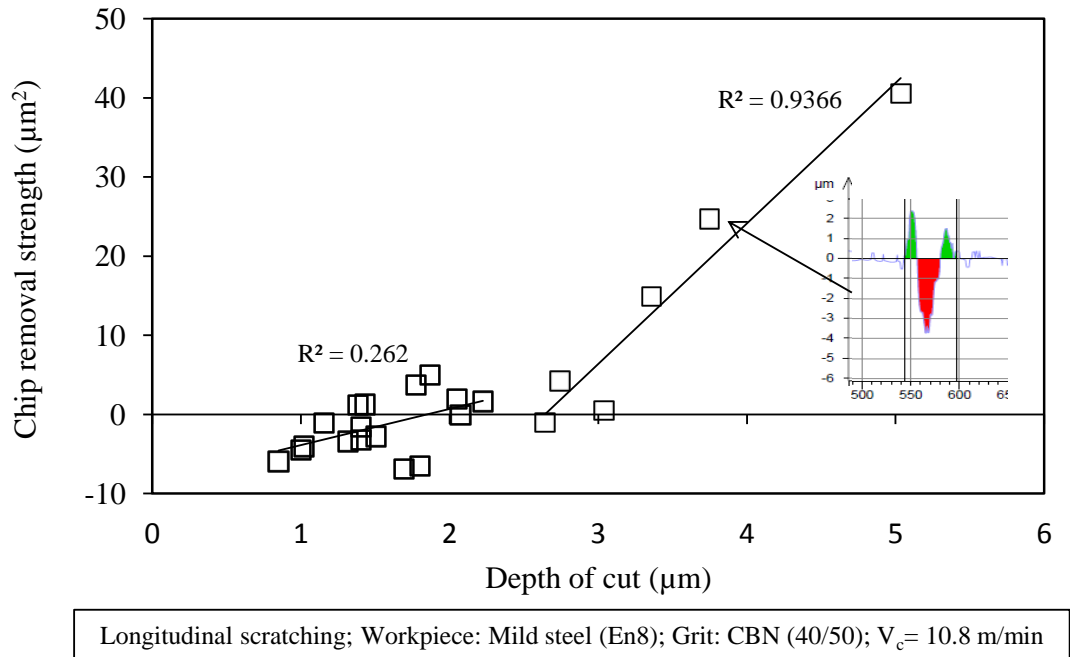


Figure 6.25 Chip removal strength versus depth of cut (single edge scratches on En8 steel)

6.2.4 Material removal mechanism along a single scratch path

In preceding sections, the material removal mechanism regarding pile-up ratio and chip removal strength has been investigated from the cross-sectional profile of the numerous scratches at the deepest point (generally found in the middle of the scratch). That investigation did not represent the material removal mechanism at the early stage of grit penetration into the workpiece or when grit was leaving workpiece in the final stage of scratching, although it did show material removal mechanism variation with respect to depths of cut and groove area. All three phases of the material removal mechanism (rubbing, ploughing and cutting) may not be observed when the investigation is limited to cross-section profiles taken from the middle of scratches, because in the middle of scratches the cutting phenomenon is dominant with some contribution by ploughing. However, the rubbing process is not supposed to occur in that section

of the scratch, rubbing should occur as a dominant factor only in the very initial stage grit-workpiece interaction within very small region and sometimes may not even be observable. Because, the rubbed region is a plastic deformation free region, the elastic deformation is momentary, only at very small depths and is recovered due to the elastic spring back effect when grit moves on to form the scratch.

In this section, the material removal mechanism regarding pile-up ratio and chip removal that takes place along a single scratch was investigated. To do this, cross-section profiles were extracted along the scratch length at approximately 3.23 μm intervals beginning from the initial stage of grit-workpiece interaction until the end of scratch where the grit left the workpiece. Figure 6.26 shows 3D cross-sectional view of a scratch performed on En24T steel. Figure 6.26 (a) demonstrates how pile-up of material at the side of the groove varies for that part of the scratch where the grit leaves the workpiece. The longitudinal sectional profile of the scratch is shown in Figure 6.26 (b) how groove depth and side pile-up vary along the entire length of the scratch.

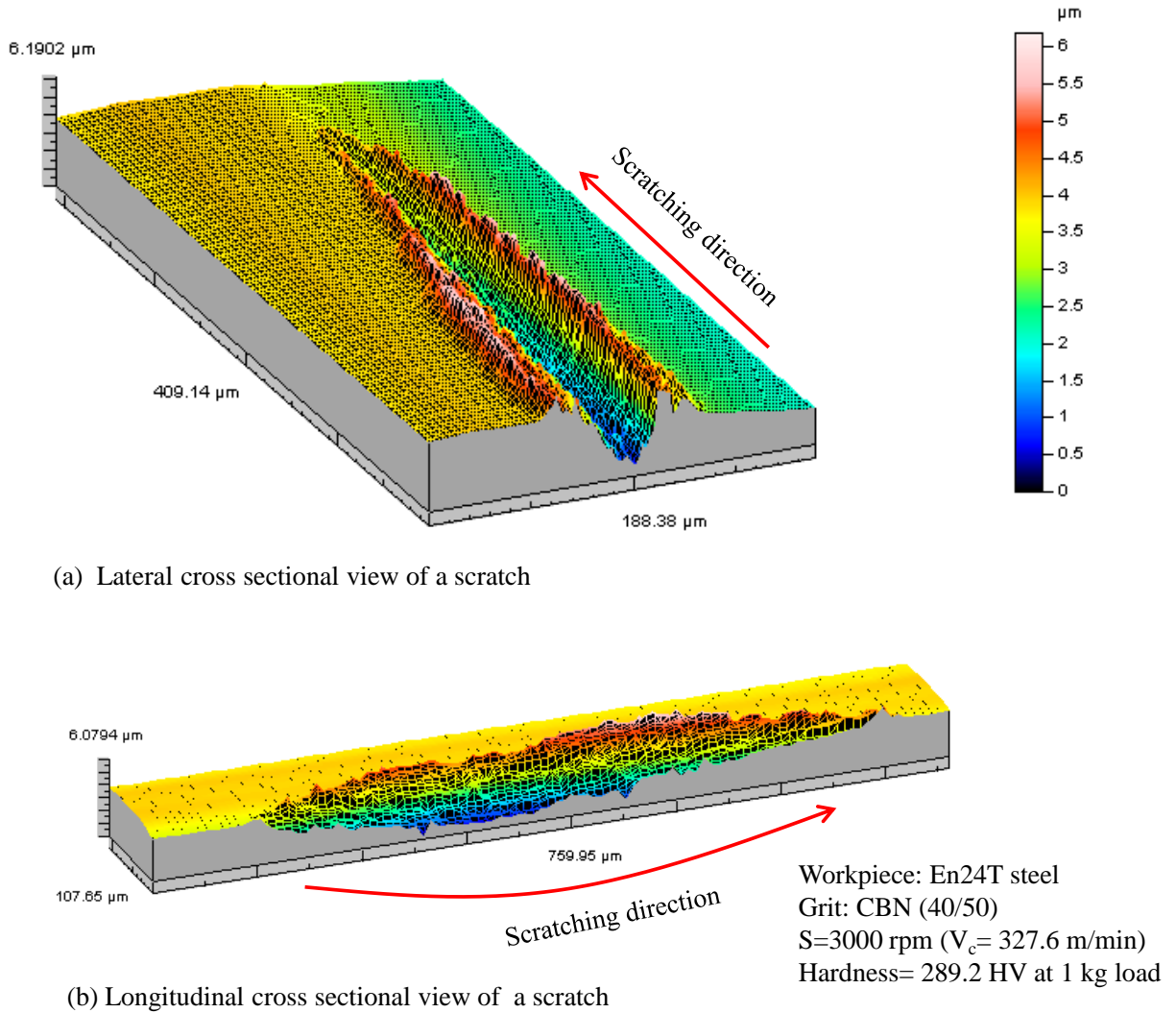


Figure 6.26 3D view of a scratch with (a) lateral cross section, (b) longitudinal cross section

The pile-up ratio variation along the single scratch performed on En24T steel is shown in Figure 6.27, where the point with highest cutting efficiency can be found by looking at the variation of pile-up ratio along the scratch length. In the initial stage of grit-workpiece interaction pile-ratio is relatively high, between 3 and 1, which shows that in that region no cutting occurs and material is swelling up due to plastic deformation. Rubbing action is supposed to occur but was not observable. Pile-up ratio gradually decreased as scratch depth increased

towards the deepest point. The scratch depth then decreased and while the grit is moving towards the end of the scratch, it pushes ploughed material forward and some portion of this material could flow along the two sides of the scratch so that the pile-up ratio increases as long as the grit interacts with workpiece. It is apparent in Figure 6.27, that pile-up ratio at the end of scratch was very high, rising rapidly to between 10 and 30.

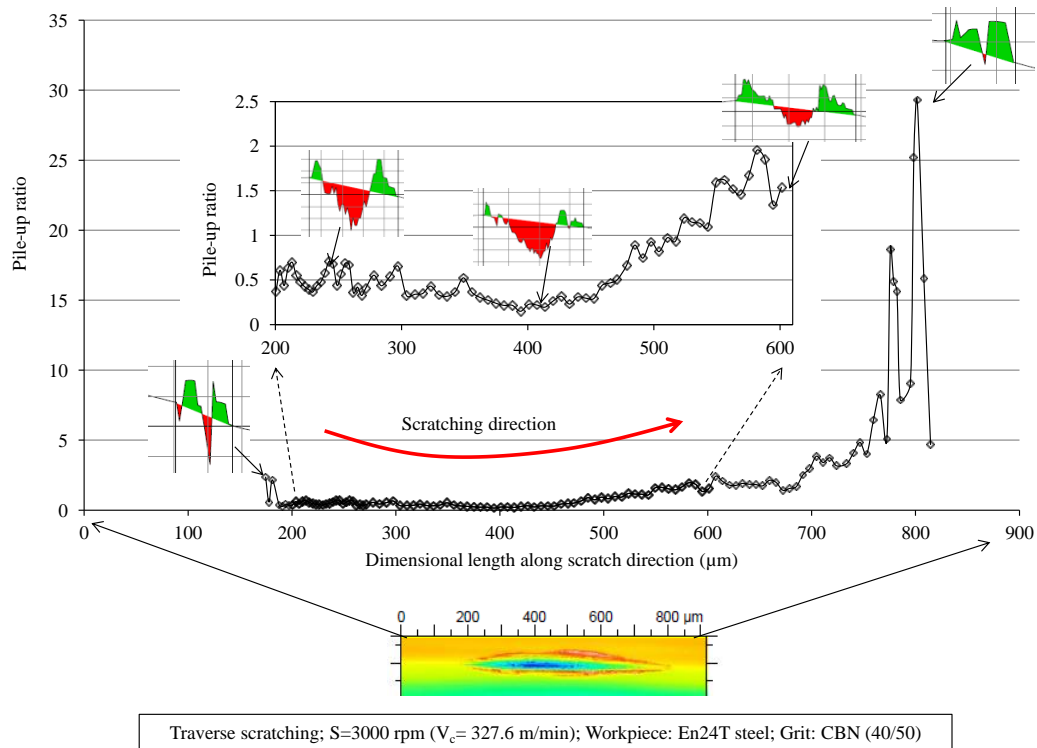


Figure 6.27 Variation of pile-up ratio along a scratch in the longitudinal direction

Figure 6.28 and Figure 6.29 show variation in pile-up ratio and chip removal strength with depth of cut, respectively. A lower pile-up ratio is found at higher depth of cut (Figure 6.28) which is consistent with the previous results. In grinding with low surface finish requirement a small a pile-up ratio as possible is always desired for high efficiency. Maximum chip removal occurs at high depth of cut, negative chip removal indicates accumulated material shifting

towards the end of the scratch. It can be inferred that cutting efficiency decreased rapidly towards the end of the scratch, but was increasing fast at the beginning of scratch until maximum depth was reached.

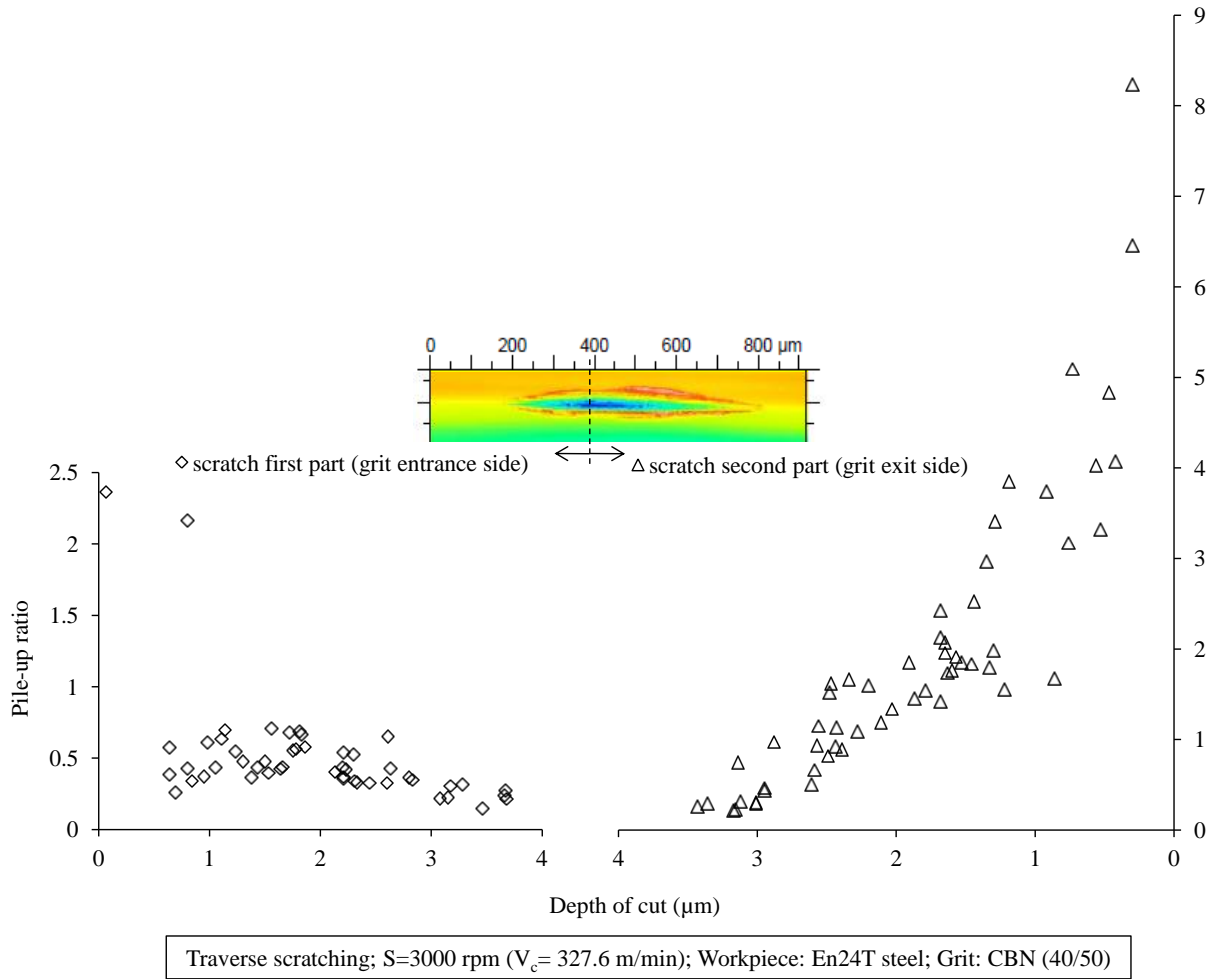


Figure 6.28 Pile-up ratio versus depth of cut along a single scratch

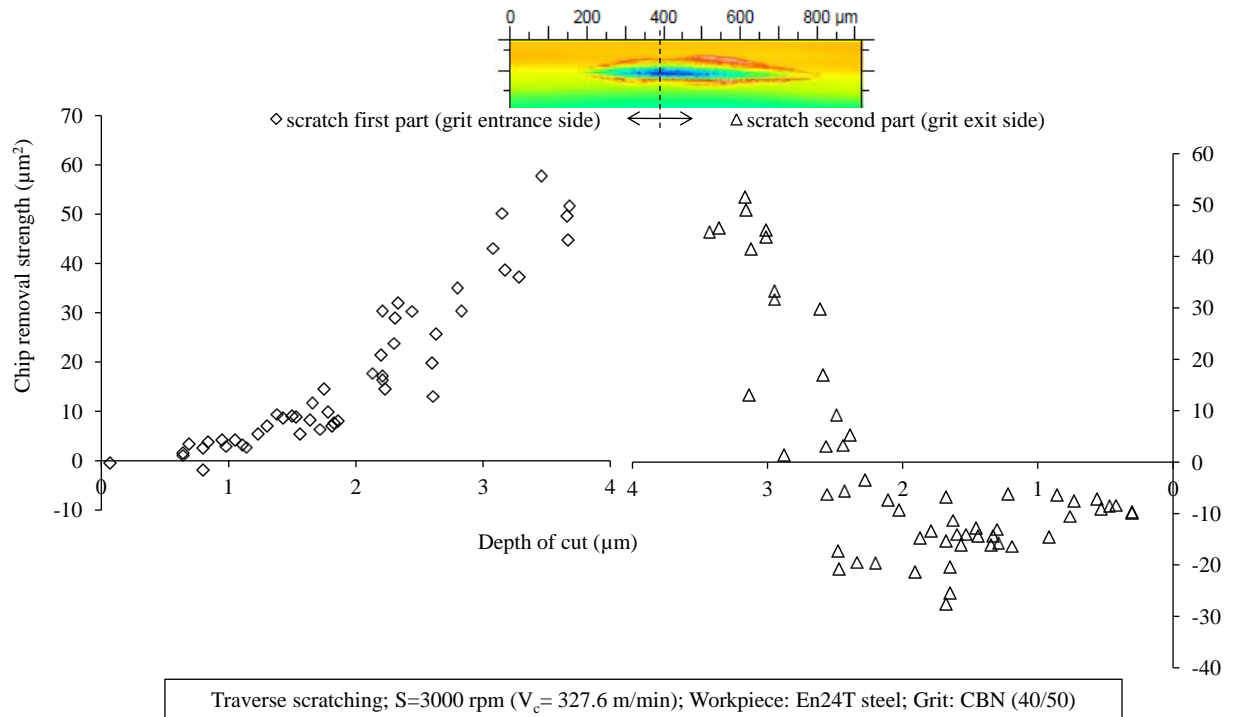
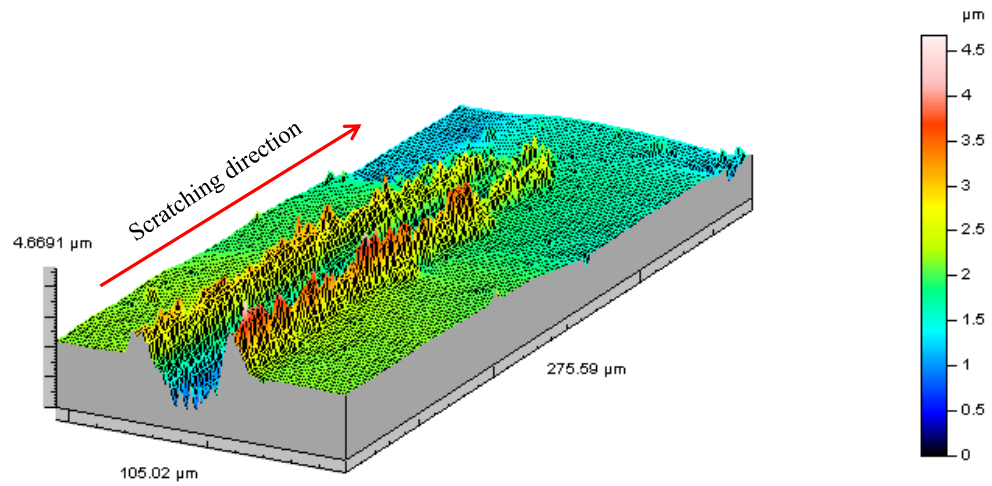
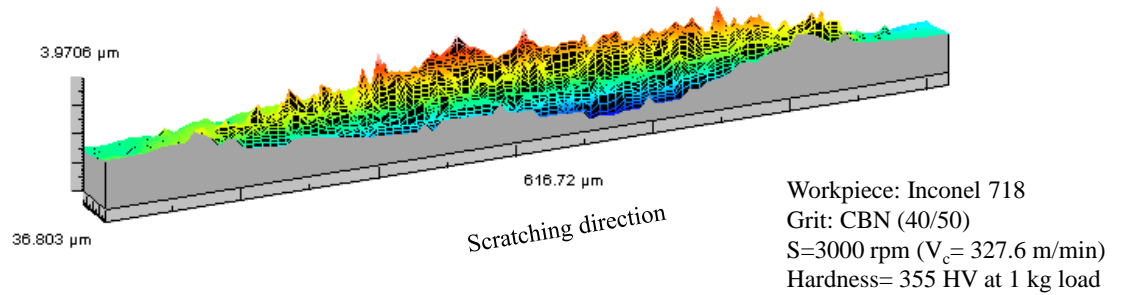


Figure 6.29 Chip removal strength versus depth of cut along a single scratch

The longitudinal and lateral cross-sections along the scratch path on Inconel 718 were also investigated, see Figure 6.30. This scratch was generated under very similar conditions to that for En24T, but it was performed with different CBN grit and shows some differences in cutting edge shape. Figure 6.31 shows variation of pile-up ratio along the length of the scratch beginning from the initial grit-workpiece interaction and continuing to the end of scratch. Similar results are obtained as in the previous test with En24T steel. The pile-up ratio at the initial stage is relatively smaller than that obtained at the end of scratch, as shown in Figure 6.31. Figure 6.32 shows that pile-up ratio decrease with increasing depth of cut.



(a) Lateral cross sectional view of a scratch



(b) Longitudinal cross sectional view of a scratch

Figure 6.30 3D view of single scratch (a) lateral cross-section, (b) longitudinal cross-section

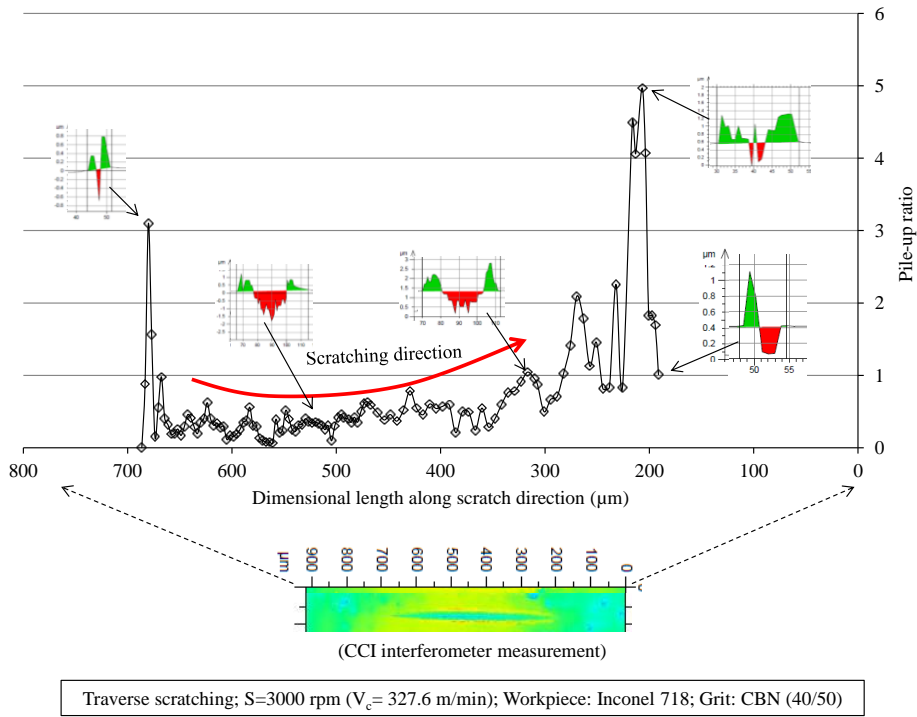


Figure 6.31 Variation of pile-up ratio along scratch length

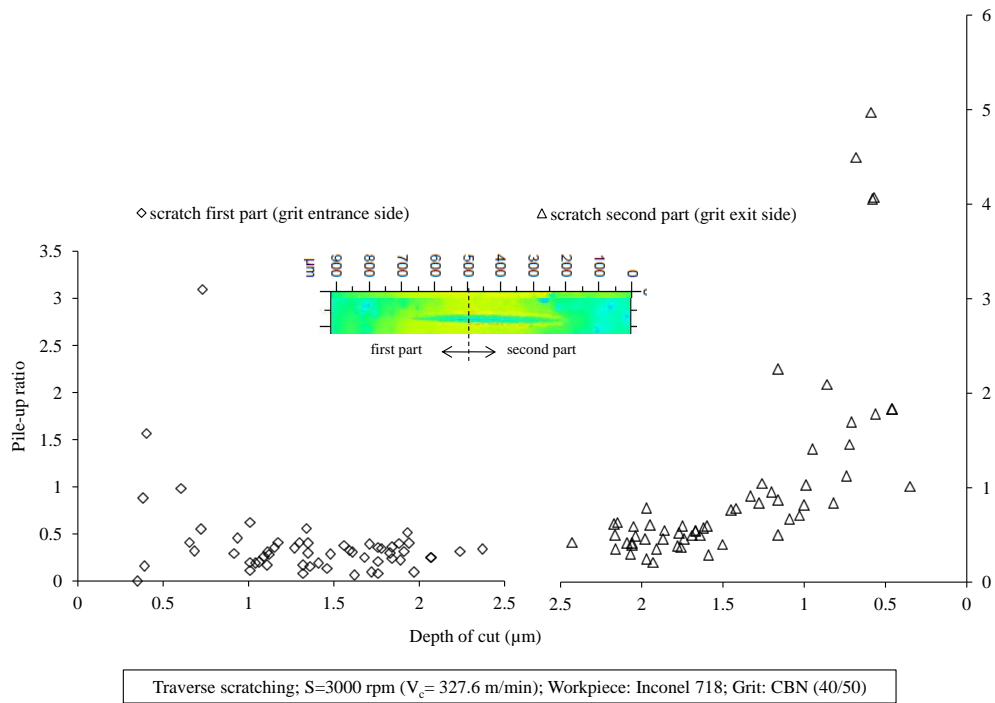


Figure 6.32 Pile-up ratio versus depth of cut along scratch length

Figure 6.33 shows that chip removal reaches its maximum value at the deepest point of the scratch and at the end of scratch negative values show ploughed material rather than chip removal. It is worthwhile to compare the results with pile-up ratios obtained for En24T steel (Figure 6.28) and Inconel 718 (Figure 6.32). The specific range of depth of cut, between 1 μm and 2 μm , in the first part of the scratch in Figure 6.28 (En24T workpiece) and Figure 6.32 (Inconel workpiece), the pile-up ratio is relatively high (around 0.5) for the scratch on the En24T compared to a value of around 0.2 ~ 0.3 for the scratch on the Inconel. The investigation performed by Buttery and Hamed (1977) on the cutting efficiency on materials having different hardness demonstrated that cutting efficiency increases as the hardness of the workpiece increases. Higher cutting efficiency may be interpreted as a lower pile-up ratio, and vice versa. Hence, the results presented in Figure 6.28 and Figure 6.32, a higher pile-up ratio for the scratch on the En24T (hardness 289.2 HV at 1 kg load) than on the Inconel (hardness 355 HV at 1 kg load), might be attributed to relative hardness of the workpiece materials and different strain hardening behaviour of materials during scratching and is consistent with Buttery and Hamed (1977). However, Buttery and Hamed used a diamond indenter and Vickers hardness tester, which is dissimilar to actual grit, because grit has no proper or controlled shape during machining. The scratches obtained in this thesis were performed using actual CBN grit (40/50) whose cutting edge geometry was continuously changing during scratching due to extremely complex wear mechanism. Thus, the lower pile-up ratio found with the Inconel workpiece could be attributed not only to hardness of workpiece material but also to change in grit cutting edge geometry during scratching. The effect of grit cutting edge shape on pile-up ratio was investigated in previous sections, see also Figure 6.21.

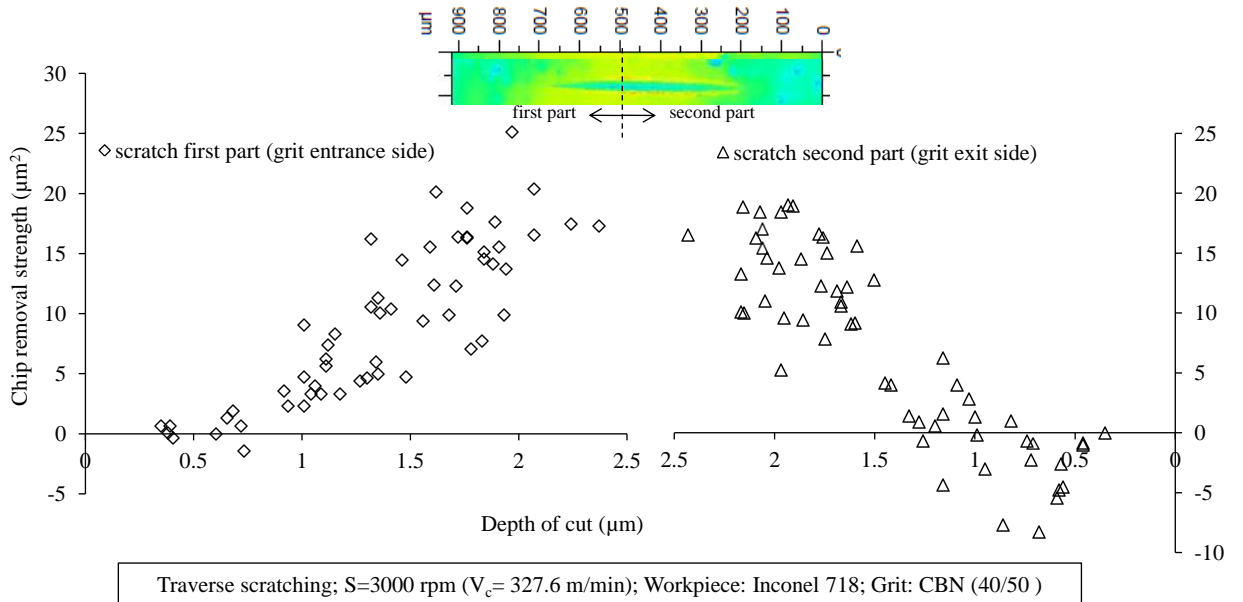


Figure 6.33 Chip removal strength versus depth of cut along scratch path

6.2.5 Effective grit engaging radius

To understand grinding mechanics in terms of contact variation, the effective grit engaging radius (EGER) was used. This assumes the measured cross-sectional profile of a scratch can be represented as an arc of a circle, see Figure 6.34, and the radius of that arc is the EGER –the grit is assumed to have a spherical shape defined by the nominal grit radius engaging with workpiece at the instant of interaction.

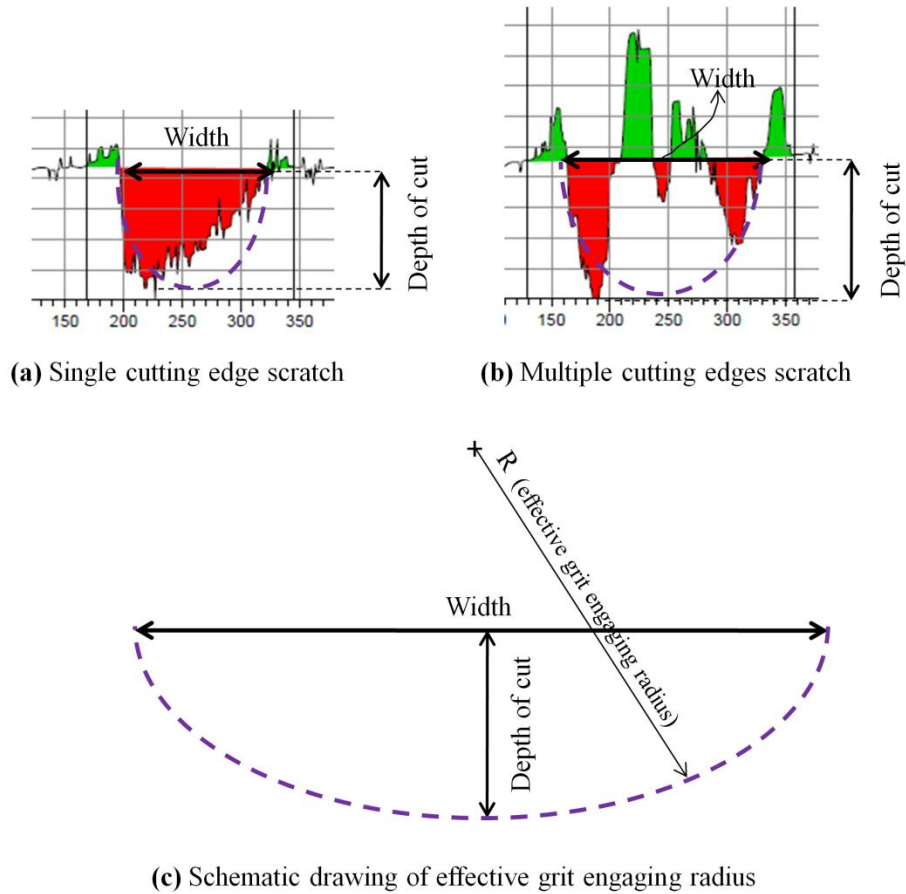
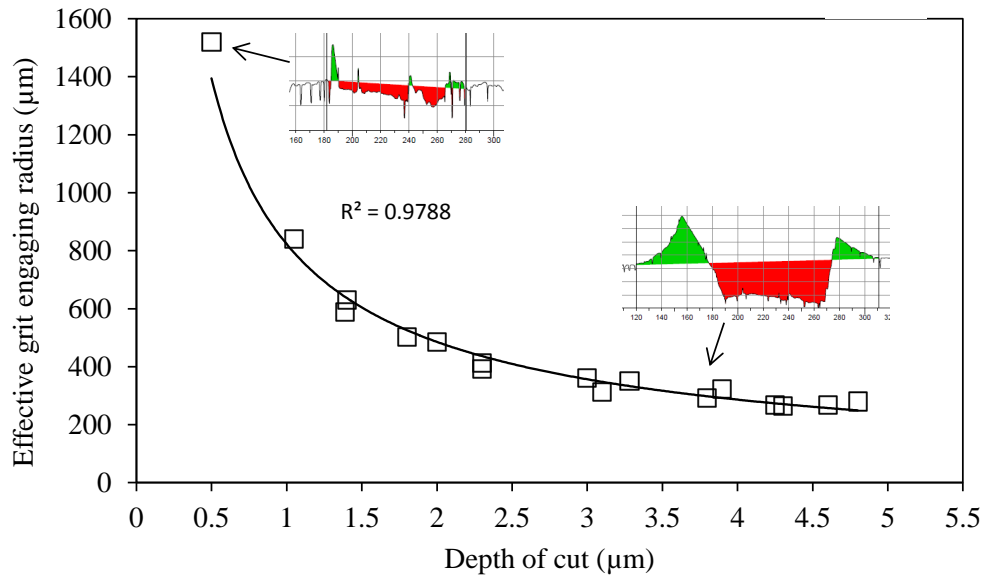


Figure 6.34 Effective grit engaging radius for ideal sphere shape grit

Figure 6.35 shows the variation of EGER with depth of cut for the scratches whose pile-up ratio with depth of cut was given in Figure 6.1. According to Figure 6.35, EGER decreases with increase of depth of cut. Figure 6.36 presents the EGER relation with groove area and show a similar trend with the depth of cut variation as shown in Figure 6.35. The pile-up ratio decreases with increase in EGER, see Figure 6.37. It should be pointed out that the bottom of the grit cutting edge is flat and wide in these figures. Figure 6.38 and Figure 6.39 show the EGER with depth of cut and groove area for the same scratches as given in Figure 6.4, where the grit has relatively sharper cutting edge.

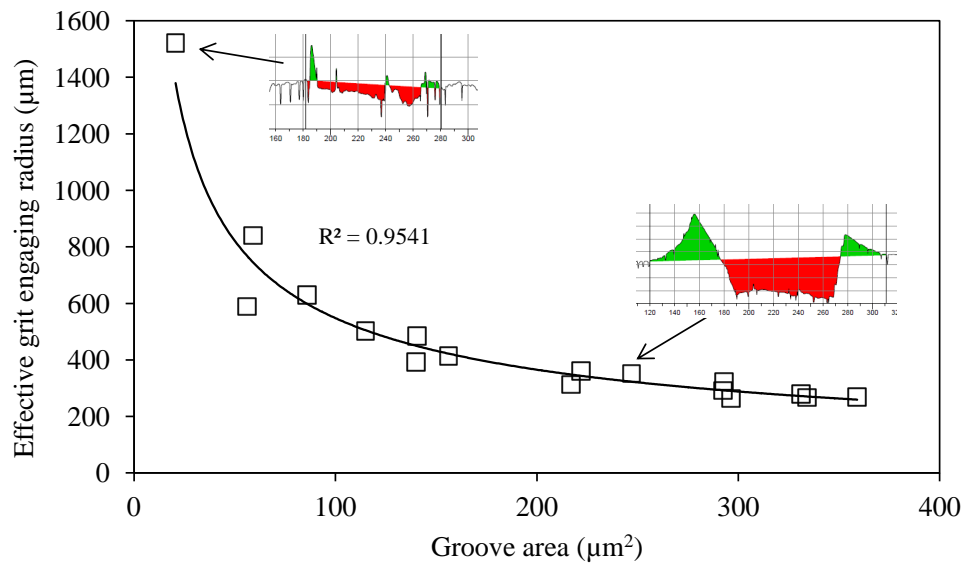
Contrary to Figure 6.35 and Figure 6.36, Figure 6.38 and Figure 6.39 show an increase of EGER with increasing depth of cut and groove area but there is a wide spread in the data points because of continuous alteration of grit cutting edge shape. In Figure 6.40 the data points are scattered to such an extent that was difficult see any clear trend between pile-up ratio and EGER. The calculated value of the EGER is slightly higher for similar depths of cut in the case of multiple edge scratches compared to single edge scratches, as shown in Figure 6.41. Interestingly, pile-up ratio increases with increasing EGER for multiple edge scratches, whereas, pile-up ratio decreases with increasing EGER for single edge scratches as shown in Figure 6.42. Hence, it is important to categorize the type of scratches as either single edge or multiple edge when determining the variation of grinding material removal mechanisms including pile-up ratio and EGER with respect to depth of cut or groove area. Multiple edge scratches have a slightly more complex forming mechanism compared to single edge scratches as it was shown in Figure 6.11.

It was obvious that the form of the single grit scratch is influenced by the grit cutting edge shape, including cutting edge sharpness, bluntness, flatness, width, etc. It was noted that pile-up ratio decreases with the increase of EGER when the grit had single cutting edges; it was reverse when the grit had multiple adjacent cutting edges (Figure 6.42). Thus, EGER can also be used as a good indicator to show material removal behaviour during single grit grinding.



Traverse scratching; Workpiece: En24T; Grit: CBN (40/50 mesh); $V_c = 546.6$ m/min

Figure 6.35 Effective grit engaging radius variation with depth of cut (flat cutting edge)



Traverse scratching; Workpiece: En24T; Grit: CBN (40/50 mesh); $V_c = 546.6$ m/min

Figure 6.36 Effective grit engaging radius versus groove area (flat cutting edge)

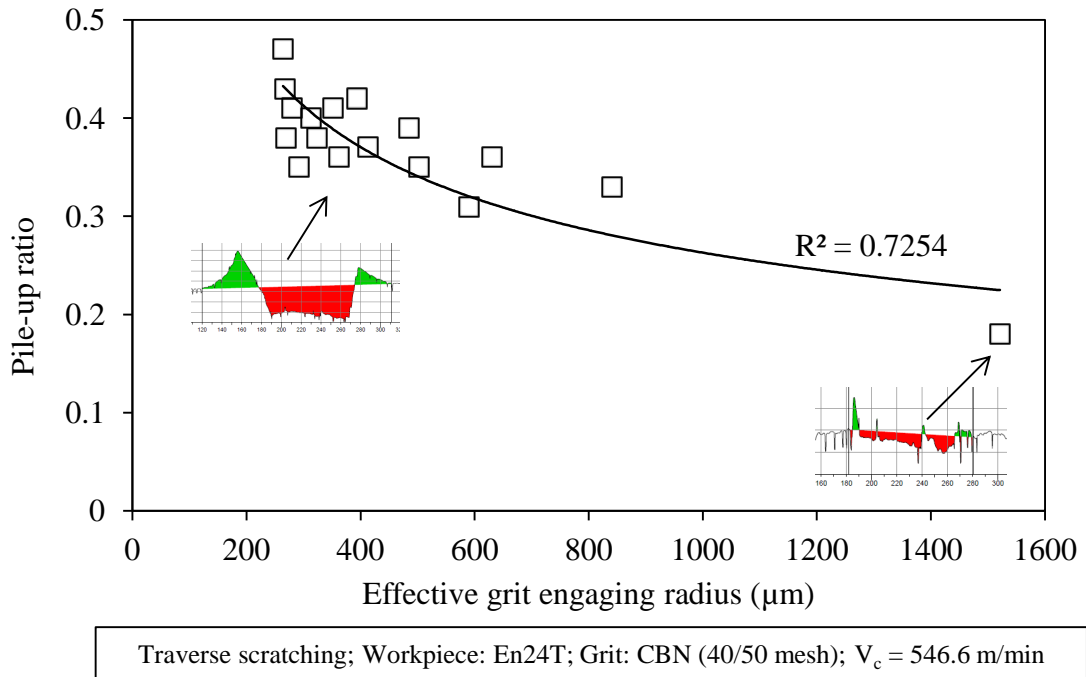


Figure 6.37 Pile-up ratio versus effective grit engaging radius (flat cutting edge)

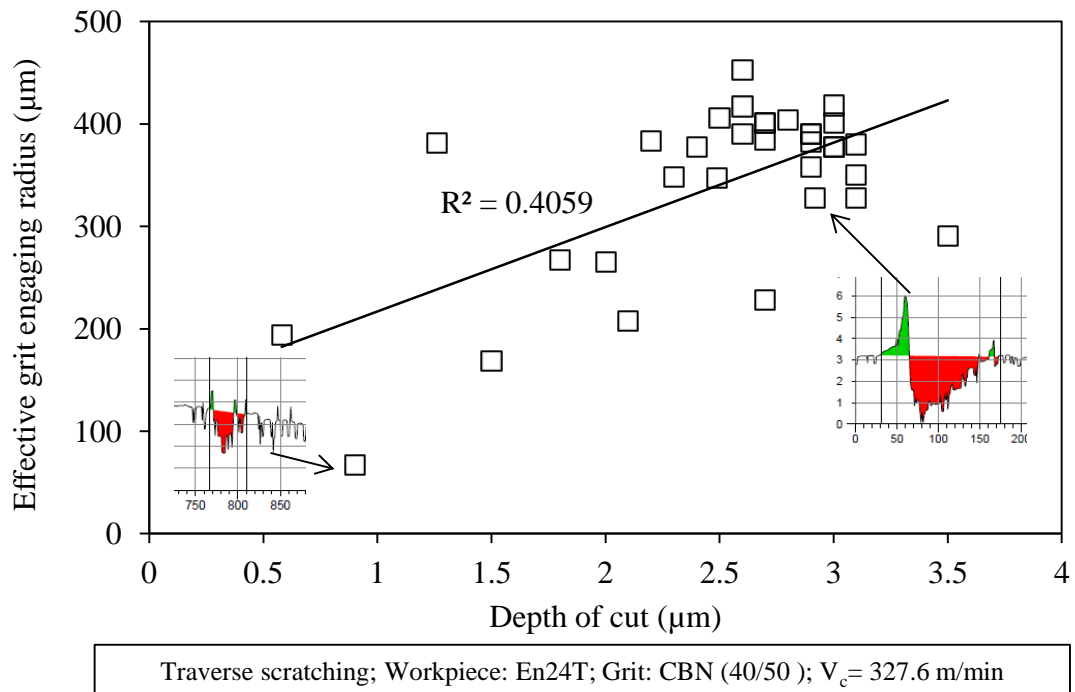


Figure 6.38 Effective grit engaging radius versus depth of cut (sharp cutting edge)

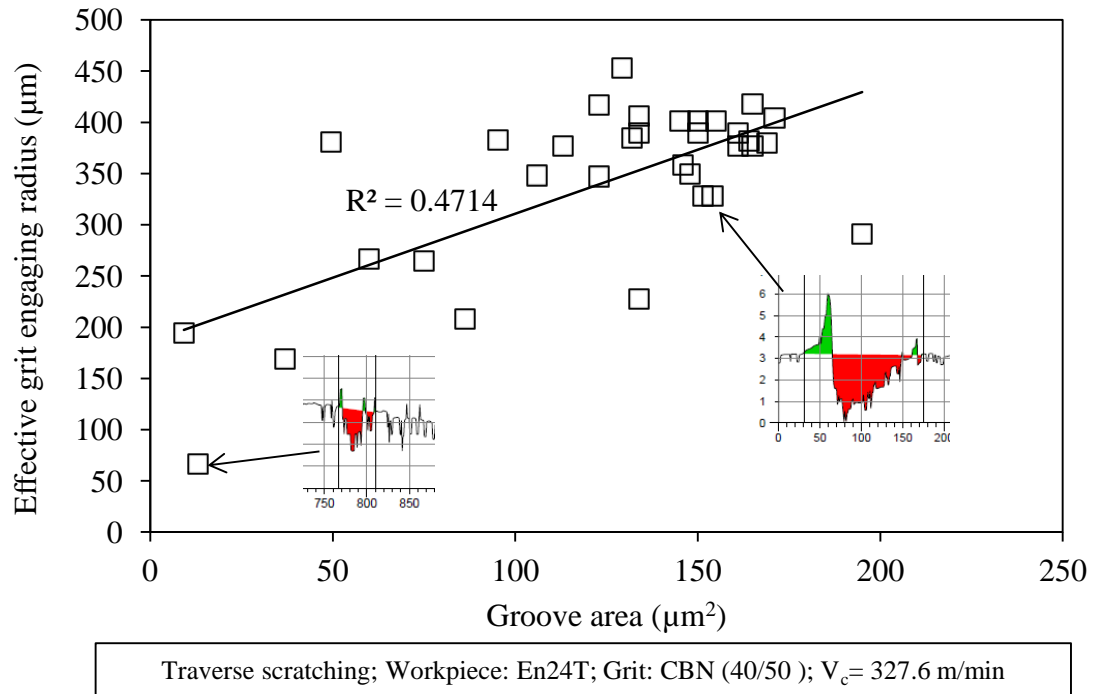


Figure 6.39 Effective grit engaging radius versus groove area (sharp cutting edge)

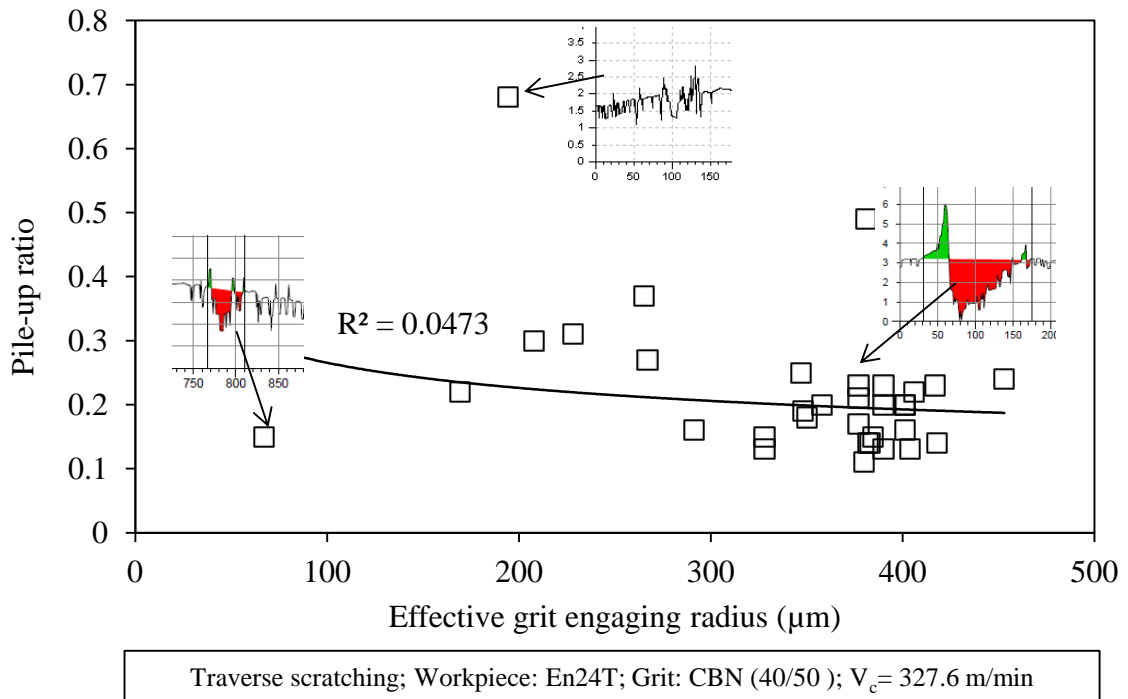


Figure 6.40 Pile-up ratio versus effective grit engaging radius (sharp cutting edge)

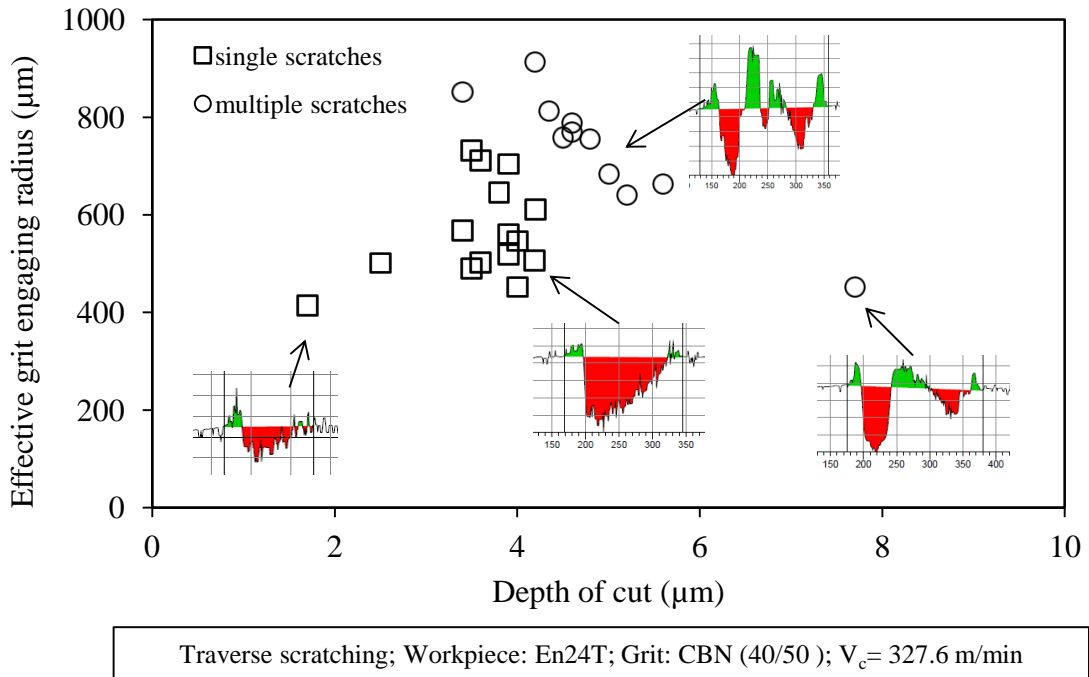


Figure 6.41 Effective grit contact radius versus depth of cut (single and multiple cutting edges)

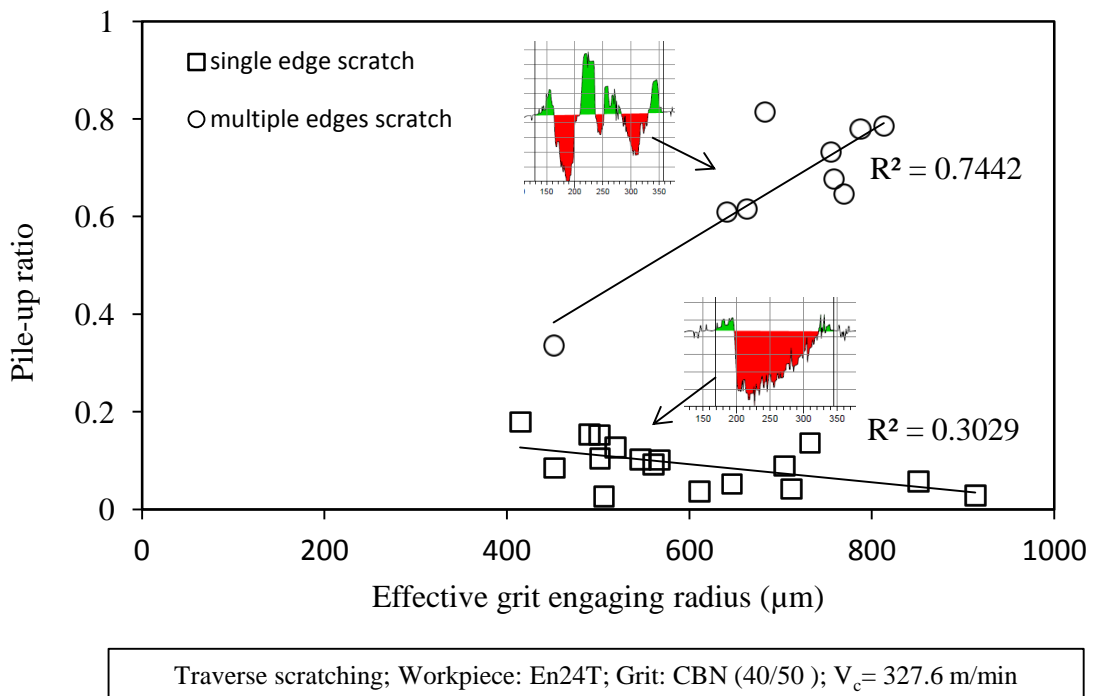


Figure 6.42 Pile-up ratio versus effective grit engaging radius (single and multiple cutting edges)

6.3 Cutting forces during single grit grinding

Cutting force analyses were grouped according to the force signal acquisition technique, either via the Labview software or the oscilloscope for the different sets of experiments. Figure 6.43 and Figure 6.44 show the variations of tangential force (F_t) and normal force (F_n) with depth of cut and groove area, respectively as measured by the Labview software.

Figure 6.43 shows that the cutting forces increase with depth of cut, but there is a highly scattered distribution. Figure 6.44 shows that the cutting forces increase with groove area but with less scatter than for depth of cut. Thus, in single grit grinding cutting forces (F_t and F_n) demonstrate better correlation with groove area compared to depth of cut.

In both Figure 6.43 and Figure 6.44 it can be seen that for cutting speed of 327.6 m/min (or 3000 rpm) there is an initial increase in F_n which reaches a maximum at a depth of cut 4.5 μm , or groove cross-section area 250 μm^2 , after which it clearly decreases.

The force ratio (F_n/F_t) might give useful information about which component of the cutting force in single grit grinding is most influenced with increase of groove area. Figure 6.45 shows that the force ratio ranges from 2 to 3.5, with the lower cutting speed ($V_c= 54.6$ m/min) having a higher force ratio than the higher cutting speed ($V_c= 327.6$ m/min). This might be because of relatively steep increase of the tangential force component at high cutting speed. The tangential force component plays a dominant role during material removal because chip removal is mainly generated by application of tangential force components rather than normal force components.

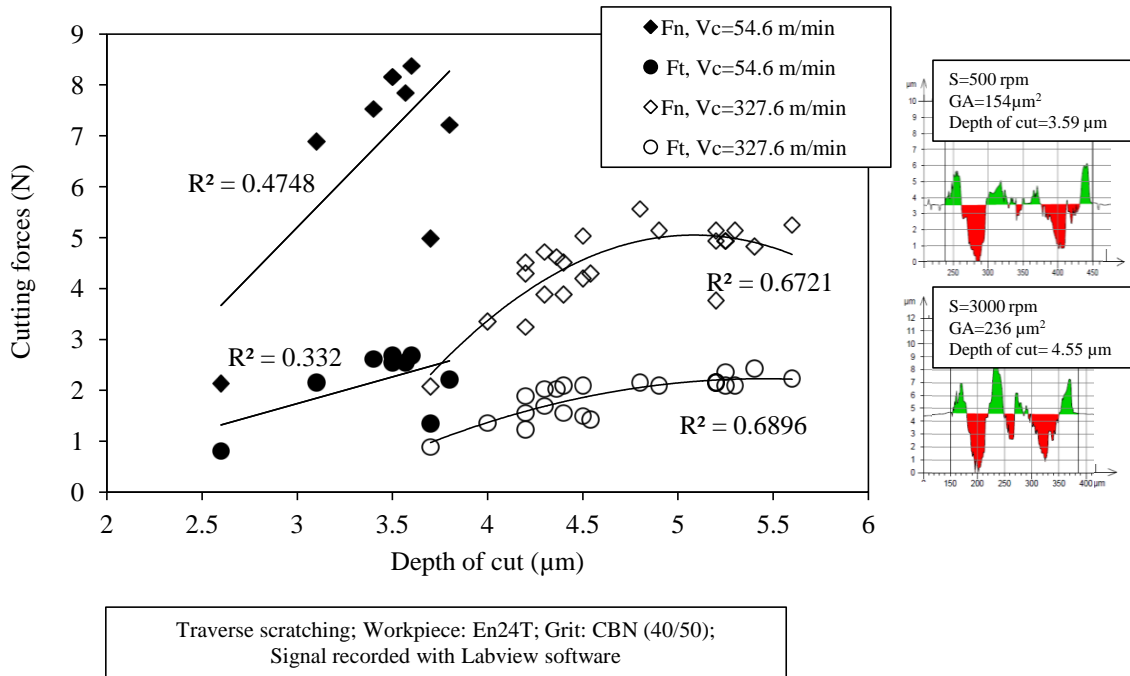


Figure 6.43 Cutting forces versus depths of cut measured using Labview software

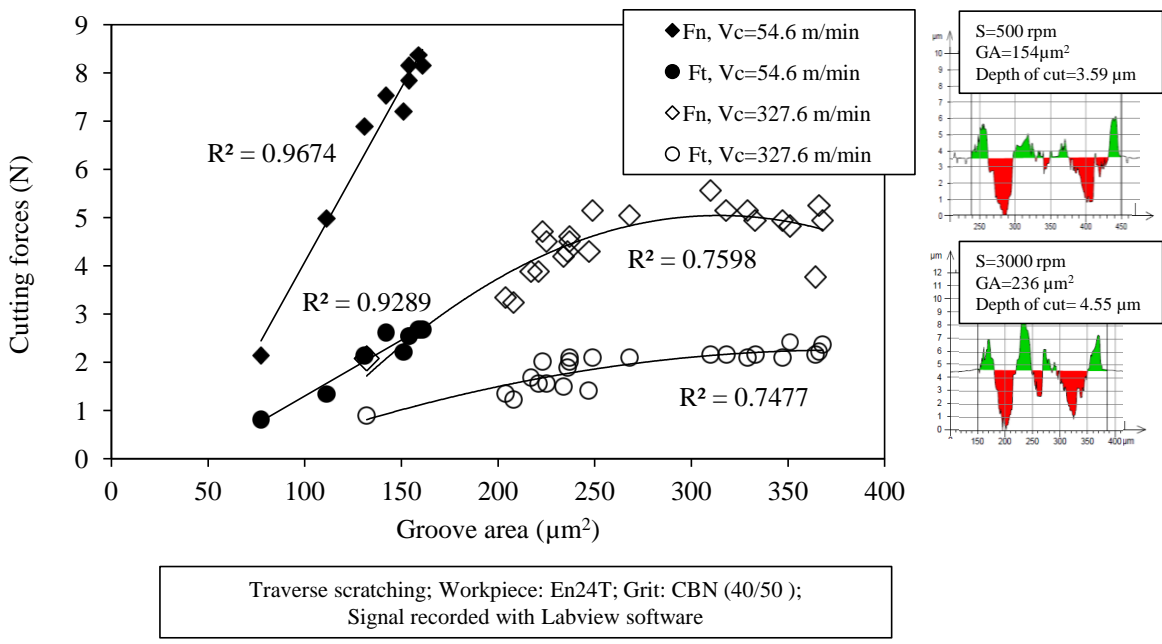


Figure 6.44 Cutting forces versus groove area measured using Labview software

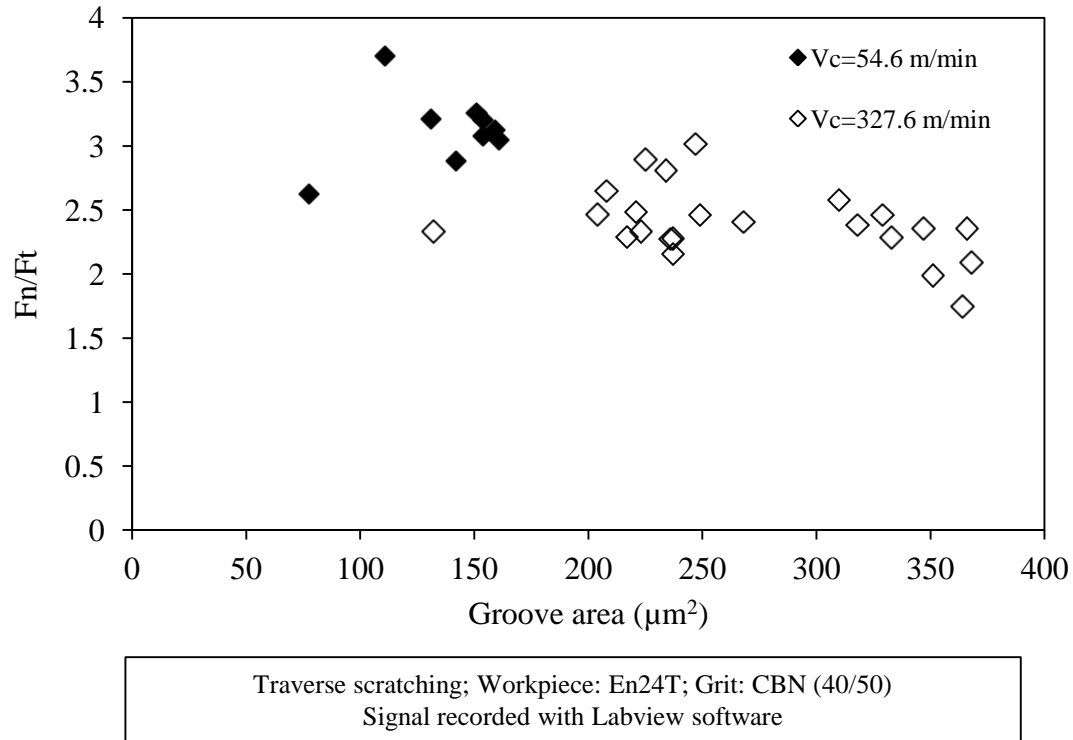


Figure 6.45 Force ratio (F_n/F_t) for Labview measurements

The cutting forces recorded with the oscilloscope were for a range of speeds; 1.08, 10.8, 109.2 and 327.6 m/min, higher than these speeds (such as 546.6 m/min) were not recorded because of oscilloscope data sampling limitation. Figure 6.46 and Figure 6.47 show variation in F_n and F_t with the different cutting speeds, for depth of cut and groove area, respectively. Looking at the force variation at speed of 327.6 m/min in Figure 6.46 and Figure 6.47, the increase of trend seems to be very slow after a certain depth of cut or groove area. This is similar to the trend observed for 327.6 m/min in Figure 6.43 and Figure 6.44. Cutting forces obtained from single edge scratches and multiple edge scratches are shown in Figure 6.48 and Figure 6.49 for depth of cut and groove area, respectively. Cutting forces show better correlation with groove area compared to depth of cut. Multiple edge scratches generate slightly higher forces than single edge scratches as shown in Figure 6.49, this can be attributed to higher material

ploughing where the cutting is less efficient. Ploughing is an undesired action in grinding since it consumes extra energy during the material removal process. The force ratio (F_n/F_t) is found to be between about 2 and 4 with a save for one outlier at 327.6 m/min, see Figure 6.50, but no clear relation is observable between force ratio and cutting speed.

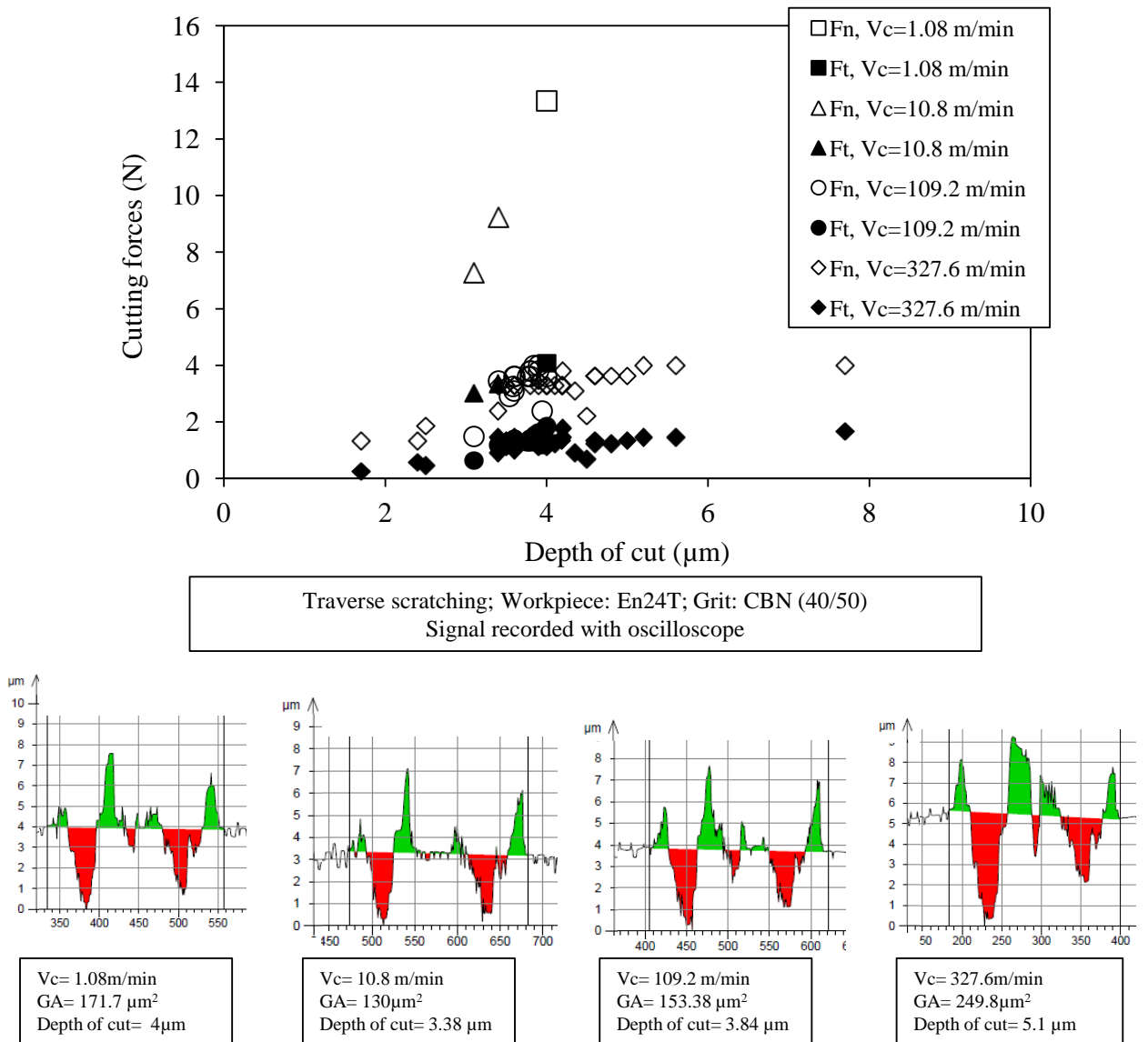
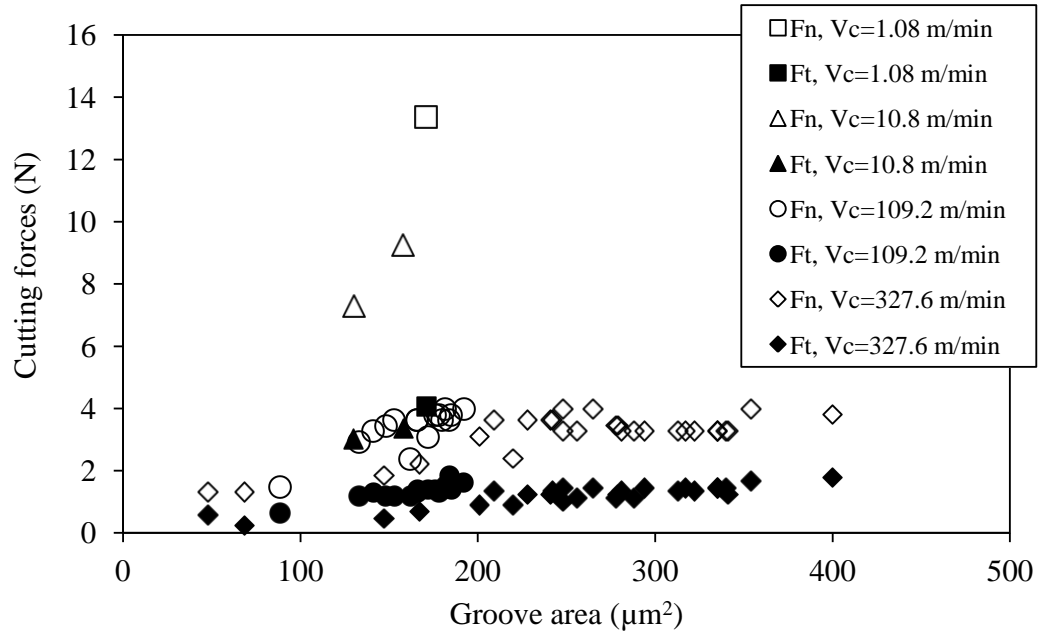


Figure 6.46 Cutting forces recorded with oscilloscope versus depth of cut



Traverse scratching; Workpiece: En24T; Grit: CBN (40/50)
 Signal recorded with oscilloscope

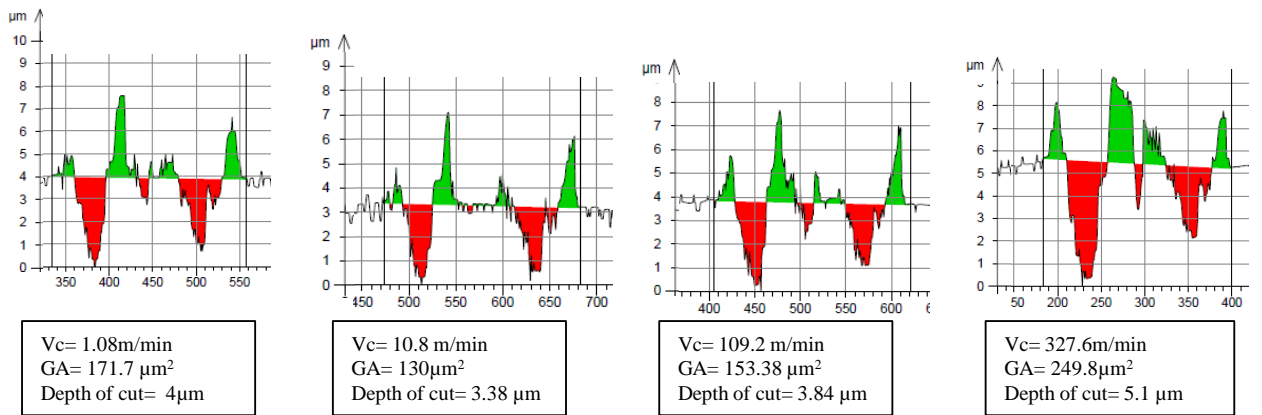


Figure 6.47 Cutting forces recorded with oscilloscope versus groove area

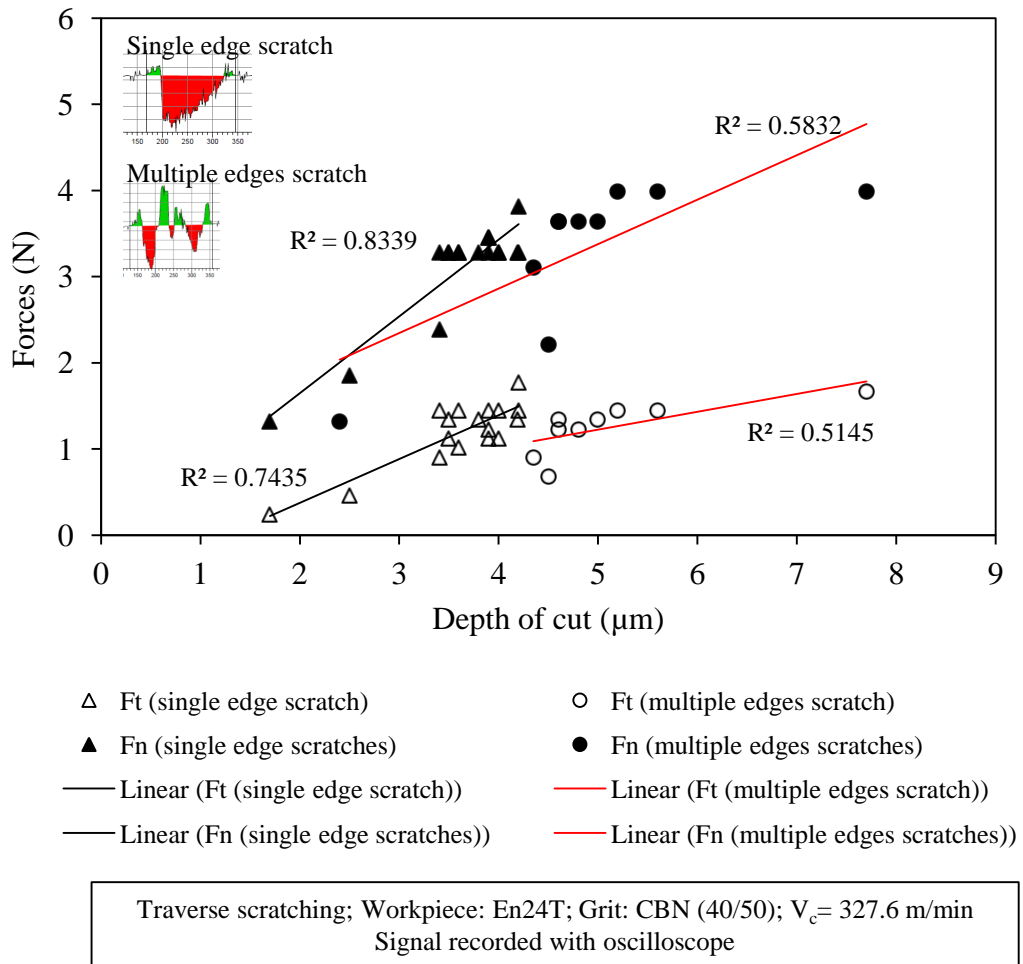


Figure 6.48 Cutting forces recorded with oscilloscope versus depth of cut for single and multiple edge scratches

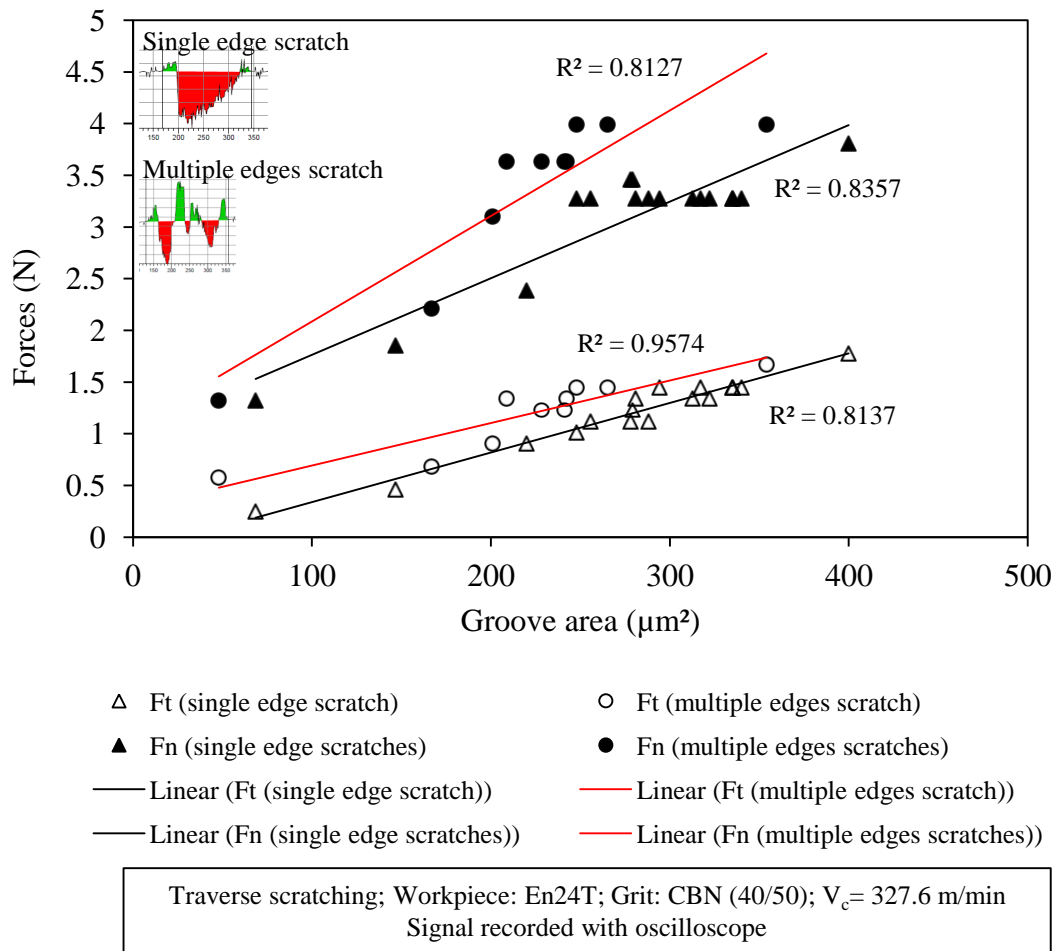


Figure 6.49 Cutting forces recorded with oscilloscope versus groove area for single and multiple edge scratches

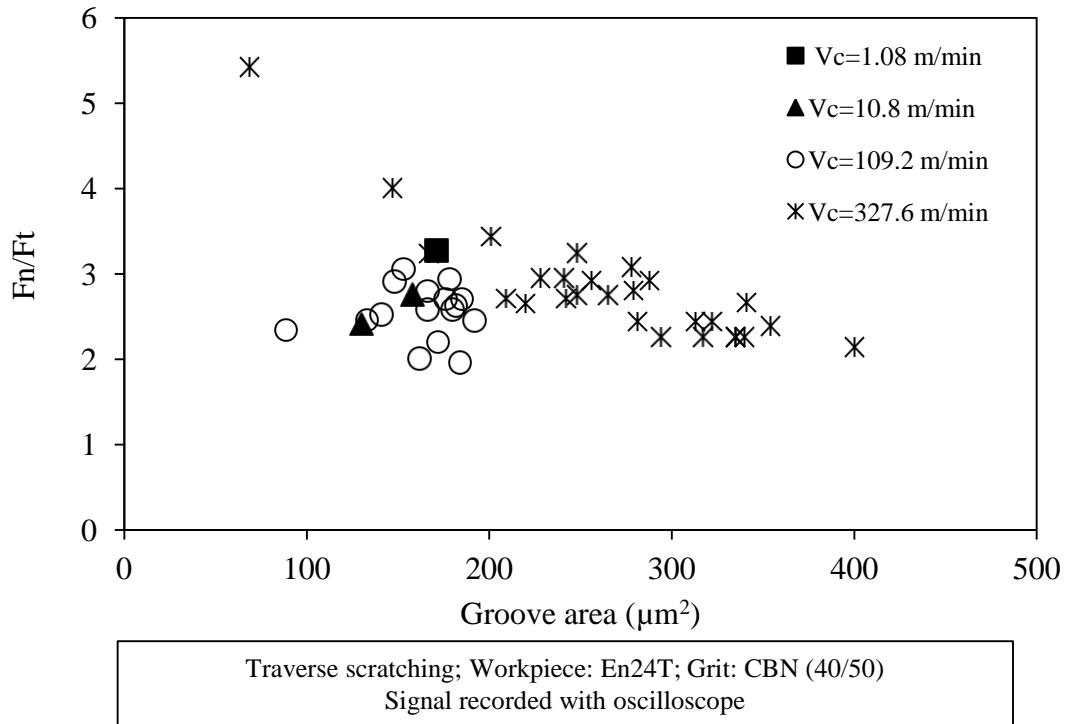


Figure 6.50 Force ratio (F_n/F_t) versus groove area for forces recorded with oscilloscope

6.4 Specific energy in single grit grinding

Figure 6.51 and Figure 6.52 show variation of specific energy with depth of cut and groove area, respectively, for the scratches whose force reactions were acquired using Labview software. From both of the figures, it is obvious that specific energy is highly dependent on cutting speed, with higher speeds generally resulting in lower specific energy. Figure 6.53 and Figure 6.54, where the forces were acquired using the oscilloscope show the same relation between specific energy and cutting speed.

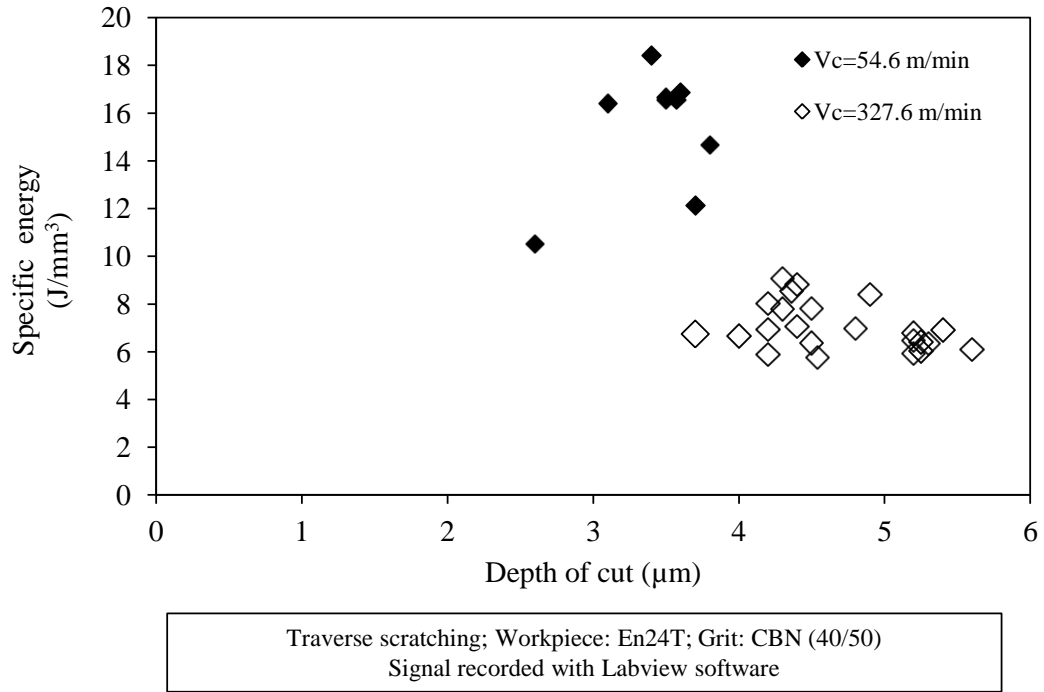


Figure 6.51 Specific energy versus depth of cut (Labview data)

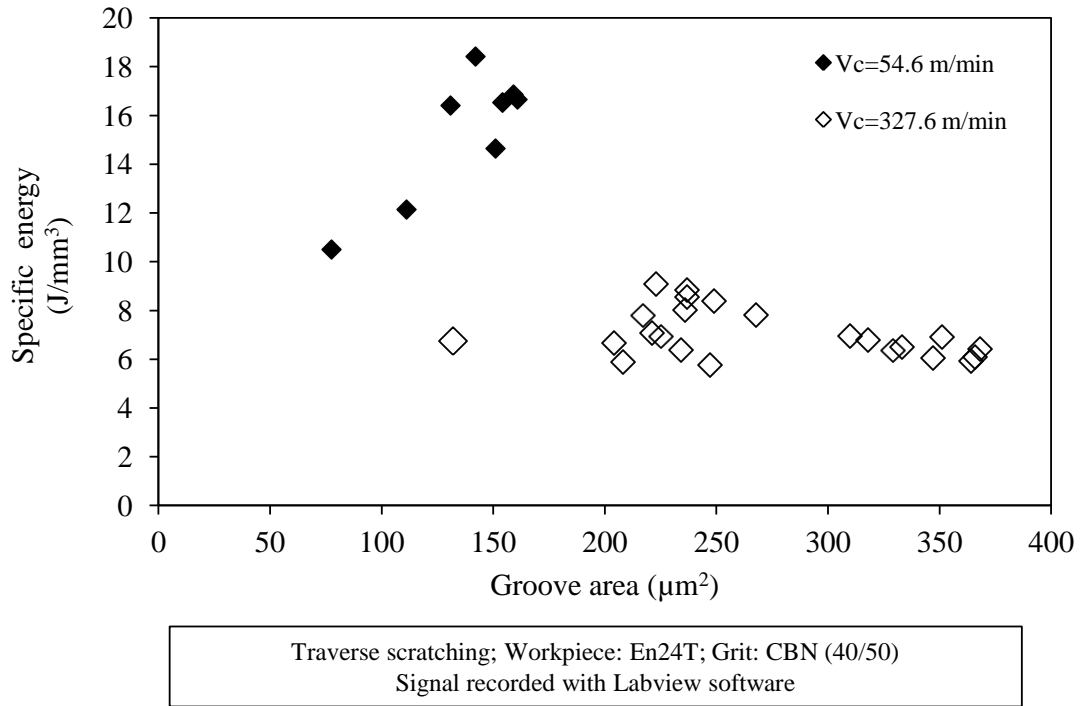


Figure 6.52 Specific energy versus groove area (Labview data)

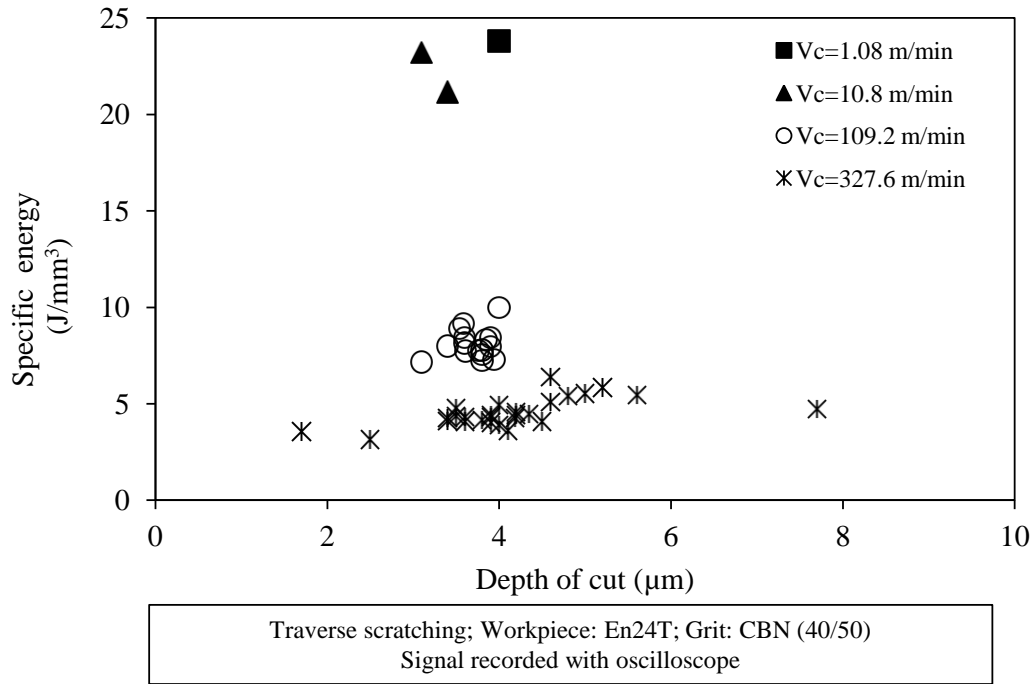


Figure 6.53 Specific energy versus depth of cut (oscilloscope data)

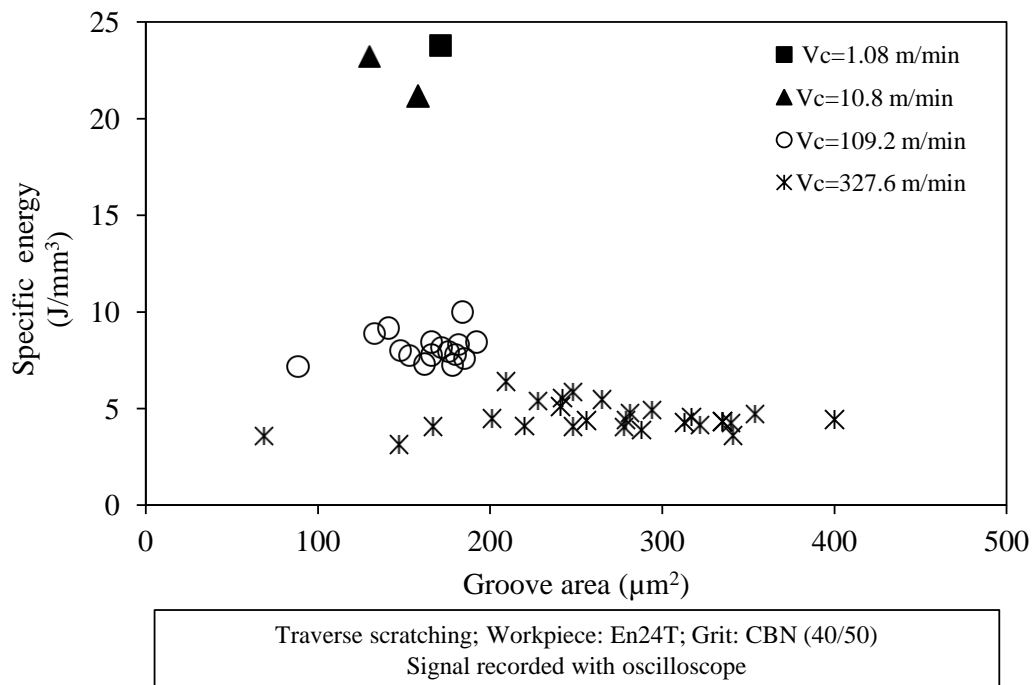


Figure 6.54 Specific energy versus groove area (oscilloscope data)

Variation of specific energy for single edge scratches and multiple edge scratches show different characteristics, see Figure 6.55 and Figure 6.56. Multiple edge scratches show relatively higher specific energy requirements compared to the single edge scratches, this is because multiple edge scratches have more ploughing action than cutting compared to single edge scratches. Such non-material removal action requires more energy than a material removal action such as cutting. It is noted that no apparent relation between specific energy and depth of cut (or groove area) was observed in these experiments. In the literature, there are observations which suggest specific energy increases with increasing depth of cut (Brinksmeier and Glwierzew, 2003; Ghosh et al., 2010) and that specific energy decreases with increase of depth of cut (Doman, 2008). Based on the research reported here, specific energy is only weakly dependent on depth of cut or groove area. This observation might be worth further study as future research.

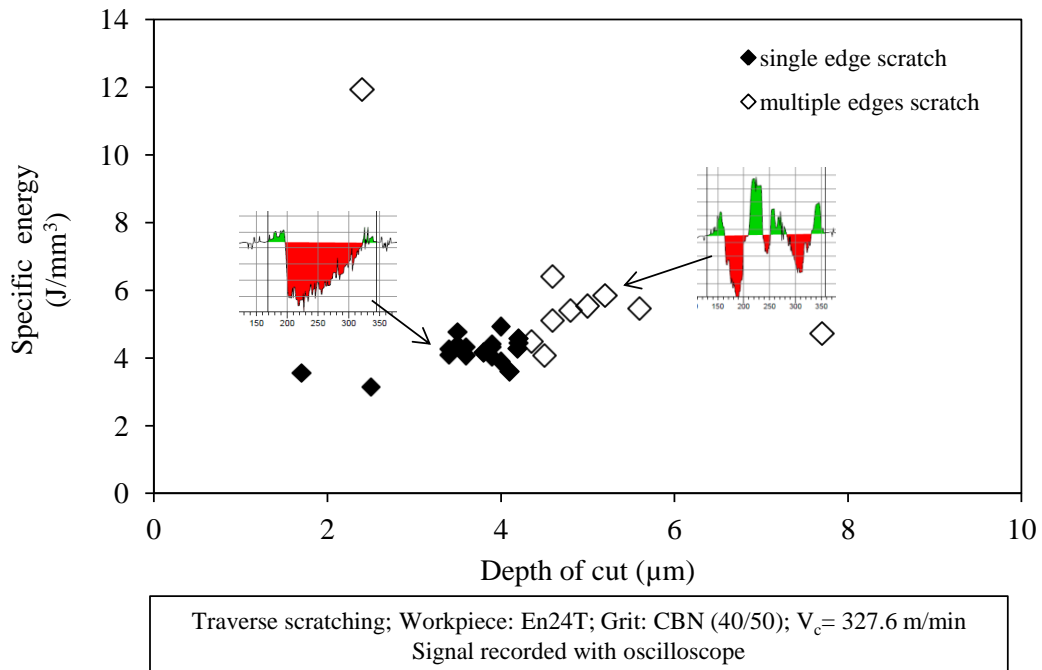


Figure 6.55 Specific energy versus depth of cut with different cutting edges

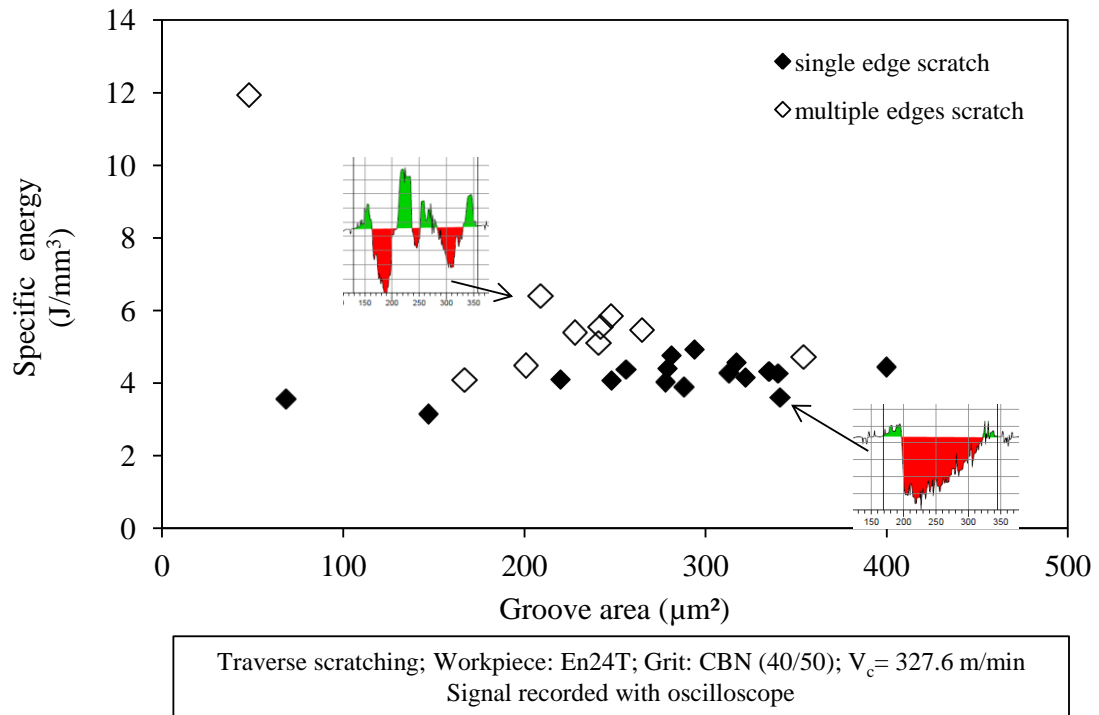


Figure 6.56 Specific energy versus groove area with different cutting edges

6.5 Summary

In this thesis, single grit grinding with CBN grit shows how output parameters such force and specific energy, and material removal parameters such as pile-up ratio with respect to depth of cut or groove area are influenced during the course of the process. Grit shape continuously changed even during formation of a single scratch; also number of cutting edges interacting with workpiece and cutting edge shape including sharpness, bluntness, wideness, etc., continuously changed with the progress of the grinding process. All these factors show how even single grit grinding process has extremely complex dynamic mechanisms compares to conventional cutting processes performed by a shaped tool. It would be easier to get certain conclusions with the use of shaped tool instead of uncontrollably shaped abrasive grit.

The single grit grinding scratches performed on En8 steel, En24T steel and Inconel 718 using CBN abrasive grit (40/50 mesh size) have been investigated to explore the material removal mechanisms in terms of pile-up ratio and chip removal strength and EGER at the micro scale. In addition, cutting forces and specific energy during scratching associated with material removal mechanisms at different depth of cuts, speeds and grit cutting edge geometry have been investigated.

According to the experimental results, pile-up ratio is highly dependent on grit cutting edge geometry (shape). In general, pile-up ratio decreases with increasing depth of cut (or groove area) as long as the grit cutting edge is sharp (refer to Figure 6.5, Figure 6.9, Figure 6.13, and Figure 6.14). However, in contrast, pile-up ratio increases with increasing depth of cut when grit cutting edges have a flat bottom (or blunt grit edge, refer to Figure 6.1). A wider cutting edge leads to a lower pile-up ratio while a narrower cutting edge leads to a higher pile-up ratio (Figure 6.21), because small width of cross-section makes the cutting edge behave as though it were sharp compared to cutting edges having larger width.

Pile-up ratio with groove area shows similar trend to depth of cut (refers to Figure 6.15 and Figure 6.17). Single grit acts like single cutting edge at first during scratching and produces single edge scratch grooves, then as the grit cutting edges become worn they might fracture to generate fresh multiple cutting edges which produce multiple edges scratch grooves (refer to Figure 6.9). Pile-up ratio is found to be always higher with multiple edges scratches as with single edge scratches (refer to Figure 6.9 and Figure 6.14).

The higher pile-up ratio at lower depth of cut is the reflection of a material removal mechanism which is dominated by ploughing action rather than cutting. When a scratch is analysed along its path, the pile-up ratio at the grit entrance side is relatively lower than that at the grit exit side of the scratch (refer to Figure 6.27 and Figure 6.31), this can be explained by

material accumulation ahead of the grit and material plastic flow in the direction of grit movement. Thus, cutting is more efficient at the entrance side of the scratch compared to exit side of the scratch. Chip removal strength with respect to depth of cut also represents a situation where ploughing and cutting are prominent (refer to Figure 6.18); a smaller slope in the chip removal trend can be interpreted as a ploughing prominent region while a steep increase in the chip removal trend could be interpreted as a cutting prominent region.

Normal forces (F_n) exerted during single grit scratching were found to be always higher than tangential forces (F_t). Both forces are also found to be highly dependent on cutting speed, with higher cutting speed leading to lower cutting forces (refer to Figure 6.43 and Figure 6.46). Cutting forces are better correlated with groove area than with depth of cut (refer to Figure 6.43 and Figure 6.44). Normal forces increase slowly with increasing depth of cut, but rate of increase in tangential force is higher. The force ratio (F_n/F_t) is generally found in the range of 2 to 4, but the ratio reduces slightly with increasing depth of cut (or groove area) due to a faster rate of increase of the tangential force with depth of cut (Figure 6.45 and Figure 6.50).

Specific energy during single grit grinding is highly dependent on cutting speed. The higher the cutting speed the lower the specific energy. Additionally, specific energy requirement is found to be lower when the cutting action is efficient (low pile-up ratio) compared to when cutting is less efficient (high pile-up ratio) (refer to Figure 6.55 and Figure 6.56).

Chapter 7 Finite Element Simulation Results

7.1 Introduction

The results of the finite element simulations which were presented in Chapter 5 are given in this chapter. The major simulation performed is chip formation using orthogonal cutting with different operational parameters and simplified single grit parameters. Although the aim of the study is to investigate the material removal mechanism of grinding using the single grit approach, orthogonal cutting simulation is also performed for better understanding of the chipping mechanism with different operational parameters. Also, cutting with a highly negative rake angle could represent the single grit cutting mechanism during grinding. By using the orthogonal cutting approach, effects of depth of cut and rake angle on chip shape, on fracture mechanism of chip formation and the corresponding cutting forces were investigated and are reported here. Simulations to represent the single grit material removal mechanism have also been performed using a simplified single grit trajectory. Simulation of cutting mechanisms in three dimensions has not been achieved due to difficulties and limitations of the FEM simulation at micron scale. Thus, mainly the ploughing and rubbing mechanisms of single grit grinding are investigated using material plastic flow behaviour. With the single grit simulation, influence of depth of cut, friction, and ground surface creation with multiple grit pass are investigated and reported.

7.2 FEM simulation of chip formation

FEM simulation of chip formation demonstrated in this section was performed using Aluminium alloy (A2024-T351), see Chapter 5 for details of material properties. Mabrouki et al.,

(2008) used aluminium alloy and reported in the literature on the application of the fracture energy concept to a FEM model. The purpose of the cutting simulation in this section is to reveal formation tendencies regarding chip types (continuous, serrated and discontinuous) rather than experimental comparison with the single grit tests conducted on En24T steel and Inconel alloy 718. Thus, usage of different material in the cutting simulation is not an issue. 2D chip simulations were performed in Abaqus/Explicit with gradually increasing fracture energy per unit area of crack generation, G_f , at two different depths of cut ($h_1=20 \mu\text{m}$ and $h_2=50 \mu\text{m}$) and four rake angles ($\gamma_1 = 22^\circ$, $\gamma_2 = 0^\circ$, $\gamma_3 = -30^\circ$, $\gamma_4 = -45^\circ$). Table 7.1 summarises the simulated conditions and corresponding chip type.

Table 7.1 Summary of cutting simulation condition and remarkable chip type

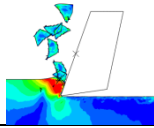
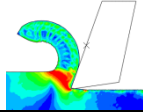
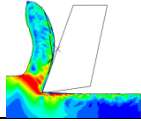
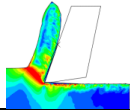
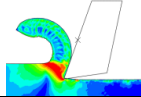
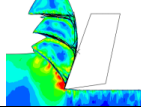
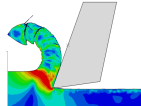
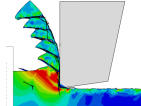
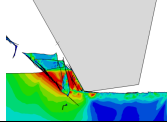
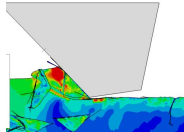
Corresponding Figure	Fracture energy per unit area G_f , (N/m)	Depth of cut h (μm)	Rake angle γ , (degree)	Cutting speed V_c , (m/min)	Friction coefficient, μ	Chip type
Figure 7.1	250	20	22°	300	0.2	Discontinuous chip 
	2500	20	22°	300	0.2	Continuous curling chip (highly curved) 

Table7.1 (Cont.) Summary of cutting simulation condition and remarkable chip type

Corresponding Figure	G_f (N/m)	h (μm)	γ (degree)	V_c (m/min)	μ	Chip type
Figure 7.1	10000	20	22°	300	0.2	Continuous curling chip (slightly curved) 
	20000	20	22°	300	0.2	Continuous straight chip 
Figure 7.2	2500	20	22°	300	0.2	Continuous curled chip 
	2500	50	22°	300	0.2	Serrated chip 
Figure 7.3	1500	20	22°	300	0.2	Continuous chip 
	1500	20	0°	300	0.2	Serrated chip 
	1500	20	-30°	300	0.2	Discontinues chip 
	1500	20	-45°	5	0.2	Discontinues chip 

7.2.1 Influence of fracture energy on chip formation

Chip simulation with gradually increasing fracture energy, G_f , has been performed to demonstrate its influence when used as a damage evolution criterion. Because of the difficulty of knowing the exact value of fracture energy at the smaller thicknesses, different values of fracture energy (250, 2500, 10000, and 20000 N/m) were used in the simulation of chip formation with an uncut chip thickness of 20 μm . The results are shown in Figure 7.1 and demonstrate that values of fracture energy of 2500 N/m and above gave continuous chip generation (see Figure 7.1 (b-d)), while the lower value of 250 N/m gave discontinuous chip generation (see Figure 7.1 (a)). Furthermore, with increase in fracture energy chip shape tended to be straighter (see Figure 7.1 (b-d)) and at lower values of fracture energy a more curled chip was produced (see Figure 7.1 (b)). Therefore, fracture energy is one of the key factors as a damage evolution criterion to determine the chip generation behaviour during cutting process simulation.

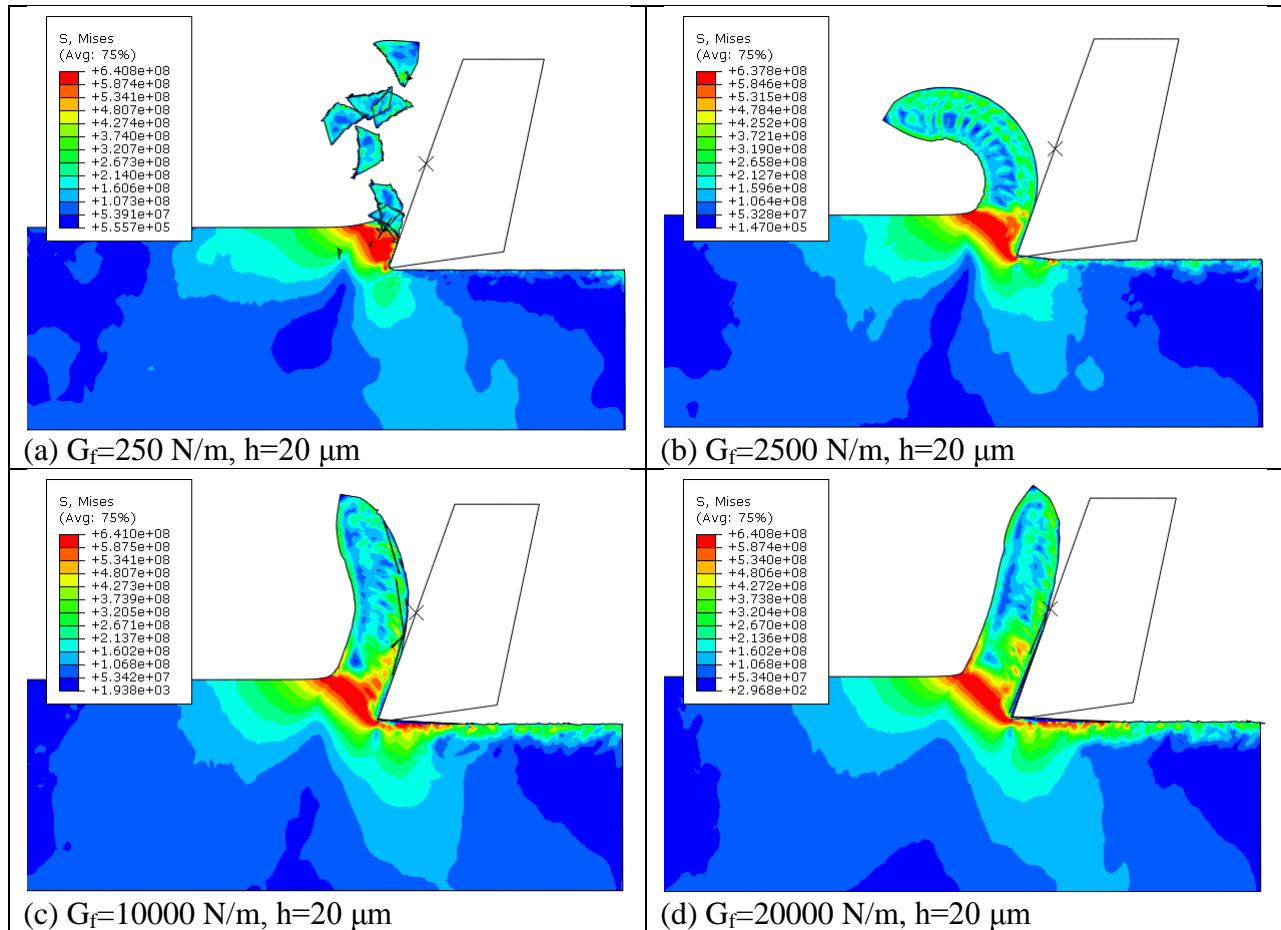


Figure 7.1 Chip simulation with varying fracture energy

7.2.2 Influence of depth of cut on chip shape

Depth of cut is another influential parameter for determining chip type. In order to show the influence of depth of cut, two simulations with different uncut chip thickness were undertaken. Continuous chip without segmentation along the chip free edge was generated with depth of cut set to $20 \mu\text{m}$, see Figure 7.2 (a). However, a serrated chip is generated when uncut chip thickness was set to $50 \mu\text{m}$ under similar simulation conditions, see Figure 7.2 (b). Serrated chip formation at higher depth of cut can be attributed to shear stress developed at the primary shear zone is increased dramatically due to intensive straining in this region. With the increasing

strain at primary shear zone because of the predefined failure criterion crack formation is initiated and material strength is weakened. As a result, each segment formed due to plastic flow tears and forms a sharp edged serrated chip as shown in Figure 7.2-(b).

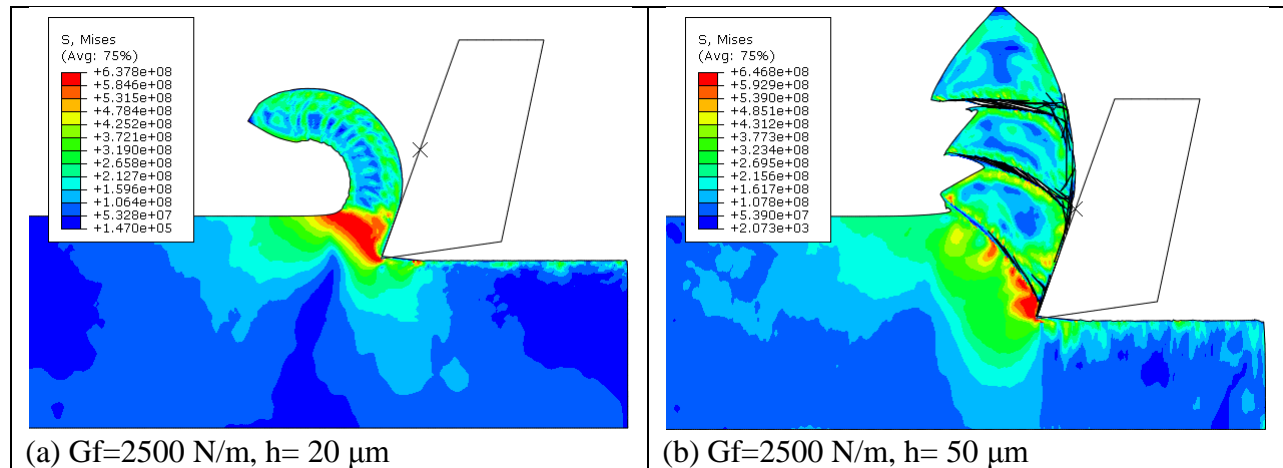


Figure 7.2 Chip formation with different depths of cut

7.2.3 Chip type with varying rake angles

Continuous, serrated and discontinuous chip types are obtained by using different tool rake angles. It is clear from the simulation results, rake angle plays a dominant role in determining chip type. Continuous chip with little segmentation is generated with a positive rake angle of 22° (Figure 7.3 (a)), serrated or saw tooth chips are generated with a zero rake angle (Figure 7.3 (b)), discontinuous chips are generated with a negative rake angle of -30° (Figure 7.3 (c)) and a discontinuous chip with two split parts is generated with a negative rake angle of -45° (Figure 7.3 (d)). Obviously, the transition from continuous to discontinuous chip formation takes place as the rake angle moves from positive to negative values. The compression on the chip increases as a result of increasingly negative tool rake face inclination. Such increasing compression results in

increased tearing stress in the primary shear region which leads to an increase in segmental separation because material strength in the primary shear region decreased with increasing straining. When the predefined damage evolution criterion is exceeded ultimate fracture occurs.

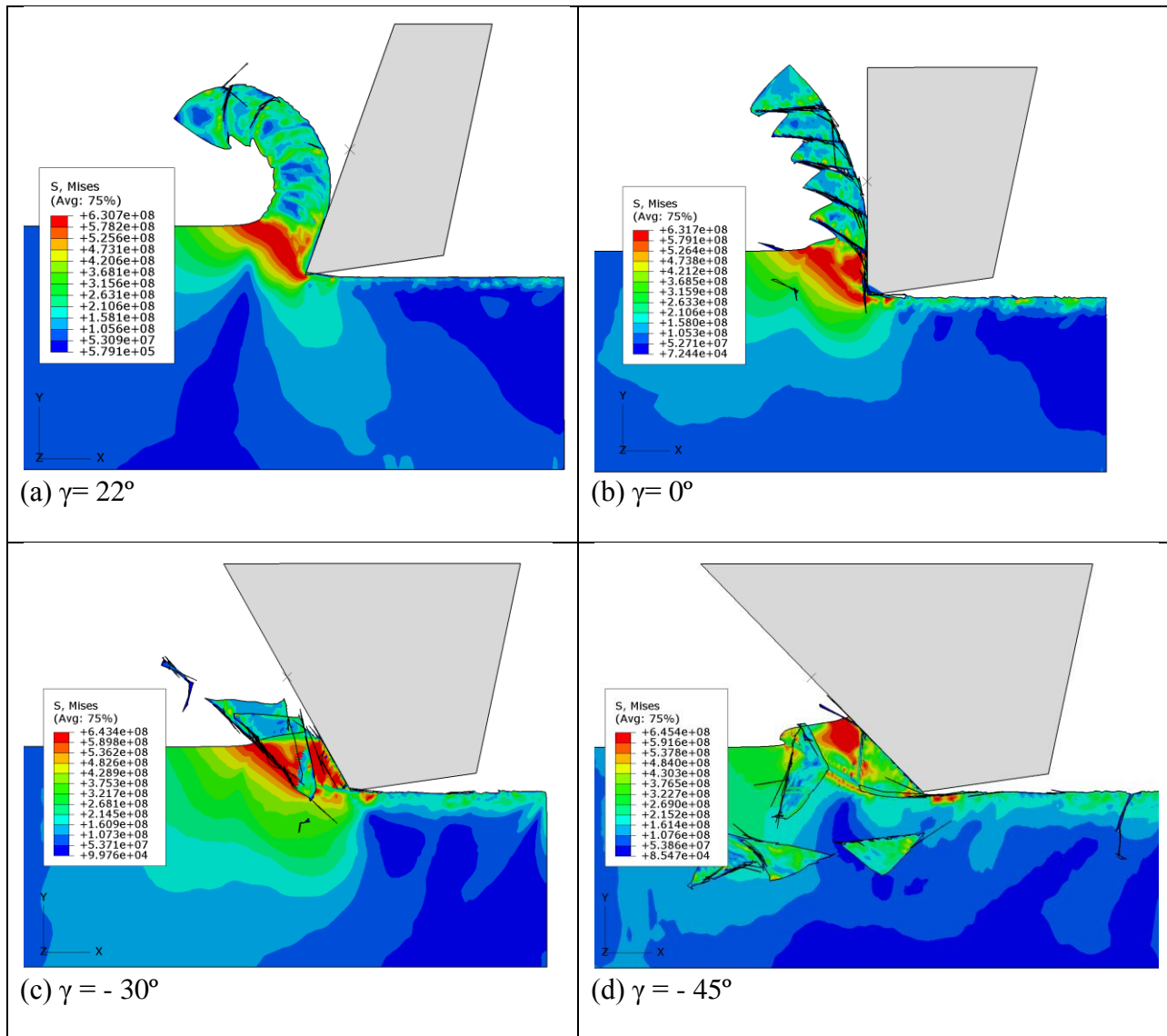


Figure 7.3 Chip shape variation alteration with change of rake angle ($G_f=1500 \text{ N/m}$ and $h=20 \mu\text{m}$)

7.2.4 Chip breakage during serrated chip formation

Chip breakage was observed during serrated chip simulation as shown in Figure 7.4. The chip length increases with increased simulation time. After reaching a certain length, the chip fractures at a weak residual shear line because curvature increases with increasing chip length such that elements in the weakened residual shear zone can no longer carry the front portion of the chip which breaks away. Unless chip breakage happens when the chip attains a certain length it could damage the machined surface, besides which such long chips are not safe during machining.

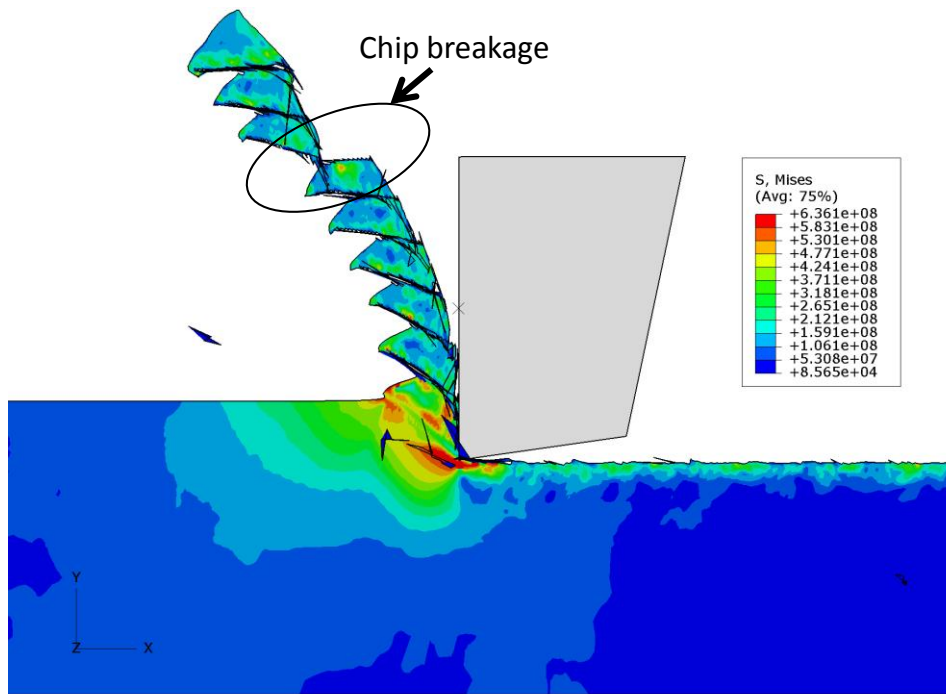


Figure 7.4 Chip breakage during serrated chip formation ($G_f=1500$ N/m, $h=20$ μ m, $\gamma=0^\circ$, $V_c = 300$ m/min, material: Aluminium alloy)

7.2.5 Chip fracture when using high negative rake angle

As is commonly known, during chip formation processes a primary shear zone is developed through from tool tip contact point along the chip free surface due to adiabatic shearing and a secondary shear zone is developed in the region of tool rake face – chip contact section. The secondary shear region shifts into the chip when the rake angle is highly negative and leads to the formation of a stagnant or dead region between secondary shear line and chip-tool rake face. This region does not move or removed as a part of chip and so called stagnant or dead region (Komanduri, 1971; Childs et al., 2000). However, in contrast this study observed a secondary shear region that developed inside the chip (see Figure 7.6) rather than at the chip-tool rake face; the part between the secondary shear line and chip-tool rake face is removed as a subsequent, secondary part of chip. Only this type of chip formation was observed in this study. The development of the two parts of the chip from beginning to ultimate formation is shown in Figure 7.5.

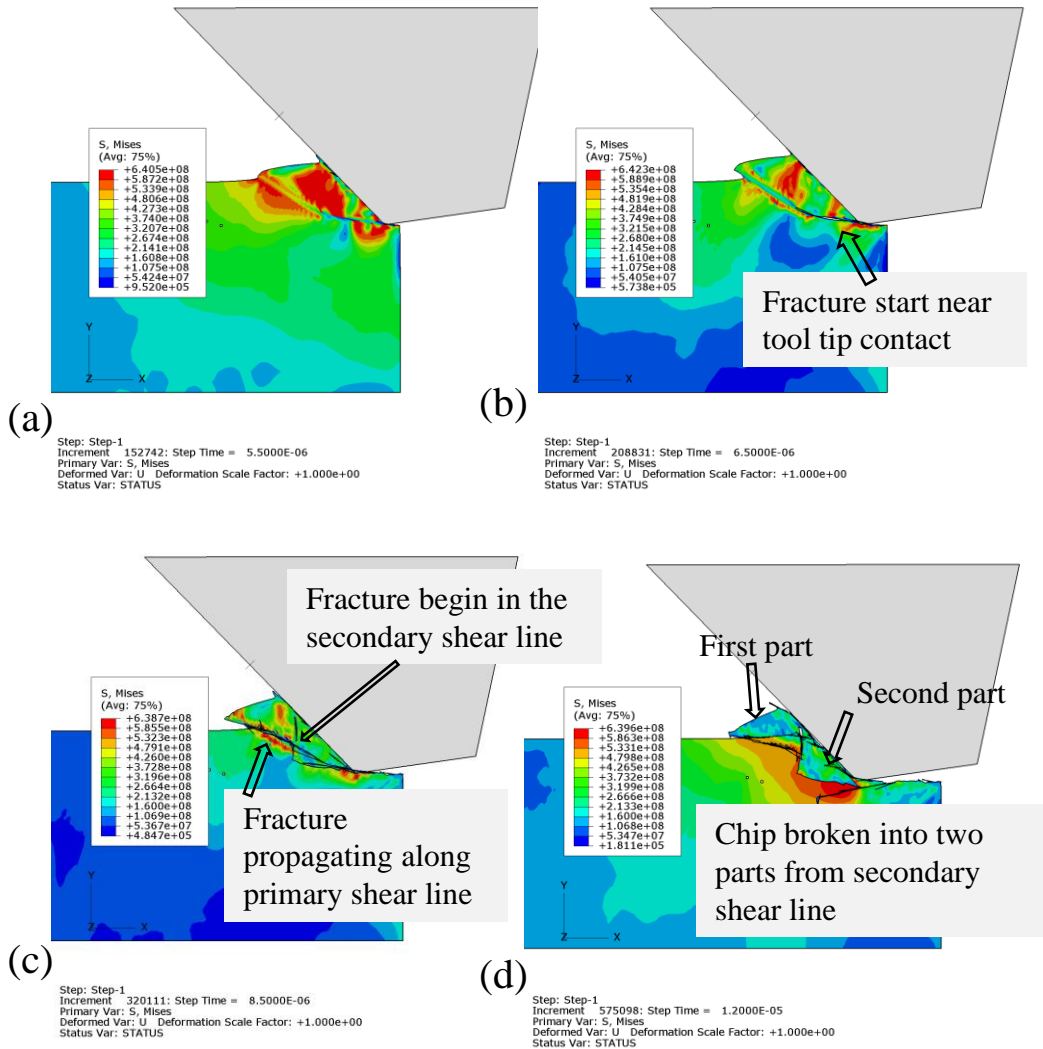


Figure 7.5 Chip fracture development at high negative rake angle ($G_f=1500 \text{ N/m}$, $h=20 \mu\text{m}$)

Chip initiation and primary shear line development is seen in Figure 7.5 (a), fracture initiation begins from the primary shear line near cutting tool tip as shown in Figure 7.5 (b), fracture propagates across the primary shear line and fracture starts in the secondary shear line from the side at the junction of primary and secondary shear lines as shown in Figure 7.5 (c). Finally the chip breaks into two parts; first the upper side of the chip is removed and this is followed by the lower part of the chip.

One reason for the formation of a second chip part (chip fracture into two parts) could be the low fracture energy ($G_f=1500 \text{ N/m}$) input as part of progressive damage evolution. The lower part of the chip could remain as a stagnant region if the fracture energy input increased. However, in case of high fracture energy a problem of program termination due to high element distortion could be encountered. These simulations were performed to show the behaviour of chip formation with varying rake angles but if we assume a material with low fracture energy, these simulations can demonstrate how the chip behaves under such conditions. Figure 7.6 (a) and Figure 7.6 (b) clearly show shear zone formation under high negative rake angle of -45° . Particularly, in Figure 7.6 (b), the shear regions are demonstrated by using material degradation (SDEG) with progressive damage included in the model, which shows a clearer picture compared to the stress distribution seen in Figure 7.6 (a).

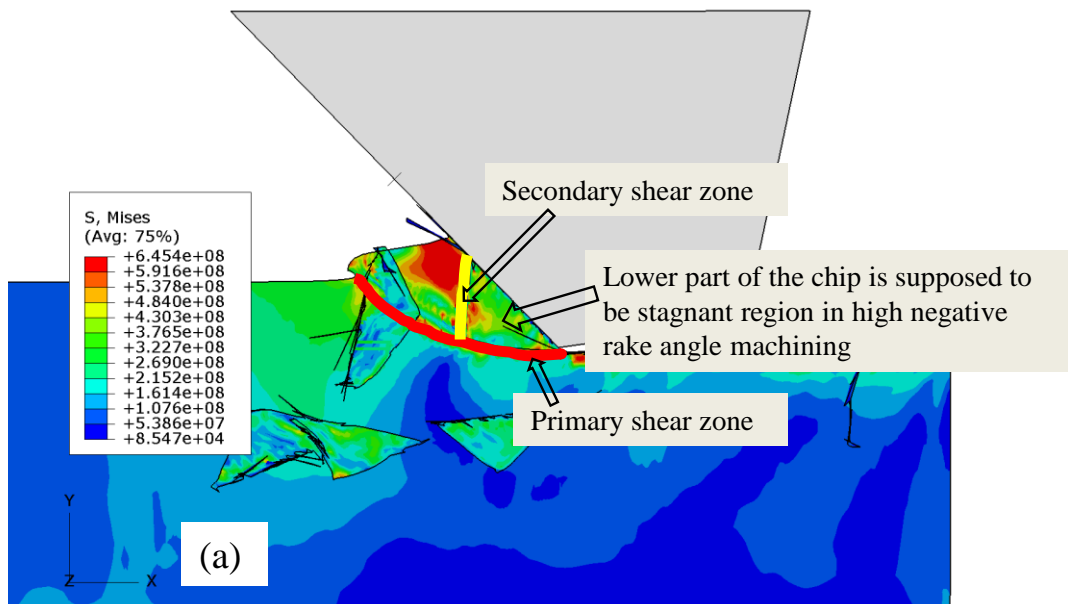


Figure 7.6 Primary and secondary shear zone demonstration at negative rake angle cutting (a) stress demonstration (b) element degradation (SDEG) demonstration (Cont. in next page)

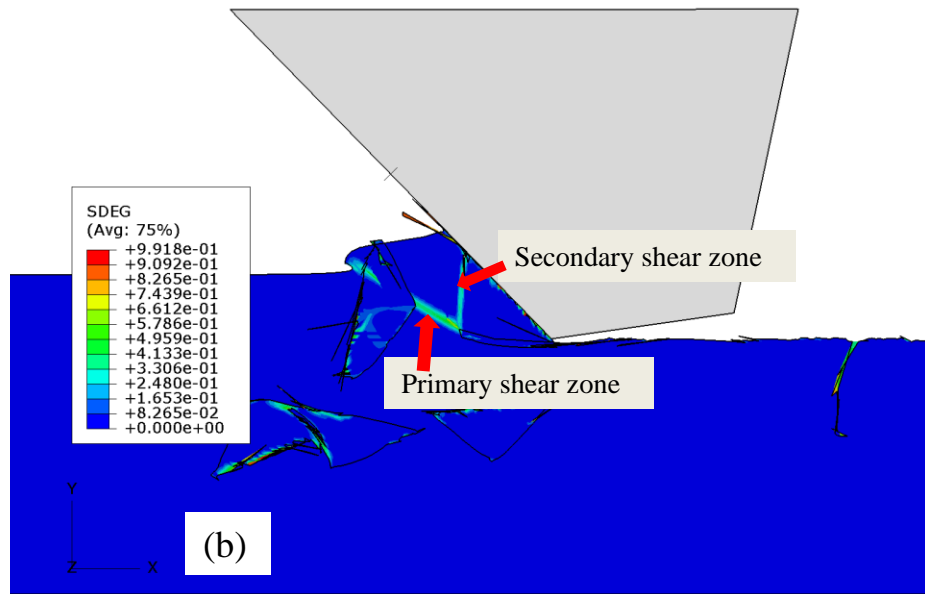


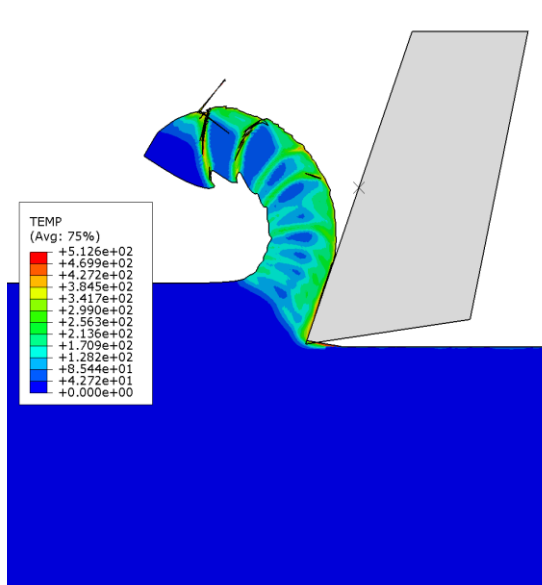
Figure 7.6 (Cont.) Primary and secondary shear zone demonstration at negative rake angle cutting (a) stress demonstration (b) element degradation (SDEG) demonstration

7.2.6 Temperature during chip formation

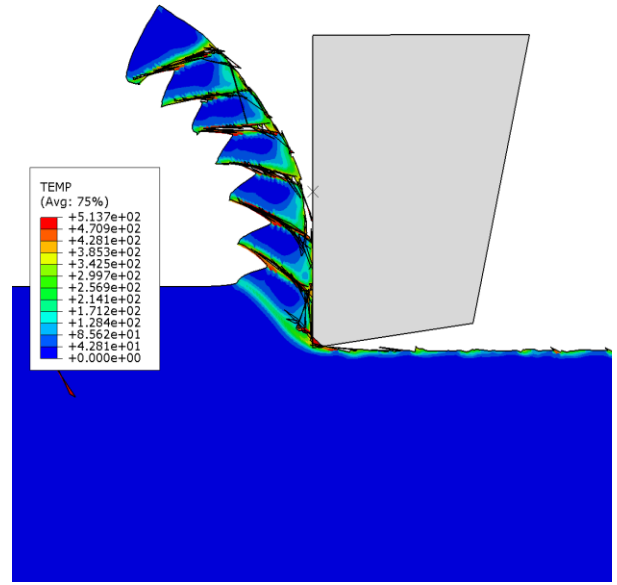
Temperature increases across the shear bands are due mainly to adiabatic heat generation induced by plastic work dissipation. In addition, temperature at the vicinity of tool-chip interface will also increase due to friction between tool-chip interfaces. Figure 7.7 shows the simulated temperature distribution with various tool rake angles while input parameters such as depth of cut (h) and fracture energy per unit area (G_f) remain constant. It is observed that temperature increases across the primary shear line when the rake angle moves from positive to negative values which can be attributed to the increase of plastic deformation intensity. However, higher temperature is observed in the vicinity of tool tip-chip interface because there is both a high level of friction and intense deformation in this region.

Figure 7.8 shows temperature distributions with various fracture energy input which is used as a damage evaluation criterion in the simulations. Both depth of cut and rake angle remain

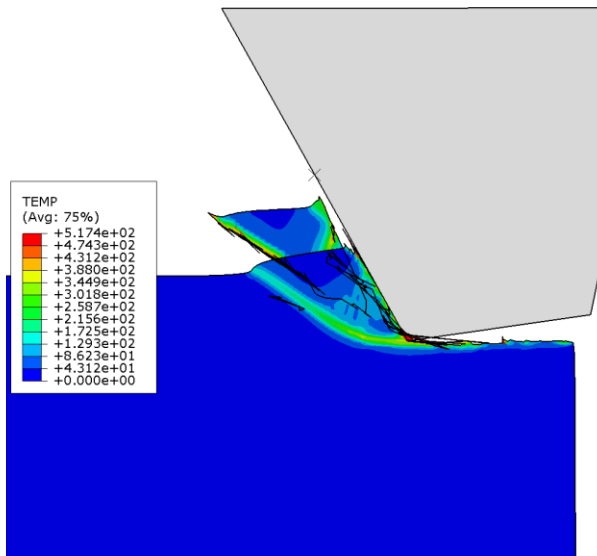
the same for the demonstration in Figure 7.8. As expected, simulations using lower fracture energy result in lower temperature rise in the chip area. Temperature distribution across the chip is more even (Figure 7.8 (d)) with high fracture energy compared to that with low fracture energy (Figure 7.8 (b)). Higher temperature is found near tool tip-chip contact area. The temperature rise along the chip-tool interface is greater for higher fracture energy. For instance, the high temperature band in Figure 7.8 (d) is larger than that in Figure 7.8 (b). This is because, when high fracture energy is used, more energy is required to remove material in the form of chip. As explained in the previous chapter, fracture energy is derived from material toughness, tougher materials need more energy to shape form and cut.



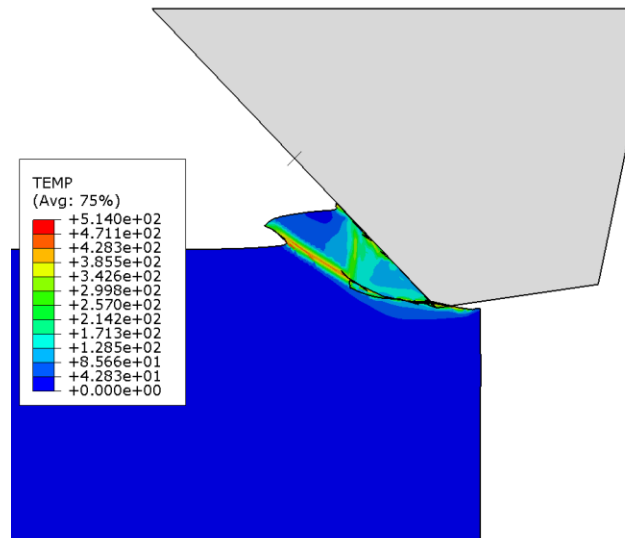
(a) Rake angle = 22°



(b) Rake angle = 0°

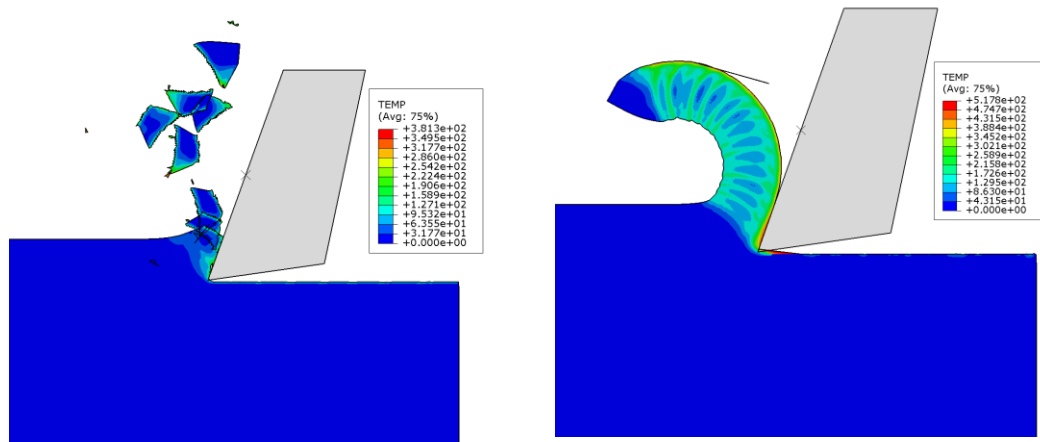


(c) Rake angle = -30°



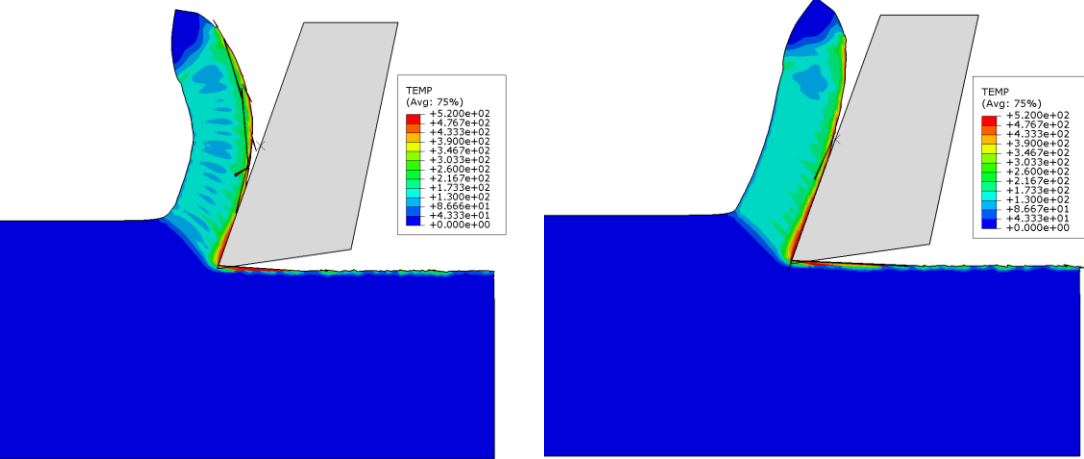
(d) Rake angle = -45°

Figure 7.7 Temperature changes during chip formation ($G_f=1500$ N/m, $h=20$ μ m, temperature unit is in °C)



(a) $G_f = 250 \text{ N/m}$

(b) $G_f = 2500 \text{ N/m}$



(c) $G_f = 10000 \text{ N/m}$

(d) $G_f = 20000 \text{ N/m}$

Figure 7.8 Temperature changes with fracture energy during chip formation (Rake angle= 22° , $h=20 \mu\text{m}$, temperature is in $^\circ\text{C}$)

7.2.7 Plastic strain and strain rate

Both plastic strain rate (ER) and equivalent plastic strain (PEEQ) are good indicators to show the intensive deformation region during chip formation. An example simulation of plastic strain rate, which indicates the deformation speed, is given in Figure 7.9 for chip formation.

According to the simulation, deformation is much faster in the primary shear region than outside the shear region.

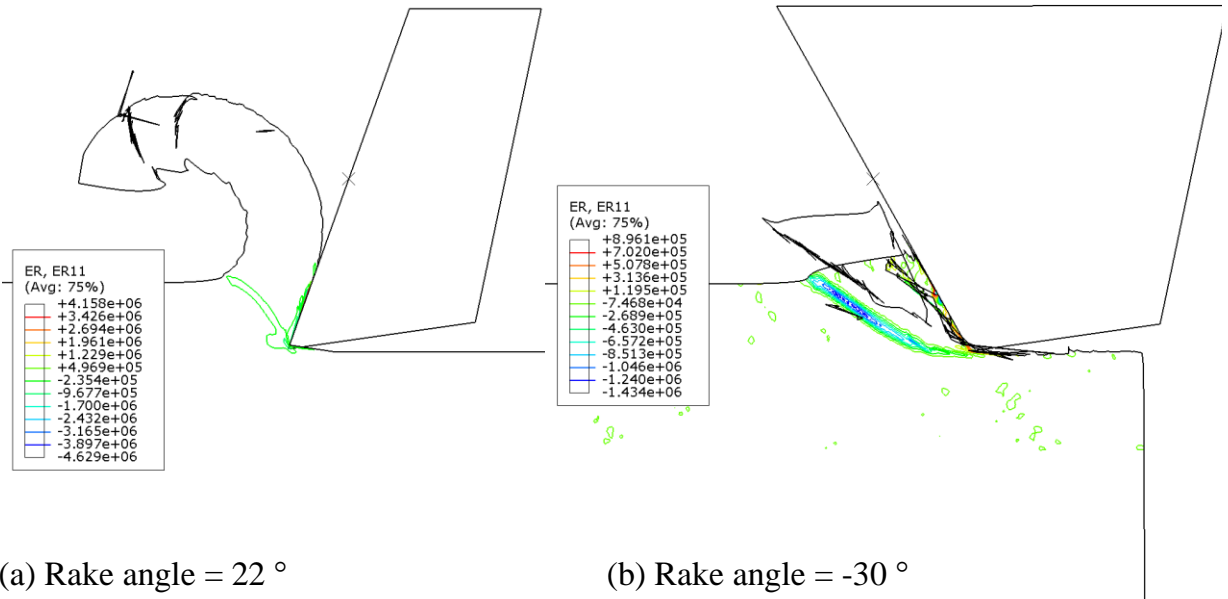
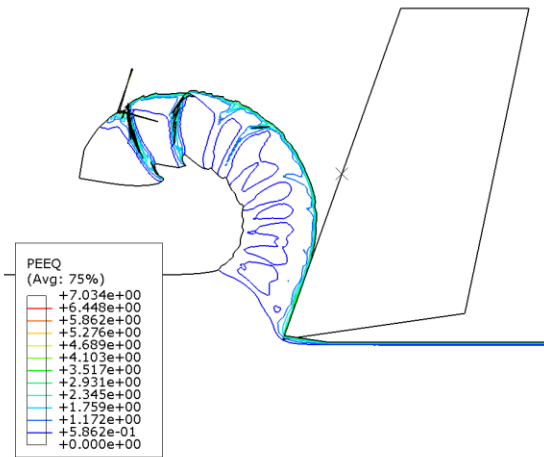
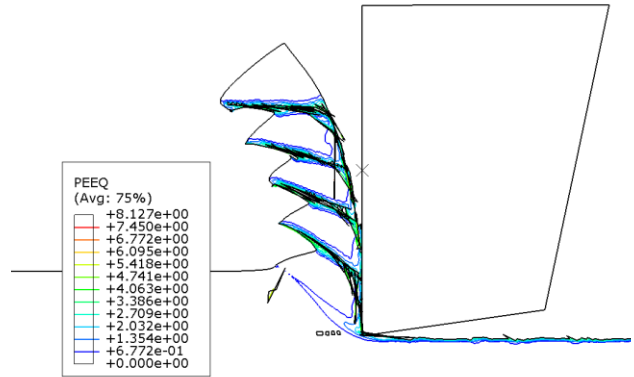


Figure 7.9 Plastic strain rate (ER11) distribution ($G_f = 1500 \text{ N/m}$, $h = 20 \text{ }\mu\text{m}$)

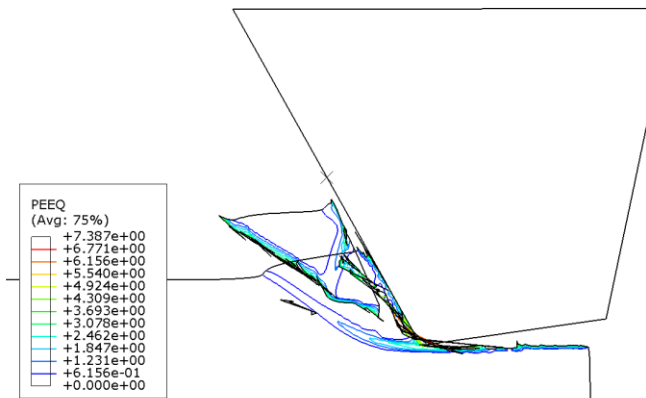
Figure 7.10 shows the PEEQ distribution across the chip formation for various tool rake angles. Strain intensity is higher when segmentation occurs compared to a continuous chip without segmentation. Quantitatively, plastic strain is dependent on the fracture energy; these simulations are performed to explore the behaviour of chip formation under different conditions disregarding real fracture energy or material toughness. So, the results are not analysed quantitatively. The shear localized region (primary shear zone) has higher plastic strain intensity than the remainder of the chip.



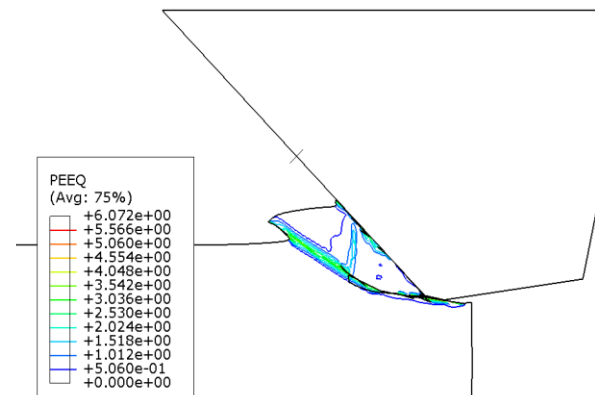
(a) Rake angle = 22 °



(b) Rake angle = 0 °



(c) Rake angle = -30 °



(d) Rake angle = -45 °

Figure 7.10 Equivalent plastic strain (PEEQ) distribution with various rake angles ($G_f= 1500$ N/m, $h=20 \mu\text{m}$)

7.2.8 Summary of cutting simulations

This part of the FEM simulation was intended to demonstrate the effects of some of the influential material parameters and operating parameters on chip formation using finite element simulation. To do this, the Johnson – Cook constitutive material model was used in conjunction

with the Johnson – Cook progressive damage model (using fracture energy as a damage evolution criterion) to reduce mesh dependency. A series of simulation was conducted to show the variation in chip formation with fracture energy, uncut chip thickness and tool rake angle. Continuous, discontinuous and serrated chips were simulated using an Abaqus/Explicit finite element package. According to simulation results, fracture energy dissipation used for damage evolution is an influential factor in determining chip morphology. Very low values of fracture energy lead to discontinuous chip formation whereas increasing the value of fracture energy resulted in continuous chips with a straighter shape. One other essential factor in chip type determination is the depth of cut. According to the simulation results, with increasing depth of cut the chip tends to become more segmented and finally serrated chip generated. In addition, the effects of rake angle in chip formation are simulated. When the tool rake angle is moving from a positive to a negative angle the chips generated tend to become serrated and eventually discontinuous. The influence of rake angle on chip formation is very suitable for investigation by simulation of single grit grinding, where the grit is positioned with a highly negative rake angle during its interaction with the workpiece. It is known the abrasive grit interacts with the workpiece at a highly negative rake angle due to the shape of the abrasive grit and smaller depth of cut compared to the depth of cut in conventional cutting. Chip formation during grinding also takes place in the form of discontinuous or segmented chip of small length compared to the continuous chips that occur during the conventional cutting process. Therefore, FEM simulation using orthogonal cutting principles can give meaningful information on the effects that influential parameters have on chip formation and behaviour in single grit cutting tests

7.3 Single grit FEM simulation results

Several single grit simulations were performed using Abaqus/Standard FEM software. Simulations were performed in 3D considering different material properties, grit simulation trajectory, and element size in the grit-workpiece contact area based on iterative remeshing. With these simulations, influence of depth of cut, friction coefficient, grit size effect and speed on material deformation, particularly ploughing and rubbing, and the forces generated have been investigated. Pile-up ratio was used as an indicator to demonstrate material deformation along the grit simulation path. Cutting phenomenon was investigated in this section because of the FEM limitation at small scale down to 1 μm depth of cut that gives rise to remeshing issues with huge computational time requirements and element distortion which caused program termination at large deformation in the case of cutting action.

Simulations performed in this section are categorized into three groups in order to provide a clear picture of the influential factor during the simulation. In the first group, artificially created plastic material properties are used, which can be considered as a mild steel or lower strength equivalent, this material is used to provide an easy understanding of elastic and plastic deformation states, which could be used to easily detect rubbing during deformation. Multiple grit pass simulations were performed to demonstrate possible ground surface creation as well as investigate friction coefficient effect. In the second group, material properties were kept constant but CBN (single crystal at 20 °C) material properties used for the grit body. Different depth of cuts (maximum depth in the simulation path) and friction effects were investigated. In the third group, the workpiece was replaced by a rate dependent plastic material, AISI4340 steel at 20 °C, together with CBN grit properties. These properties are more consistent with the experimental test conditions (En24T steel, which is equivalent to AISI4340, and CBN grit were used in the

experimental tests) for possible result comparison. Smaller and larger grit size with a radius of 20 μm and 250 μm , respectively, were used to investigate grit size effect on material deformation and simulation working conditions. Using smaller grit size makes the grit act as though it has a sharper cutting edge while grit having large radius makes the grit blunter. Cross-section profiles of the simulated scratches were extracted from Abaqus, and analysed in Matlab to calculate pile-up area and groove area. Area calculation was performed by using trapezoidal numeric integration (using Matlab command: $Z=\text{trapz}(X, Y)$ in Matlab 7.8.0 R2009a).

The reason for the use of three different simulation conditions is that all conditions have some drawbacks to obtaining the necessary simulation output or to observing some important phenomenon. For instance, simulation is easily terminated by heavy element distortion in the case of coarse mesh grit but it works well using a finer grit mesh size. However, coarse mesh size grit might represent real grit better due to having sharp edges (grit asperities). In addition, coarse mesh in the contact area of the workpiece results in poor scratch profile while finer elements in the workpiece contact area results in a relatively good scratch profile but increases computational time. The phenomena investigated here is more about understanding the single grit action physically in respect of the FEM numerical approach rather than modelling using a specific material. The model should be transferrable to simulate single grit action using any material properties.

7.3.1 First group simulations: Using artificially created plastic properties

7.3.1.1 Simulation conditions

The grit and workpiece model is shown in Figure 7.11. Grit radius is 50 μm and grit body was meshed using coarse element size of around 12 μm , while the element size at the contact

region of the workpiece is around 4 μm . Material properties both for grit (similar to Al_2O_3 grit property) and workpiece material (similar to mild steel) is given in Table 7.2. Grit simulation trajectory is illustrated in Figure 7.12, which is composed of five steps. In this group of simulations clearance is 2 μm , and maximum depth of 2 μm is also used to represent depth of cut, see Figure 7.12. Grit speed is not considered and simulation step time is 1 sec for each step, so simulations were performed at very slow speed (100 $\mu\text{m/s}$ horizontal speed).

Table 7.2 Material properties of grit and workpiece for the first group of simulations

Grit material properties (similar to Al_2O_3)		Workpiece material properties (similar to mild steel)	
Mass density (kg/ m^3)	4000	7800	
Young's modulus E (GPa)	530	200	
Poisson's ratio ν	0.2	0.3	
Yield stress σ (GPa)	Plastic strain ϵ_p (mm/mm)	Yield stress σ (MPa)	Plastic strain ϵ_p (mm/mm)
15	0	180	0
15.4	0.03	200	0.1
16	0.2	250	0.25
16.5	0.5	300	0.3

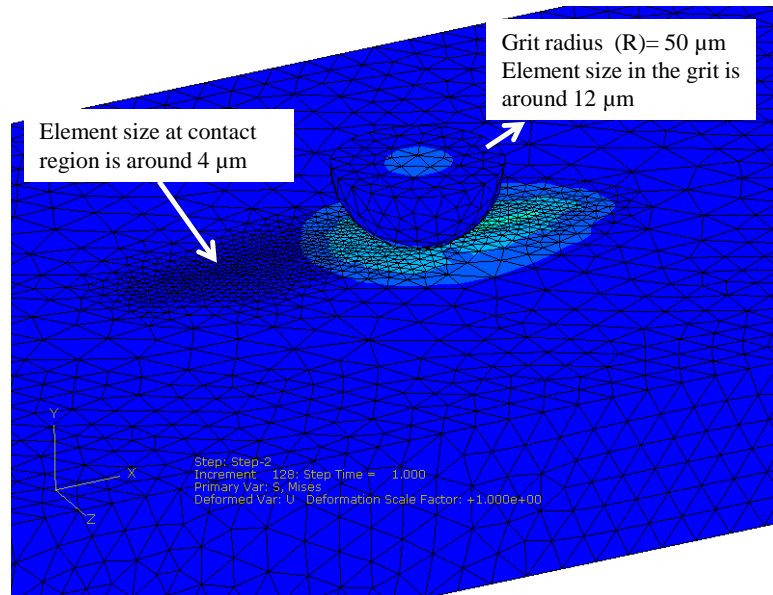


Figure 7.11 Grit and workpiece model for the set of simulations in this group

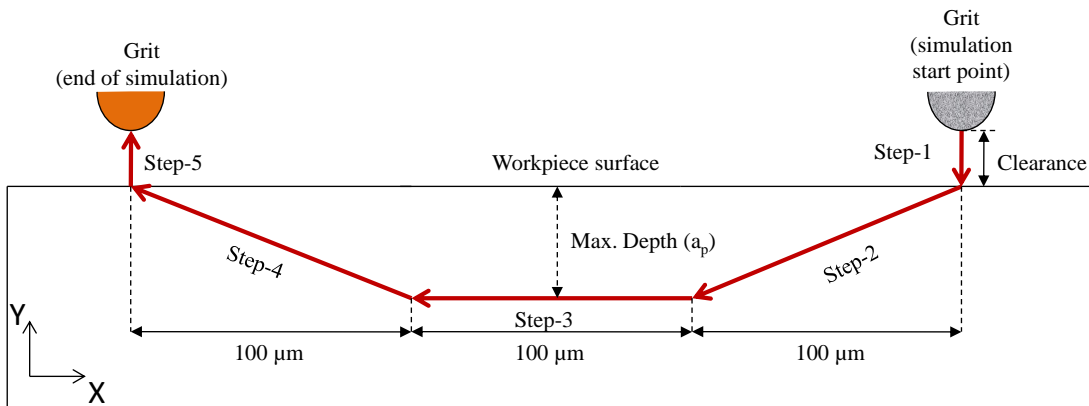


Figure 7.12 Single grit trajectory during simulation using five steps

7.3.1.2 Elastic-plastic deformation

Scratch formation in the single grit grinding process normally begins with a rubbing action, followed by ploughing and finally cutting. The rubbing action does not include plastic

deformation, it occurs at the initial elastic stage of scratching when the grit starts to penetrate into the workpiece; in this range the grit only slides over the workpiece without generating any permanent marks but this range is extremely small and is difficult to measure in either experiment or simulation. However, ploughing action includes both elastic and plastic deformation and is more apparent. Looking at the simulation results, Figure 7.13 shows the stress distribution along the single grit scratch. Ploughing action that occurred during simulation is captured from the end of step-3 is as shown in Figure 7.13 (a). Elastic-plastic deformation at the moment of grit-workpiece engagement is very obvious because of the artificial plastic properties used. The deepest point shows the elastic and plastic deformation together where the grit engaged with workpiece at that instant. Elastic deformation recovered after grit moved away from the contact, and only plastic deformation effects remain in the workpiece material. Front pile-up ahead of the grit is also seen; this can be attributed to the initial step of chip formation which can occur when the front pile-up reaches a certain amount and meets the chip formation criteria, which is not the case in these simulations.

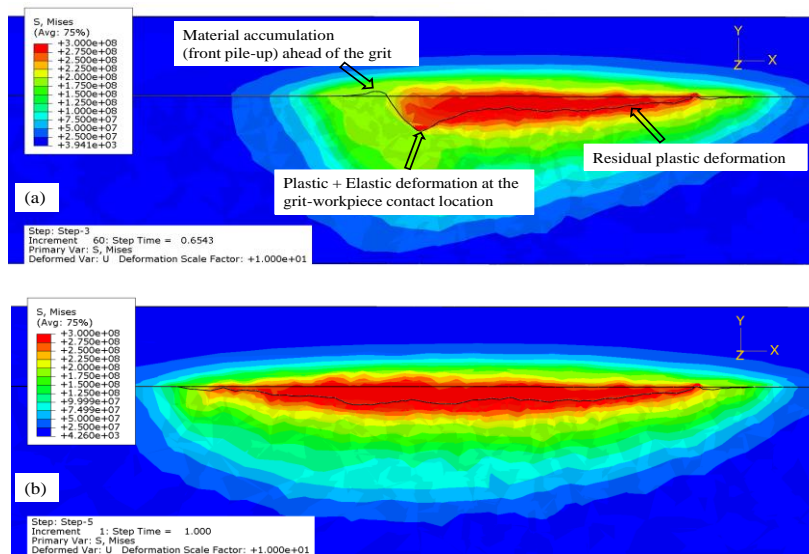


Figure 7.13 Stress and elastic-plastic deformation state representation (frictionless simulation result longitudinal representation of scratch)

Elastic deformation depends on the conditions when the grit engages with the workpiece. Observation of the rubbing phase is quite difficult using FEM simulation because the rubbing phase is supposed to not include any plastic deformation, but in practice the meshed elements show plastic strain components even at first contact. To measure parameters associated with the rubbing phase, it is necessary to make some acceptable assumptions on a measurement method. If maximum plastic strain is used as an indicator, contour plastic strain distribution along the simulated scratch will give some information about the rubbing phase as shown in Figure 7.14. The length between first contact point and starting point of light blue colour plastic strain distribution can give an approximate measure of rubbing length. With this method, the rubbing length is measured as $5.825 \mu\text{m}$ in the simulated frictionless condition. Because the plastic strain will affect the adjacent area, this method gives a lower estimate of the value. In order to measure the indentation depth at the end of the rubbing phase, initial grit indentation due to grit asperity caused by coarse mesh size must be taken into consideration. The indentation depth at the end of step-1 is measured as $0.205 \mu\text{m}$. The indentation depth at the end of rubbing length is evaluated as $0.322 \mu\text{m}$.

Rubbing length can also be measured by making a different assumption; the rubbing phase exists until the deformation along the scratch length become obvious. Deformations after a certain length, which depends, on depth become heavier and it looks like there is a transition point as shown in Figure 7.15. This region certainly includes plastic deformation but the rate is very small compared to the later sections of the scratch, so this small region can be attributed to the rubbing phenomenon occurring in actual grinding. In this case, rubbing length is measured around $24 \mu\text{m}$ while rubbing transition depth is measured as $0.685 \mu\text{m}$. Such a measure will be larger than the real value. Therefore the rubbing stage length can be judged to be in the range of $5.825 \mu\text{m}$ to $24 \mu\text{m}$ (where the mesh sizes are around $4 \mu\text{m}$ in the workpiece contact region). It

can be seen that the rubbing phase occurs over a very small portion of a scratch and the length of the rubbing region will depend on depth of cut of the individual grits during grinding. Recently, Doman et al., (2009^a) tried to distinguish between rubbing and ploughing phases using FEM, they used force variation to catch the transition point, and suggest that the rubbing-ploughing transition occurs at a 3 μm depth for AISI4340 steel. FEM simulation results presented in this thesis show that plastic deformation (ploughing phase) certainly exists at less than 3 μm depth for the steel. The results suggest that further study is needed on the elastic-plastic boundary.

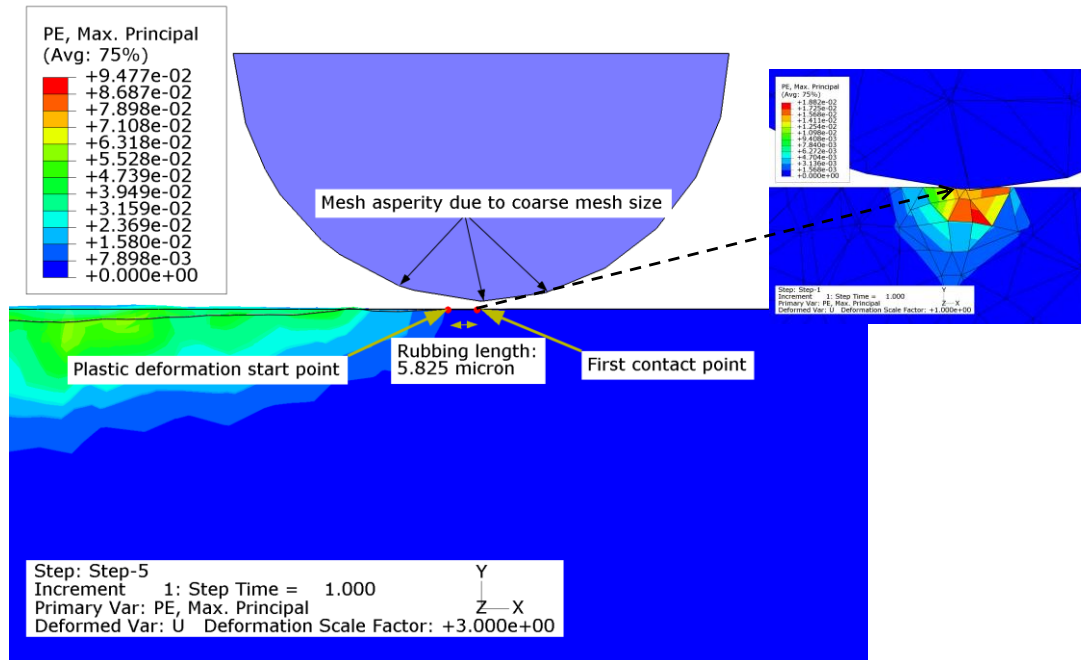


Figure 7.14 Rubbing phase demonstration using plastic strain contour as an indicator (frictionless simulation result)

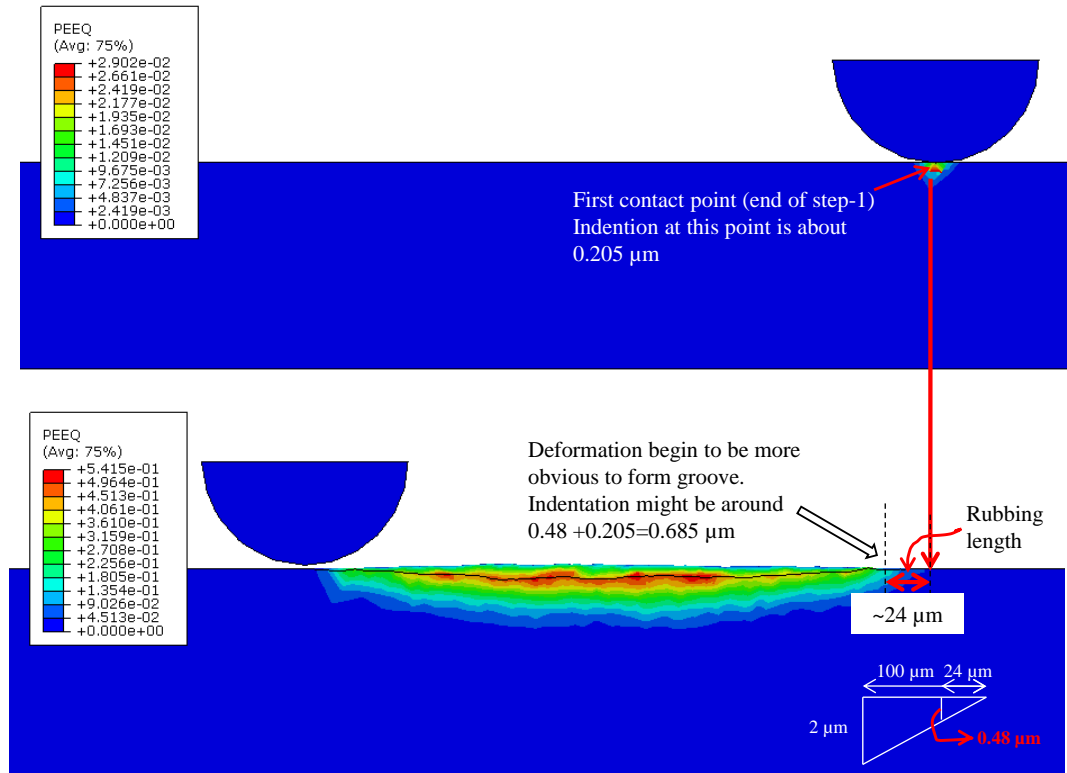


Figure 7.15 Rubbing phase demonstration using heavily deformation region as an indicator (frictionless simulation result)

7.3.1.3 Multiple-pass simulation to represent ground surface creation

In grinding, the rubbing phase is an elastic deformation which does not create new surface. Ploughing is a plastic deformation which pushes material away from its original position, forming a new surface. Chip formation removes materials from workpiece due to excessive plastic deformation. In grinding, a large proportion of the grinding action is ploughing and this is the major factor that in determining final surface features. A simulation has been designed to demonstrate how ploughing could affect the generation of ground surface in grinding. Single grit transverse scratching was performed three times 10 μm apart. Figure 7.16 shows the surface generated after three consecutive grit scratches.

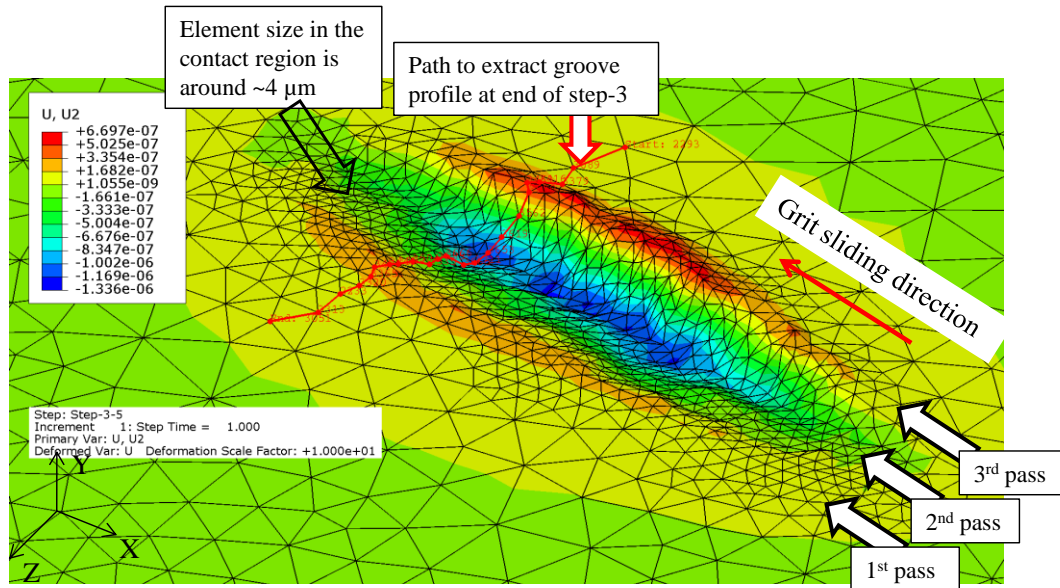


Figure 7.16 Simulated multiple pass surface creation

Figure 7.17, obtained from the end of step-3 in the grit simulation path, shows consecutive grit passes push material aside forming ridges which alter the ground surface. Cross-sectional scratch profiles were extracted using a path based on element nodal locations selected at the end of step-3 as shown in Figure 7.16. Using this scratch profile, pile-up ratios are calculated based on the ratio of pile-up area to groove area, see Figure 7.18. There is no significant change on pile-up ratio with subsequent scratch formation. Both pile-up area and groove area increases at every subsequent scratch and the pile-up ratio vary between 0.72 and 0.86. However, subsequent scratches give larger groove depth and the groove shape becomes non-symmetrical as shown in Figure 7.17 and Figure 7.18. The depth of groove increases with subsequent scratches and this can be attributed to the elastic-plastic deformation mechanism. With subsequent scratches the grit deforms material which was already deformed by a prior grit pass, thus the elastic recovery behaviour of the material become weaker with the increase in number of scratches. The change in elastic-plastic behaviour of the material results in a deeper groove with increase in scratch

number during multiple pass scratch formation. Subsequent scratches increase the pile-up area on both sides but increase rate is higher in the direction of the grit's traverse movement.

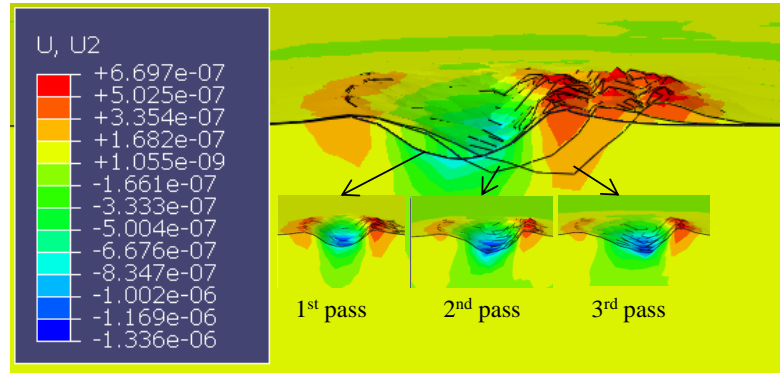


Figure 7.17 Deformation in the simulation of three parallel scratch passes 10 μm apart.

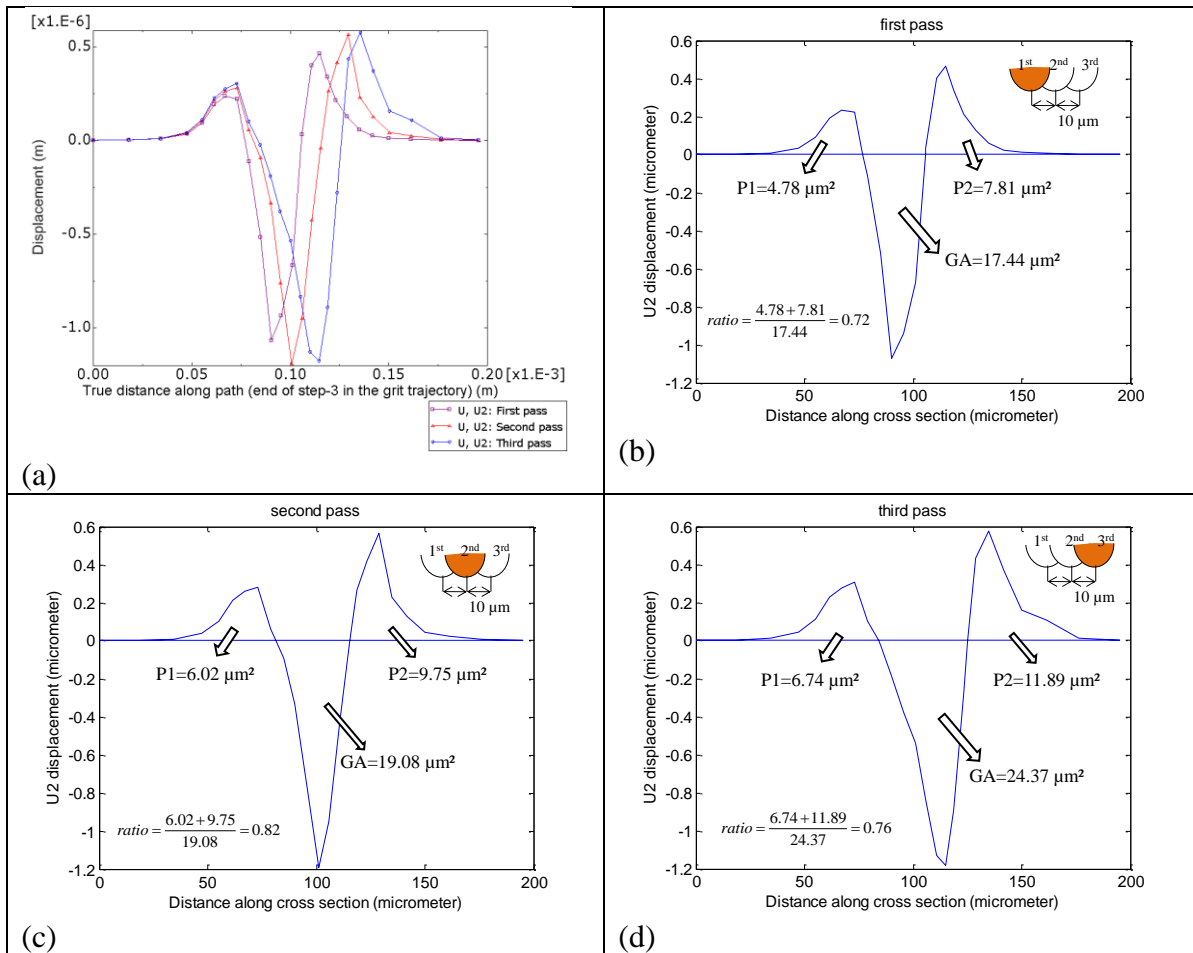


Figure 7.18 Multi-pass scratch profiles

7.3.1.4 Friction effects on deformation

Finite element simulation has provided results that satisfactorily illustrate the influence of friction coefficient in grinding. By using different coefficients between contact surfaces it has revealed that the friction coefficient promotes the ploughing rate in both vertical and horizontal directions as shown in Figure 7.19, where the ploughing ridge is the highest when $\mu = 0.5$ and lowest without friction ($\mu = \text{zero}$).

The simulation also shows that ploughing pushes materials forwards while the grit advances, which can be seen from the cross-sectional profile obtained at the end of step-3 in Figure 7.20. Thus, the higher the friction, the more material pushed forward. Deformation in transverse direction (see Figure 7.20) increases with increase of friction coefficient. Thus, the simulated scratch ridge formed in the absence of friction is narrower than the ridge formed when friction is present. The pictures are captured from the Abaqus viewport and the deformed part is magnified 10 times otherwise it is not easy to see the ridge and deformation on the figure.

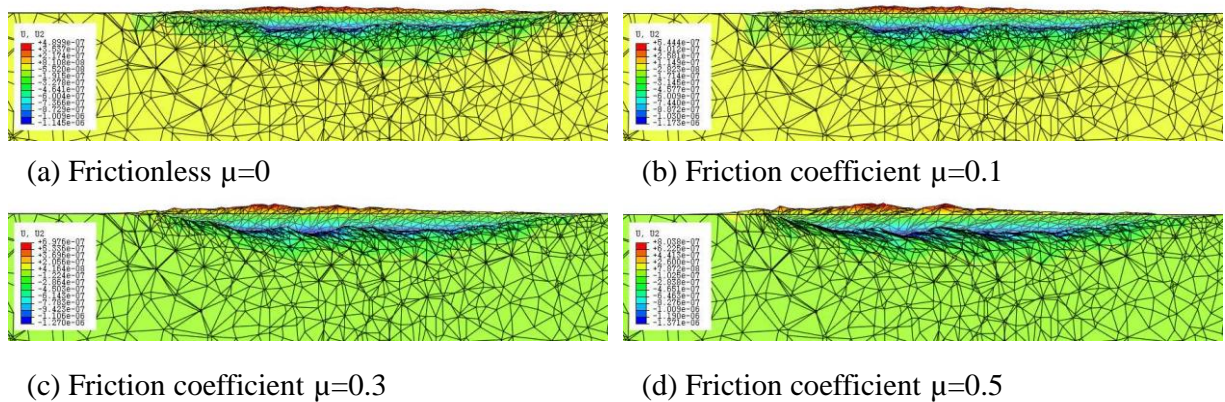


Figure 7.19 Scratches formed using different friction coefficients (sectional view from longitudinal direction)

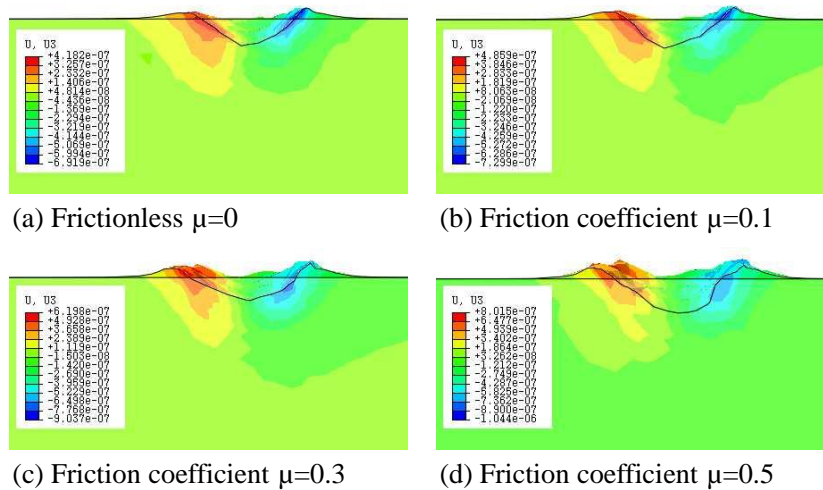


Figure 7.20 Ploughing action profiles taken from the cross-section at the end of step-3

Cross section profiles at the end of step-2 and step-3 were also extracted from Abaqus, analysed in the Matlab and the cross-sectional profiles plotted in Figure 7.21. Looking at the cross-sectional profiles extracted at the end of step-2 (Figure 7.21 (a)), it can be seen that the greater the friction coefficient the deeper the cross-section profiles obtained, but no significant change in side pile-up (ridge) was observed with change in friction coefficient. The cross-sectional profiles extracted at the end of step-3 (Figure 7.21 (b)) have almost similar depth while the side pile-up becomes significantly larger. Both height and width of the pile-up material increased with increased friction coefficient and with the further advance of grit in the horizontal direction.

Cross-sectional groove area and pile-up area profiles at the end of step-2 and step-3 are evaluated in Figure 7.22. Pile-up ratio is calculated based on pile-up area and groove area as shown in Figure 7.23. At the end of step-2 the pile-up ratio decreases slightly with increase of friction coefficient. However, at the end of step-3 the pile-up ratio increases with the increase of friction coefficient. Note that the end of step-3 is the beginning of step-4 where the grit is

moving up. The difference in trends for the pile-up ratio with change in friction coefficient shows that the deformation mechanism is different when grit is moving down (step-2) and moving up (step-4). Thus, friction between surfaces is more effective in deforming the material plastically when the grit moves downward. Increase of friction coefficient makes it more effective to push the material ahead of the grit when moving in a horizontal direction and results in more material accumulation in front of the grit. Also note that scratch profiles at the end of step-2 and step-3 are approximate locations picked using element nodes but the same path was used for profiles at the same steps.

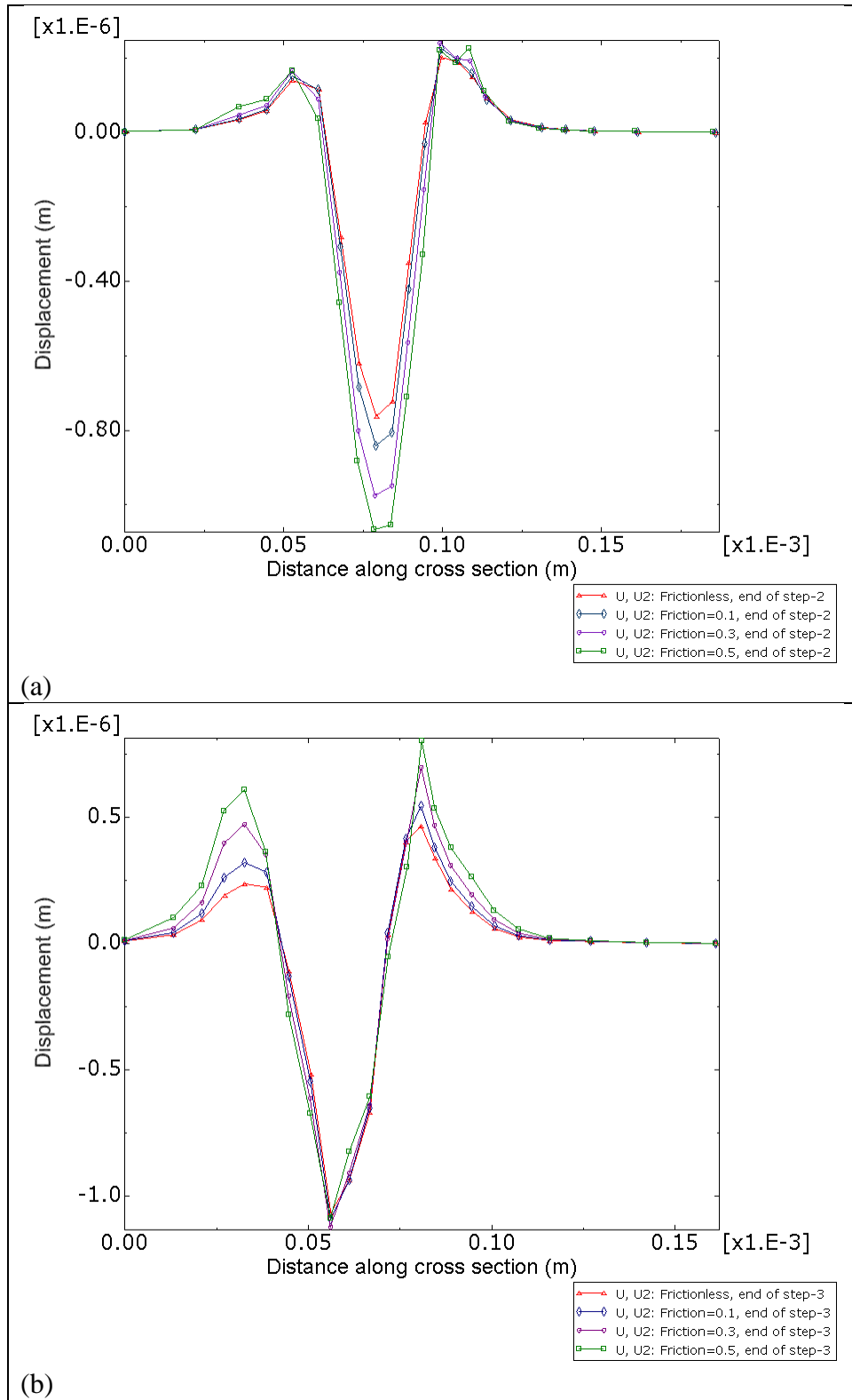


Figure 7.21 Scratch cross-section profiles (a) at the end of step-2 and (b) at the end of step-3 using different friction coefficient

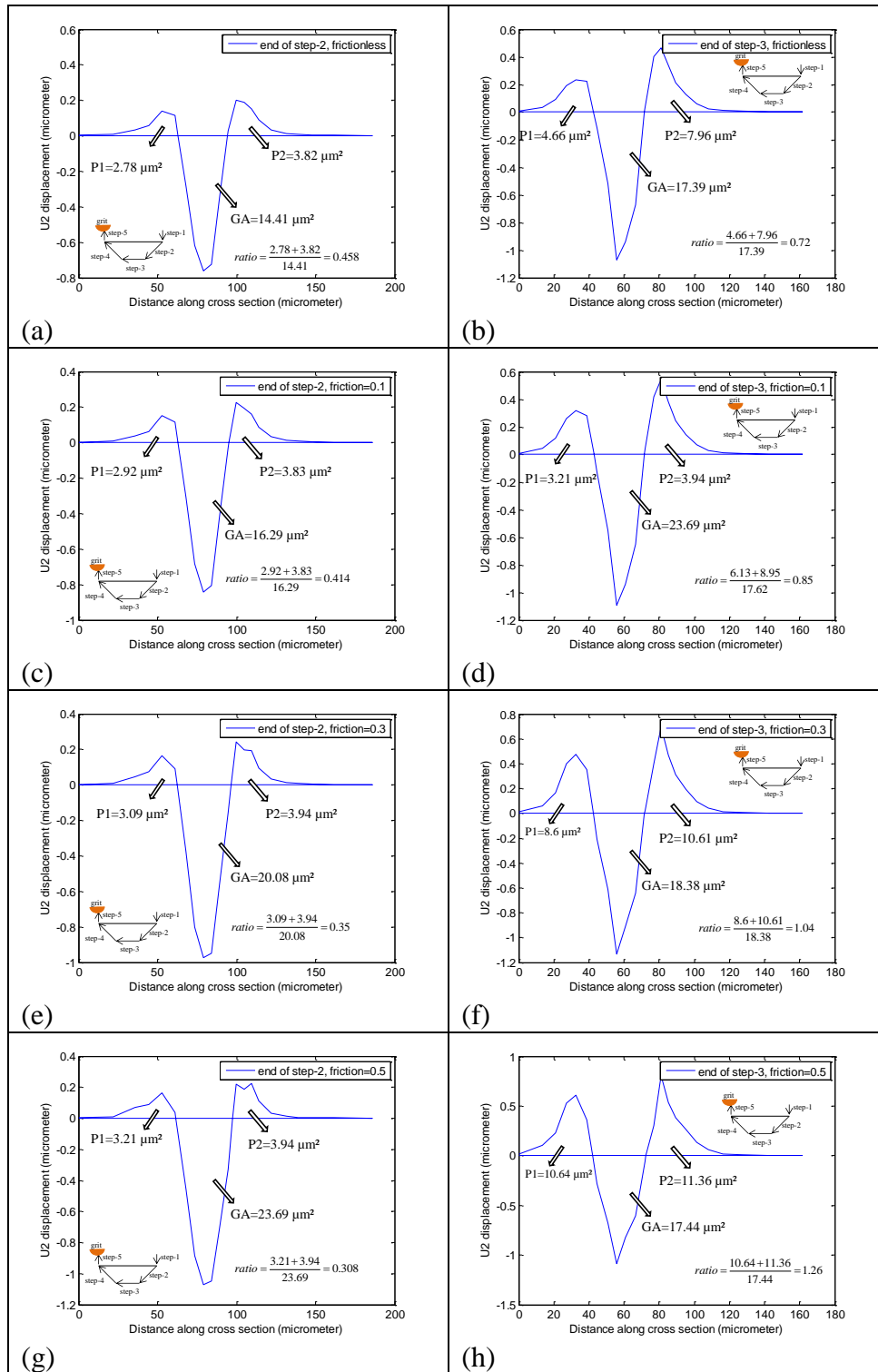


Figure 7.22 Cross section profiles of the starches using different friction coefficient

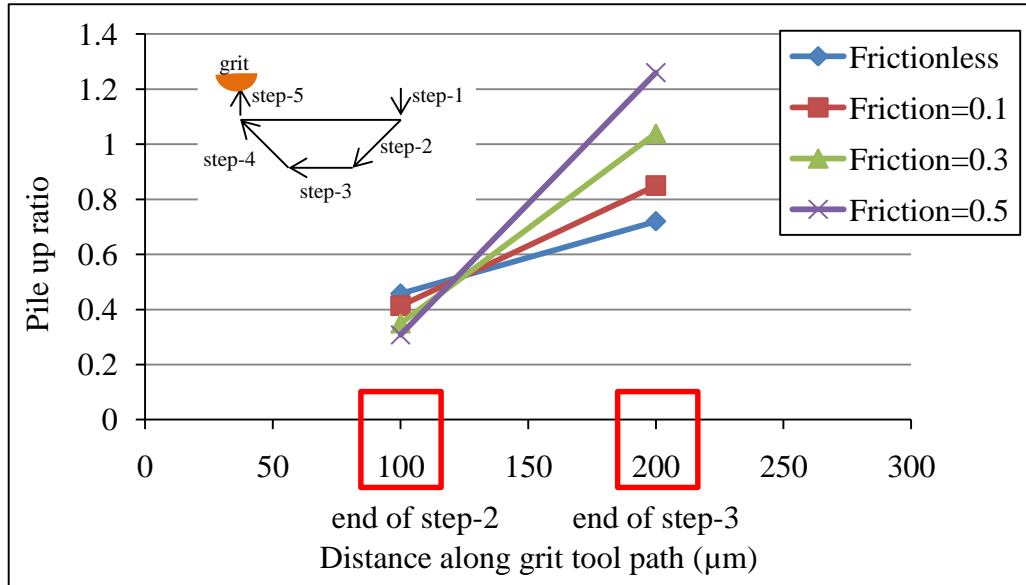


Figure 7.23 Pile-up ratio at the end of step-2 and step-3 using different friction coefficients

7.3.1.5 Force analysis

Force variation in single grit simulation depends on the grit simulation path. Figure 7.24 shows the grit simulation path with steps and corresponding horizontal distances, which can be useful for reference when describing force variation. Figure 7.25 shows the force variation through the grit simulation path for three consecutive cross passes. There is little variation in either the normal force (F_y) or the tangential force (F_x) between first, second and third passes, except for step-3 where F_y appears to be slightly higher in the first grit pass. However, increasing volume of side ploughing with number of cross passes leads to an increase of traverse force component (F_z). Material accumulation (front ploughing) ahead of the grit when the grit advances along step-3 leads to increase of tangential forces (F_x) for every cross passes as shown in Figure 7.25.

Friction coefficient between grit and workpiece surface also affects the force variation along grit simulation path. Both tangential (F_x) and normal (F_y) forces increase with the friction coefficient as shown in Figure 7.26, however, the increase of tangential force is higher than that of the normal force. The greater increase in tangential forces could be influenced by the increasing rate of front ploughing (material accumulation ahead of the grit) with increasing friction coefficient. The more material accumulates ahead of the grit the more force is required to move the material. Figure 7.27 shows the variation in total force for the three cross passes with different friction coefficients. Total forces were greater at every subsequent cross pass with increase of friction coefficient. In the first pass, total force gradually increases along step-3 (constant depth of cut) with grit advancement. However by the third pass the total forces are almost constant along step-3. This can be attributed to passes-1 and 2 which loosen the material accumulation and the force become more stable at a given depth of cut.

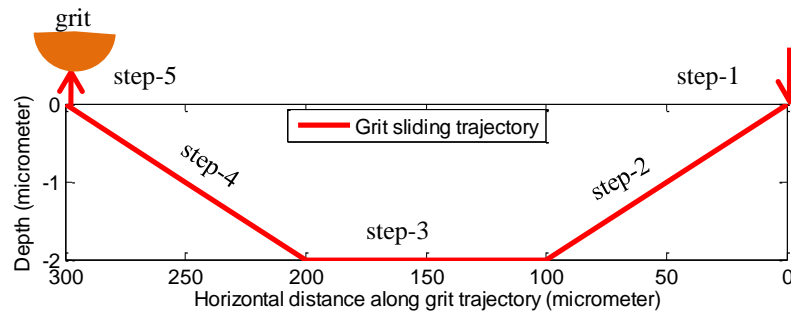


Figure 7.24 Single grit simulation path with depth and horizontal distance demonstration

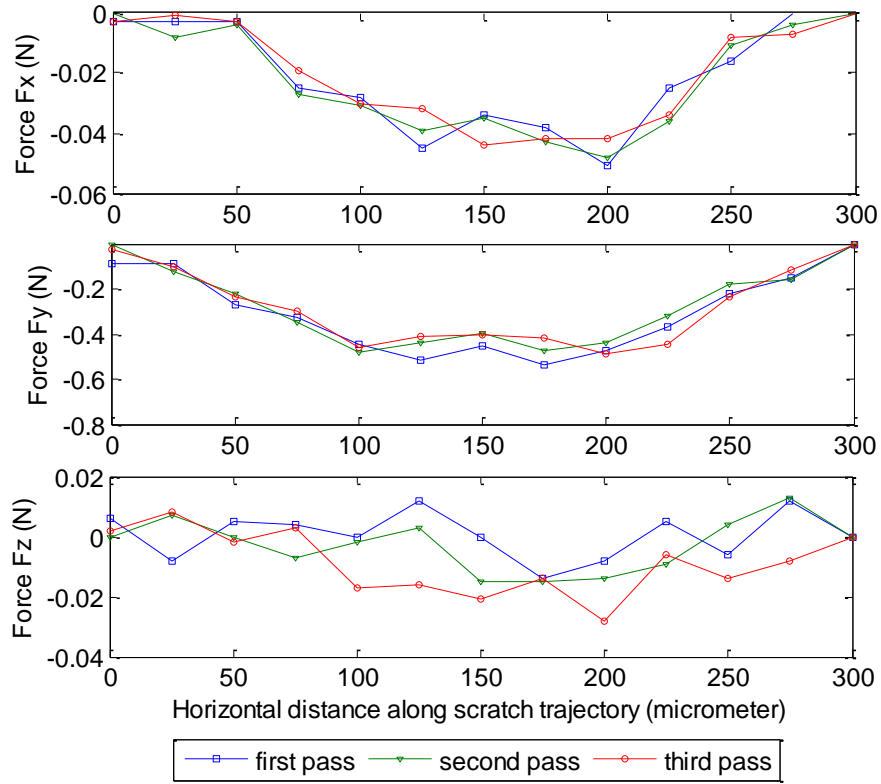


Figure 7.25 Force components for multi pass simulation (frictionless condition)

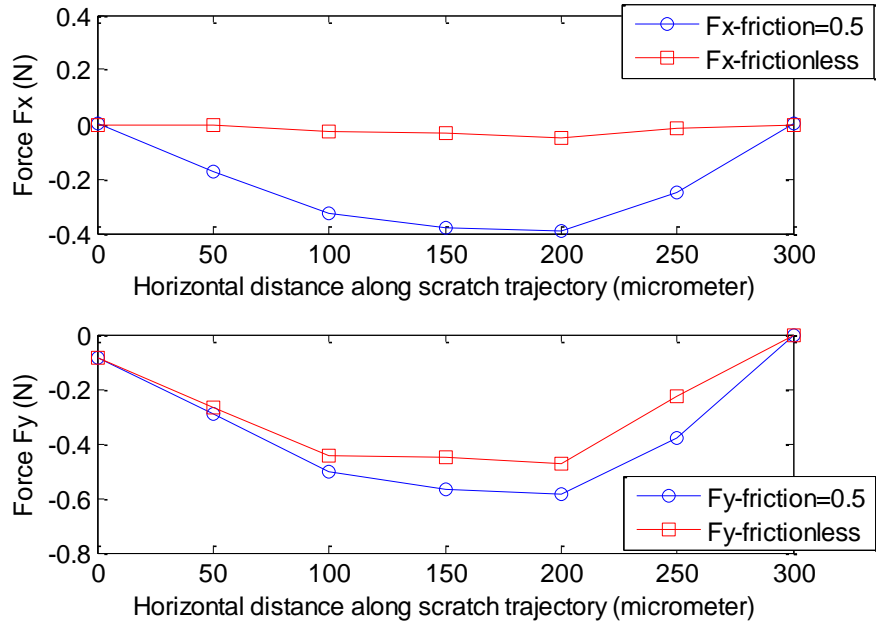


Figure 7.26 Force components: frictionless and friction coefficient of 0.5

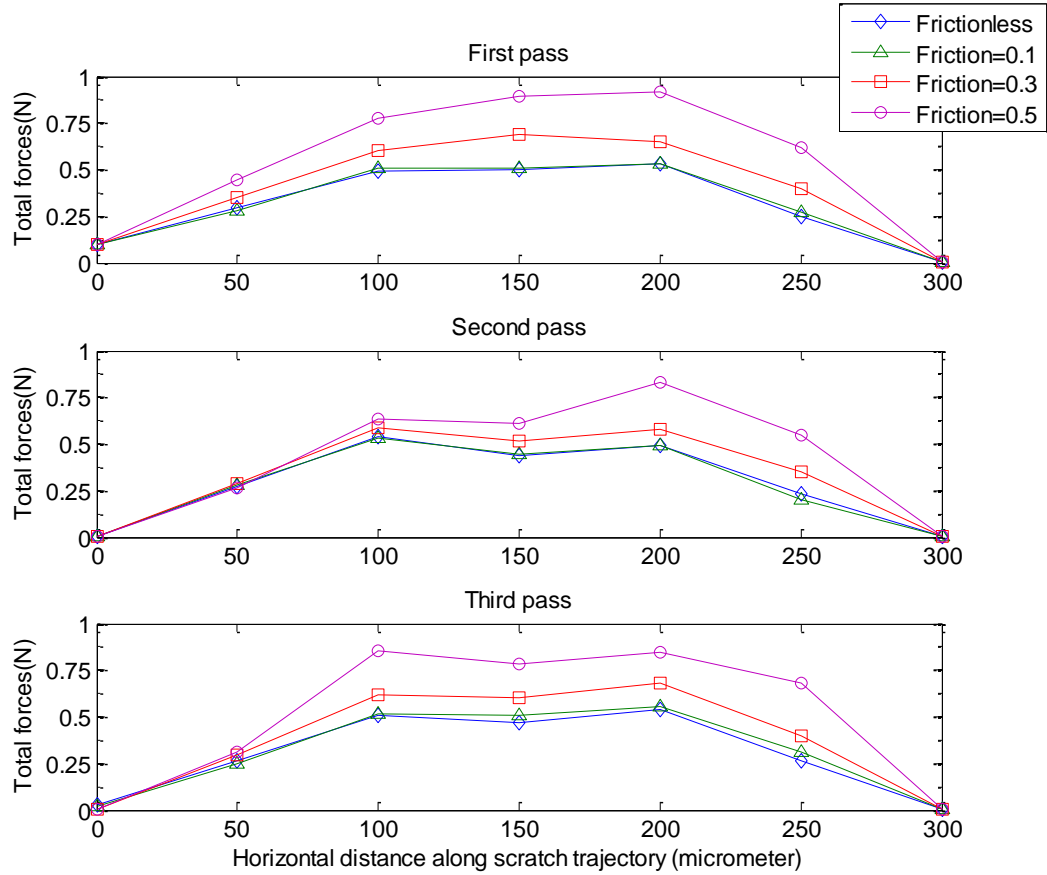


Figure 7.27 Variation in total force (absolute values) with friction coefficient and cross-pass scratching

7.3.2 Second group simulations: Using CBN grit properties

7.3.2.1 Simulation conditions

The workpiece material properties remained the same as given in Table 7.2 but the grit was replaced by CBN (Cubic Boron Nitride) with Young's modulus $E=909$ GPa, Poisson's ratio $\nu=0.121$, and density $\rho=3400$ kg.m⁻³, in the shape of a hemispherical solid with a radius 100 μm . Further remeshing was applied to the workpiece to reduce the element size and increase scratch profile accuracy. Element size in the workpiece contact region is less than 1 μm while element

size in the grit body is around $4\ \mu\text{m}$. The grit-workpiece model is shown in Figure 7.28. A similar grit simulation path was used as in the first group simulation, see Figure 7.12. The maximum depth defined in step-3 was changed from $0.5\ \mu\text{m}$ to $5\ \mu\text{m}$ using friction coefficients of zero and 0.2 to investigate the effect on ploughing and grit forces. Other parameters remained constant with the simulations performed as the first group. Total number of elements used in the simulation is 184085. Approximate CPU time for each simulation is 48 hours using a computer with an Intel(R) core(TM) i7 CPU 960 @ 3.20 GHz and 12 GB of RAM. Figure 7.29 shows a 3D view during grit simulation when maximum depth setting is $2\ \mu\text{m}$ and without friction. Material accumulation while the grit advances along the scratch path is better performed using finer mesh size in the contact area.

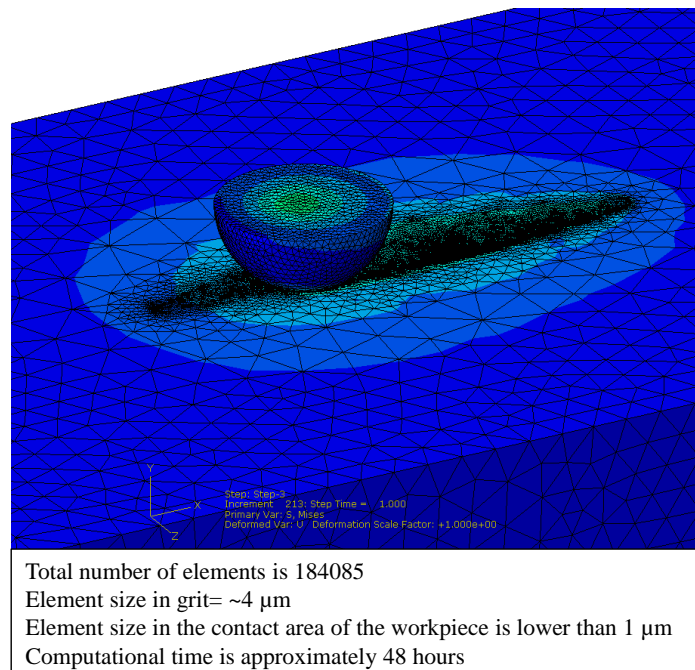


Figure 7.28 Grit-workpiece model used in the second group simulations

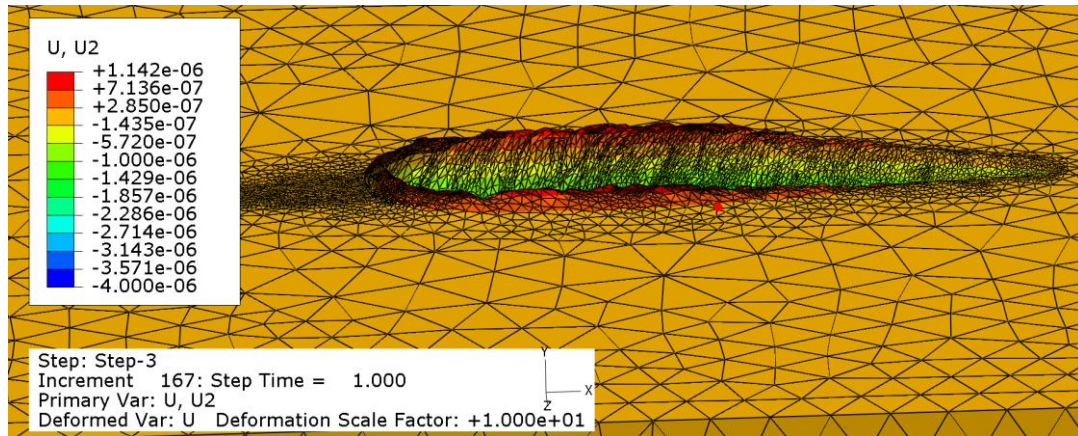


Figure 7.29 A view during grit advancement showing accumulation of workpiece material in front and side of grit ($a_p = 2 \mu\text{m}$ and $\mu = 0$)

7.3.2.2 Simulation results

Figure 7.30 shows the deformation due to grit contact for the first scratch for frictionless contact with maximum depth of $5 \mu\text{m}$; at the end of step-1 there is material ploughing with side pile-up across the simulation. Figure 7.30 (middle picture) also shows elastic and plastic deformation during grit-workpiece engagement at the end of step-3. At this point, the total deformation during grit-workpiece engagement at the end of step-3. At this point, the total deformation in vertical direction including elastic and plastic components is around $5.36 \mu\text{m}$, but total deformation at the end of simulation after grit is moved away at the end of the simulation path is around $4.1 \mu\text{m}$. The difference of $1.16 \mu\text{m}$ can be attributed to elastic deformation occurring during the simulation caused by the (artificial) plastic properties of the workpiece material. Looking at the bottom picture in Figure 7.30, the groove depth at the end of step-3 is smaller than given depth of cut ($5\mu\text{m}$). This probably happened due to grit moving upward in step-4, and the grit pushed down some material under it and this leads to a decrease of groove depth when commencing the step-4. Figure 7.31 demonstrates the deformation of material with various depth of cut and friction coefficient due to grit slide, where the figures were captured

when the grit positioned at the end of step-3. All the simulations have an initial indentation of $0.41 \mu\text{m}$ at the first step, and maximum depth is added onto the initial indentation. According to results, the height of pile-up material is around half of maximum depth for the frictionless condition, and is almost the same as the maximum depth when friction coefficient is 0.2. This means friction between grit and workpiece results in increase of ploughed material in grinding. The cross-sectional profiles were extracted and analyzed to calculate groove area and pile-up area in Matlab. Figure 7.32 shows the cross sectional profiles for the approximate middle of step-2, end of step-2, end of step-3 and approximately the middle of step-4 together with calculated pile up and groove areas as well as corresponding pile-up ratios. Profiles in Figure 7.32 are analysed and discussed in Figure 7.33 and Figure 7.34.

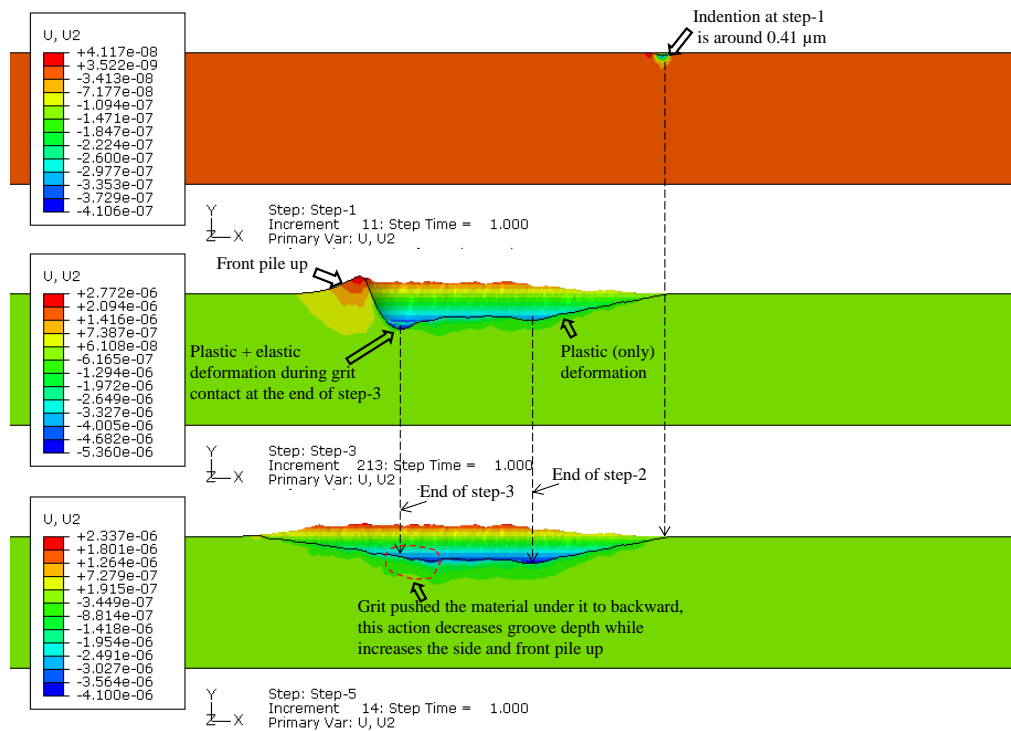
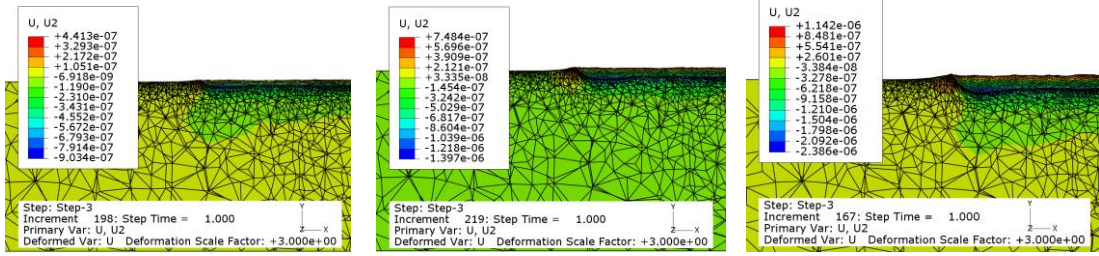


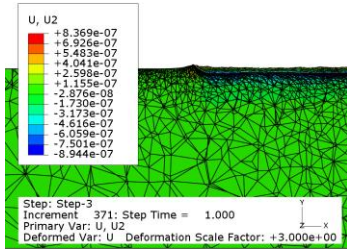
Figure 7.30 Simulation of grit progress at first indentation, middle and end of simulation (frictionless; $a_p = 5 \mu\text{m}$)



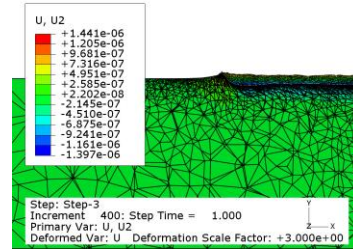
(a) frictionless, $a_p=0.5 \mu\text{m}$

(b) frictionless, $a_p=1 \mu\text{m}$

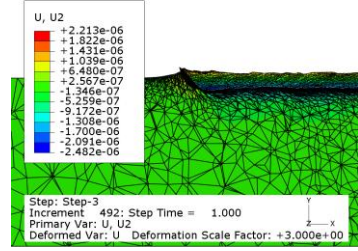
(c) frictionless, $a_p=2 \mu\text{m}$



(d) $\mu=0.2$, $a_p=0.5 \mu\text{m}$



(e) $\mu=0.2$, $a_p=1 \mu\text{m}$



(f) $\mu=0.2$, $a_p=2 \mu\text{m}$

Figure 7.31 Deformation due to ploughing effects with single grit simulation (a_p : maximum depth)

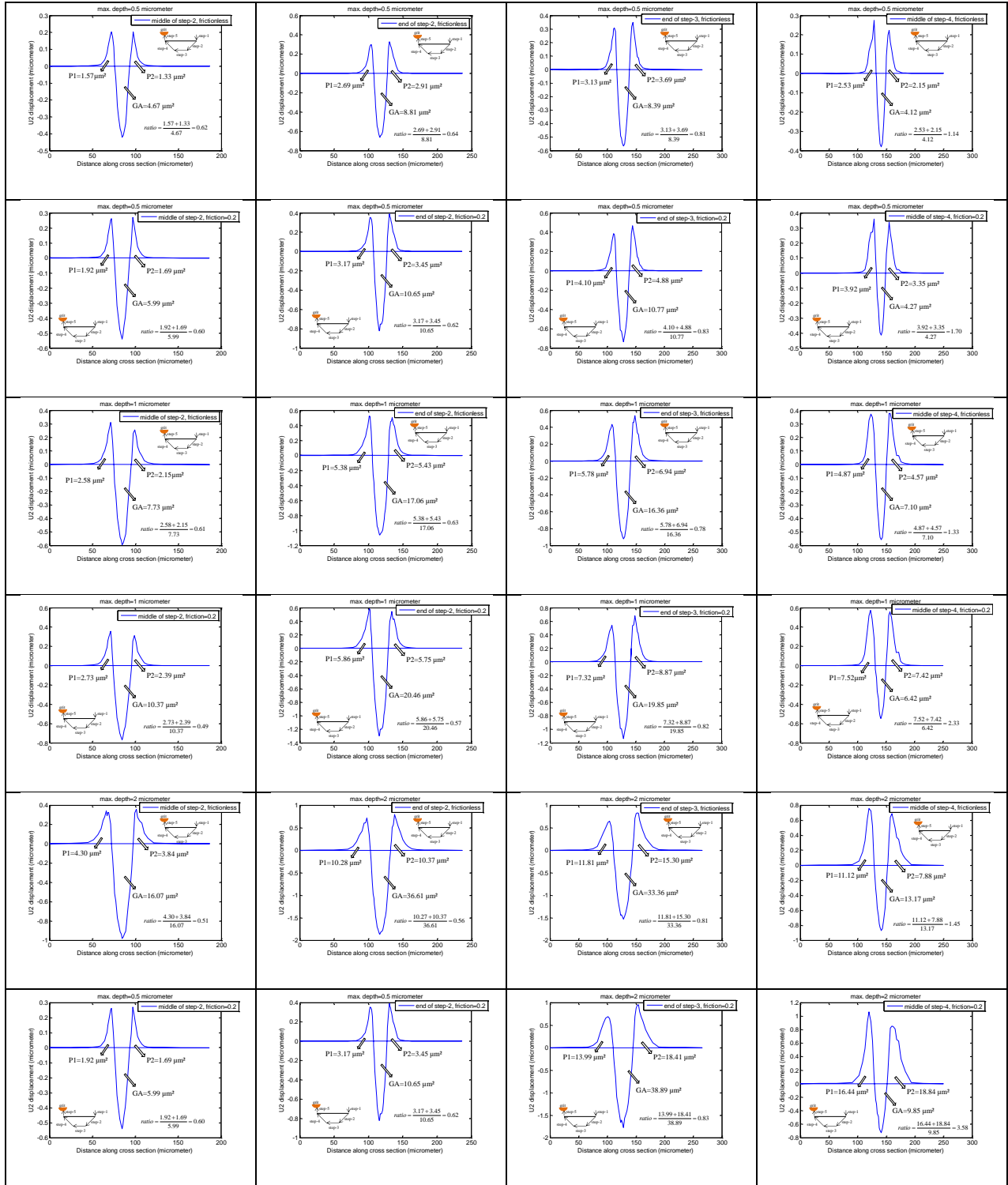


Figure 7.32 Cross-section profiles of the simulations using CBN grit (see Figure 7.33 for the analyses of profiles)

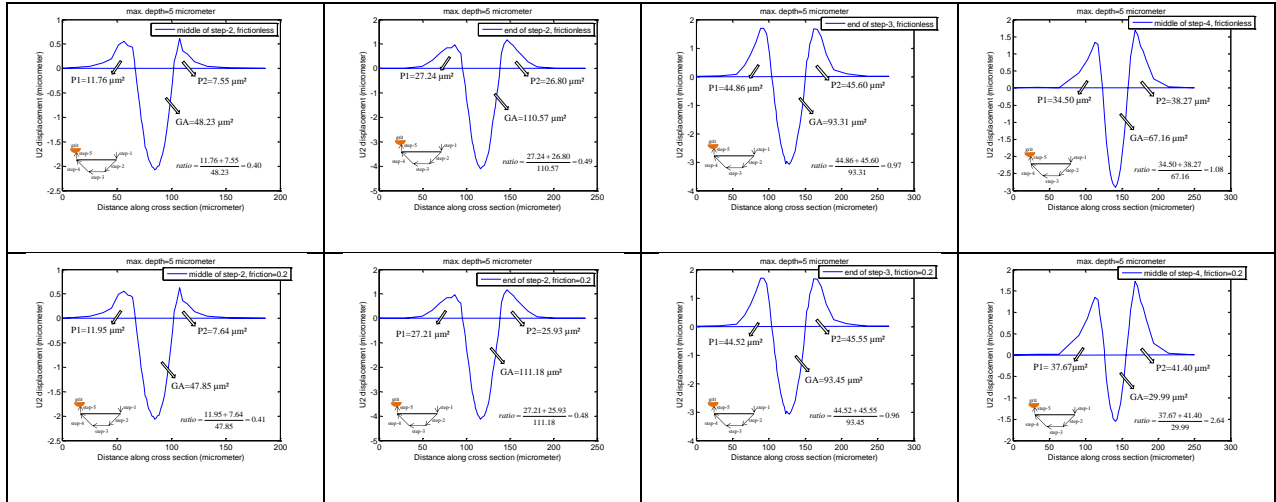


Figure 7.32 (Cont.) Cross-section profiles of the simulations using CBN grit (see Figure 7.33 for the analyses of profiles)

Figure 7.33 shows the variations in pile-up ratio along the single grit simulation path. Pile-up ratios gradually increase along step-3 due to material accumulation with the grit advancement, and the deeper the cut the faster the increase. However in step-4 there is a dramatic increase in pile-up ratios and from the observations in the middle of step-4 (distance 250 μm in Figure 7.33) pile-up ratios increase with increase in maximum depth. This is because the grit climbs right up to the end of the scratch simulation. This shows that the ploughing mechanism is completely different in the grit entrance and grit exit during grinding. Simulation results are strongly supported by the single grit experimental tests; see Figure 6.27 in Chapter 6. Pile-up ratios are also affected by the friction coefficient. It is clear from Figure 7.33, higher pile-up ratios are obtained with friction present.

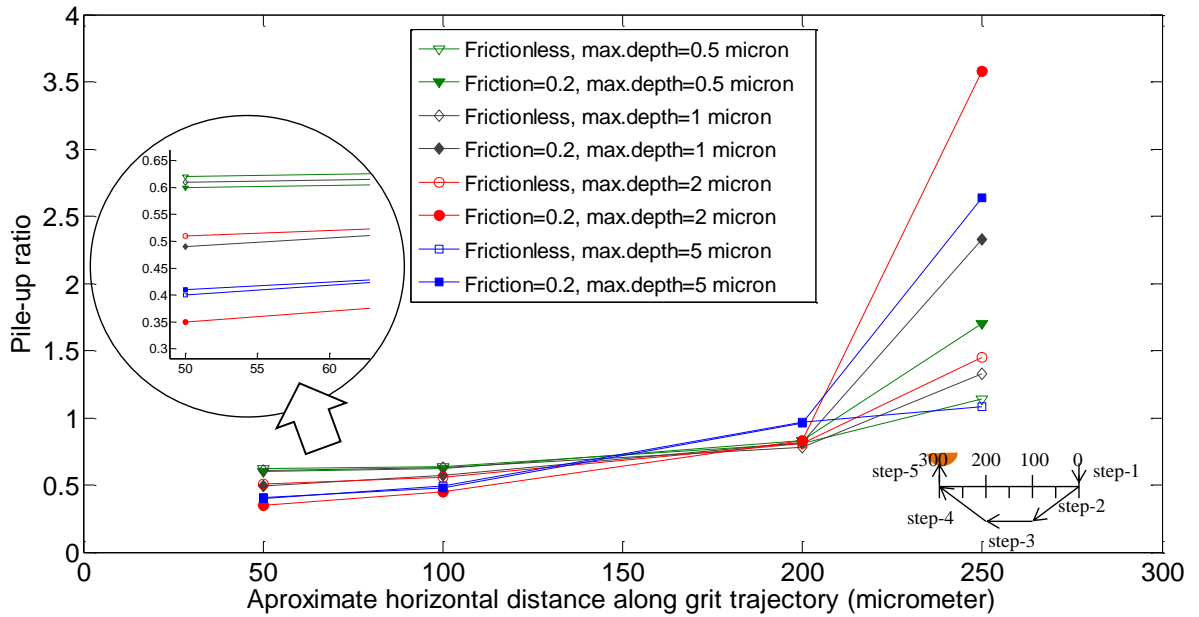


Figure 7.33 Pile-up ratio along scratch length using different maximum depths and friction coefficients

Figure 7.34 shows the variation in pile-up ratio with groove area along the grit simulation path. Pile-up ratios obtained in the middle of step-2 decrease with increasing groove area, while pile-up ratio with a frictionless surface condition is slightly higher than that obtained with frictional surface contact. The trend remains similar at the end of step-2. Pile-up ratios obtained at the end of step-3 increase with increasing groove area. The presence of friction does not significantly change the pile-up ratios obtained at the end of step-3. However, in the middle of step-4, pile-up ratios with friction are significantly higher than pile-up ratios without friction

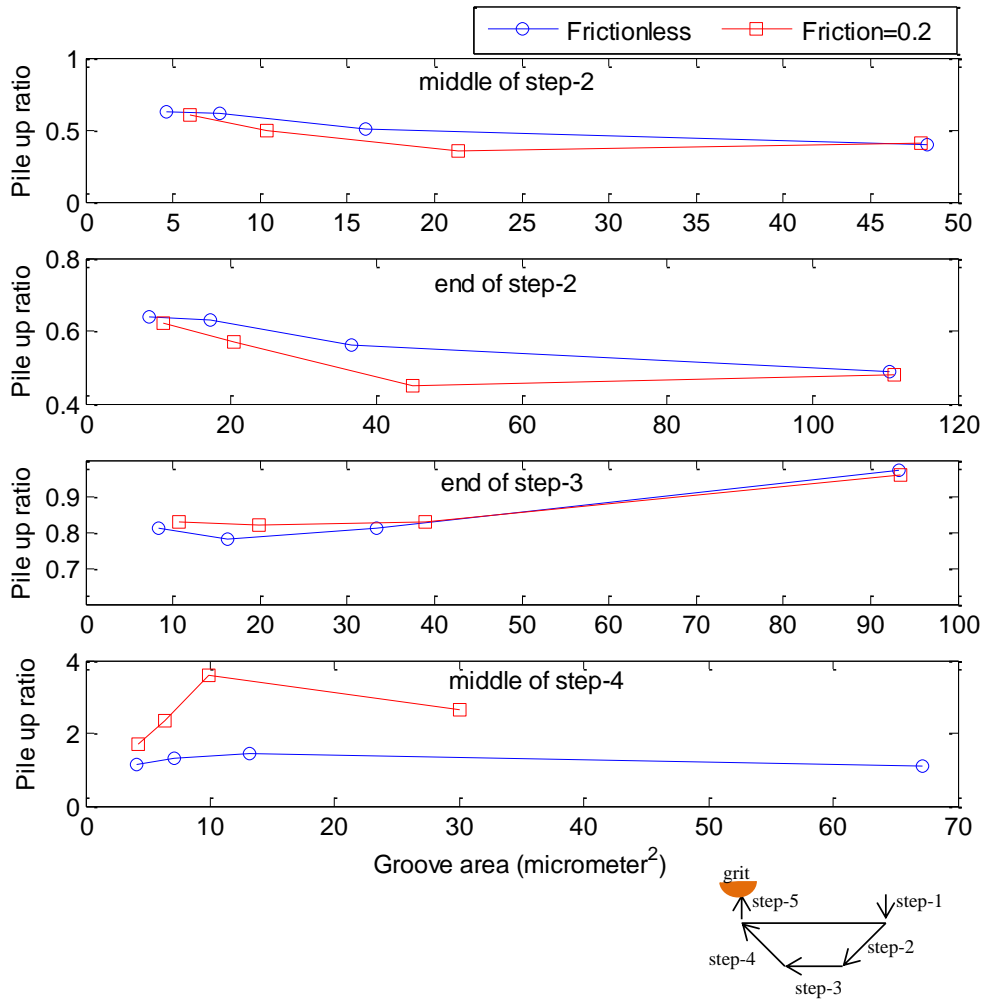


Figure 7.34 Pile-up ratio versus groove area at different steps along scratch length

7.3.2.3 Force analysis

The general pattern in force variation throughout the grit simulation path remained similar irrespective of depth of cut or friction coefficient. But, total force dramatically increased with increasing depth of cut, and slightly increased with increase of friction coefficient as shown in Figure 7.35. Total force along step-3 increased due to ploughed material accumulation ahead of the grit, although maximum depth remained constant along step-3.

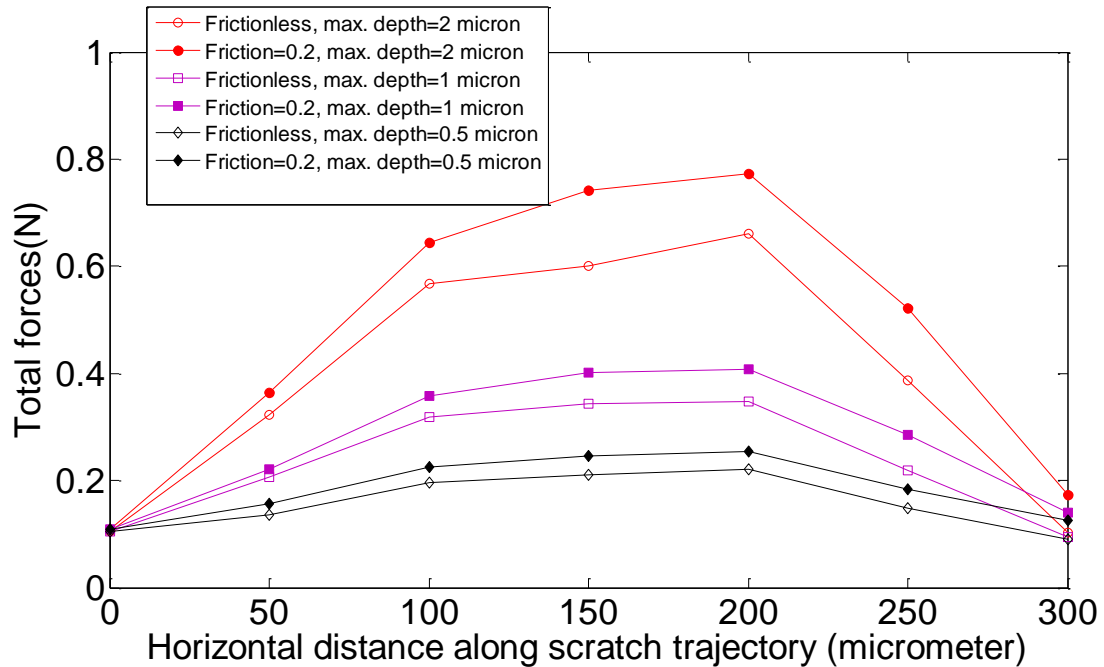


Figure 7.35 Variation in total force along grit simulation path

Total force increases linearly with groove area as was found in the single grit experimental test. Increase in total force shows better correlation with groove area rather than with depth of cut, this was already found in the experimental tests and was explained in Chapter-6. FEM simulations also show a similar trend with experimental tests. From the limited data available an almost linear relationship was found between total force and groove area when the forces and groove areas are extracted from the same location (where the grit engaged the workpiece) as shown in Figure 7.36. The forces obtained at the end of step-2 are slightly lower than that obtained at the end of step-3 when groove area is smaller. However, the two force lines gradually diverge from each other as the groove area gets larger, see Figure 7.36. This can be attributed to higher pile-up ratio with higher depth at the end of step-3 which, as found in Figure 7.33, leads to increase in force.

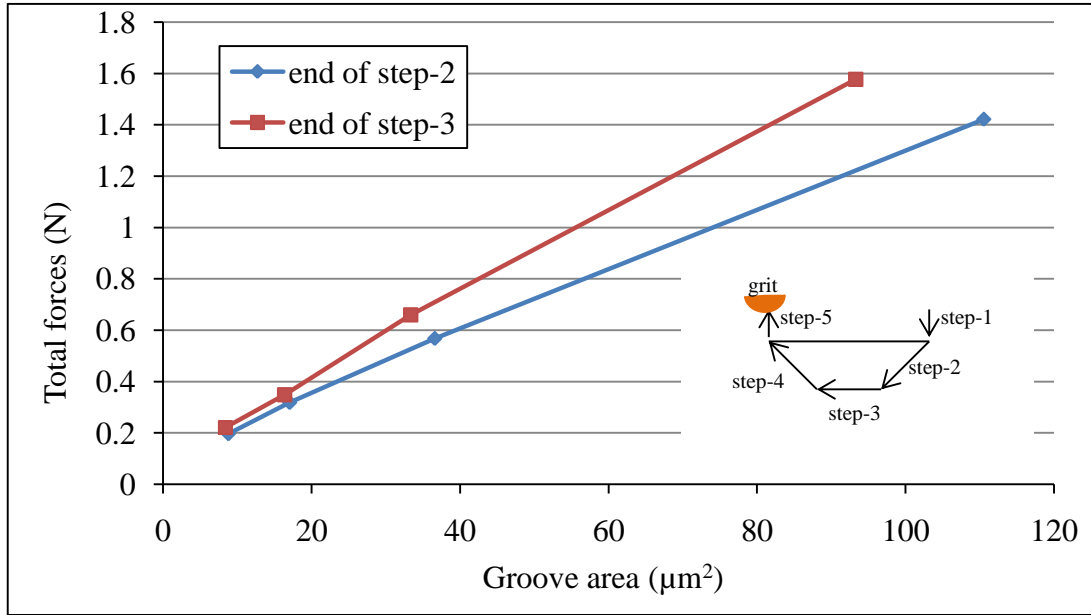


Figure 7.36 Total forces with respect to groove area (simulated frictionless condition)

7.3.3 Third group simulations: Using AISI4340 steel and CBN grit properties

7.3.3.1 Simulation conditions

Workpiece material was replaced by AISI4340 steel using rate dependent plastic behaviour. Grit and workpiece material properties used in this group of simulations are given in Table 7.3. In the simulations, temperature effects have not been considered because of the low speed and short contact time during single grit grinding. A strain rate power law dependency was used in accordance with Shet and Deng (2000):

$$\dot{\epsilon}_p = D \left(\frac{\sigma}{\sigma_0} - 1 \right)^p \quad \text{for } \sigma \geq \sigma_0 \quad 7.1$$

Where $\dot{\epsilon}_p$ is the effective plastic strain rate, σ is the instant yield stress, σ_0 is the initial yield stress. D and p are the temperature independent material properties for the power law hardening, having values of $2.21 \times 10^5 \text{ s}^{-1}$ and 2.87, respectively (Shet and Deng, 2000).

Table 7.3 Material properties used in the simulation set

Elastic properties	Grit (CBN)	Workpiece material (AISI4340) properties at 20 °C (Shet and Deng, 2000)		
Density (kg/ m ³)	3400	7800	Flow stress σ (MPa) at 20 °C	Plastic strain ϵ_p (mm/mm) at 20 °C
Young's modulus E (GPa)	909	207	414	0
			517	0.01
Poisson's ratio ν	0.121	0.3	759	0.09
			1100	0.9

To avoid indentation at the first contact as it happened in previous simulations, the grit simulation path was modified and the number of steps was reduced from 5 to 3; step-1 and step-5 in the previous grit path were removed. The modified grit simulation path is shown in Figure 7.37. This simulation path can allow to grit indentation into workpiece gradually while moving in horizontal direction which might lead to observation of the rubbing region in better way. Grit radius of 20 μm was used in these simulations with a maximum depth (a_p) of 1 μm and clearance of 1 μm ., various simulation time steps were used to change the speed of the grit. Friction coefficient between grit and workpiece surfaces remained constant at 0.2 for all simulations. Grit travel speed was controlled by using a time step because displacement boundary conditions were already defined to control the grit simulation path. Simulations with greater depth (for instance $a_p = 2 \mu\text{m}$) were aborted due to excessive element distortion when a grit radius of 20 μm was used. Grit with smaller radius acts like sharp cutter and tried to penetrate into the workpiece rather than just sliding over it. Grit with higher radius ($R=250 \mu\text{m}$) seemed to have no problem to give higher depth.

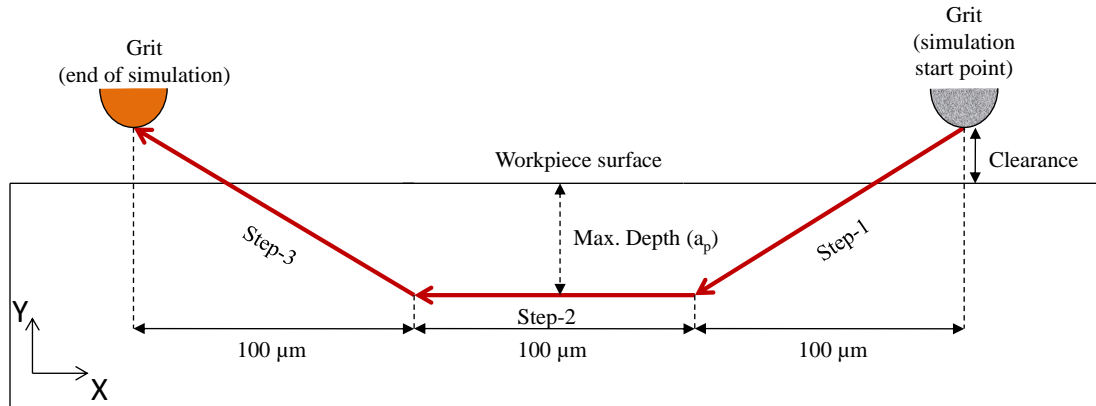


Figure 7.37 Grit trajectory with three steps used in the simulation

7.3.3.2 Simulation results

Figure 7.38 shows simulation results for the three steps run shown in Figure 7.40. Indentation induced by first contact is reduced to 8 nm using the modified grit simulation path, but this did not help with the analysis of the rubbing phase which occurred at initial grit penetration into the workpiece. Even at this initial indentation, plastic deformation exists.

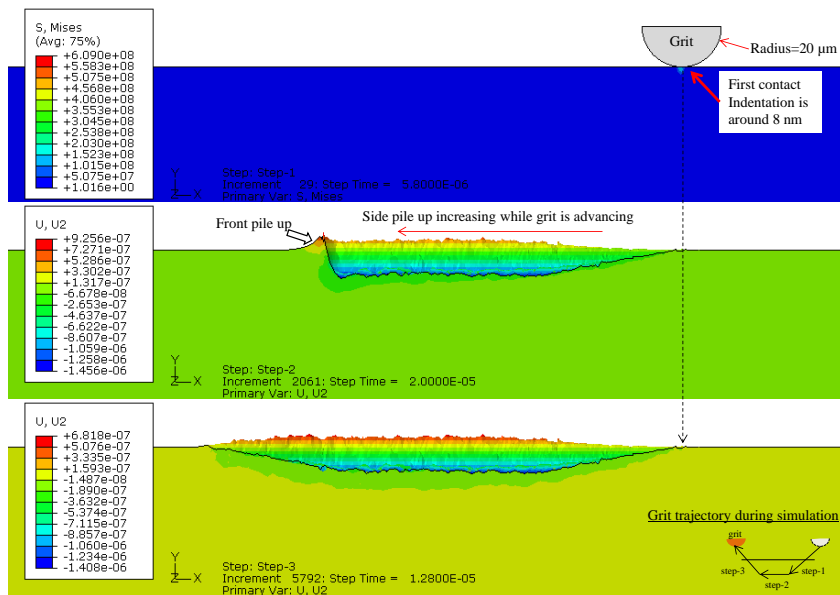


Figure 7.38 First contact and deformation along scratch using grit with radius of 20 μm and horizontal speed of 300 m/min

Material ploughing across the grit path has been simulated for different horizontal grit speeds. Figure 7.39 shows the cross-section profile of scratched grooves at the end of step-1 and step-2 for different grit speeds. There is no significant change in the groove profiles at lower speeds (3 m/min (0.05 m/s), 6 m/min (0.1 m/s) and 12 m/min (0.2 m/s)), but with the dramatic increase of speed (300 m/min (5 m/s)) the height of side pile-up decreases slightly. In previous studies, this phenomenon of low ploughing with higher speed was attributed to increase of cutting efficiency. However, cutting action does not exist in these simulations but side material ploughing is still reduced with increasing grit speed. This can be explained by the elastic recovery of material and less efficient plastic deformation with higher speed.

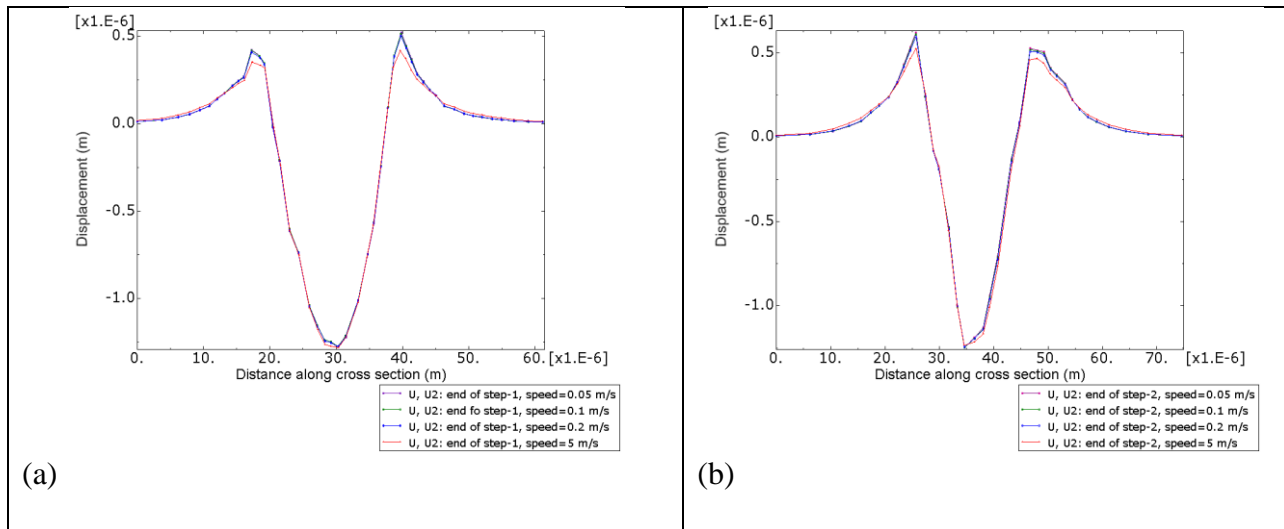


Figure 7.39 Overlapped cross-section profiles at different grit speeds; at the end of step-1 (a), and at the end of step-2 (b)

Cross-section profiles with pile-up and groove area calculations, and corresponding pile-up ratios at the end of step-1 and step-2 are given in Figure 7.40 for simulations with different speeds. Very small differences on both pile-up areas and groove areas at different speed are observed and the relation is plotted in Figure 7.41. Pile-up ratio is found higher at the end of

step-2 than at the end of step-1 because of material accumulation with the advancement of grit along the simulation path. Pile-up ratio decreases slightly with increasing speed but there is no significant change as shown in Figure 7.41, the work of Anderson et al., (2011) work supports this observation.

Stresses and displacement profiles have been extracted at the end of step-1 and at the end of step-2 where the grit is engaged with the workpiece and when the grit is moving to the end of the simulation path. The stress and displacement profiles are shown in Figure 7.42. Displacement profiles show that the depth of groove is higher during grit-workpiece engagement compared to that found when grit was at the end of simulation path. The depth differences are $0.14\ \mu\text{m}$ at the end of step-1 and $0.17\ \mu\text{m}$ at the end of step-2. These differences can be attributed to elastic recovery behaviour of workpiece material during scratching. However, ploughed material (or side pile-up) is found to be higher when the grit is at the end of simulation path. Thus, material elastic recovery contributes to increase in the ploughed portion of material during the single grit grinding process.

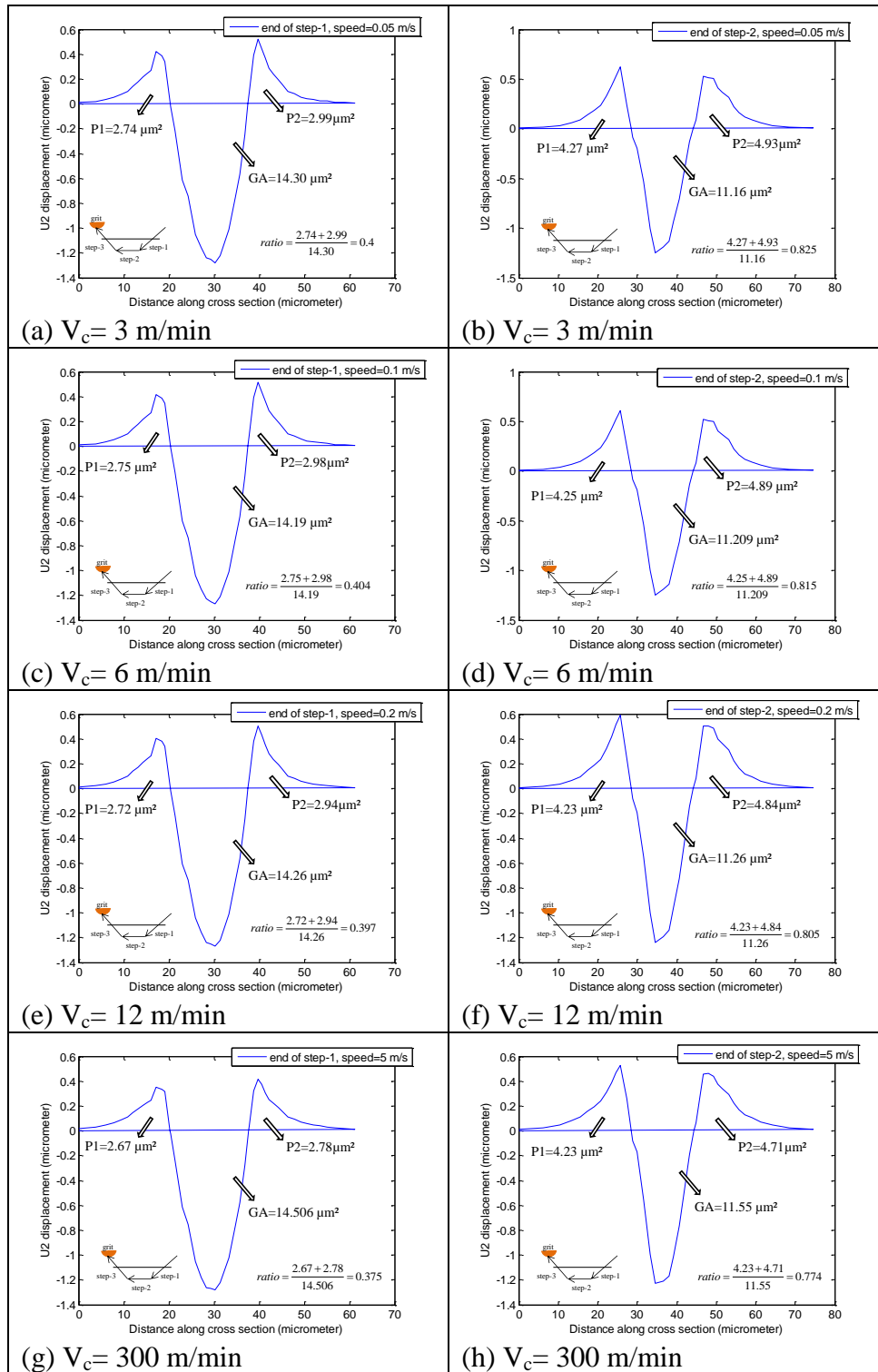


Figure 7.40 Cross section profiles at the end of step-1 and step-2 using different speeds

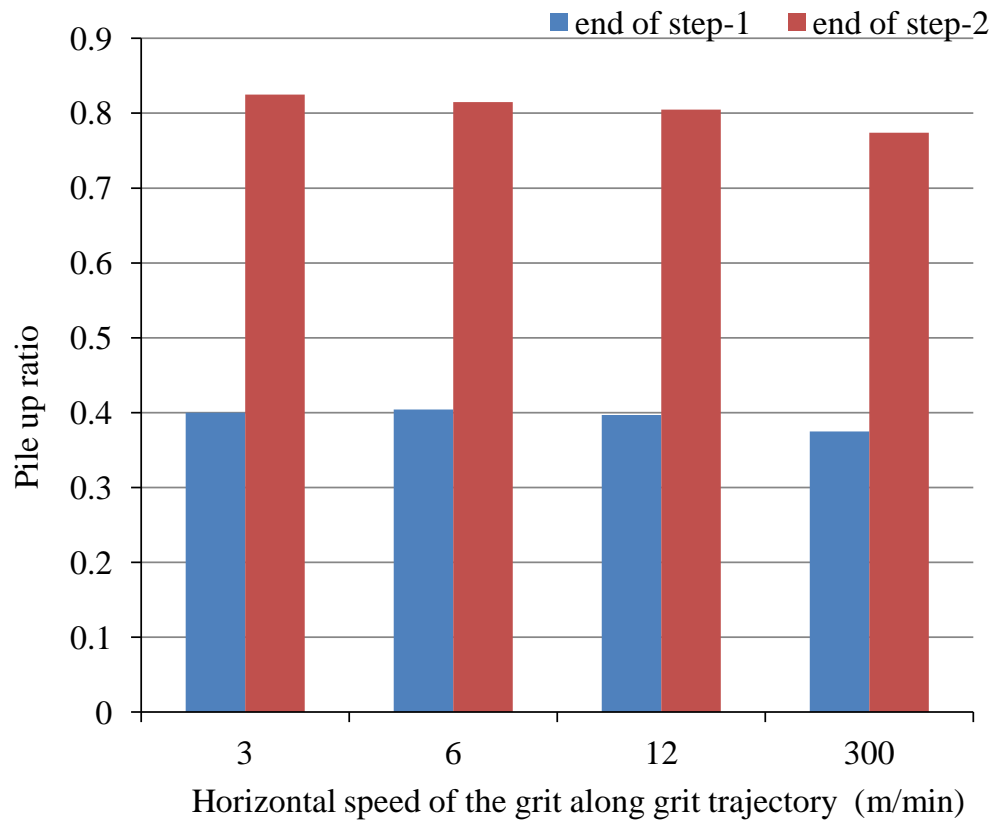


Figure 7.41 Pile-up ratio versus grit horizontal speed, at the end of step-1 and step-2

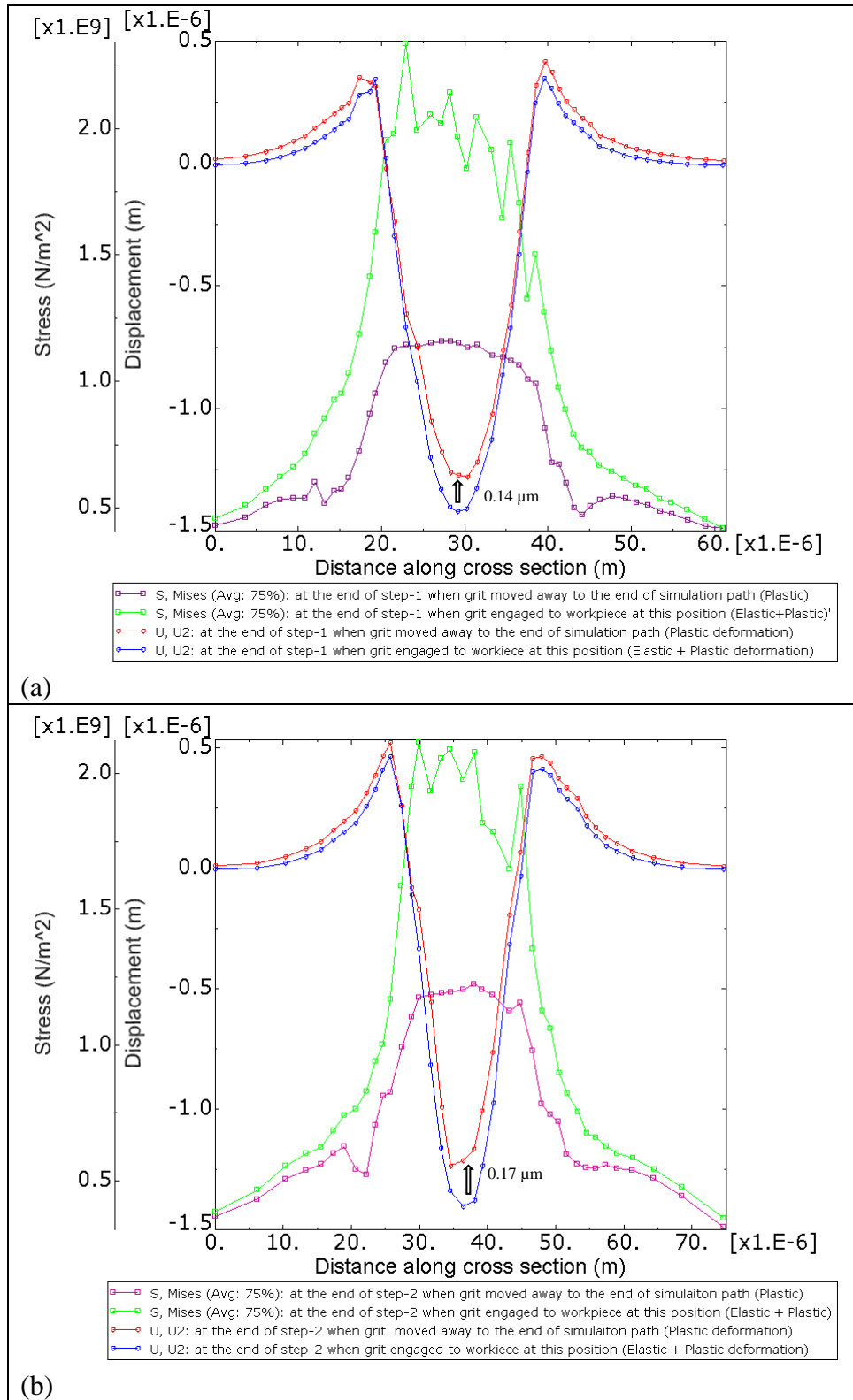


Figure 7.42 Cross -section profiles obtained (a) at the end of step-1 and (b) at the end of step-2 with stress distribution (Grit radius=20 μm and horizontal speed= 300 m/min)

7.3.3.3 Force analysis

Variation of force along the grit simulation path is shown in Figure 7.43. Normal force (F_y) is found to be always higher than the tangential force (F_x). Force components are highly influenced by grit travel speed and in this simulation higher forces were obtained with increasing grit speed. Negative values in forces are due to grit movement direction which is towards $-X$ (longitudinal movement) and $-Y$ (for depth) direction, so when comparing forces, absolute values of forces should be taken into account. This is contrary to experimental results where it was found that the forces decreased with increasing grinding speed. This could be due to assumed simplified elastic-plastic behaviour of workpiece materials compared to material deformation behaviour in real grinding processes. Also, chip formation phenomena during experimental tests could affect the forces, but the current simulations do not involve cutting mechanism. However, the work of Anderson et al., (2011^a) supports the FEM simulation results in Figure 7.43. Their study showed that normal forces increased with increase of cutting speed but tangential forces decreased with increase of cutting speed although they did use lower coefficient of friction for higher speeds. In our simulation friction coefficient remained constant at 0.2. This could cause an increase in the tangential forces with increasing cutting speed, as in Figure 7.43. The increase of normal forces with cutting speed can be attributed to strain rate hardening of the workpiece (Anderson et al., 2011). Since higher speed causes higher strain rate, and higher strain rate leads to increase of material strength; the so-called strain rate hardening phenomenon (see Figure 5.4 for the effect of strain rate on material strength).

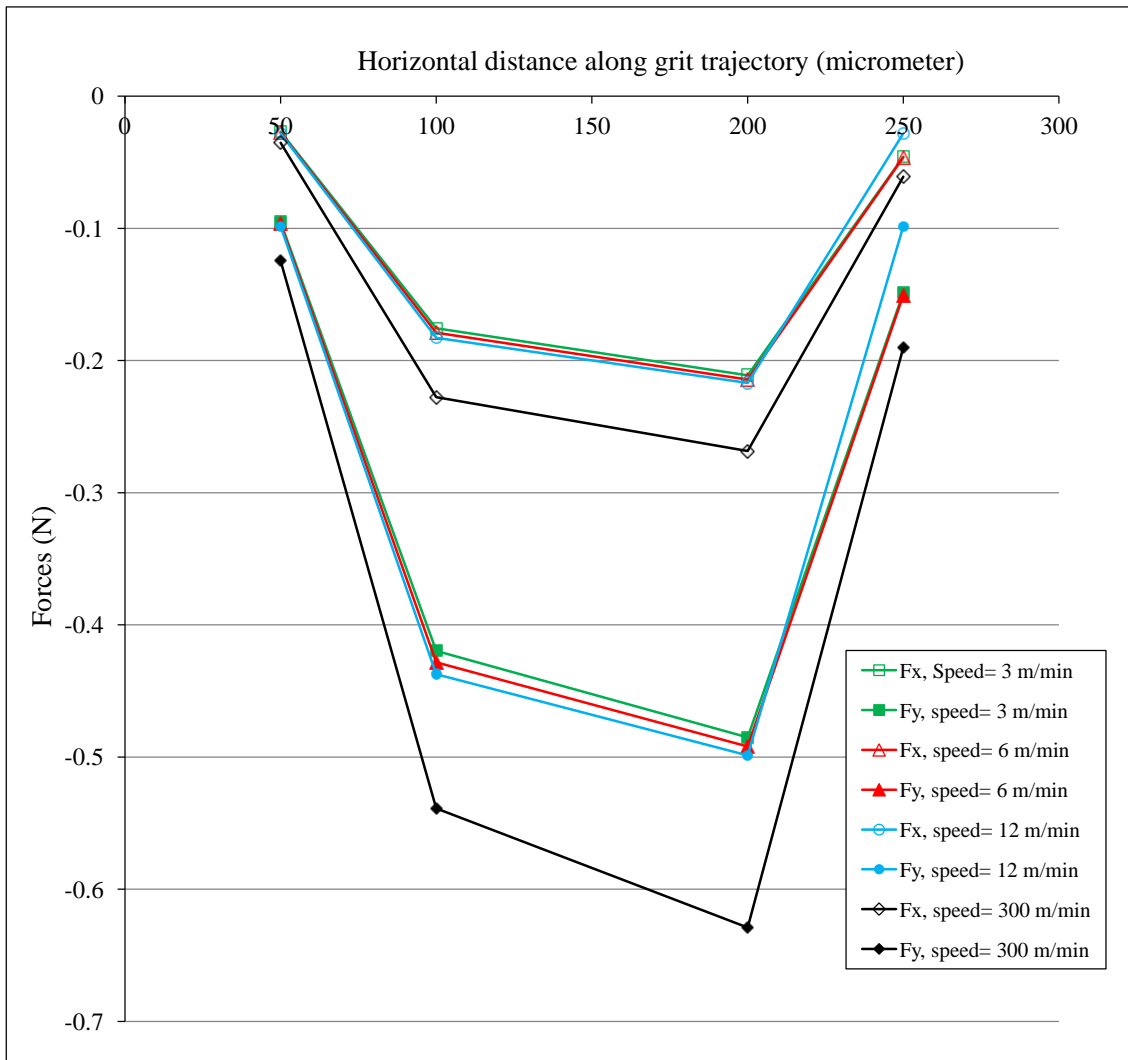


Figure 7.43 Forces along the scratch length at different speed (max. depth (a_p) was set to $1 \mu\text{m}$ disregarding the indentation due to grit asperity which is also around $0.4 \mu\text{m}$)

7.3.3.4 A simulation using a grit radius of $250 \mu\text{m}$

A simulation was performed using a larger grit size to demonstrate variation in ploughing action and forces when the grit contact area becomes larger. Figure 7.44 shows the grit-workpiece model and simulation results. All simulation conditions were the same as for previous

simulations except for the grit radius which was set at 250 μm . The grit horizontal speed was 5 m/s and maximum depth at step-2 was 2 μm .

A wider ploughed lip is obtained in front of larger grit (see the front pile-up in Figure 7.44) compared to that obtained using smaller grit. Scratch cross-section profiles at the end of step-1 and at the end of step-2 were extracted and both pile-up area and groove area were calculated, see Figure 7.45. Pile-up ratios at the end of step-1 and step-2 were found to be 0.138 and 0.477, respectively. These ratios were around 0.4 and 0.8 in case of smaller grit with a radius of 20 μm . It can be concluded that larger grit size lead to lower pile-up ratios when the other conditions remain similar.

Force variation along the grit simulation path is shown in Figure 7.46. The forces were found to be greater than for the actual single grit grinding test if groove area is taken as a base reference because cutting forces show quite a linear relation with increase of groove area (see Figure 7.36). It is possible to obtain different force values between experiments and simulations, because transverse forces across the scratch length are affected by many factors including grit shape, grit orientation, grit sharpness or bluntness, grit speed, as well as well as the grit's material properties.

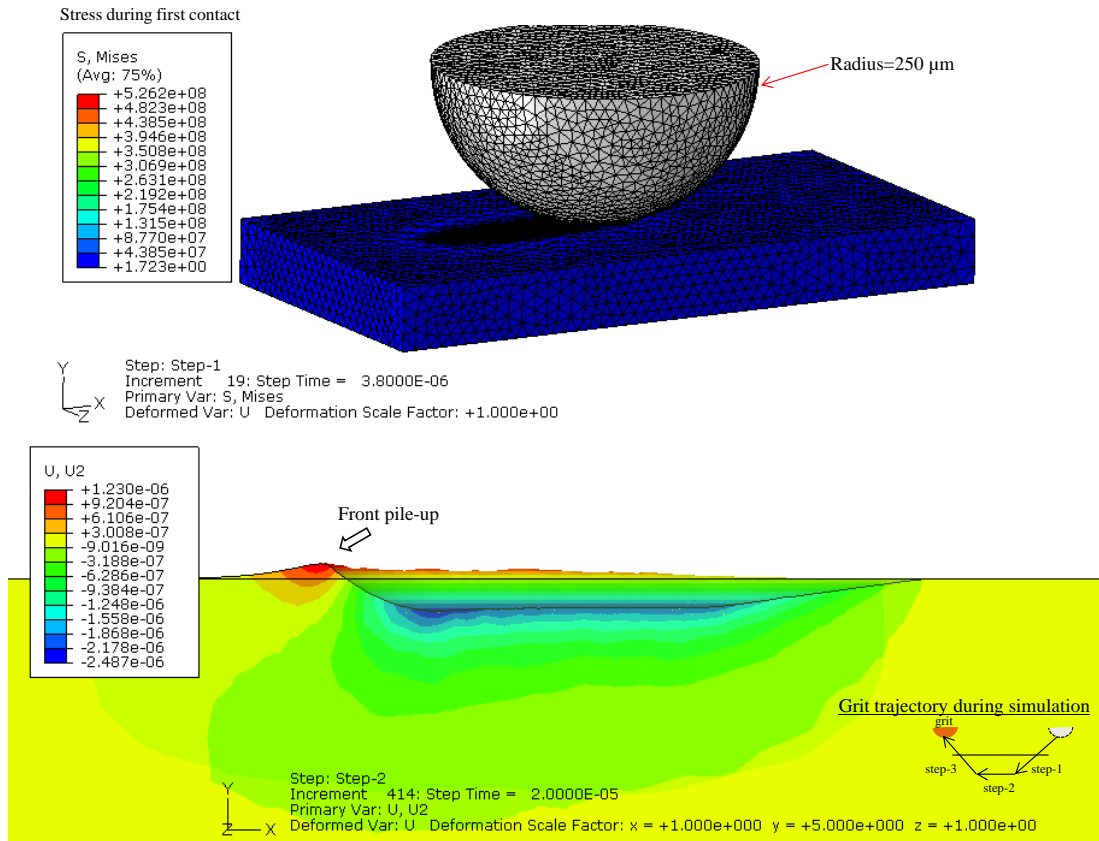


Figure 7.44 Simulation model using grit radius of 250 μm and speed of 300 m/min

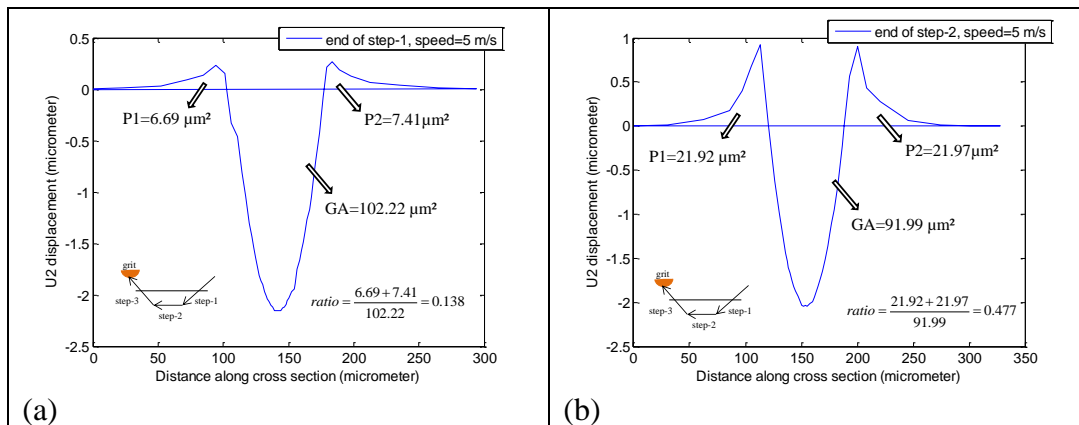


Figure 7.45 Cross section profiles (a) at the end of step-1 and (b) at the end of step-2 for the grit having radius of 250 μm and speed of 300 m/min

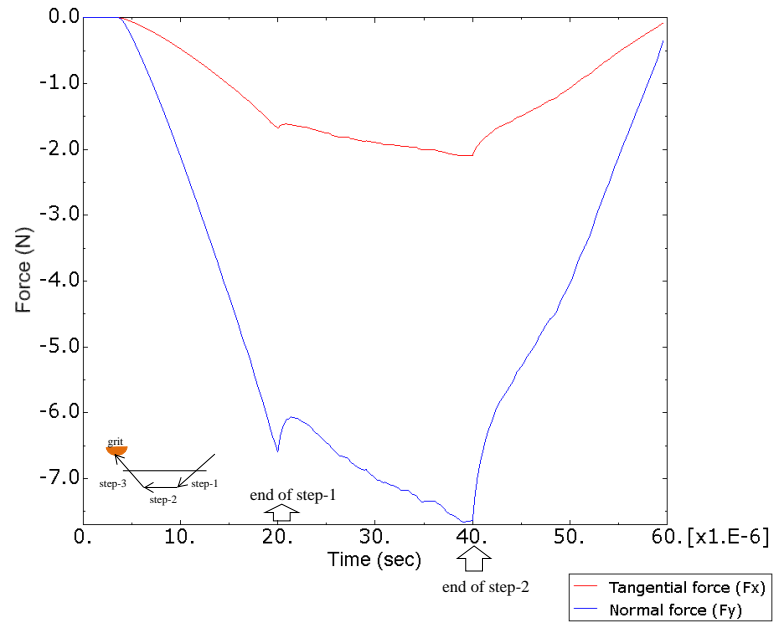


Figure 7.46 Force variation along grit trajectory for the grit having radius of 250 μm and speed of 300 m/min

Stress and displacement profiles were extracted at the end of step-1 and at the end of step-2 when the grit was engaged with the workpiece at these locations and when the grit was moving away at the end of the simulation path. The stress and displacement profiles are plotted in Figure 7.47. Displacement profiles show that the depth of groove is higher during grit-workpiece engagement compared to that found when the grit is at the end of simulation path (no interaction between grit and workpiece) position. The depths are 0.28 μm at the end of step-1 and 0.37 μm at the end of step-2. The results are similar to those presented in Figure 7.42, but the larger value means more elastic deformation exists.

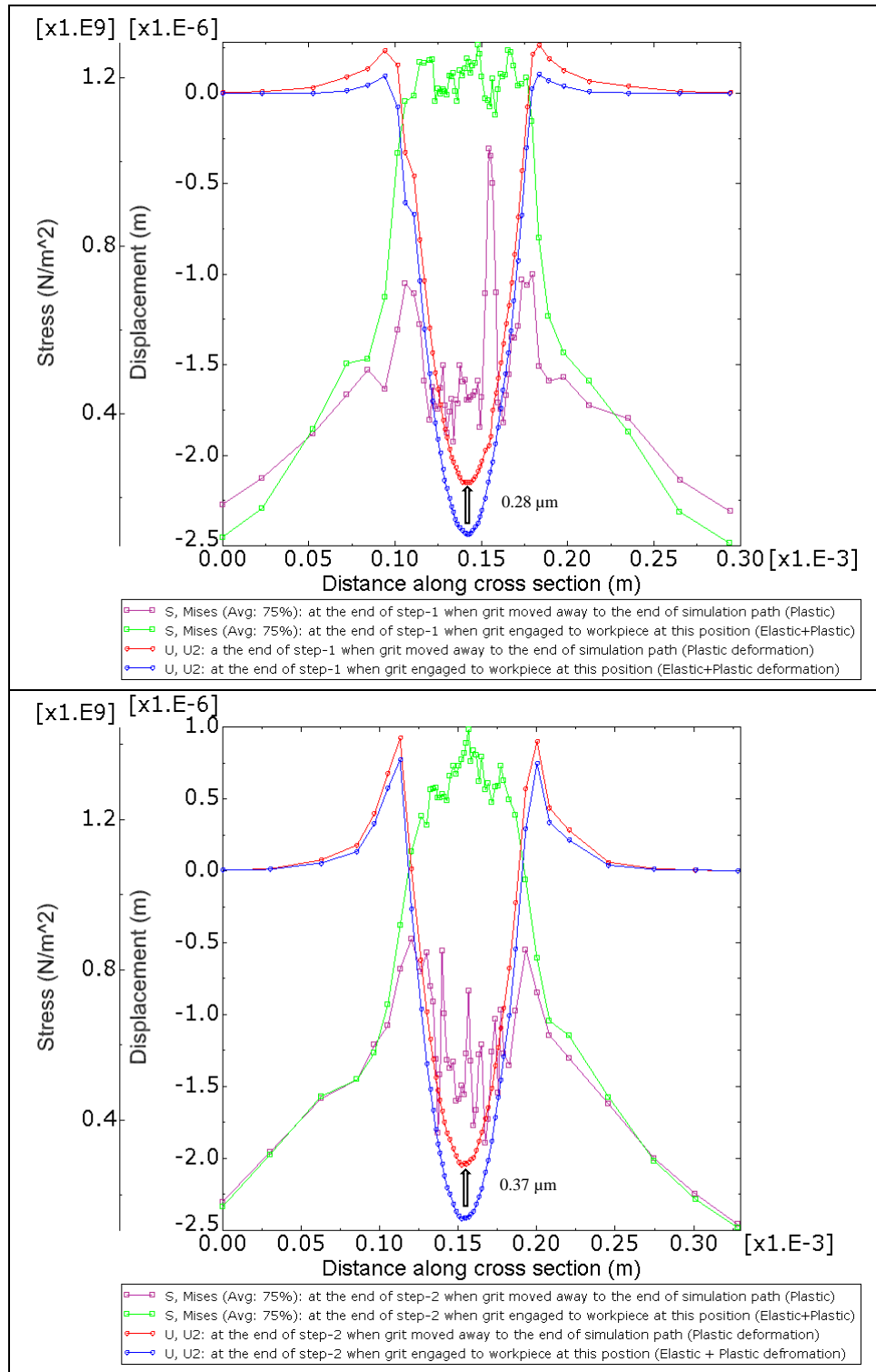


Figure 7.47 Cross- section profiles obtained (a) at the end of step-1 and (b) at the end of step-2 with stress distribution (Grit radius=250 μm and horizontal speed= 300 m/min)

7.3.4 Comparison of FEM simulation results with single grit grinding experiments

FEM simulation was performed using the properties of AISI4340 steel (equivalent to En24T steel) and the results obtained compared with the single grit grinding experiments performed on En24T for consistency of material removal behaviour. Comparison is possible on pile-up ratio trends and cutting force variation. The FEM simulations did not include cutting action but the experiments did, also the FEM simulation was performed for a spherical shaped grit body while in the experiments grit shape changed continuously due to wear and fracture. Thus, comparison is only possible for trends in behaviour rather than quantitative comparison. Experimental variation of pile-up ratio along the scratch path is shown in Figure 6.27 and the FEM simulation is shown in Figure 7.33. These two figures show a consistent trend in pile-up ratio which increases dramatically towards the end of the scratch where grit leaves the workpiece. Pile-up ratio differs numerically since the experiment included cutting action, and scratch length was around 700 μm in the experiment (see Figure 6.27 for details of scratch condition) whereas the FEM simulation did not include cutting action and scratch length was limited to 300 μm .

Cutting force ratio variation in the experiments and the FEM simulations also demonstrate consistency. Force ratio (F_n/F_t) ranges from 2 to 4 in the experiments (see Figure 6.45 and Figure 6.50). Similarly, force ratio ranges from 3 to 4 in the FEM simulations (see Figure 7.43 and Figure 7.46). Cutting forces F_t and F_n were measured experimentally at around 4 N and 13.5 N, respectively, at cutting speed of 1.08 m/min when groove section area was measured at around 170 μm^2 (see Figure 6.47). In FEM simulation, the average cutting forces were, $F_{x_{ave}} = 0.195$ N (since F_x ranging from 0.18 N to 0.21 N) and $F_{y_{ave}} = 0.45$ (since F_y ranging from 0.42 N

to 0.48 N) at a cutting speed of 3 m/min (Figure 7.43) for a average groove area of $12.73 \mu\text{m}^2$ (average of $14.3 \mu\text{m}^2$ and $11.16 \mu\text{m}^2$ at corresponding force values, see Figure 7.40-(a-b)). If these results are linearly extrapolated to a groove area of $170 \mu\text{m}^2$ as was found in the experiments (Figure 6.47), the cutting forces increase to $F_{x_{ave}} = 2.6 \text{ N}$ and $F_{y_{ave}} = 6 \text{ N}$ which are lower than the forces measured experimentally (see Figure 7.48). To fulfil the extrapolation with a limited data, cutting forces (F_t , F_n) is assumed zero when the groove area is zero (F_t and $F_n = 0$ when $GA = 0$). Cutting speed is not needed to extrapolate since they already have very close values (1.08 m/min in the experiment and 3 m/min in the simulation). The big difference between cuttings forces in the experimental and extrapolated simulation data, as seen in Figure 7.48, could be due to the cutting mechanism. The FEM simulation only shows ploughing which increases the cutting (ploughing) forces continuously while experiments include real cutting (material removal) which means the cutting forces do not increase dramatically due to the presence of ploughing material ahead of the grit. In experimental test, both cutting mechanism and forces are highly dependent on grit shape, groove area, cutting speed and scratch length, and the cutting mechanism shows completely different characteristics with varying conditions. However, in the FEM simulation, grit shape (spherical) was not altered, scratch length was limited to $300 \mu\text{m}$, and cutting (material removal) was not performed due to limited capability of the FEM simulation at the micro scale. Furthermore, linear extrapolation might not appropriate for the cutting force trend, it may not always show linear trend. In order to validate the FEM simulation using an experimental scratch test, shaped grit body (e.g. spherical) should be used in both the FEM simulation and experiment with similar conditions to obtain better match. This will remain for future research.

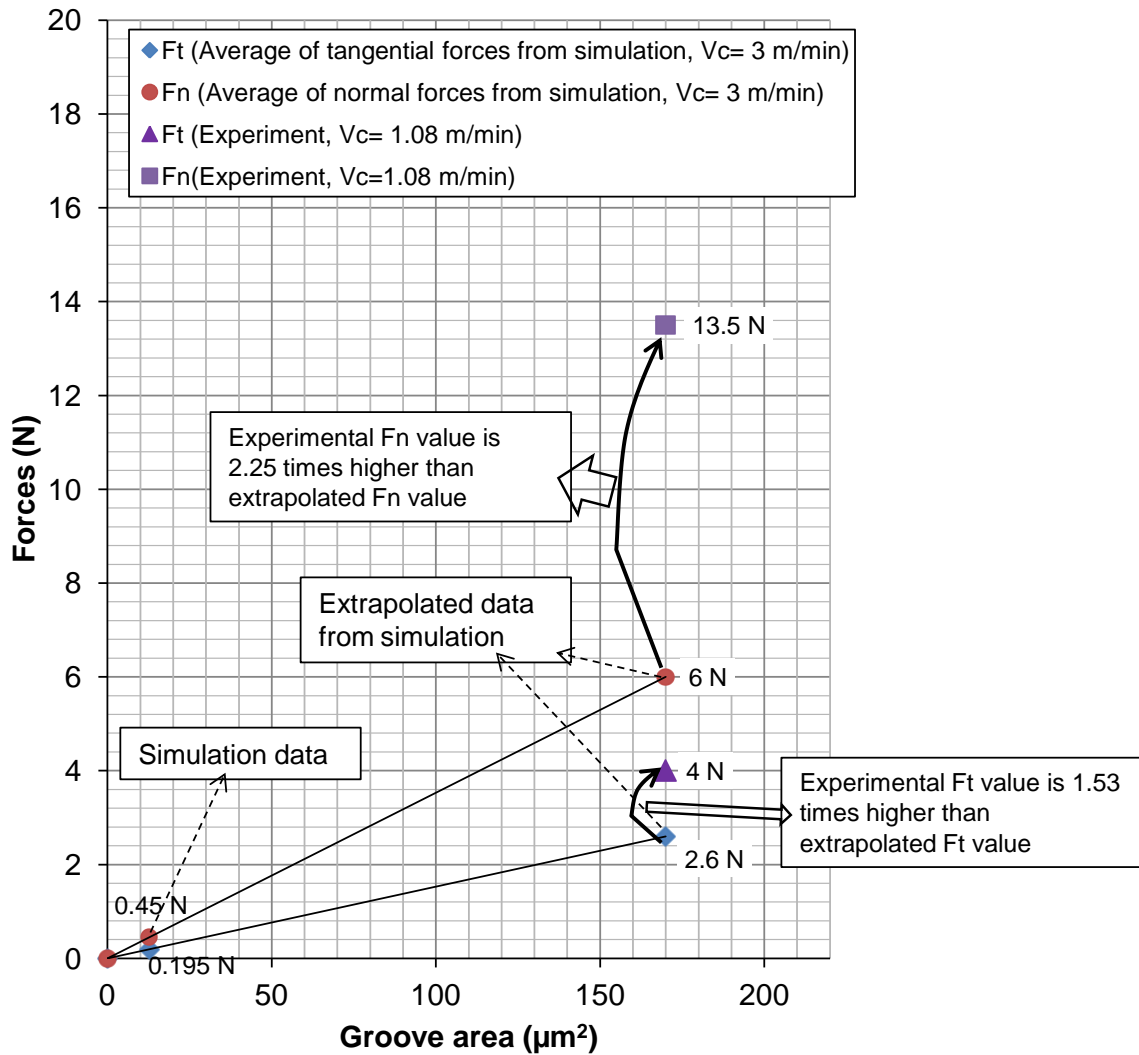


Figure 7.48 Comparison of some cutting forces (F_t and F_n) from FEM simulation, extrapolated data from FEM and experimental results (from single grit scratching tests)

7.3.5 Summary

Single grit grinding using a simplified grit scratching path has been demonstrated in this section using FEM simulation. Mainly, the ploughing phase of grinding has been investigated using different simulated conditions including artificial material with plastic properties and the

properties of AISI4340 steel. The effects of varying grit size, friction coefficient, depth of cut, scratch length, cutting speed on material ploughing, pile-up ratio and normal and tangential forces have been investigated. Multiple pass simulations were performed to demonstrate the ground surface created using FEM technology. Rubbing phase (plastic deformation free region with material elastic recovery) was captured using intuitive determination at the grit penetration stage. Elastic and plastic deformation states were successfully demonstrated together during scratching. Throughout the investigation, simulation results such as forces, pile-up ratios cannot be compared quantitatively with experimental test results since the simulation and experimental conditions were quite different in terms of usage of material properties, grit geometry, and limitations of the capability of the FEM to accurately simulate the model cutting process to small depths such as 1 μm . However, material deformation phenomenon, especially ploughing of material ahead of the grit, shows a quite realistic trend compared to the single grit experimental results.

Chapter 8 Conclusive Discussion

Material removal mechanisms during grinding process have been investigated using single grit abrasive action on the workpiece. Single abrasive grit action includes the fundamental scratch formation mechanisms of rubbing, ploughing and cutting. Of these three mechanisms chip formation by the conventional cutting processes, such as turning and milling, has been studied analytically, simulated using FEM techniques and investigated experimentally at the macro scale. Conventional cutting processes are performed with a shaped cutting tool so that a numerical approach (such as finite element simulation) can use a defined model to study the cutting mechanisms. However, the grinding mechanism is different from conventional cutting processes in terms of cutting tool geometry, and size and number of cutting edges. The cutting tools in grinding are numerous abrasive grits each with a different shape and size and the material removal process is carried out at a smaller depth of cut compared to conventional cutting process, possibly down to sub-micrometre size.

Investigation of material removal mechanisms in single grit grinding is generally limited to experimental work because of the complexity of the material removal mechanisms. In this thesis, single grit grinding material removal mechanisms have been investigated both experimentally and numerically. Experimental studies were performed using CBN grits (40/50 mesh) whose sizes ranged from 450 μm to 550 μm in diameter, where the active cutting edge radii are in the range of 50 μm to 1500 μm (EGER). Mainly the ploughing and rubbing mechanism were investigated at different depths of cut and cutting speeds by measuring pile-up ratios at different stages of the scratches. According to experimental results, pile-up ratio is a good indicator of the

material removal mechanism. When the cutting mechanism is prominent, scratch profile measurements give a lower pile-up ratio than when ploughing was prominent.

Abrasive grit has several cutting edges and they are continuously changing during the course of grinding process. Even at very small depth of cut the cutting mechanism can be actively removing material from the workpiece surface. Because of the uncontrollable grit size and geometry during scratching, it is difficult to separate the ploughing and cutting mechanism from each other. However, it is possible to determine those conditions where the ploughing mechanism is more prominent than rubbing or cutting. In general, the cutting mechanism is more effective with increasing depth of cut. However, grit shape factor plays a significant role in determining what proportion material is removed by the ploughing mechanism. Grit with a flat bottom gives greater ploughing with increasing depth of cut in contrast to grits having sharp edges. Rubbing action is more difficult to capture than ploughing, because it is meant to include only elastic deformation, not plastic deformation.

Knowledge of the force acting during single grit grinding is necessary to analyse the performance of grinding process and grinding power. With reliable force acquisition, grinding defects both on grinding wheel and workpiece can be detected and analysed, and remedies can be suggested. In this study, force acquisition was performed using a Kistler piezoelectric force sensor (9602A3201), which is not capable of measuring the forces accurately at high speed (~ 300 m/min) due to the low natural frequency of the sensor and small contact time during scratching. However, at low speeds some forces were acquired and analysed and to determine a relation with depth of cuts and groove areas. According to these results, cutting force gives a better correlation with groove areas than depth of cuts. To improve force acquisition and to obtain more reliable results, a force sensor with greater sensitivity and higher working frequency is necessary to measure force profile along the scratch length. If the force profile along the

scratch length becomes available, material removal phases across the scratch length, first rubbing, then ploughing and finally cutting will be analysed based on force variation.

Numerical study of single grit scratching based on FEM simulation is very challenging to accurately create the features of scratch formation in a computer environment is difficult. Up to now, no-one has achieved any complete single grit grinding simulation with FEM, capable of demonstrating the material removal processes in one pass of grit simulation for a depth of cut less than 5 μm . Generally, FEM simulations fail to model cutting of material at a small scale because of excessive element distortion during cutting. To mitigate element distortion very small size elements are required in the cutting region, and this increases the frequency of remeshing dramatically. Frequent remeshing during simulation will increase the computational time substantially. Besides, with further reduction in the size of the finite elements also causes failure because numeric integration formulations are not valid when the model diverges from the continuum mechanics range. An increasingly common problem in the use of Abaqus software is related to the unavailability of a continuous remeshing procedure, which is necessary in metal cutting simulations. The iterative adaptive remeshing and ALE adaptive meshing which are found in Abaqus have limited capability and work with a limited type of element and formulation, which might not be suitable for machining. Further investigation of single grit grinding relies on the future development of FEM.

In this thesis, mainly the ploughing action of grit has been investigated. A new approach to ground surface creation using multiple passes of the grit is demonstrated and it shows how material deformation acts regarding side ploughing in grinding. Increasing the number of passes results in increase of computational time. In the current study, three grit passes were performed in the cross direction to generate multiple pass ground grooves to show the feasibility of grinding surface creation with minimum number of grit passes. Furthermore, a simplified model of single

grit scratching, with various conditions (such as depth of cut, friction coefficient, cutting speed, sphere radius), shows that ploughing action can be successfully simulated using FEM.

FEM simulation and experimental results both show a similar trend in pile-up ratio along single grit scratch path due to material accumulation ahead of the grit. Pile-up ratio changes from 0.1 to 0.8 occur both in FEM and experiments when the measurement was performed at the deepest point of the scratches. Also, pile-ratio increases dramatically towards the end of scratch and its value was greater than 1 at all times, both in FEM and experiment. FEM simulation of grit scratching has not been quantitatively compared to experimental results because simulation conditions and experimental conditions were different. The important output obtained from FEM simulations was the behaviour of the material when it was subjected to grit scratching. The only contradiction between experimental results and FEM simulations is the variation of forces with various speeds. Experiments show that the cutting forces decrease with increasing speeds whereas FEM simulations show that the cutting forces increase with increasing speeds. The trend obtained from experiments are supported by previous studies (Feng and Cai, 2001), where the grinding forces were found to decrease with increase of cutting speed, however, FEM simulation results are also supported by some previous studies performed on single grit processes by Anderson et al., (2011^a) who found normal forces increases while tangential forces decrease with the increase of cutting speed. These differences can be attributed to other parameters involved in the experiments and simulations. Experimental tests are highly dynamic and forces could be influenced by the continuously changing grit shape and grit-workpiece contact area, by grit fracture during scratching, by chip formation, and will also depend on depth of cut, friction coefficient and material flow behaviour. However simulation conditions are comparatively stable, depending on the user provided inputs. Therefore, it is unsuitable to compare the results quantitatively.

Chapter 9 Conclusions and Suggestions for Future Work

9.1 Conclusions

The fundamentals of grinding material removal mechanisms can be studied from the viewpoint of single grit grinding. Characteristics of scratch formation have been investigated under several different input conditions. Experimental and FEM simulation results provide a significant contribution to understanding scratch formation mechanisms in terms of rubbing, ploughing and chip formation.

The following conclusions are drawn from the study and contribute to the understanding of material removal mechanism in grinding.

- Grit cutting edge shape is found to be a more influential factor than cutting speed, depth of cut or workpiece material properties in determining the material removal mechanism: ploughing or cutting.
- Material pile-up ratio during scratching is highly influenced by the shape of grit cutting edges. When the grit tip is sharper, increasing of depth of cut leads to lower pile-up ratio. This implies that sharp grit should be applied for greater depth of cut to achieve higher cutting efficiency. However, grit cutting edges having a flat bottom can be considered as blunt cutting edges, giving higher pile-up ratios with increasing depth of cut. Therefore when grit becomes blunt, the depth of cut should be small to avoid high grinding force and low cutting efficiency.

- The transition point from ploughing to cutting is highly dependent on the material properties, grit shape factor and other machining conditions. For example, transition from ploughing as the dominant mechanism to cutting as the dominant mechanism happens at a depth of cut of around 1.5 μm for Inconel 718 but at around 2.5 μm for the En8 mild steel.
- During the course of single grit machining, grit fractured and multiple new cutting edges were generated. Scratches produced by single cutting edge and multiple cutting edges show significant differences in removal mechanism in terms of ploughing and cutting. It was found that pile-up ratios were significantly higher with multiple edge scratches than with single edge scratches. In another words, cutting is more prominent in scratches produced by single cutting edge than by multiple cutting edges.
- Material removal mechanism across a single scratch also shows significant variation. Pile-up ratios at the grit entrance side of the scratch are found to be lower than the pile-up ratios on the grit exit side of the scratch. Due to material accumulation along the scratch path, dramatically high pile-up ratios are found, up to 25. In the middle of scratches where the depth of cut becomes the largest, the pile-up ratio has its lowest value due to the increase of cutting efficiency.
- Cutting forces decrease with increase of cutting speed while normal forces were always higher than tangential forces in the single grit grinding experiments. The force ratio (F_n/F_t) varied from 2 to 4.
- FEM simulation of the single grit grinding process shows good agreement with experimental results when considering the ploughing action and pile-up ratio behaviour across the single grit scratches. Similar trends were captured for ploughing of material; however simulated chip formation with depth of cut less than 5 μm is not practical due to limitations of FEM technology. Software capability with respect to remeshing procedure is another obstacle during single grit cutting.

- Cutting (chip formation) simulations are feasible both for 2D (using Abaqus/Explicit) and 3D (using Deform3D) machining when the cutting depth is higher than that used in single grit machining. Prediction of chip shape using FEM simulations is feasible for machining under different conditions. Continuous, serrated and discontinuous chips were developed in this study. It was found that rake angle, depth of cut, and material properties are the most influential parameters in generation of different chip shapes. When the rake angle moved from positive to negative values, continuous chip, serrated chip and discontinuous chip were produced in sequential order.
- A new approach to predict ground surface creation using the FEM model was performed and results show that surface creation is feasible with multiple pass scratching, but it requires huge amounts of computational time to create a moderate size surface for surface roughness analysis. In the thesis, multiple pass scratching was performed with three sequential cross passes of a grit to demonstrate the feasibility of grinding surface creation and also to predict the material deformation tendency in each sequential pass.

9.2 Possible future work

FEM techniques have been widely used for metal cutting simulation at the macro scale where depth of cut is relatively large as in conventional machining. Finite element simulation of single grit grinding is extremely cumbersome due to its depth of cut being as little as 1 μm . The main difficulty in the FEM simulation of single grit grinding is element distortion due to large deformations during the cutting process. This problem exists both in the macro scale (depth of cut greater than about 10 μm) and micro-scale (depth of cut down to 1 μm or less). Influence of element distortion at the macro scale can be mitigated by using techniques such as element deletion (which can reduce accuracy of simulation), introduction of a damage model and, in some cases, continuous remeshing or ALE adaptive meshing. However, influence of element

distortion is not easily reduced at the micro-scale. Besides, very small elements are needed around the cutting area to properly simulate a chip at the micro-scale, this is not achieved computationally with remeshing, and even if it is obtained with manual meshing it become impractical in terms of computational cost.

To reduce the drawbacks of finite element techniques in machining simulation, a meshless or mesh-free simulation technique such as Smooth Particle Hydrodynamics (SPH) method is suggested as suitable for the single grit cutting process. In SPH simulation, a workpiece is formed by clouds of particles rather than element mesh as in FEM. Thus, element distortion due to large deformation during metal cutting is eliminated by using the SPH method. There exist very little research into machining simulation with SPH compared to machining with FEM; this is due to the complexity of SPH during the development stage. In the SPH method, a physical domain is discretized using particles, a shape function is formed using particles and an approximate solution is performed at the level of particles, thus no mesh is required. Material failure implementation in the FEM is cumbersome and includes several ambiguities. State of the art to determine failed elements in FEM consists of calculating damage at every element and to remove those elements which are highly distorted, this requires specifying a damage criterion and when that criterion is satisfied the element is removed from the calculation. This element removal also means loss of material from the simulation which can reduce the accuracy of the FEM calculation. However, material failure in SPH can be achieved by removal of cohesion between neighbouring SPH particles and the SPH particles are then separated from each other so there is no material loss in the SPH method (Heinstein and Segalman, 1997). The SPH method was first applied to orthogonal cutting problem by Heinstein and Segalman (1997) and is recommended for future research of single grit grinding.

In order to verify the simulation results with experimental tests quantitatively, single grit grinding tests are required to be performed using shaped grit instead of irregular shaped grit. If the grit shape can be controllable by the user, single grit experiments with different grit orientations can be performed. Ploughing effects, chip removal and cutting forces are needed to be investigated the influential parameters during single grit grinding.

The single grit grinding process provides significant understanding of grinding mechanics at the micro scale. Prediction of maximum forces during single grit grinding is useful in the design stage of grinding wheels. Bond fracture between grits increases the loss of grinding wheel during grinding, and it also increases the dressing frequency to obtain new grit cutting edges on the wheel surface. These are unwanted during manufacturing since they increases manufacturing costs as well as production time. To reduce bond fracture during grinding, maximum forces obtained from single grit tests can be used to determine the bond strength of the grinding wheel. More information is urgently needed on how grit shape and grit orientation effects scratch formation, ploughing and chip removal for further development of grinding wheel design. Investigation on design of grinding wheels considering the influence of grit orientation is necessary to obtain optimum performance in material removal.

References

- Abaqus User's Manual, Abaqus/CAE Version 6.8 documentation, 2009
- Ambati R. and Yuan H. (2010) FEM mesh-dependence in cutting process simulation. *The International Journal of Advanced Manufacturing Technology* 53: 313-323
- Anderson D., Warkentin A., Bauer R., (2011^a) Experimental and numerical investigations of single abrasive-grain cutting. *International Journal of Machine Tools and Manufacture* 51: 898-910
- Anderson D., Warkentin A., Bauer R. (2011^b) Novel Experimental Method to Determine the Cutting Effectiveness of Grinding Grits. *Experimental Mechanics* 51: 1535-1543
- Anderson D., Warkentin A., Bauer R., (2012) Development of an experimentally validated abrasive-grain cutting model using a hybrid Euler-Lagrangian finite element formulation. *Finite Element Analysis and Design*. 53: 1-12
- Andrade U., Meyers M., Vecchio K., Chokshi A. (1994) Dynamic recrystallization in high-strain, high-strain-rate plastic deformation of copper. *Acta Metallurgica et Materialia* 42: 3183-3195
- Archard, J.F. (1953) Contact and Rubbing of Flat Surfaces. *Journal of Applied Physics* 24(8) pp: 981-988
- Arrazola P.J., Villar A., Ugarte D., and Marya S. (2007) Serrated chip prediction in finite element modeling of the chip formation process. *Machining Science and Technology* 11(3): 367-390
- Asad M., Girardin, F., Mabrouki T., and Rigal J.-F. (2008) Dry cutting study of an aluminium alloy (A2024-T351): a numerical and experimental approach. *International Journal Material Forming* 1: 499-502
- Astakhov V.P. and Quteiro J.C. (2008) Metal cutting mechanics, Finite element modelling. In: *Machining Fundamentals and Recent Advances*, Editor: Davim J.P., Springer Verlag
- Aurich J.C. Bil H. (2006) 3D finite element modelling of segmented chip formation. *Annals of the CIRP* 55 (1): 47-50
- Aurich J.C., Biermann D., Blum H., Brecher C., Carstensen C., Denkena B., Klocke F., Kroger M., Steinmann P., Weinert K. (2009) Modelling and simulation of process: machine interaction in grinding. *Production Engineering. Research Development* 3:111-120
- Backer W.R., Marshall E.R., and Shaw M.C.(1952) The size effect in metal cutting, *Transaction of the ASME* 74:61-72
- Bağci E. (2011) 3-D numerical analysis of orthogonal cutting process via mesh-free method. *Int. Journal of the Physical Sciences* 66(6): 1267-1282

- Barge M., Kermouche G., Gilles P., Bergheau J.M. (2003) Experimental and numerical study of the ploughing part of abrasive wear. *Wear* 255: 30-37
- Barge M., Rech J., Hamdi H., Bergheau J.-M. (2008) Experimental study of abrasive process. *Wear* 264: 382-388
- Bathe K.-J. (1996) *Finite element procedures*. Prentice Hall, Upper Saddle River, New Jersey 07458
- Batra R.C., Liu D.S. (1990) Adiabatic shear banding in dynamic plane strain compression of a viscoplastic material. *International Journal of Plasticity* 6: 231-246
- Bäker M., Rösler J., Siemers C. (2002) A finite element model of high speed metal cutting with adiabatic shearing. *Computers & Structures* 80: 495-513
- Belhadi S., Mabrouki T., Rigal J-F., Boulanouar L (2005) Experimental and numerical study of chip formation during straight turning of hardened AISI 4340 steel. *Proceedings of the Institution of Mechanical Engineers, Part B: Journal of Engineering Manufacture* 219: 515-524
- Bil H., Kılıç S.E., Tekkaya A.E. (2004) A comparison of orthogonal cutting data from experiments with three different finite element models. *International Journal of Machine Tools and Manufacture* 44:933-944
- Brinksmeier E. and Glwerzew A. (2003) Chip formation mechanisms in grinding at low speeds. *CIRP Annals – Manufacturing Technology* 52(1): 253-258
- Brinksmeier E., Aurich J.C., Govekar E., Heinzl C., Hoffmeister H.-W., Klocke F., Peters J., Rentsch D., Stephenson D.J., Ulmann E., Weinert K., Wittmann M. (2006) *Advances in Modeling and Simulation of Grinding Processes*. *Annals of the CIRP* 55(2): 667-696
- Bucaille J.L., Felder E., Hochstetter G. (2001) Mechanical analysis of the scratch test on elastic and perfectly plastic materials with the three-dimensional finite element modelling. *Wear* 249: 422-432
- Buttery T.C. and Hamed H.S. (1977) Some factors affecting the efficiency of individual grits in simulated grinding experiments. *Wear* 44: 231-245
- Calamaz M., Coupard D., Girot F. (2008) A new material model for 2D numerical simulation of serrated chip formation when machining titanium alloy Ti-6Al-4V. *International Journal of Machine Tools and Manufacture* 48: 275-288
- Calamaz M., Coupard D., Nouari M., Girot F. (2011) Numerical analysis of chip formation and shear localization processes in machining the Ti-6Al-4V titanium alloy. *The International Journal of Advanced Manufacturing Technology* 52: 887-895
- Carslaw, H.S. and Jaeger, J.C. (1959) *Conduction of heat in solids* (second edition). Clarendon Press, Oxford

- Chae J., Park S.S., Freiheit T. (2006) Investigation of micro cutting operations. *International Journal of Machine Tools and Manufacture* 46: 313-332
- Chen X. and Rowe W.B. (1996^a) Analysis and simulation of the grinding process. Part II: Mechanics of Grinding. *International Journal of Machine Tools and Manufacture* 36(8): 883-896
- Chen X. and Rowe W.B. (1996^b) Analysis and simulation of the grinding wheel process. Part I: Generation of the Grinding Wheel Surface. *International Journal of Machine Tools and Manufacture* 36(8): 871-882
- Chen X., Rowe W.B., Mills B. and Allanson D.R. (1996) Analysis and simulation of the grinding process. Part III: Comparison with Experiment. *International Journal of Machine Tools and Manufacture* 36(8): 897-906
- Chen X., Rowe W.B., Mills B. and Allanson D.R. (1998) Analysis and simulation of the grinding process. Part IV: Effects of Wheel Wear. *International Journal of Machine Tools and Manufacture* 36(1-2): 41-49
- Childs T.H.C, Maekawa K., Obikawa T., and Yamane Y. (2000) *Metal machining: theory and applications*, Arnold England
- Childs T.H.C. (2009) Modelling orthogonal machining of carbon steels. Part I: Strain hardening and yield delay effects. *International Journal of Mechanical Sciences* 51: 402-411
- Childs T.H.C. (2010) Surface energy, cutting edge radius and material flow stress size effects in continuous chip formation of metals. *CIRP Journal of Manufacturing Science and Technology* 3: 27-39
- Chong S., Jiangmin D., Lida Z. (2011) Simulation research on cutting process on single abrasive grain based on FEM and SPH method. *Advanced Materials Research* 186:353-357
- Chuang, T.-J., Jahanmir, S., Tang, H. C. (2003) Finite element simulation of straight plunge grinding for advanced ceramics. *Journal of the European Ceramic Society* 23(10): 1723-1733
- Doman, D.A. (2008) *Rubbing and Ploughing in Single Grain Grinding*. PhD Thesis, Dalhousie University, Canada
- Doman D.A., Bauer R., Warkentin A. (2009^a) Experimentally validated finite element model of the rubbing and ploughing phases in scratch tests. *Proceedings of the Institution of Mechanical Engineers, Part B: Journal of Engineering Manufacture* 223:1519-1527
- Doman D.A., Warkentin A., Bauer R. (2009^b) Finite element modelling approaches in grinding. *International Journal of Machine Tools and Manufacture* 49:109-116
- Dornfield D. A. (1999) Process monitoring and control for precision manufacturing. *Production Engineering* 6:29-34

- Doyle E.D. (1973) On the formation of a quick stop chip formation during single grit grinding. *Wear* 24: 249-253
- El-Magd E., Treppmann C., and Korthäuer M. (2003) Constitutive modelling of CK45N, AlZnMgCu1.5 and Ti-6Al-4V in a wide range of strain rate and temperature. *Journal de Physique IV (Proceedings)* 110(1): 141-146
- Farmer D.A., Brecker J.N., Shaw M.C. and Nakayama K. (1967) Study of the finish produced in surface grinding. *Proceedings of the Institution of Mechanical Engineers, Conference Proceedings* pp: 171-179
- Fang L., Cen Q., Sun K., Liu W., Zhang X., Huang Z. (2005) FEM computation of groove ridge and Monte Carlo simulation in two-body abrasive wear. *Wear* 258: 265-274
- Feng B.F. and Cai G.Q. (2001) Experimental study on the single grit grinding titanium alloy TC4 and superalloy GH4169. *Key Engineering Materials* 202-203: 115-120
- Garrison Jr W.M. and Moody N.R. (1987) Ductile fracture. *Journal of Physics and Chemistry of Solids* 48 (11): 1035-1074
- Ghosh S., Chattopadhyay A.B., Paul S. (2008) Modelling of specific energy requirement during high-efficiency deep grinding. *International Journal of Machine Tools and Manufacture* 48: 1242-1253
- Ghosh S., Chattopadhyay A.B., Paul S. (2010) Study of grinding mechanics by single grit grinding. *International Journal of Precision Technology* 1(3-4): 356-367
- Gonzalez R. C., Woods R. E., Eddins S. L. (2004) *Digital Image Processing Using MATLAB®*, Pearson Prentice-Hall, Pearson Education, Inc. Upper Saddle River, New Jersey 07458
- Griffin J. (2007) Pattern recognition of micro and macro grinding phenomenon with a generic strategy to machine process monitoring. PhD Thesis, University of Nottingham, UK
- Guo Y.B., and Yen D.Y. (2004) A FEM study on mechanisms of discontinuous chip formation in hard machining. *Journal of Materials Processing Technology* 155-156: 1350-1356
- Günay M., Aslan E., Korkut I., and Seker U. (2004) Investigation of the effect of rake angle on main cutting force. *International Journal of Machine Tools and Manufacture* 44: 953-959
- Hahn R.S. (1962) On the nature of the grinding process. *Proceeding of the 3rd International Machine Tool Design & Research Conference*, pp: 129-154 (Pergamon Press, Manchester)
- Hagadekotte V., Huber N., Kraft O. (2005) Finite element based simulation of dry sliding wear. *Modelling and Simulation in Materials Science and Engineering* 13: 57-75
- Hamdi H., Zahouani H., Bergheau J.-M. (2004) Residual stresses computation in a grinding process. *Journal of Materials Processing Technology* 147: 277-285

- Hassui A., Diniz A.E., Oliveira J.F.G., Felipe J. and Gomes J.J.F. (1998) Experimental evaluation on grinding wheel wear through vibration and acoustic emission. *Wear* 217: 7-14
- Heinstein M. and Segalman D. (1997) Simulation of orthogonal cutting with Smooth Particle Hydrodynamic. Sandia National Laboratories, California
- He M. and Li F. (2010) Modified transformation formulae between fracture toughness and CTOD of ductile metals considering pre-deformation effects. *Engineering Fracture Mechanics* 77: 2763-2771
- Hillerborg A., Modeer M., and Petersson P.E. (1976) Analysis of crack formation and crack growth in concrete by means of fracture mechanics and finite Elements. *Cement and Concrete Research* 6: 773–782
- Hou Z.B. and Komanduri R. (2003) On the mechanics of the grinding process – Part I. Stochastic nature of the grinding process. *International Journal of Machine Tools and Manufacture* 43: 1579-1593
- Hortig C. and Svendsen B. (2007) Simulation of chip formation during high-speed cutting. *Journal of Materials Processing Technology* 186: 66-76
- Hsu N.N. and Breckenridge F.R. (1981) Characterization and calibration of acoustic emission sensors. *Materials Evaluation* 39: 60-68
- Huang J.M., Black J.T. (1996) An Evaluation of chip separation criteria for the fem simulation of machining. *Journal of Manufacturing Science and Engineering – Transactions of the ASME* 118: 545-554
- Hwang T.W., Whitenton E.P., Hsu N.N., Blessing G.V., Evans C.J. (2000) Acoustic emission monitoring of high speed grinding of silicon nitride. *Ultrasonics* 38: 614-619
- Iqbal S.A., Mativenga P.T. and Sheikh M.A. (2007) Characterization of machining of AISI 1045 steel over a wide range of cutting speeds. Part2: evaluation of flow stress models and interface friction distribution schemes. *Proceedings of the Institution of Mechanical Engineers, Part B: Journal of Engineering Manufacture* 221: 917-926
- Iqbal S.A., Mativenga P.T. and Sheikh M.A. (2008) Contact length prediction: mathematical models and effect of friction schemes on FEM simulation for conventional to HSM of AISI 1045 steel. *International Journal of Machining and Machinability of Materials* 3(1/2): 18-33
- Iturrospe A., Dornfield D., Atxa V., Abete J.M. (2005) Bicepstrum based blind identification of the acoustic emission (AE) signal in precision turning. *Mechanical Systems and Signal Processing* 19: 447-466
- Jaeger J.C. (1942) Moving heat sources of heat and the temperature at sliding contacts. *Proceeding of the Royal Society of New South Wales* 76(3): 202-224

- Jaspers S.P.F.C. and Dautzenberg J.H. (2002^a) Material behaviour in metal cutting: strains, strain rates and temperatures in chip formation. *Journal of Materials Processing Technology* 121: 123-135
- Jaspers S.P.F.C. and Dautzenberg J.H. (2002^b) Material behaviour in conditions similar to metal cutting: flow stress in the primary shear zone. *Journal of Materials Processing Technology* 122: 322-330
- Jinsheng W., Yadong G., Gabriel A., Jean A.F, Jiashun S. (2009) Chip formation analysis in micromilling operation. *The International Journal of Advanced Manufacturing Technology* 45: 430-447
- Johnson G.R. and Cook W.H. (1983) A constitutive model and data for metals subjected to large strains, high strain rates and high temperatures. *Proceeding of the seventh international symposium on ballistics, Hague, Netherland*, pp: 541-547
- Johnson G.R. and Cook W.H. (1985) Fracture characteristics of three metals subjected to the various strains, strain rates, temperatures and pressures. *Engineering Fracture Mechanics* 21: 31-48
- Kannappan S. and Malkin S. (1972) Effects of grain size and operating parameters on the mechanics of grinding. *Journal of Engineering for Industry – Transactions of the ASME* 94(3): 833-842
- Klocke F., Beck T., Hoppe S., Krieg T., Müller N., Nöthe T., Raedt H.-W., Sweeney K. (2002) Examples of FEM application in manufacturing technology. *Journal of Materials Processing Technology* 120(1-3): 450-457
- Klocke F. (2003) Modelling and Simulation of grinding process. 1st European Conference on Grinding, Aachen 6-7 November, 2003
- Komanduri R. (1971) Some aspects of machining with negative rake tools simulating grinding. *International Journal of Machine Tool Design and Research* 11: 223-233
- König W., Steffens K. and Ludewig T. (1985) Single grit tests to reveal the fundamental mechanism in grinding, in: Milton C. Shaw (Ed.) *Grinding Symposium*, Miami Beach, FL, pp: 141-154
- Kun L., and Liao T.W. (1997) Modelling of ceramic grinding processes. Part I. Number of cutting points and grinding forces per grit. *Journal of Materials Processing Technology* 65(1-3): 1-10
- Lai X., Li H., Li C., Lin Z., Ni J. (2008) Modelling and analysis of micro scale milling considering size effect, micro cutter edge radius and minimum chip thickness. *International Journal of Machine Tools and Manufacture* 48: 1-14
- Lambropoulos J.C., Xu S., Fang T., and Golini D. (1996) Twyman effect mechanics in grinding and microgrinding. *Applied Optics* 35(28): 5704-5713

- Lee D.E., Hwang I., Valente C.M.O., Oliveira J.F.G., Dornfield D.A. (2006) Precision manufacturing process monitoring with acoustic emission. *International Journal of Machine Tools and Manufacture* 46: 76-188
- Li J. and Beres W. (2006) Three-dimensional finite element modelling of the scratch test for a TiN coated titanium alloy substrate. *Wear* 260: 1232-1242
- Liu W.J., Pei Z.J., and Xin X.J. (2002) Finite element analysis for grinding and lapping of wire-sawn silicon wafers. *Journal of Materials Processing Technology* 129 (1): 2-9
- Lorentzon J., Järvståt J.N., and Josefson B.L. (2009) Modelling chip formation of alloy 718. *Journal of Materials Processing Technology* 209: 4645-4653
- Mabrouki T., Girardin F., Asad M., Rigal J.F. (2008) Numerical and experimental study of dry cutting for an aeronautic aluminium alloy (A2024-T351). *International Journal of Machine Tools and Manufacture* 48: 1187-1197
- Mackarle J. (2003) Finite element analysis and simulation of machining: an addendum: A bibliography (1996-2002). *International Journal of Machine Tools and Manufacture* 43(1): 103-114
- Maekawa K., Shirakashi T., and Usui E. (1983) Flow stress of low carbon steel at high temperature and high strain rate (part2) – flow stress under variable temperature and variable strain rate. *Bulletin of the Japan Society of Precision Engineering* 17(3): 167-172
- Maksoud T. M. A., Atia M.R., Koura M.M. (2003) Applications of artificial intelligence to grinding operations via neural networks. *Machining Science and Technology* 7(3): 361-387
- Malkin S. and Guo C. (2008) *Grinding Technology Theory and Application of Machining with Abrasives*, second edition, Industrial Press Inc., New York.
- Marusich T.D. and Ortiz M. (1995) Modelling and simulation of high speed machining. *International Journal for Numerical Methods in Engineering* 38: 3675-3694
- Matsuo T., Toyoura S., Oshima E., Ohbuchi Y. (1989) Effect of grain shape on cutting force in superabrasive single grit tests. *Annals of the CIRP* 38(1): 323-326
- Mamalis A.G., Horváth M., Branis A.S., Manolakos D.E. (2001) Finite element simulation of chip formation in orthogonal metal cutting. *Journal of Materials Processing Technology* 110: 19-27
- Mamalis A.G., Kundrak J., Manolakos D.E., Gyani K., and Markopoulos A. (2003) Thermal modeling of surface grinding using implicit finite element techniques. *The International Journal of Advanced Manufacturing Technology* 21: 929-934
- Mahdi M. and Zhang L. (1995) The finite element thermal analysis of grinding processes by ADINA, *Computers & Structures* 56: 313-320

- Mahdi M. and Zhang L. (2000) A numerical algorithm for the full coupling of mechanical deformation thermal deformation, and phase transformation in surface grinding. *Computational Mechanics* 26: 148-156
- Merchant M.E. (1945) Mechanics of the metal cutting process. *Journal of Applied Physics* 16: 267-277
- Movahhedy M.R., Gadala M.S. and Altintas Y. (2000) Simulation of Chip Formation in Orthogonal Metal Cutting Process: An ALE Finite Element Approach. *Machining Science and Technology* 4(1): 15-42
- Moulik P.N., Yang H.T.Y., and Chandrasekar S. (2001) Simulation of thermal stresses due to grinding. *International Journal of Mechanical Sciences* 43(3): 831-851
- Nakayama K., Takagi J., and Abe T. (1977) Grinding wheel with helical grooves – an attempt to improve the grinding performance. *Annals of the CIRP* 25 (1): 133-138
- Oluwajobi, A.O. and Chen. X. (2010) The fundamentals of modelling abrasive machining using molecular dynamics. *International Journal of Abrasive Technology* 3(4): 354-381
- Ohbuchi Y. and Matsuo T. (1991) Force and chip formation in single grit orthogonal cutting with shaped CBN and diamonds grains. *Annals of the CIRP* 40(1): 327-330
- Ohbuchi Y. and Obikawa T. (2003) Finite element modelling of chip formation in the domain of negative rake angle cutting. *Journal of Engineering Materials and Technology Transaction of the ASME* 125: 324-332
- Ohbuchi Y. and Obikawa T. (2006) Surface generation model in grinding with effect of grain shape and cutting speed. *JSME International Journal Series C Mechanical Systems, Machine Elements and Manufacturing* 49(1): 114-120
- Öpöz T.T. and Chen X. (2012) Influential parameters in determination of chip shape in high speed machining. *Key Engineering Materials* 496: 211-216
- Oxley, P.L.B. (1989) *Mechanics of Machining: An analytical approach to assessing machinability*, London: Ellis Horward
- Özel T. (2006) The influence of friction models on finite element simulations of machining. *International Journal of Machine Tools and Manufacture* 46: 518-530
- Özel T. and Zeren E. (2007) Finite element modeling the influence of edge roundness on the stress and temperature fields induced by high speed machining. *The International Journal of Advanced Manufacturing Technology* 35: 255-267
- Özel T (2009) Computational modelling of 3-D turning with variable edge design tooling: Influence of micro-geometry on forces, stresses, friction and tool wear. *Journal of Materials Processing Technology* 209: 5167-5177

- Park H.W., Liang S.Y., and Chen R. (2007) Microgrinding force predictive modeling based on microscale single grain interaction analysis. *International Journal of Manufacturing Technology and Management* 12 (1): 25-38
- Pantalé O., Bacaria J-L., Dalverny O., Rakotomalala R., Caperaa S. (2004) 2D and 3D numerical models of metal cutting with damage effects. *Computers Methods in Applied Mechanics and Engineering* 193: 4383-4399
- Ram A., Danckert J. and Faurholdt T. (2003) Finite element analysis of stresses due to normal and sliding contact conditions on an elastic surface. 4th European LS-DYNA Users Conference, pp: 21-34
- Racy A., Elmadagli M., Altenhof W.J., and Alpas A.T. (2004) An Eulerian finite-element model for determination of deformation state of a copper subjected to orthogonal cutting. *Metallurgical and Materials Transactions A* 35A: 2393-2400
- Ramezani M., Ripin Z.M. (2010) Combined experimental and numerical analysis of bulge test at high strain rates using split Hopkinson pressure bar apparatus. *Journal of Materials Processing Technology* 210: 1061-1069
- Rhim S.-H. and Oh S.-I. (2006) Prediction of serrated chip formation in metal cutting process with new flow stress model for AISI 1045 steel. *Journal of Materials Processing Technology* 171: 417-422
- Rowe W.B. and Chen X. (1997) Characterization of the size effect in grinding and the sliced bread analogy. *International Journal of Production Research* 35(3): 887-899
- Rowe W.B., Black S.C.E., Mills B., Morgon M.N., Qi H.S. (1997) Grinding temperatures and energy partitioning. *Proceeding of the Royal Society of London. Series A: Mathematical, Physical and Engineering Sciences* 453(1960): 1083
- Rowe, W.B. (2009) *Principles of Modern Grinding Technology*. William Andrew Publishing
- Ruttimann N., Buhl S. and Wegener K. (2010) Simulation of single grain cutting using SPH method. *Journal of Machine Engineering* 10(3): 17-29
- Sathyanarayanan G., Lin I.J., Ming K.C. (1992) Neural network modelling and multiobjective optimization of creep feed grinding of superalloys. *International Journal of Production Research* 30(10):2422-2438
- Shaw M.C. (1950) A quantized theory of strain hardening as applied to the cutting of metals. *Journal of Applied Physics* 21(6): 599-606
- Shaw M.C. (1971) A new theory of grinding. *Proceedings of the International Conference on Science in Industry*, Monash University, Australia, pp: 1-6
- Shaw M.C. (1995) Precision finishing, *Annals of the CIRP* 44 (1): 343-348
- Shaw M.C. (1996) *Principles of Abrasive Processing*. Clarendon Press, Oxford

- Soo S.L., Aspinwall D.K. and Dewes R.C. (2004) 3D FE modelling of the cutting of Inconel 718. *Journal of Materials Processing Technology* 150: 116-123
- Sima M. and Özel T. (2010) Modified material constitutive models for serrated chip formation simulations and experimental validation in machining of titanium alloy Ti-6Al-4V. *International Journal of Machine Tools and Manufacture* 50: 943-960
- Strenkowski J. S. and Carroll J.T. (1985) A finite element model of orthogonal metal cutting. *Journal of Engineering for Industry – Transactions of the ASME* 107: 347-354
- Shet C. and Deng X. (2000) Finite element analysis of the orthogonal metal cutting process. *Journal of Materials Processing Technology* 105: 95-109
- Sisto T.S.D., Carr F.L. and Larson F.R. (1964) The influence of section size on the mechanical properties and fracture toughness of 7075-T6 aluminium, 6Al-6V-2Sn titanium, and AISI 4340 steel. Material testing laboratory U.S. Army Materials Research Agency Watertown, Massachusetts
- Takenaka N. (1966) A study on the grinding action by single grit. *Annals of the CIRP* 13: 183-190
- Tawakoli T. (1993) High Efficiency Deep Grinding, VDI – Verlag GmbH and Mechanical Engineering Publications, London
- Taylor Habson precision (2006) Talysurf CCI 3000 manual
- Teng X. and Wierzbicki T. (2006) Evaluation of six fracture models in high velocity perforation. *Engineering Fracture Mechanics* 73: 1653-1678
- Tönshoff H.K., Peters J., Inasaki I. and Paul T. (1992) Modelling and Simulation of Grinding Processes. *Annals of the CIRP* 41(2): 677-688
- Usui, E. And Shirakashi T. (1982) Mechanics of machining- ‘From descriptive to predictive theory’ On art of cutting metals – 75 years later. *ASME Production Engineering Division* 7: 13-35
- Vaziri M.R., Salimi M. and Mashayekhi M. (2011) Evaluation of chip formation simulation models for material separation in the presence of damage models. *Simulation Modelling Practice and Theory* 19: 718-733
- Wang H. and Subbash G. and Chandra A. (2001) Characteristics of single grit rotating scratch with a conical tool on pure titanium. *Wear* 249: 566-581
- Wang J., Gong Y., Abba G., Francois J. and Shi J. (2009) Chip formation analysis in micromilling operation. *The International Journal of Advanced Manufacturing Technology* 45: 430-447
- Wanheim T. and Bay N. (1978) A model for friction in metal forming processes. *Annals of the CIRP* 27(1): 189-194

- Woon K.S., Rahman M., Fang F.Z., Neo K.S., and Liu K. (2008) Investigations of tool edge radius effect in micromachining: A FEM simulation approach. *Journal of Materials Processing Technology* 195: 204-211
- Wu H.Y., Lee W.B., Cheung C.F., To S. and Chen Y.P. (2005) Computer simulation of single-point diamond turning using finite element method. *Journal of Materials Processing Technology* 167: 549-554
- Xiaozhi, Hu (2011) Size effect on tensile softening relation. *Materials and Structures* 44:129-139
- Xie J.Q., Bayoumi A.E. and Zbib H.M. (1996) A study on shear banding in chip formation of orthogonal machining. *International Journal of Machine Tools and Manufacture* 36(7): 835-847
- Yao Y., Schlesinger M. and Drake G.W. (2004) A multiscale finite-element method for solving rough-surface elastic-contact problems. *Canadian Journal of Physics* 82: 679-699
- Zerilli F. J. and Armstrong R.W. (1987) Dislocation mechanics based on constitutive relations for materials dynamics calculations. *Journal of Applied Physics* 61(5): 1816-1825
- Zhang L. (1994) Grindability of some metallic and ceramic materials in CFG regimes. *International Journal of Machine Tools and Manufacture* 34(8): 1045-4057
- Zhang B. and Peng X. (2000) Grinding damage prediction for ceramics via CDM model. *Journal of Manufacturing Science and Engineering* 122: 51-58
- Zerilli F. J. and Armstrong R.W. (1987) Dislocation mechanics based on constitutive relations for materials dynamics calculations. *Journal of Applied Physics* 61(5): 1816-1825
- Zorev M.N. (1963) Inter-relationship between shear processes occurring along tool face and shear plane in metal cutting. *International Research in Production Engineering*, ASME, New York, pp: 42-49